Respiratory Adaption to Running Exercise : A Behavioral and Neuronal Circuits Study in Mice

Coralie Herent

Thèse de doctorat

NNT : 2021UPASL001

université PARIS-SACLAY

Respiratory adaptation to running exercise: a behavioral and neuronal circuits study in mice

Thèse de doctorat de l'université Paris-Saclay

École doctorale n°568 : signalisations et réseaux intégratifs en biologie (Biosigne)
Spécialité de doctorat : Sciences de la vie et de la santé
Unité de recherche : Université Paris-Saclay, CNRS, Institut des neurosciences Paris-Saclay, 91190, Gif-sur-Yvette, France.
Référent : Faculté de médecine

Thèse présentée et soutenue à Gif-sur-Yvette, le 29/01/2021, par

Coralie HERENT

Composition du Jury

Micaela GALANTE PU, Université Paris-Saclay	Présidente
Réjean DUBUC Directeur, Professeur, Université du Québec à Montréal	Rapporteur & Examinateur
Nicolas VOITURON PU, Université Sorbonne Paris Nord	Rapporteur & Examinateur
Pascal BRANCHEREAU PU, Université de Bordeaux	Examinateur
Matilde CORDERO-ERAUSQUIN CR, HDR, Université de Strasbourg	Examinatrice
Julien BOUVIER CR, Université Paris-Saclay	Co-directeur de thèse
Gilles FORTIN DR, Ecole Normale Supérieure	Co-directeur de thèse

TABLE OF CONTENTS

LIST OF SCIENTIFIC PAPERS

Paper 1

Hérent C, Diem S, Fortin G and Bouvier J. 2020. Absent phasing of respiratory and locomotor rhythms in running mice. eLife. 2020;9:e61919. doi: 10.7554/eLife.61919.

Paper 2

Hérent C, Diem S, Fortin G and Bouvier J. Distinct neuronal drives from locomotor circuits upregulate breathing rate during running exercise. (Manuscript).

Paper 3 (Annex 1)

Usseglio G, Gatier E, Heuzé A, **Hérent C**, Bouvier J. 2020. Control of Orienting Movements and Locomotion by Projection-Defined Subsets of Brainstem V2a Neurons. Current Biology. 2020;S0960-9822(20)31345-2. doi:10.1016/j.cub.2020.09.014.

Paper 4 (Annex 2)

Skarlatou S, **Hérent C**, Toscano E, Mendes CS, Bouvier J, Zampieri N. 2020. Afadin Signaling at the Spinal Neuroepithelium Regulates Central Canal Formation and Gait Selection. Cell Reports. 31(10):107741. doi:10.1016/j.celrep.2020.107741.

INTRODUCTION

This PhD work will address interactions between the respiratory and the locomotor central networks that support rapid adaptation to exercise of the respiratory neural command. The metabolic adaptation to exercise is complex and integrates cardio-vascular and respiratory changes. Clearly, lung ventilation, cardiac output, and blood pressure are highly labile physiological variables that are continually adjusted by the central nervous system to match the metabolic requirements of specific behaviors (Bevan et al., 1969; Feldman et al., 2003). I have focused my interest on the interface of respiratory and locomotor circuits and thus will not touch upon the circuits controlling attendant cardiovascular responses. As my work will reveal, a respiratory node of this interface is the RTN, a structure known to mediate the chemoreflex, an increase in breathing in response to elevated blood CO_2 ($PaCO_2$). Using $PaCO_2$ as a guide, I will now briefly expose ventilatory/cardiovascular interplays that must take place in parallel to the regulations that my work will unveil that future work should attempt to dissect with the tools deployed in my work.

Unlike lung ventilation, $PaCO_2$ usually remains constant around a set-point that is characteristic of a particular individual (Haldane and Priestley, 1905). This classic example of homeostatic regulation suffers few exceptions. For example, under hypoxia and/or during strenuous exercise, $PaCO_2$ falls because maintaining the oxygen supply takes priority over the need to keep CO_2 constant. Such temporary deviations from homeostasis are adaptive and in keeping with the concept of stability through change. The mechanisms that maintain CO_2 constant despite large variations in the metabolic production of this gas are complex (Forster et al., 2012). For example, during exercise, central command, and reflexes originating from muscle mechano- and metabotropic receptors cooperate to activate breathing to a degree roughly commensurate with the rise in whole body metabolism and CO_2 production (Eldridge et al., 1985; Eldridge, 1994; Dempsey, 2012).

The cardiovascular effects of hypercapnia result from influence of CO_2 at multiple levels and involves sympathetic and parasympathetic mediation (Ursino et al., 2001). CO_2 tends to lower arterial pressure while chemoreceptor stimulation activates the sympathetic nervous system which counteracts, via vasoconstriction, and increases the cardiac output. As a result, arterial pressure may change and engage baroreceptor feedbacks to mitigate or potentiate the effects of chemoreceptors. Chemoreceptor stimulation activates the respiratory central generator which increases breathing and has multiple effects on the neural control of the circulation. For example, increased discharge of sensory afferents from the lung reflexively inhibits cardio-vagal parasympathetic outflow, increasing heart rate and thereby contributing to raising cardiac output. The respiratory central generator also inhibits cardio-vagal preganglionic neurons to increase the heart rate.

Integrating all these components in the physiological adaptation to exercise would be a daunting task, by considering here respiration only, I propose a first delineation of respiratory and locomotor neural nodes crucial for respiratory adaptation to exercise. This together with the help of the methodological tools used in my work paves the way for later

description, with cellular and synaptic resolutions, of the putative implication of these nodes in cardio-respiratory adaptation to exercise.

Chapter 1: Interactions between respiration and locomotion

From birth to death we breathe in a continuous and reliable manner to ensure the essential gas exchanges necessary for life in all mammals. Although breathing[1] is a rhythmic and autonomous behavior, it is precisely modulated by the metabolic demand which is impacted by changes in internal or external states and strongly influenced by other motor behaviors. The adaptations that breathing undergoes during locomotion or exercise are probably the most striking examples. Indeed, when animals move, whether it is to hunt, escape predators, feed or mate, the demand in oxygen (O_2) and the production of carbon dioxide (CO_2) increase to match the augmented metabolism. In support to this, respiration[1] must increase, and the particular signatures have been commonly described in the literature: **1)** an increase in breathing depth and rate (or hyperpnea[1]), **2)** a transition from passive to forced, or active, expiration and **3)** a possible temporal synchronization (or phase-locking) between respiratory and locomotor rhythms.

I. Characteristics and specifications of hyperpnea during running

Examining the specifications of respiratory changes during running, and the interaction between respiratory and locomotor rhythms, helps formulate hypothesis regarding the underlying physiological substrate. *We will therefore present here the major signatures of respiratory changes during running, together with the associated ambiguities.*

1. An immediate response

In most species including humans, respiratory adaptation to exercise, is most commonly studied during running tasks on a motorized treadmill or an ergometer. On these, it appears that the key signature is an abrupt increase of breathing frequency, often accompanied by an increase in respiratory amplitude, altogether termed hyperpnea. These changes are immediate at the onset of exercise in humans, horses, sheep, dogs and mice running on a treadmill (Figure 1.1A, B) (Krogh, 1913; Dejours et al., 1959; Flandrois et al., 1971; Pearce and Milhorn, 1977; Robinson, 1985; Mateika and Duffin, 1992, 1995; Haouzi et al., 2004; Tsuchiya et al., 2012).

2. A possible dependency on limb velocity

In addition to being immediate, the respiratory increase to exercise has been classically defined as commensurate to the speed of the treadmill or the pace of cycling in humans, suggesting a dependence of exercise hyperpnea on the velocity of limb movements (Dejours et al., 1959; Duffin and Bechbache, 1983; Casey et al., 1987; Mateika and Duffin, 1995; Wells et al., 2007). Very little documentation is available for other mammals, although similar observations have been reported in horses and ponies (Figure 1.1C) (Pan et al., 1983; Honda, 1985; Robinson, 1985). However, contradictory findings can also be found in the literature where no clear influence of the stride rate on ventilation[1] could be established during treadmill exercise sessions in humans (Figure 1.1D) (Kay et al., 1975; Berry et al., 1985; Buono et al., 2015). Interestingly, data in lampreys, distant vertebrates that share a lot of basic features with mammals (Robertson

Respiration: exchange of O_2 and CO_2 across a membrane (lungs or gills). Breathing: qualifies the behavior. Hyperpnea: respiratory frequency & amplitude increase. Ventilation: volume of gas inhaled and exhaled from the lungs per min.

et al., 2014) and use swimming for locomotion, show that respiratory frequency is not dependent on the locomotor frequency (Figure 1.1E) (Gravel et al., 2007). Hence, the dependence of breathing on locomotor velocity remains controversial and we will address this question later in running mice.

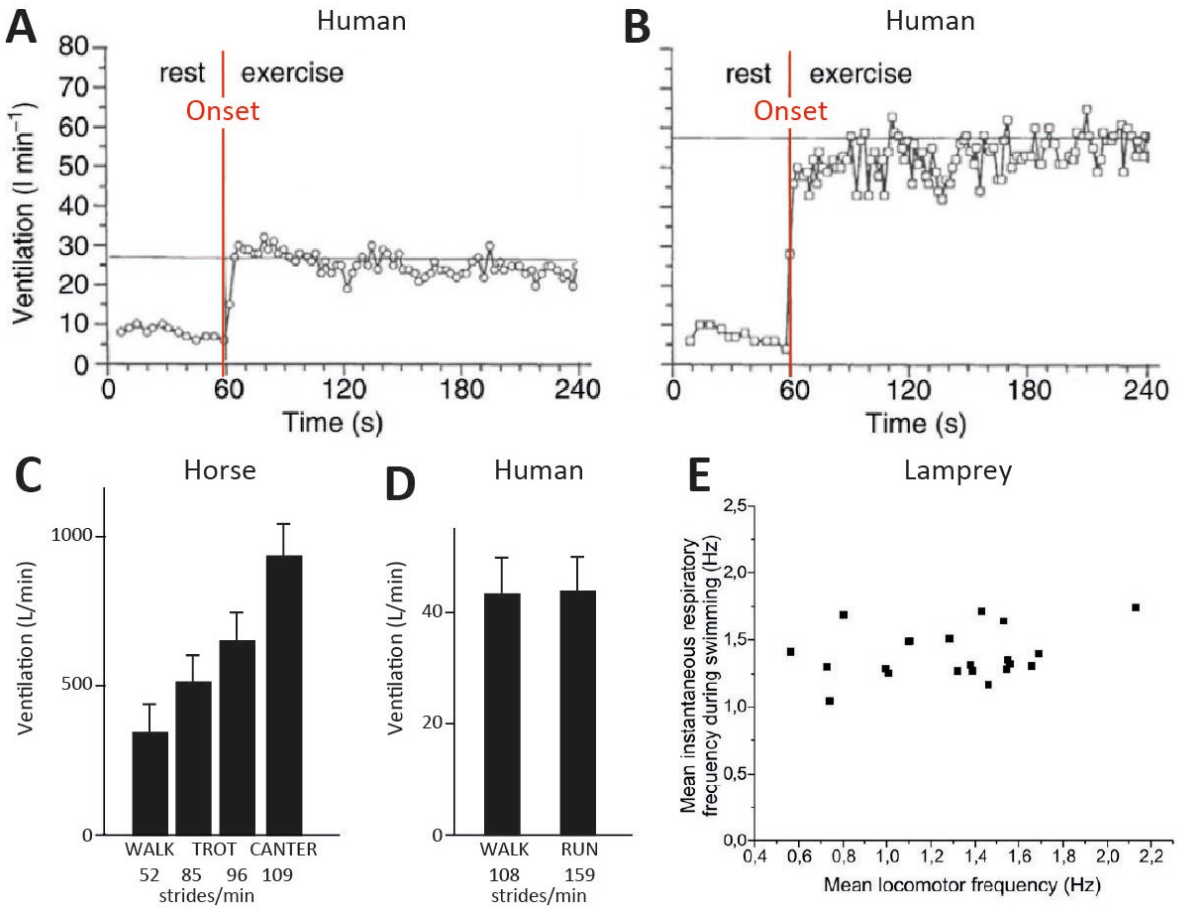

Figure 1.1. Immediate increase in ventilation at the onset of exercise and relation to limb velocity. (A-B) Ventilation change to treadmill exercise in human at a low speed (**A**) and at a faster speed (**B**). Note that the ventilation increase is immediate, at the onset of exercise (red bar). Also, the ventilation increase is greater at the faster speed. Adapted from Duffin (2014). **(C-D)** Ventilation change to different speeds and gaits in horse (**C**) and human (**D**). Note that Lafortuna et al. (1996) show that the ventilation increases in a speed and gait-dependent manner in horses (**C**), while Berry et al. (1985) find that human ventilation is similar during walking and running when the metabolic state is kept stable (**D**). Graphs are compiled from available data in the corresponding studies. **(E)** Frequency change to different swimming frequencies in lampreys, showing no clear relation between respiratory and locomotor frequencies. Adapted from Gravel et al. (2007).

3. Breathing changes can precede movements and occur during fictive exercise

Another important feature of breathing augmentation during exercise is that it may occur even in situations where movements are not performed. For instance, subjects told to imagine cycling or running (without any movement), increase their respiratory rate proportionally to the imagined exercise intensity and the respiratory response is reminiscent to the response seen during actual exercise (Figure 1.2A) (Decety et al., 1991; Decety et al., 1993; Thornton et al., 2001). In addition, when subjects are instructed to move after a given delay, breathing rate increases before the onset of movement (Tobin et al., 1986). Interestingly, studies in cats, geese, and lampreys showed that breathing increases just before a spontaneous movement (Butler and Woakes, 1980; Eldridge et al., 1985; Gariepy et al., 2012) (Figure 1.2B). Therefore, this "anticipatory" exercise hyperpnea seems to be conserved amongst vertebrates and might play a crucial part in mediating important respiratory changes (but also cardiovascular changes (Decety et al., 1993; Thornton et al., 2001)) in preparation of exercise, to anticipate important forthcoming metabolic changes.

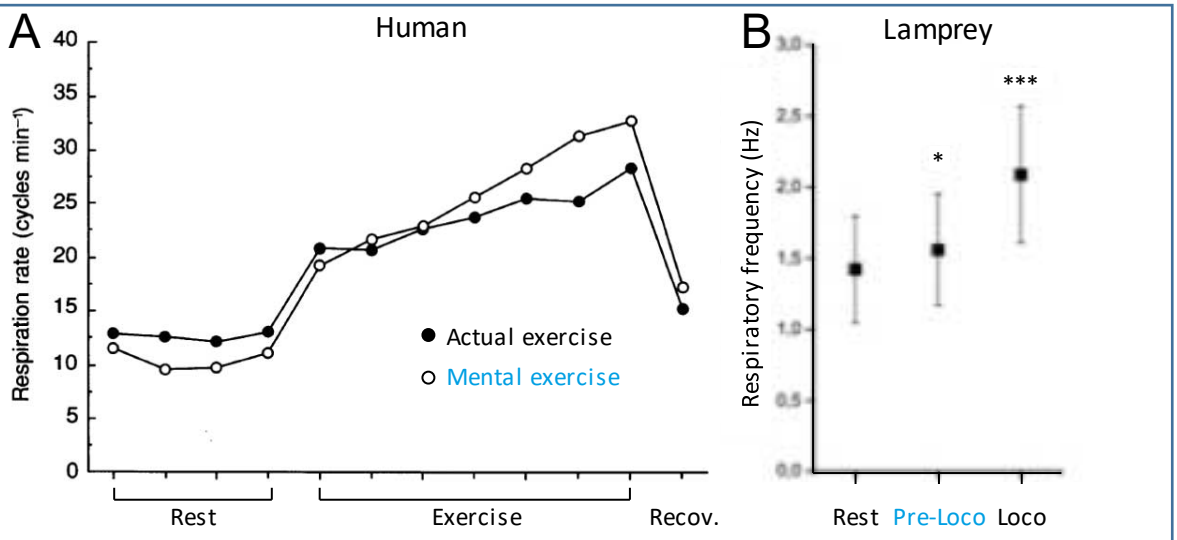

Figure 1.2. Breathing increase can occur without, and even prior to, the movement. (A) Respiratory rate in human at rest, during actual (black circle) or mental (white circle) exercise, and after exercise (Recov.). Note the increase in breathing frequency during mental exercise, similar to an actual exercise. Adapted from Decety et al. (1993). **(B)** Respiratory frequency in lamprey at rest, before (pre-Loco) and during (Loco) bouts of swimming. Note the increase in frequency prior to the movement. Adapted from Gariepy et al. (2012).

4. The mobilization of active expiration

Breathing is based on permanent rhythmic movements of the rib cage enabling the repetition of sequential inspiratory and expiratory phases. Inspiration is a systematically active mechanism which involves the concerted muscular contraction of dedicated inspiratory pump muscle groups, of which the diaphragm is the main muscle. Instead, expiration is a passive mechanism at rest due mainly to the relaxation of the inspiratory muscles and lung recoil. However, under certain physiological conditions where the respiratory drive is increased, like

during high level exercise, forced or active expiration takes place (Iscoe, 1998; Jenkin and Milsom, 2014). The abdominal "expiratory" muscles become actively involved in breathing to produce rapid exhalation and enhance even more respiratory rate and volume. The level of activation of abdominal muscles in mammals during exercise tends to increase as a function of exercise intensity in ponies, dogs and humans (Figure 1.3) (Gutting et al., 1988; Ainsworth et al., 1989; Abraham et al., 2002). *We will see in Chapter 2.II.2.a. that a respiratory region, thought to generate active expiration upon increased metabolic demand, might be involved in exercise hyperpnea.*

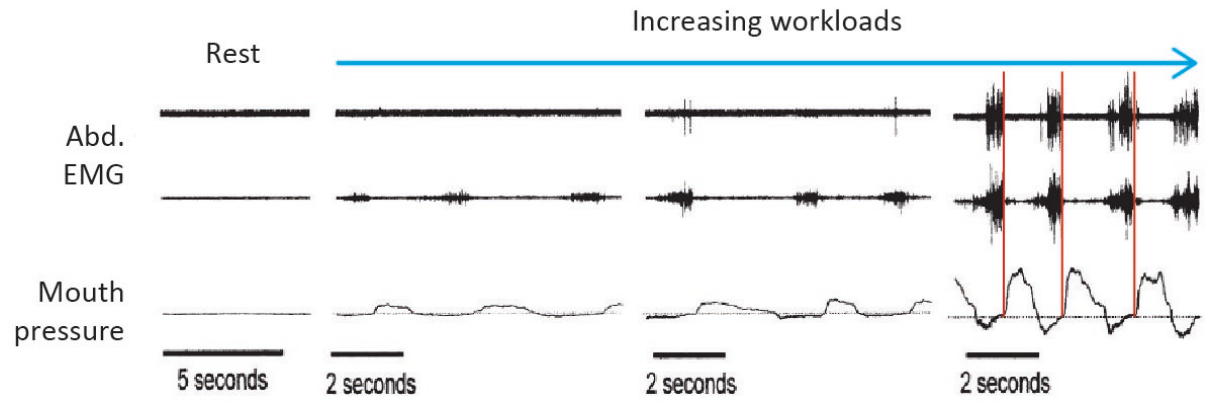

Figure 1.3. Intensity-dependent recruitment of abdominal muscles during exercise. Electromyogram (EMG) of abdominal muscles (top traces, Abd. EMG) and mouth pressure (down trace, inspiration upwards) at rest and during increasing bicycle workloads in one subject. The beginning of each inspiration is highlighted with red lines. Note that abdominal muscles are strongly recruited at high workloads. Adapted from Abraham et al. (2002).

5. A temporal coordination of breathes to strides?

Another feature of respiratory adjustments to exercise that has been alleged in humans and animals is the temporal synchronization of locomotor and respiratory rhythms (Boggs, 2002; Stickford and Stickford, 2014). Initially, studies in humans running on a treadmill or cycling on an ergometer showed that the respiratory frequency was a submultiple of the stride rate (Bannister et al., 1954; Bechbache and Duffin, 1977; Bramble and Carrier, 1983; Corio et al., 1993) and similar observations were made in horses, dogs, sheep, cats, rabbits, hares etc. (Iscoe, 1981; Bramble and Carrier, 1983; Entin et al., 1999; Simons, 1999). On this basis, an indicator has been classically used in the literature, the locomotor-respiratory coupling (LRC), which most often refers to number of locomotor events per breaths (Figure 1.4A) (Bramble and Carrier, 1983; Boggs, 2002; Stickford and Stickford, 2014). For example, a ratio of 1:1 implies that the frequency of respiratory movements is not statistically distinct of that of limb movements. However, this analysis does not speak to a possible synchronization of breaths and strides on a cycle-to-cycle basis. In other words, the fact that the frequencies of respiratory and locomotor movements are related does not imply that breaths systematically occur at the same moment of the stride. This distinction will become extremely relevant when thinking on the neuronal basis of running hyperpnea (see Chapter 1.II.2.). It is important to stress here that some studies have indeed reported that a temporal coupling on a cycle-to-cycle basis can exist. This is notably demonstrated in running-

and flying-performant species like horses and geese, where breaths were found to be phase-locked to limb or wing movements (Figure 1.4B) (Butler and Woakes, 1980; Bramble and Carrier, 1983; Lafortuna et al., 1996). This suggests that one periodic system (i.e., locomotion) exerts an influence on the other (i.e., breathing). Similar observations can be found in humans running on a treadmill (Figure 1.4C, top) (Bramble and Carrier, 1983; Bernasconi and Kohl, 1993). Interestingly, the temporal coupling is more frequent upon engagement in high-speed locomotor gaits like gallop, where one breath is temporally synchronized to each stride, while more variability can be found for lower speeds/gaits (Iscoe, 1981; Bramble and Carrier, 1983; Lafortuna et al., 1996). However, contradictory findings can be found which show heterogeneous degrees of coupling to no coupling at all within the same tested specie in humans and cats (Figure 1.4C, bottom) (Kay et al., 1975; Bechbache and Duffin, 1977; Iscoe, 1981; Bramble and Carrier, 1983; Bernasconi and Kohl, 1993). Also, external auditory stimuli have been shown to improve the degree of temporal coupling on a cycle-to-cycle basis when subjects exercise with a metronome (Bernasconi and Kohl, 1993; van Alphen and Duffin, 1994; Hoffmann et al., 2012). Additionally, studies have found that running or cycling athletes tend to more frequently lock their breaths to

A Locomotor-respiratory coupling LRC in mammals

Species	Gait or speed	LRC ratios
Gerbil	Gallop	1:1
Hare	Half bound	1:1, 2:1
	Galloping	1:1
Domestic rabbit	Gallop	1:1
	Lower speeds	Variable
Cat	Gallop	1:1
Dik-Dik	Gallop	1:1
Dog	Trot	1:1, others
	Gallop	1:1
Sheep	Gallop	1:1
Horse	Trot	1:1, 3:2, 2:1, 5:1
	Gallop	1:1
Rhinoceros	Gallop	1:1
Bat	Flight	1:1
Tammar wallaby	Hopping	1:1
Tree kangaroo	Trot	1:1
Bettong	Hopping	1:1
Potoroo	Gallop	1:1
	Hopping	1:1
Humans	Bipedal running	3:1, 2:1, 5:2, 3:2, 4:1, 7:2

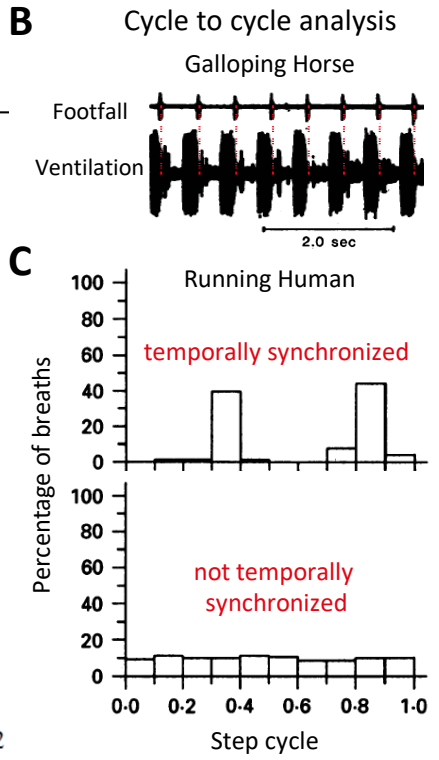

Figure 1.4. Influence of locomotor strides on breaths: locomotor-respiratory coupling (LRC) and temporal cycle-to-cycle analysis. (A) Non-exhaustive table recapitulating LRC in mammals. Note that at high-speed locomotion, the preferred ratio is 1:1 (locomotor events divided by respiratory events). Adapted from Boggs (2002). **(B-C)** Cycle-to-cycle analysis of strides and breaths. **(B)** Analysis in one galloping horse showing a clear one to one temporal synchronization at this gait (red dotted lines). Adapted from Bramble and Carrier (1983). **(C)** Occurrence of breaths during the step cycle, defined between 0 and 1, in the same human cohort running on a treadmill. (Top) Example of synchronized breaths, occurring at two preferred moments of the step cycle. (Down) Example of non-synchronized breaths, occurring randomly in the step cycle. Adapted from Bernasconi and Kohl (1993).

their strides than inexperienced subjects, suggesting that the coupling may be learnt through training (Kohl et al., 1981; Bramble and Carrier, 1983). There might thus be important inter- and intra-species differences in individuals' ability to lock breaths to strides.

There is another important source of confound that must be stressed here. Indeed, studies that have analyzed the temporal correlation of breaths to strides on a cycle-to-cycle basis, and those that only report the ratios of respiratory and locomotor frequencies, often rely on the same terminology, the LRC, or sometimes the "locomotor-respiratory entrainment". Admittedly, some of the former studies have used the terms "% of LRC" or "degree of LRC" or "LRC ratio" to refer to the percent of breaths that fall in the same moment of the locomotor cycle. Yet, globally, it is often not clear to which of the analysis a given, say 1:1, "coupling" or "entrainment" refers to. In spite of this, it is commonly assumed that during exercise breaths and strides are temporally synchronized in most, if not all, species.

Therefore, although a cycle-to-cycle coordination of breaths to strides can occur, it is far from clear that it is a mandatory requirement to sustain aerobic exercise in all species. My work will address later this dogma in laboratory mice, an animal model whose environment can be controlled in a standardized manner. We will look at synchronization between strides and breaths using precise cycle-to-cycle analysis (see Paper 1).

II. The physiological substrate of running hyperpnea

Physiologists have been intrigued by the mechanisms that regulate breathing during exercise. The commonly observed signatures of respiratory adjustments to exercise have paved the way to formulate pertinent hypothesis regarding the nature and origin - being humoral, mechanical, or neuronal - of the activating signal. Even after a century of investigations, this is still under debate. Indeed, contradictory data have questioned the validity of each hypothesized mechanism. As a result, there has never been a real consensus among scientists as to the existence and the exact nature of a prominent mechanism that mediates respiratory adaptation to exercise. While still debated, the above characteristics have given rise to three (non-exclusive) major hypothetical sources of drive causal to exercise hyperpnea: 1) chemoception, 2) peripheral feedback and 3) central command hypotheses (Gariepy et al., 2010).

1. The chemoception hypothesis

Physiologists initially hypothesized that blood chemical changes leading to hypercapnia (increase in CO_2) or hypoxia (decrease in O_2), could trigger exercise hyperpnea. Indeed, a small increase in inspired CO_2 concentration or large decrease in inspired O_2 strongly stimulates breathing (Haldane and Priestley, 1905; Remmers, 2005). Chemoreceptors (i.e., neurons capable of sensing local changes in the blood gas composition) are present both in the periphery and centrally. The former resides in the carotid bodies and detect essentially O_2 changes. The latter comprises specialized groups of neurons in the brain, including in close proximity to respiratory centers (see Chapter 2.II.2.a.), and detect CO_2 changes (Heymans and Heymans, 1927; Nattie, 1999; Guyenet et al., 2008). Activation of either peripheral or central chemoreceptors do indeed results in increased ventilation (Regan and Majcherczyk, 1982). Conversely, suppressing peripheral chemoreceptors during prolonged running exercise results in a reduced hyperventilation by 15 % in humans and goats (Bisgard et al., 1982; Honda, 1985; Jeyaranjan et

al., 1987). However, many opposing arguments can be found in the literature. Firstly, because exercise hyperpnea is immediate (i.e., at the onset of exercise) chemical blood changes cannot account for the fast ventilatory response during an acute exercise (Krogh, 1913; Gravel et al., 2007). Secondly, the partial pressures of CO_2 and O_2 (respectively pCO_2 and pO_2) actually remains very stable and pCO_2 even decreases slightly in prolonged and moderate running sessions in humans, goats, ponies and rats (Bisgard et al., 1982; Hastings et al., 1982; Pan et al., 1983; Fregosi and Dempsey, 1984; Mateika and Duffin, 1995). This is in fact not surprising since the goal of adaptative breathing is exactly to prevent any increase in pCO_2 or drop in pO_2, despite their inevitable change in production and demand. Thirdly, and possibly most importantly, mental simulation or mere anticipation of exercise in humans triggers hyperpnea (Tobin et al., 1986; Decety et al., 1993; Thornton et al., 2001).

For all of these reasons, exercise hyperpnea does not seem to be critically driven by an increase in pCO_2 nor a reduction in pO_2. It may rather rely on neural mechanisms being of peripheral and/or central origin. Interestingly however, we will see that a CO_2-chemosensitive structure in the brainstem might be involved in augmenting ventilation during exercise, but by mechanisms that are independent from their chemoceptive function (see Chapter 2.II.2.a).

2. The peripheral feedback hypothesis

The peripheral feedback hypothesis refers to the potential influence of sensory afferences (or feedbacks) from exercising muscles on the respiratory network. This hypothesis is attractive because the transmission of sensory afferents activity through spinal circuits could account for a rapid increase in breathing at the onset and throughout exercise, although their role in exercise hyperpnea is not fully understood. Indeed, periodic stimulations of cutaneous or muscular afferents increase the respiratory rhythm (Howard et al., 1969; Iscoe and Polosa, 1976). In addition, when limbs are moved passively in humans, dogs, and rats, breathing rate increases rapidly (Flandrois et al., 1967; Waisbren et al., 1990; Zhuang et al., 2009; Giraudin et al., 2012), albeit does not reach the same magnitude as when caused by active movements (Bell and Duffin, 2006).

The role of sensory feedbacks, particularly from the limbs, has received particular attention since they may support the alleged temporal coordination of breathes to strides described above. Indeed, passive limb movements in decorticated rabbits and semi-isolated preparations of neonatal rats were shown to trigger a respiratory discharge and even reinitialize (or reset) the respiratory rhythm (Palisses et al., 1988; Morin and Viala, 2002; Giraudin et al., 2012). Furthermore, electrical stimulation of muscular or cutaneous afferences, rhythmically active during locomotion (Duysens et al., 2000), can reset the respiratory rhythm in cats *in vivo* (Iscoe and Polosa, 1976). Interestingly, *ex vivo* isolated brainstem preparations still attached to the cervical and lumbar spinal cord of neonatal rats allow the recording of respiratory activity on cervical motor nerves while manipulating sensory spinal afferences (or dorsal nerves) normally activated by contracted locomotor muscles that are not present in the preparation (Figure 1.5A). Interestingly, in these preparations, electrical stimulation of cervical or lumbar dorsal nerves can strictly phase-lock respiration to the stimulations, even in the absence of the muscle itself (Figure 1.5A) (Morin and Viala, 2002; Giraudin et al., 2008; Giraudin et al., 2012). Interestingly, pharmacological blockage of synaptic transmission at the lumbar or thoracic spinal level did not suppress breathing resetting induced by the stimulations, while synaptic blockage of the entire

spinal cord did. This suggests the existence of at least one spinal relay, likely at the cervical level of the spinal cord, in the ascending pathway to the brainstem. Additional data implicate another relay in the pons, i.e., the lateral parabrachial/Kölliker-Fuse nuclei (**lPB/KF,** see Chapter 2.II.3.) (Figure 1.5B). Altogether, the authors suggest that this ascending drive from the spinal cord to the lPB/KF could be the neuronal basis for phase-locking breathes to strides *in vivo*. Although as mentioned previously, few studies have shown a strict temporal synchronization of the respiratory and locomotor rhythms. Furthermore, its existence in rodents has not been investigated yet, and part of my PhD will address this issue later in running mice (see Paper 1 (Hérent et al., 2020)). Thus, the functional significance and the biological relevance of proprioceptive afferent drive in respiratory adaptation to exercise remains unclear.

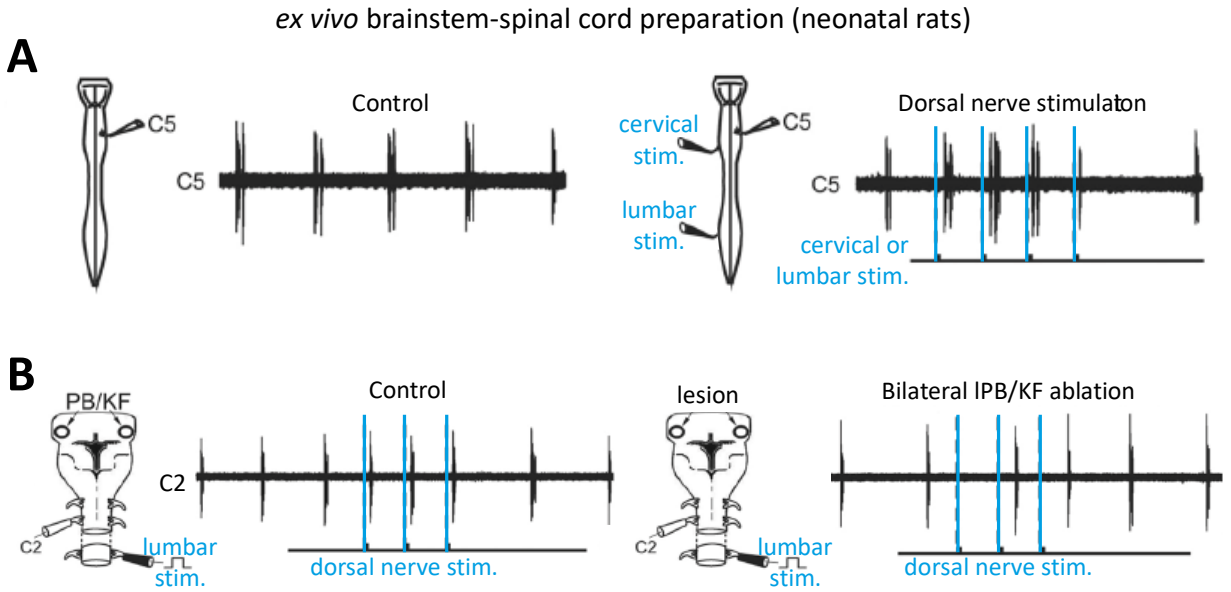

Figure 1.5. Peripheral feedback hypothesis. *Ex vivo* reduced brainstem-spinal cord preparation in neonatal rats that retains inspiratory activities, recorded on cervical ventral roots (2nd or 5th cervical nerve, C2 or C5), that resemble the one *in vivo*, i.e., inspiratory-like activities. **(A)** (Left) Inspiratory-like activity in control condition. (Right) Inspiratory-like activity during electrical stimulation of dorsal nerves (blue lines) that normally comes from contracted forelimb (cervical) and hindlimb (lumbar) muscles. Note that each stimulation triggers an inspiratory burst. **(B)** (Left) Inspiratory-like activity during electrical stimulation of dorsal nerves (blue lines). (Right) Similar experiment after physical ablation of the lateral parabrachial/kölliker-fuse (lPB/KF). Note that dorsal nerve stimulations fail to trigger inspiratory burst in absence of the lPB/KF. Adapted from Giraudin et al. (2012).

Peripheral feedbacks from contracting limbs may not be the only source of sensory afferences capable of modulating breathing. Indeed, during exercise in quadrupeds, locomotor cycles impose mechanical constrains onto the respiratory apparatus which could be a source of internal mechanical conflicts and explain the necessity for synchronizing respiratory and locomotor rhythms. In the so-called "visceral piston" hypothesis, the internal movement of the viscera may constrain the timing of breaths (Alexander, 1989; Boggs, 2002). However, viscera oscillations do not match with respiratory phases in horses, rabbits, and potentially other

quadrupeds (Alexander, 1989; Bramble and Jenkins, 1993). Therefore, although the mechanical effect of strides on breathing has been described, its relative importance in coupling respiratory and locomotor cycles remains largely elusive in mammals. In addition, such mechanical forces are less likely to be involved in bipedal running or cycling in humans due to the vertical position of the body (Banzett et al., 1992).

While the peripheral feedback hypothesis could account for some aspects of hyperpnea during exercise, and possibly a coordination of breaths to strides, extensive debates remain (Eldridge et al., 2006; Haouzi, 2006; Waldrop and Iwamoto, 2006). One should also keep in mind that the qualifications of such respiratory-locomotor coupling are highly ambiguous (see more details in Chapter 1.I.5.). Furthermore, sensory afferents cannot explain the important increase in ventilation caused by either mental exercise or in anticipation of exercise (Tobin et al., 1986; Decety, 1993; Gariepy et al., 2012). These observations altogether suggest that peripheral afferents may not be major contributors to exercise hyperpnea.

3. The central command hypothesis

The central command hypothesis postulates that groups of neurons located in the central nervous system and directly involved in the planning or execution of the locomotor behavior can modulate breathing by directly contacting respiratory neurons. This possibility is appealing as it is the only one that can support a regulation of breathing at the onset and during a run, but also before a run or during mental simulation of exercise.

a. Evidences for supraspinal control of breathing

One of the first evidence for a central command came from studies in decerebrated cats (Eldridge et al., 1981; DiMarco et al., 1983; Eldridge et al., 1985) where the authors stimulated supraspinal brain regions known to initiate locomotor stepping, i.e., the **diencephalic locomotor region** or DLR (Orlovsky, 1969) (see Chapter 3.II.1.) and the **mesencephalic locomotor region** or MLR (Shik et al., 1966) (see Chapter 3.II.2.). Interestingly, the authors found that the activation of each of these locomotor regions triggered locomotion but, importantly, imposed an associated increase in respiration frequency and amplitude (Figure 1.6A). The demonstration of a central command was further examined by blocking muscular contraction with curare, and thus peripheral feedback, while maintaining PCO_2 levels stable. In these conditions, activation of the locomotor centers produced a so called “fictive locomotion”, i.e., a rhythmic and patterned activation of the nerves innervating the limbs, but without any actual movement. Importantly, such paralyzed animals displayed a similar increase in respiratory frequency and amplitude than the control, non-paralyzed groups. In addition, respiratory frequency increase occurred in the absence of movement, during subthreshold stimulations, i.e., stimulations that did not trigger movement (Figure 1.6B). The authors concluded that supraspinal locomotor structures can increase breathing rate through mechanisms that do not require the activation of limb effectors. This suggested the existence of direct neuronal connections from such locomotor centers to respiratory circuits. Recently, the involvement of the MLR in exercise hyperpnea was more directly demonstrated in the lamprey (Gariepy et al., 2012). Similar to the pioneer studies in cats (Eldridge et al., 1985), activation of the MLR in lamprey preparations increases breathing frequency and amplitude, and this despite the absence of sensory feedback from contracting

muscles. Interestingly, they show that breathing frequency increases prior to the occurrence of movement and also in the absence of movement using subthreshold MLR stimulation, i.e., stimulation that does not trigger swimming-like activities. Importantly, the authors further show the existence of a direct, monosynaptic, and glutamatergic connectivity from the MLR to the paratrigeminal respiratory group, the candidate site for respiratory rhythm generation in this species (Mutolo et al., 2007). Such connections in mammals and their function have however not yet been described.

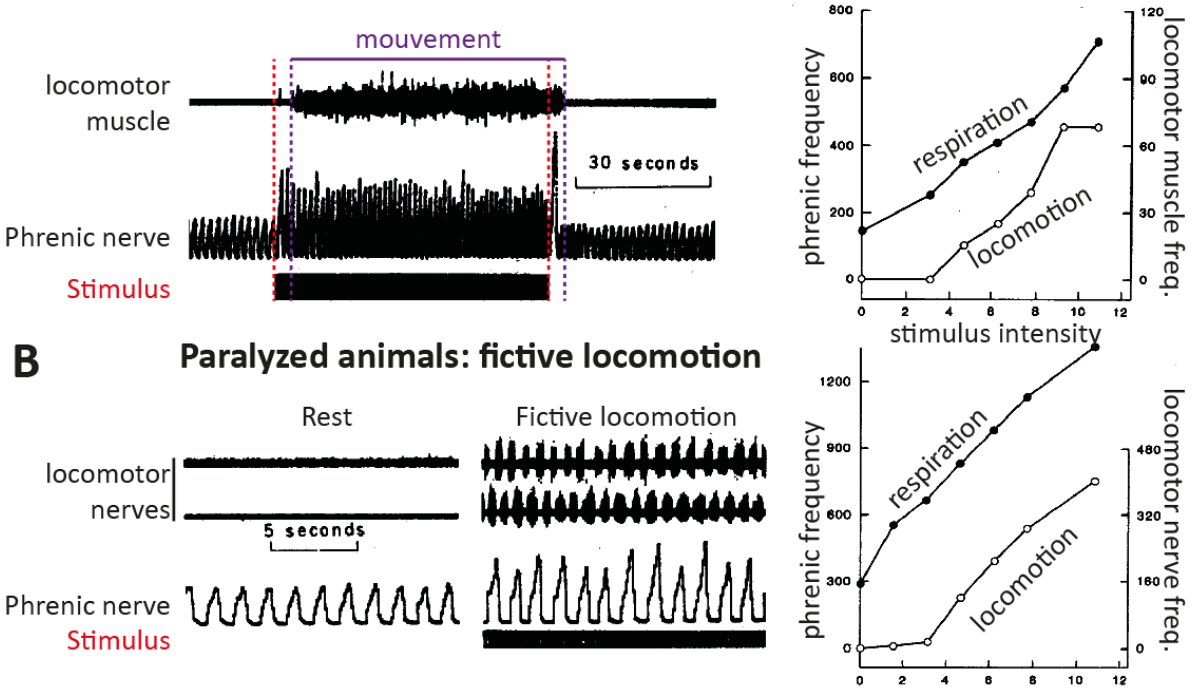

Figure 1.6. Central command hypothesis: supraspinal locomotor centers. (A) Recording of respiration during electrical stimulation of brainstem locomotor centers (here the diencephalic locomotor region, DLR). (Left) Recording of a locomotor muscle activity, respiratory activity (phrenic nerve) and the stimulus applied (between the red dotted lines). Note the increase in respiratory frequency and amplitude following activation of the DLR during movement (purple dotted lines) and even prior to the movement. (Right) Graph showing respiratory and locomotor frequencies in relation to the intensity of the electrical stimulation. **(B)** Similar recordings in paralyzed cats where muscular contraction is blocked. (Left) Recordings of spinal locomotor nerves, that normally innervate locomotor muscles, silent at rest. Upon DLR stimulation, locomotor nerves exhibit locomotor-like activities ("fictive locomotion"). (Right) Note the similar increase in respiratory frequency as compared to non-paralyzed cats (**A**). Adapted from Eldridge et al. (1981).

Another evidence for a central command of breathing during running is provided by examinations in human participants during imagined/mental exercise (Decety et al., 1993; Thornton et al., 2001). These studies showed that the mere imagination of exercise is sufficient to increase breathing rate in the absence of actual movements (as seen previously in Chapter 1.I.3.). Importantly, the combination of mental exercise with neuronal imaging revealed that

several structures involved in the brain locomotor command are activated during mental exercise, including cortical and cerebellar areas, and importantly a region that corresponds to the anatomical location of the MLR (Thornton et al., 2001; Jahn et al., 2008; Karachi et al., 2010), a prime candidate in the central command hypothesis.

b. Evidences for spinal control of breathing

Other studies have investigated the implication of the executive circuits that, in the spinal cord, generate rhythmic and patterned contraction of locomotor muscles and often referred to as **locomotor central pattern generators** or CPGs ((Kiehn, 2006), see Chapter 3.II.4.). Indeed, in reduced *ex vivo* brainstem-spinal cord preparations of neonatal rats (without the above structures initiating locomotion nor the peripheral feedbacks), pharmacological activation of the locomotor CPG in the lumbar spinal cord triggered an increase of respiratory frequencies (Morin and Viala, 2002; Le Gal et al., 2014; Le Gal et al., 2020) (Figure 1.7). Importantly, this ascending drive does not require a spinal relay, suggesting a direct connectivity to the brainstem, and potentially brainstem respiratory centers. Interestingly, this study has started to examine the nature of the targeted respiratory neurons, and hints at a possible implication of another group of respiratory neurons involved in respiratory rhythm generation, the parafacial respiratory region (pF) that we will detail later (see Chapter 2.II.2.).

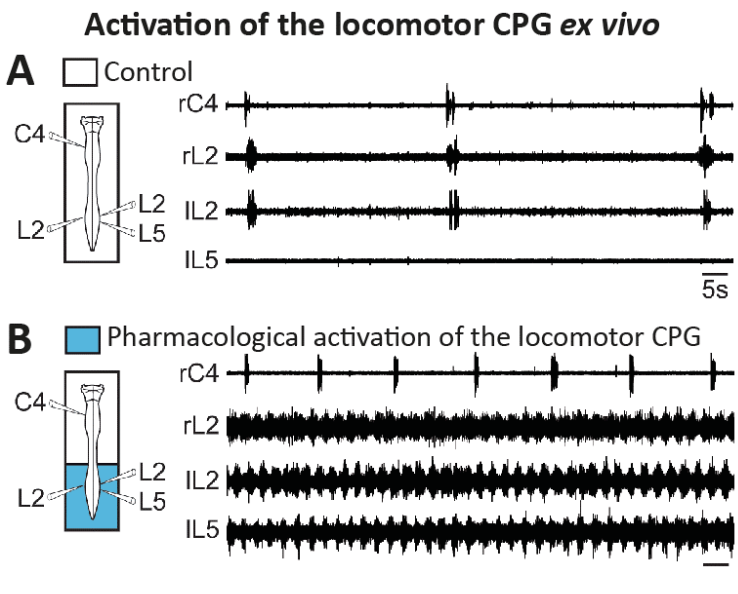

Figure 1.7. Central command hypothesis: spinal locomotor executive center. Recording of inspiratory- (C4) and locomotor-like (right L2, left L2 and left L5) nerves in brainstem-spinal cord *ex vivo* preparation of neonatal rats. **(A)** In control conditions, basal respiration is recorded on C4 (inspiratory) and L2 (expiratory). **(B)** Pharmacological activation of the lumbar locomotor CPG triggers locomotor-like activity on locomotor nerves and accelerates inspiratory frequency. Adapted from Le Gal et al. (2014).

Overall, human and animal studies suggest that different levels of the central control of locomotor movements, from cortical to the brainstem command centers and to the spinal cord executive centers, may directly influence breathing during, and even before, running exercise. Yet, the exact identity of the neuronal substrates, in locomotor and respiratory networks, that support this assessment are poorly documented.

PhD objectives

The exact nature of respiratory adaptations to exercise and their physiological, likely neuronal substrate, have vexed physiologists for more than a century. It is now accepted that one obligatory feature of respiratory adaptation to exercise is the increase in breathing rate and depth which occurs at the onset and throughout a locomotor action and can even precede the locomotor movement. In contrast, the proportional increase of breathing to limb velocity and the temporal coupling of breaths to locomotor cycles remain controversial. Thus, it is still not clear whether these two latter features are mandatory for the adaptive control of breathing during exercise. Mice have become the premier model to investigate the control of motor behaviors like breathing and locomotion. Importantly, laboratory mice can grant access to the hardwired components of respiratory adaptations to exercise, with controlled influence of external stimuli or prior training.

Therefore, the aim of **Paper 1** (Hérent et al., 2020) was to identify and document the specifications of respiratory changes in running mice. We searched for robust breathing features at different speeds, gaits, and examined the impact of limb velocity to derive hardwired features of running hyperpnea. Importantly, we looked at the coordination of breathing drives and running movements using a cycle-to-cycle analysis.

We discussed above that the central command theory seems to play a pivotal role in mediating breathing adaptations to exercise. However, the underlying connectomics is still poorly documented (if at all existing) especially in mammals, owing to the limited tool boxes for the species tested. In contrast, mice give access to a wide range of genetic and molecular tools for anatomical, functional, and behavioral studies.

Therefore, the aim of **Paper 2** was to identify the neurons and circuits underlying exercise hyperpnea in running mice. We searched, in the brain and the spinal cord, for locomotor neurons that send the activatory signal and for the respiratory neurons that receive this signal. Particularly, we investigated the possibility that both the locomotor center that initiate locomotion, i.e., the mesencephalic locomotor region (MLR), and the locomotor executive circuit, i.e., the lumbar locomotor central pattern generator (locomotor CPG) could also modulate breathing during exercise. Furthermore, we investigated the possibility that the respiratory neurons targeted by these locomotor circuits might reside in the respiratory CPG, the preBötzinger complex (preBötC) and the parafacial respiratory region (pF).

The next two chapters will be dedicated to the understanding of respiratory and locomotor control in mammals while key respiratory and locomotor structures candidate to mediate exercise hyperpnea will be highlighted.

Chapter 2: Control of respiration and candidate neurons

Several times in every minute of every day, we take a breath, in an effort less and most of the time unconscious manner and hopefully without major interruptions, even while we sleep. Indeed, breathing is essential for life, as it metabolically supports all physiological processes in the body. It is a robust and infallible behavior from birth to death, which in close interaction with the cardiovascular system, ensures the gas exchanges necessary for the continuous maintenance of tissue homeostasis.

In this second chapter, I will describe the general aspects of respiratory behavior in mammals as well as the central organization of the respiratory neurons responsible for generating and patterning breathing movements, with emphasis on respiratory neurons candidates to mediate respiratory adaptation during running exercise.

I. Generalities on respiratory control

1. Breathing movements: inspiration and expiration

Breathing is based on cyclical movements of the rib cage which serve to fill and empty the lungs, to ensure the continuous supply of O_2 and the elimination of CO_2 (Figure 2.1). **Inspiration** (or inhalation) is a systematically active mechanism which involves the concerted muscular contraction of dedicated pump muscle groups which expand the rib cage and consequently fill the compliant lungs. The main inspiratory muscle is the diaphragm, activated by the phrenic nerve. Unlike inspiration, **expiration** (or exhalation) is a passive mechanism in resting and calm

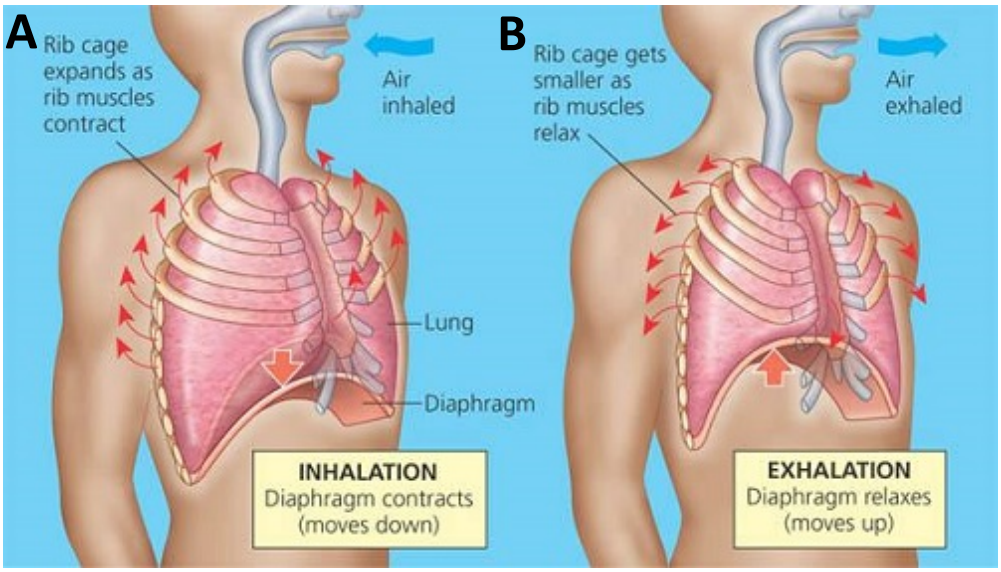

Figure 2.1. Breathing mechanics at rest. (A) Inspiratory movement. When the diaphragm and intercostal muscles contract, the rib cage is moved down in the abdomen, the pressure inside the lungs becomes negative and the air charged in O_2 from the atmosphere is inhaled. **(B)** Expiratory movement. The relaxation of inspiratory muscles constricts the rib cage, leading to a switch from negative to positive pressure and the lungs recoil, releasing the air charged in CO_2. Image is from https://www.knowswhy.com/difference-between-inhalation-and-exhalation/.

conditions. However, under certain physiological conditions where the respiratory drive is increased (hypercapnia or intense exercise), the expiration becomes an active breathing phase. Expiratory muscles (abdominal and thoracic) are recruited to push the diaphragm upwards imposing intra-thoracic positive pressure that forces the expulsion of the air out of the lungs.

2. Neural bases of breathing control

Breathing is the only behavior that requires permanent and rhythmic contractions of skeletal muscles. We breathe about 600 million times in a lifespan owing to spatially and functionally organized respiratory neurons in the brain forming the respiratory rhythm generator (RRG) or central pattern generator (CPG) that generates and patterns rhythmic motor sequences.

The respiratory CPG hosts two critical neural circuits, which generate the rhythmic inspiratory and expiratory activities: the **preBötzinger complex** (preBötC) in the vicinity of the nucleus ambiguous, and more rostrally near the facial motor nucleus the **parafacial respiratory group** (pF) (Figure 2.2). The preBötC is composed of excitatory and inhibitory inspiratory neurons, that constitute the core rhythmogenic microcircuit for generating inspiration (Smith et al., 1991; Feldman et al., 2003; Feldman and Del Negro, 2006; Del Negro et al., 2018). From embryonic to neonatal stages, the pF acts as a second oscillator, coupled to the preBötC, to generate inspiratory rhythm (Onimaru et al., 1987; Onimaru and Homma, 2003; Thoby-Brisson et al., 2009). In adults, upon increased metabolic drive (hypercapnia, i.e., increase in blood CO_2), the pF acts as a conditional expiratory oscillator to generate active expiration (Janczewski et al., 2002; Mellen et al., 2003; Janczewski and Feldman, 2006). The inspiratory and expiratory activities are then transmitted to premotor neurons in the caudal and ventral medulla that convey the respiratory command onto specific spinal motoneurons. The **rostral ventral respiratory group** (rVRG),

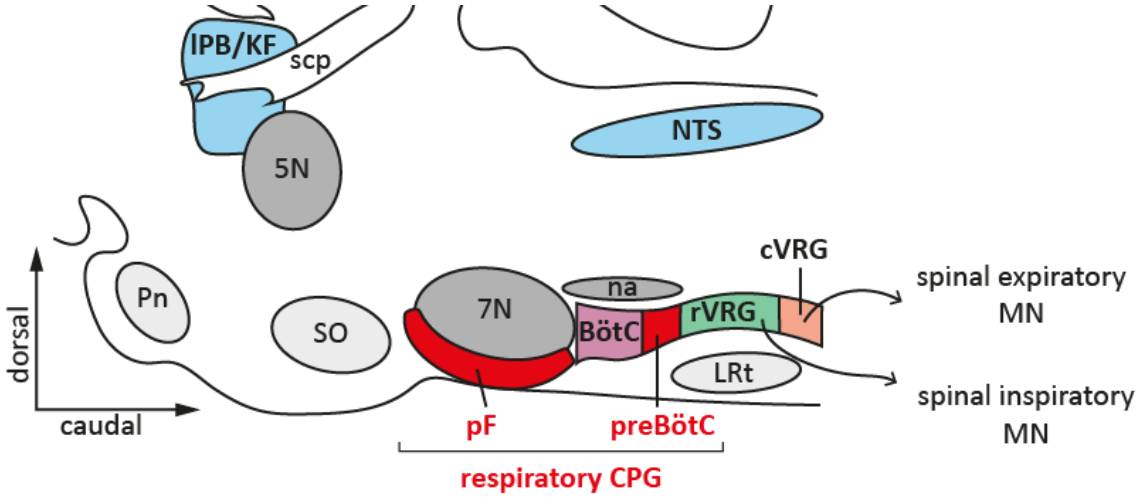

Figure 2.2. Location of essential brainstem neurons for breathing control. Sagittal view of the mouse brainstem. The respiratory CPG in red contains the preBötzinger complex (preBötC) and the parafacial respiratory region (pF). The location of other essential respiratory neurons are highlighted in the figure: the Bötzinger complex (BötC), the nucleus of the solitary tract (NTS), the lateral parabrachial/Kölliker-Fuse nuclei (lPB/KF) and the pre-motoneurons in dedicated ventral respiratory groups (VRG). *scp, superior cerebellar peduncle. Pn, ventral pontine nucleus. 5N: trigeminal motor nucleus. SO, superior olive. 7N, facial motor nucleus. na, nucleus ambiguous. LRt, lateral reticular nucleus.* Adapted from Feldman et al. (2013).

directly caudal to the preBötC, is mostly composed of inspiratory premotor neurons relaying inspiratory drive to the phrenic spinal motoneurons which innervate the diaphragm, the main inspiratory muscle (Alheid and McCrimmon, 2008; Qiu et al., 2010; Wu et al., 2017). The **caudal ventral respiratory group** (cVRG) contains expiratory neurons relaying expiratory drive to the abdominal spinal motoneurons (Janczewski et al., 2002; Giraudin et al., 2008). Although the respiratory CPG is sufficient to generate all respiratory phases, it is interconnected with dorsal and ventral medullary, and pontine respiratory groups that regulate respiratory pattern and other autonomic or motor responses. In the ventral medulla, the **Bötzinger complex** (BötC) containing inhibitory expiratory neurons promotes inspiratory-expiratory phase transition during normal breathing (Burke et al., 2010). In the dorsal medulla resides the **nucleus of the solitary tract** (NTS) that contains almost exclusively inspiratory neurons (Bianchi et al., 1995). The NTS is a secondary sensory relay receiving visceral afferents drives including those that provide critical respiratory-related information about the status of lungs and reflexively regulates lung volume (i.e., Herring-Breuer reflex) and promotes the transition from inspiration to expiration (Kalia and Mesulam, 1980). Also, previous investigation in the lab have shown that the NTS is required to produce the expiratory drive required for innate vocalization (Hernandez-Miranda et al., 2017). More generally, the NTS is an essential center for the integration of visceral functions, i.e., cardiovascular, digestive, and respiratory (Kalia and Mesulam, 1980; Boscan et al., 2002; Spyer and Gourine, 2009). In the dorsolateral pons the **lateral parabrachial/Kölliker-Fuse** nuclei (lPB/KF) contains inspiratory and expiratory neurons (Bertrand et al., 1973; Song et al., 2006) that regulate the inspiratory-expiratory transition (Dutschmann and Herbert, 2006; Smith et al., 2007; Mörschel and Dutschmann, 2009). The lPB/KF also regulates cardiovascular function (Davern, 2014) and integrates information about noxious stimuli (Jiang et al., 2004; Chiang et al., 2019).

II. Candidate respiratory neurons for mediating exercise hyperpnea

1. The PreBötzinger complex (preBötC)

a. The core circuit for inspiratory generation

In 1991, the preBötC was discovered in medullary slices as a group of neurons with intrinsic inspiratory bursting properties and suggested as the prime oscillator for inspiratory rhythm generation (Figure 2.4A) (Smith et al., 1991). The preBötC was later described in diverse species including mice, goats, lampreys, rabbits, bats (Ramirez et al., 1996; Wenninger et al., 2004; Mutolo et al., 2007; Pantaleo et al., 2011; Tupal et al., 2014) and presumably humans (Ramirez, 2011; Schwarzacher et al., 2011). Since its discovery, experiments that lesioned or perturbed the activity of the preBötC (*in vitro* in slices or *in vivo*) confirmed its role as the "kernel" for inspiratory rhythmogenesis, containing neuronal circuits that produce basic rhythmic inspiratory activity at all developmental stages (Figure 2.4B, C) (Gray et al., 2001; McKay et al., 2005; Feldman and Del Negro, 2006; Tan et al., 2008; Bouvier et al., 2010; Wang et al., 2014; Alsahafi et al., 2015; Baertsch et al., 2018; Del Negro et al., 2018; Vann et al., 2018; Menuet et al., 2020).

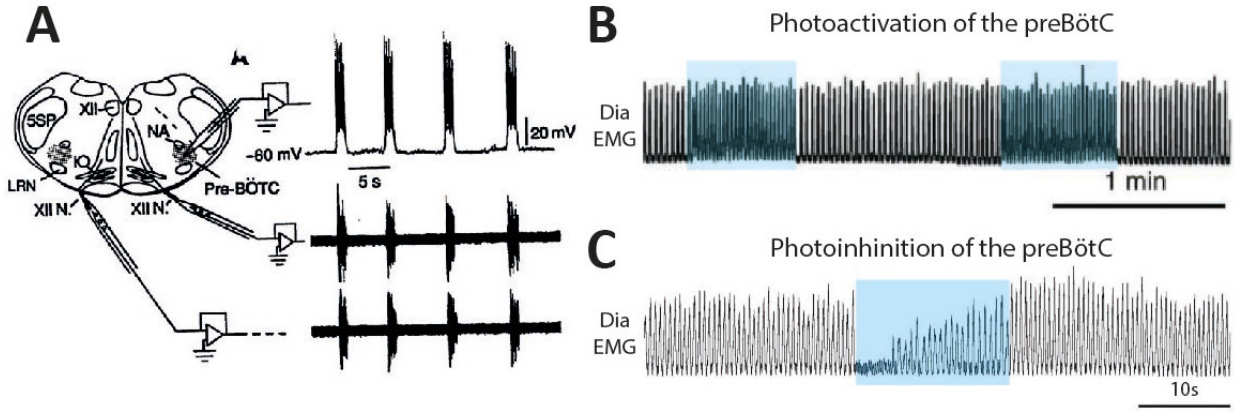

Figure 2.4. The PreBötC is necessary and sufficient for inspiratory rhythmogenesis. (A) (Left) Medullary slice containing the preBötC. (Right) Intracellular recording of a preBötC neuron and bilateral recording of hypoglossal inspiratory nerves (XII). Note that the preBötC is rhythmically active during inspiration and is sufficient to generate inspiratory rhythm. *NA, nucleus ambiguous. 5SP, Spinal trigeminal nucleus. LRN, lateral reticular nucleus.* Adapted from Smith et al. (1991). **(B)** Photoactivation of the preBötC *in vivo* increases inspiration (diaphragm electromyogram: Dia EMG). Adapted from Alsahafi et al. (2015). **(C)** Photoinhibition of the preBötC leads to a long apnea *in vivo*. Adapted from Menuet et al. (2020).

The glutamatergic preBötC: core circuit for generating inspiration

To this day, no marker exclusive to the PreBötC has been found. However, subsets of PreBötC neurons have been characterized anatomically and functionally using markers and modern genetic tools. Anatomically, PreBötC neurons can be defined by the expression of the neurokinin 1 receptor (NK1R), or the neuropeptide somatostatin (SST) (Gray et al., 1999; Stornetta et al., 2003). A most used anatomical signature to localize the preBötC is the immunoreactivity to SST and/or NK1R staining (Figure 2.5A, B). Ablation of $NK1R^+/SST^+$ PreBötC neurons leads to an ataxic respiratory rhythm or even persistent apneas, suggesting their importance in generating respiratory rhythm (Figure 2.5C) (Gray et al., 2001; Tan et al., 2008).

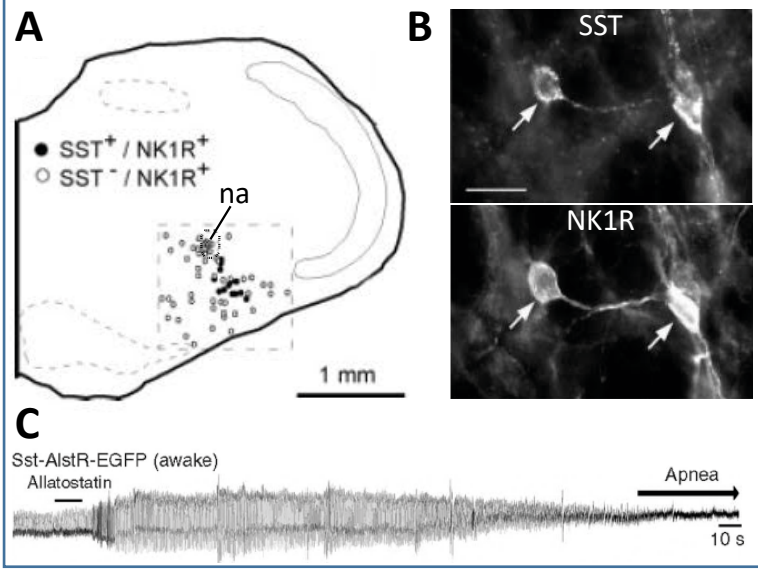

Figure 2.5. SST preBötC neurons are essential for inspiratory rhythm generation. (A) Coronal brainstem region showing the distribution of somatostatin and neurokinin 1 receptor positive preBötC neurons (SST^+ / $NK1R^+$, black circles). *na, nucleus ambiguous.* **(B)** PreBötC SST neurons also express high levels of NK1R. Adapted from Stornetta et al. (2003). **(C)** Genetic viral silencing of SST preBötC neurons triggers persistent apneas in rats *in vivo*. Adapted from Tan et al. (2008).

Most preBötC neurons are rhythmically active during inspiration (Smith et al., 1991; Connelly et al., 1992; Schwarzacher et al., 1995; Guyenet and Wang, 2001).

A consensus view about rhythm generation in the preBötC, known as the group pacemaker hypothesis (Ramirez et al., 2004; Feldman and Del Negro, 2006), posits that the rhythm emerges from the redundant excitatory connectivity of its constituent neurons in combination with a palette of intrinsic membrane conductance that supports their bi-stable behavior. This comes from series of experiments demonstrating that the preBötC rhythm is abrogated after pharmacological challenges disrupting glutamatergic synaptic transmission (Smith et al., 1991; Funk et al., 1993; Koshiya and Smith, 1999; Gray et al., 2001) or after genetic invalidation of glutamatergic synaptic release (Wallén-Mackenzie et al., 2006) while in these conditions some preBötC neurons are able to maintain their rhythmic behaviour suggesting their role as pacemaker-like neurons (Thoby-Brisson and Ramirez, 2001; Del Negro et al., 2002; Peña et al., 2004; Thoby-Brisson et al., 2005). As it turns out, pharmacological blockade of candidate ionic conductances supporting pacemaker-like neuronal behaviour failed to disrupt the rhythm in slices *in vitro* (Del Negro et al., 2005) calling for the prominence of synaptic over intrinsic properties of network elements for rhythm generation. Recent developments invoke a selective class of "burstlet" neurons as critical for rhythm generation on the basis that these neurons maintain unperturbed rhythmic activity while the rhythmic commands to output motor neurons can be changed but only by quantal increments corresponding to the burstlet rhythmic period. As such, this observation doesn't enlight mechanistic aspects of rhythm generation *per se*, at best it re-orients the question towards a prefered subset of neurons with yet unidentified molecular signatures and undescribed anatomical organization in the preBötC, that may take on rhythmogenic ambition (Kam et al., 2013; Sun et al., 2019). Finally, an important contributing phenomenon to rhythmogenesis is the existence, manifest in slices, of a refractory period maximal after the preBötC burst and progressively waning as the inter-burst interval elapses. This refractory period may rely on conductances that maintain the hyperpolarization of preBötC neurons after bursting (Baertsch et al., 2018) or may involve synaptic depletion (Guerrier et al., 2015; Kottick and Del Negro, 2015; Morgado-Valle et al., 2015). The net effect of the refractory period is to limit the percolation of excitation within the network and through waning to progressively increase the spiking probablity and therefore the cellular recruitment within the preBötC neuronal assembly until a point when the entire preBötC effective of neuron collectively discharges to form the preBötC burst. As will be briefly alluded to in the discussion of my results, this refractory period may be shortened by the stimulation of preBötC inhibitory neurons while prolonged by the stimulation of excitatory ones (see below for more details, (Baertsch et al., 2018)). This means that the timing of preBötC responses to incoming signals and up or down regulation of the rhythm frequency are respectively temporally constrained during the interburst interval and dependent on the excitatory or inhibitory nature of the targeted preBötC neurons.

A previous study in the laboratory showed that PreBötC neurons derive from the ventral P0 domain of progenitors of the developing hindbrain neural tube, that expresses the homeobox transcription factor *Dbx1* and gives rise to V0 type interneurons (Pierani et al., 1999; Pierani et al., 2001; Bouvier et al., 2010). Bouvier et al. (2010) studied *Dbx1* null mutants and reported a complete abrogation of breathing due to a functional disruption of the preBötC (Figure 2.6). This largely owes to re-specification of PreBötC V0 neurons that no longer express the classical

markers NK1R and SST and importantly are no longer glutamatergic. This elegant study, corroborated by others (Gray et al., 2010; Wang et al., 2014; Vann et al., 2016; Vann et al., 2018), placed PreBötC V0 neurons as the core elements for inspiratory rhythmogenesis.

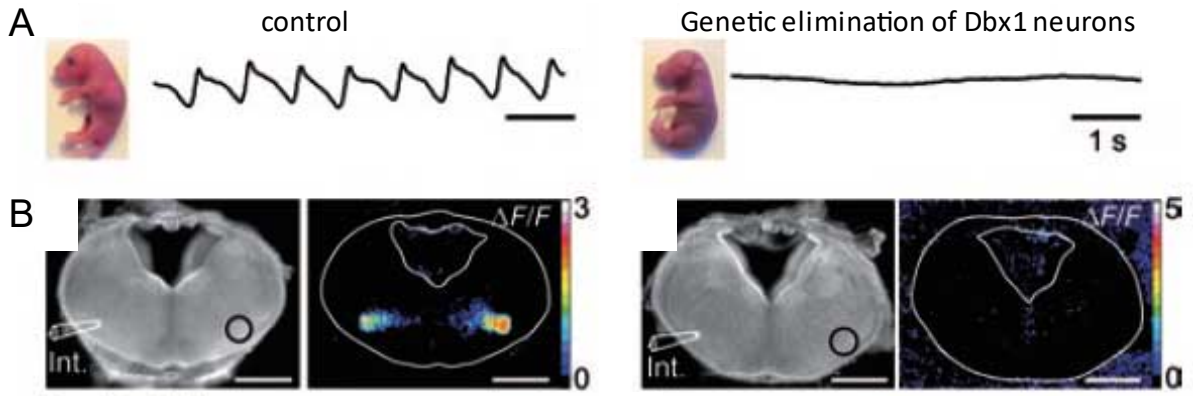

Figure 2.6. Glutamatergic *Dbx1* preBötC neurons are essential for rhythmogenesis. (Left) Wild type mice. (Right) *Dbx1*-depleted mice. **(A)** Plethysmographic recordings of breathing in neonatal mice. **(B)** Calcium imaging of the preBötC in embryos. Note that genetic elimination of *Dbx1*-derived neurons abolishes inspiratory rhythm. Adapted from Bouvier et al. (2010).

Commissural preBötC neurons are essential for synchronizing left and right inspiratory rhythms

Bilateral synchronization of the rhythm again owes to the V0 nature of preBötC neurons which are commissural (i.e., bear axons that cross the midline) and thus innervate the contralateral preBötC. When midline navigation of V0 neurons is prevented genetically by invalidation of Robo3 receptor guiding midline crossing, de-synchronized rhythms ensue on the left and right preBötC (Figure 2.7) (Thoby-Brisson et al., 2005; Bouvier et al., 2010; Wu et al.,

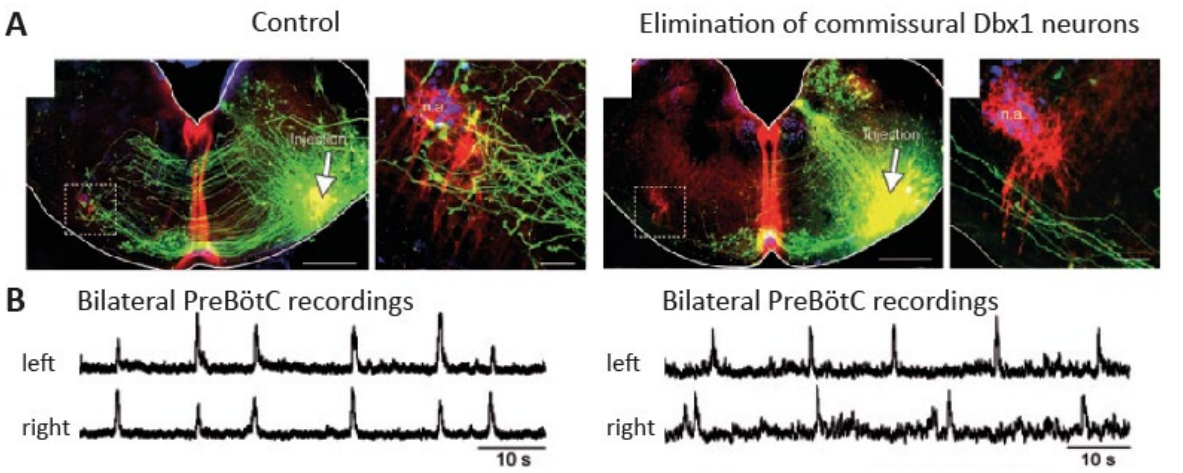

Figure 2.7. Glutamatergic *Dbx1* preBötC neurons are essential for left-right rhythm synchronization. Genetic elimination of commissural preBötC neurons disrupts the left-right coordination of inspiratory rhythm. **(A)** Injection of a retrograde marker (green) in the right preBötC (white arrows) labels the left preBötC in control (left) but not in mutant (right) mice. **(B)** Bilateral recordings of the preBötC show a disruption of left-right rhythm synchronization in mutant mice (right) as compared to control (left). Note that commissural connectivity is not required for rhythm generation. Adapted from Bouvier et al. (2010).

2017). These commissural connections, including SST neurons, were found to be principally glutamatergic (Bouvier et al., 2010; Koizumi et al., 2013). Therefore, the generation and the bilateral synchronization of the inspiratory rhythm has been proposed to rely on V0 glutamatergic commissural neurons in the preBötC. *This anatomical feature will be used later in my PhD tracing work to target preBötC neurons.*

Inhibitory preBötC neurons are critical to control breathing rhythm frequency

Although the generation of inspiratory rhythm and the bilateral synchronization rely on excitatory commissural interneurons of the preBötC, half of preBötC neurons are inhibitory (glycinergic and GABAergic) (Liu et al., 2001; Kuwana et al., 2006; Winter et al., 2009; Morgado-Valle et al., 2010; Koizumi et al., 2013) and rhythmically active, mostly during inspiration (Connelly et al., 1992; Kuwana et al., 2006; Winter et al., 2009; Morgado-Valle et al., 2010). Their role in rhythmogenesis is still debated as rhythmicity persists even when synaptic inhibition is blocked *in vivo* (Janczewski et al., 2013; Sherman et al., 2015). Interestingly, an elegant study from Baertsch et al. (2018) showed that blockade of inhibitory transmission, in PreBötC slices, 1) increases the duration of the refractory period and 2) delays the bursting probability thus decreases the rhythm frequency (Figure 2.8). They further show that excitatory preBötC neurons have a limited capacity to generate rapid breathing *in vivo.* Therefore, inhibitory neurons within the preBötC network are critical to up-regulate inspiratory rhythm frequency above the frequency mediated by excitatory preBötC neurons.

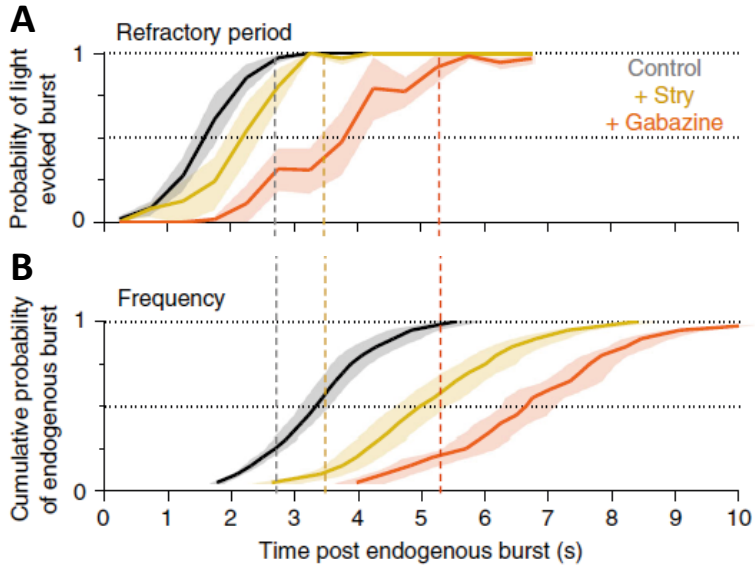

Figure 2.8. Inhibition controls the refractory period and bursting frequency of excitatory preBötC neurons. Short light stimulation and recordings of ChR2-expressing glutamatergic preBötC neurons in control (gray) and after inhibition blockade using strychnine (Stry, brown) and Gabazine (orange). Blockage of inhibition in the preBötC lengthens the refractory period (**A**) and decreases excitatory preBötC bursting frequency (**B**). Adapted from Baertsch et al. (2018).

b. Involvement in exercise hyperpnea

The preBötC plays a primordial pacing role in breathing, it is therefore reasonable to assume that it might be targeted by locomotor inputs during exercise. We saw previously that breathing rate can be increased prior to or in the absence of movements in humans, cats, geese and lampreys (Butler and Woakes, 1980; Eldridge et al., 1985; Tobin et al., 1986; Decety et al., 1991; Decety et al., 1993; Gravel et al., 2007) (see Chapter 1.I.3.). In addition, similar observations were found upon stimulation of the locomotor initiation centers in the brain, i.e., the diencephalic locomotor region (DLR) and/or the mesencephalic locomotor region (MLR) in cats and lampreys

(Eldridge et al., 1981; Eldridge et al., 1985; Gariepy et al., 2012) (see Chapter 1.II.3.a.). These data strongly suggested the existence of a direct connectivity from these brain locomotor centers onto respiratory circuits in the brainstem to mediate exercise hyperpnea in anticipation of, and during exercise. As previously mentioned, in lampreys, the MLR was shown to directly contact the paratrigeminal respiratory group (Gariepy et al., 2012). Interestingly, this structure may be homologue to the mammalian preBötC (Mutolo et al., 2007). The authors also show that the MLR neurons contacting the preBötC homologue are distinct from the one contacting descending locomotor circuits, suggesting that different subpopulations of MLR neurons drive respiratory and locomotor signals. Therefore, the preBötC is a prime candidate for integrating brain locomotor signals and mediating respiratory changes to meet the energetic demand associated with exercise. However, the existence of such mechanism has not been documented yet in other species. In addition, the cell types and exact synaptic connectivity need to be ascertained capitalizing on in-depth knowledge about the organization of both locomotor and respiratory control networks and a wide range of genetic and molecular tools available in mice, enabling their manipulation.

2. The parafacial respiratory region (pF)

a. A second oscillator for respiratory generation and modulation

In 1987, another neuronal respiratory group was proposed to take part in respiratory rhythm generation. This group of neurons, found in newborn rats, is located rostral to the PreBötC in the parafacial region, and was called the **parafacial respiratory group** (pFRG) (Onimaru et al., 1987; Onimaru and Homma, 2003). The pFRG happened to coincide with the location of a previously found chemosensory region of the adult cat, called the **retrotrapezoid nucleus** (RTN) (Mitchell et al., 1963; Smith et al., 1989).

The pFRG: an inspiratory oscillator coupled to the preBötC

Initial work has been carried out using an *ex vivo* isolated preparation of the brainstem still attached to the cervical spinal cord in neonatal rats (Suzue, 1984). In this preparation, a constitutive respiratory rhythm persists - “respiratory-like activities” - that can be monitored on the 4th cervical motor nerve (C4) where exits the phrenic nerve that innervates the diaphragm *in vivo*. *This type of preparation and recording will be used in my work to monitor respiratory-like activities in mouse pups.* In this frame, Onimaru and colleagues first described a rhythmically active region, confined near the ventrolateral surface under the facial motor nucleus (Figure 2.9A), comprised of neurons presenting with activity preceding and following the inspiratory burst recorded on C4 that were defined as pre-inspiratory (pre-I) although they also discharge after inspiration (post-I) (Figure 2.9B) (Onimaru et al., 1987). We will see that the functional assignments of pFRG neurons was somewhat guided by researchers biased towards considering the importance of the pre-I or post-I burst prompting respective roles in rhythm generation or expiratory control. Electrical stimulation of these neurons resets the rhythm (Figure 2.9B) and bilateral lesions of the pFRG causes the rhythm to slow down (Onimaru et al., 1987; Onimaru and Homma, 2003). Important experiments later demonstrated that the generation of the inspiratory rhythm at birth requires the functional coupling between the preBötC and the pFRG (Mellen et al., 2003) and that most pre-I pFRG express the transcription factor *Phox2b* (paired-like homeobox 2b) (Onimaru et al., 2008). In the adult however, there is no evidence for the existence of rhythmic pre-I pFRG neurons, rather in this region *Phox2b*-expressing neurons are either found silent or

tonic (Mulkey et al., 2004; Fortuna et al., 2008; Pagliardini et al., 2011). This may be indicative that the pFRG has only a transient rhythmogenic role to ensure robustness of breathing at birth. In any case, *Phox2b*-neurons in this area are involved in CO_2 chemoception (see below) from birth onwards and thus can modulate the respiratory rhythm throughout. My work will therefore investigate their putative role in mediating respiratory adaptation to exercise.

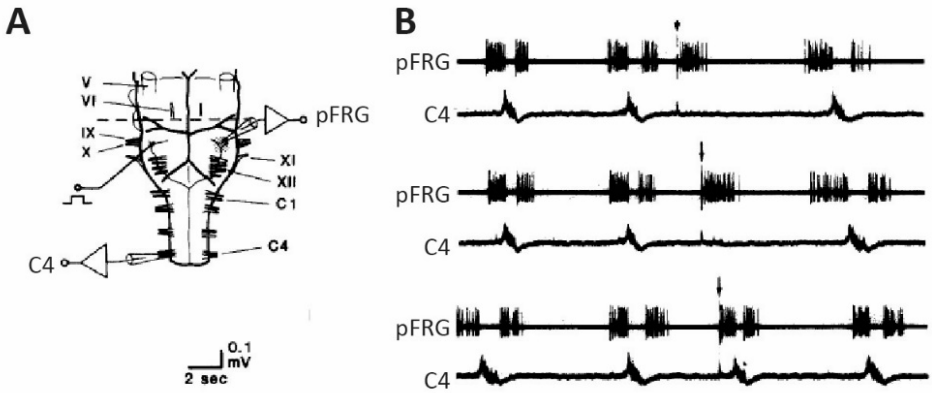

Figure 2.9. pFRG and preBötC are coupled oscillators required for inspiratory generation. (A) Ventral *ex vivo* brainstem-cervical spinal cord preparation showing the setup for recordings of the pFRG and the 4th cervical inspiratory motor nerve (C4). **(B)** Single electric stimulations of the pFRG (black arrows) resets the inspiratory rhythm recorded on C4. Adapted from Onimaru et al. (1987).

The RTN: an independent and genetically defined chemoceptive region

Blood pCO_2 is strongly regulated to remain at a certain set-point, non-toxic for cells physiology and survival, despite all metabolic demand variations including exercise (Bisgard et al., 1982; Forster et al., 1986; Forster et al., 2012). Extensive work has now demonstrated that glutamatergic *Phox2b*+ neurons located beneath and caudal to the facial motor nucleus (Figure 2.10A), termed the RTN in the adult, form a CO_2 chemoceptive structure required for completion of the chemoreflex, whereby breathing rates increase upon elevation of blood pCO_2. The RTN is intrinsically able to detect local pCO_2 changes or the attendant pH variations, increase their firing rate and in turn up-regulate the rhythm, and this independently from the activity of the respiratory CPG itself or peripheral information (Mulkey et al., 2004; Guyenet et al., 2005; Ramanantsoa et al., 2011; Ruffault et al., 2015).

The role of *Phox2b*-expressing neurons in chemosensitivity was first revealed by observation that mutations in PHOX2B cause congenital central hypoventilation syndrome (CCHS) in human, a rare disease defined by the lack of chemoreflex and sleep apneas (Amiel et al., 2003). All RTN CO_2-responsive neurons were shown to express the transcription factor *Phox2b* (Stornetta et al., 2006). The CCHS-causing *Phox2b* mutation was then transposed in mice (mouse line: *Phox2b*$^{27ala/+}$) which recapitulated the blunt chemoreflex and revealed an atrophic RTN in newborns (Dubreuil et al., 2008; Dubreuil et al., 2009; Ramanantsoa et al., 2011), suggesting the existence of an equivalent structure in humans. In adult, photo-activation of the *Phox2b*-expressing RTN results in an increase in respiratory rate (Abbott et al., 2009; Basting et al., 2015; Souza et al., 2020) while inhibition of the same cells depresses the response to CO_2 *in vivo* (Marina et al., 2010; Takakura et al., 2014). So, the *Phox2b*-expressing RTN can modulate respiratory

frequency under specific physiological conditions where the metabolic demand is increased. The RTN is therefore in favorable position to regulate the activity of the preBötC and could potentially mediate respiratory modulation driven by exercise.

Importantly, chemosensitive RTN neurons share a genetic lineage as they are derived from the co-expression of *Phox2b*, *Atoh1* (Protein atonal homolog 1), *Egr2* (Early growth response protein 2, also known as *Krox20*) (Figure 2.10A), and *Lbx1* (Ladybird homeobox gene) (Dubreuil et al., 2008; Dubreuil et al., 2009; Ramanantsoa et al., 2011; Ruffault et al., 2015). Previous work in the lab showed that ablation of the *Phox2b/Atoh1* RTN cells, thereafter termed RTN$^{Phox2b/Atoh1}$ cells, (mouse line: *Egr2-Cre; Phox2b*^{27AlaCKI}) also blunted the chemoreflex in neonates, therefore providing the utmost specific genetic signature for the CO_2-sensitive RTN (Figure 2.10) (Dubreuil et al., 2008; Dubreuil et al., 2009; Ramanantsoa et al., 2011; Ruffault et al., 2015). Furthermore, in agreement with the above data obtained in adults, optogenetic stimulation of RTN$^{Phox2b/}$Atoh1 neurons, in neonatal *ex vivo* preparation, was shown to trigger an inspiratory burst recorded from

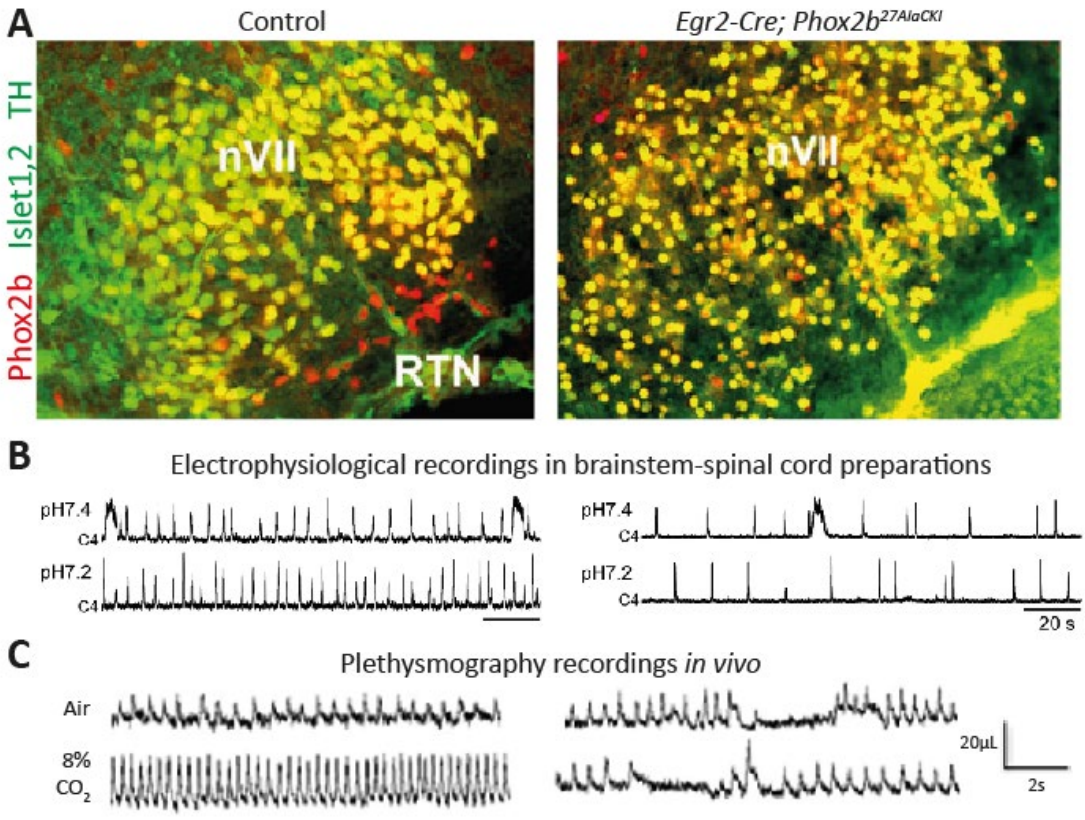

Figure 2.10. The RTN: a central chemosensitive center. (A) (Left) Localization of the RTN. The RTN is located ventral to the facial motor nucleus (nVII) and is Phox2b^{+}, TH^{-} and Islet1,2^{-}. TH is a marker of catecholaminergic neurons. Islet1,2 labels motoneurons. (Right) Genetic elimination of *Phox2b/Atoh1* RTN (RTN$^{Phox2b/Atoh1}$) neurons during development using the transgenic line *Egr2-Cre; Phox2b*^{27AlaCKI}. **(B)** (Left) Increase in inspiratory frequencies, recorded on the 4th cervical motor nerve C4, in response to an increase in CO_2 *ex vivo*. (Right) Elimination of RTN$^{Phox2b/Atoh1}$ neurons blunts to response to CO_2. **(C)** (Left) Increase in breathing frequencies in response to an increase in CO_2 in the air *in vivo*. (Right) Elimination of RTN$^{Phox2b/Atoh1}$ neurons prevents breathing frequency increase to CO_2. Adapted from Ramanantsoa et al. (2011).

C4 where exits the phrenic nerve innervating the diaphragm (Ruffault et al., 2015). Together with their CO_2 sensitivity this demonstrated that a chemosensitive change of their activity could translate in a change of the respiratory command thus defining them as *bona fide* CO_2 chemoceptive neurons. *We will use later in this work the Phox2b/Atoh1 genetic signature to selectively manipulate the RTN during a running exercise.*

A debate remains unsolved regarding the anatomical and functional overlapping of the rhythmogenic non-chemosensitive pFRG and the non-rhythmogenic chemosensitive RTN. RTN and pFRG both respond to CO_2/pH changes and share marker gene expression including *Phox2b* (Mulkey et al., 2004; Stornetta et al., 2006; Ruffault et al., 2015). However, chemosensitive neurons in neonates retain their central chemoreceptor properties and their ability to activate the respiratory rhythm in adulthood (Mulkey et al., 2004; Kanbar et al., 2010; Marina et al., 2010), while the persistence of the rhythmogenic properties is less clear (Guyenet et al., 2005; Oku et al., 2007). RTN and pFRG might be identical structures or might largely overlap at different stages (Onimaru et al., 2009; de Britto and Moraes, 2017). *We will see in the next section that the rhythmogenic pFRG might acquire a different firing property throughout adulthood.*

The pF: a conditional expiratory oscillator

Despite the fact that the pFRG action potentials occurs before and after inspiration, these neurons were called pre-I (Onimaru and Homma, 2003), which is potentially misleading. Indeed, several lines of evidence suggest that neurons in the parafacial respiratory region (pF) might drive active expiration upon metabolic changes. In neonatal and juvenile rats, hypercapnia (i.e., increase in CO_2) was shown to trigger active expiration (Figure 2.11A) (Abdala et al., 2009). Importantly, active expiration was abolished when the pF was eliminated or chemically suppressed. Also, in adult anesthetized rats, photo-activation, or local disinhibition of the pF triggers active expiration (Figure 2.11B). Importantly, previously silent pF neurons become rhythmically active during the expiratory phase and fire in synchrony with abdominal bursts (Figure 2.11B) (Pagliardini et al., 2011; Huckstepp et al., 2015; de Britto and Moraes, 2017). These results suggest that active expiration results from the activation of a conditional pF oscillator that persists in adulthood and is coupled to the inspiratory rhythm generator. Altogether, there is increasing consensus that the pF, in addition to play a central part in chemoception, contributes

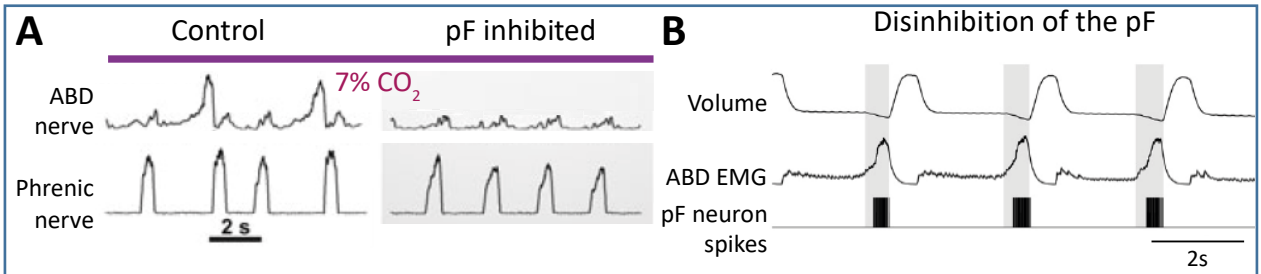

Figure 2.11. The pF is essential for the generation of active expiration. (A) Recordings of abdominal (ABD, expiratory) and phrenic (inspiratory) nerves in juvenile rats under 7% CO_2. (Left) In control animals, hypercapnia triggers active expiration. (Right) Chemical silencing of the parafacial respiratory region (pF) abolishes hypercapnia-driven active expiration. Adapted from Abdala et al. (2009). **(B)** Recordings of the respiratory volume, abdominal muscle, and pF neuronal firing. Disinhibition of the pF using injections of bicuculline/strychnine triggers active expiration *in vivo*. Previously silent pF neurons become rhythmically active during active expiration (shaded rectangles). Adapted from Pagliardini et al. (2011).

to the generation of active expiration, and is coupled to the preBötC. In this sense, the pF is a contender for mediating respiratory modulation upon other high metabolic demands like exercise.

To conclude on the pFRG, RTN and pF, it is worth noting that despite intensive work, a clear view on the anatomical and functional overlap of the neurons that these denominations include is missing. *Because this debate is beyond the scope of my PhD we will refer to it thereafter as the pF.* Assigning specific subsets of pF neurons with precise functional tasks is the only way to get a comprehensive view of the cellular bases of its multifunctional implications. *Therefore, in this work, I have chosen to focus on chemoceptive RTN$^{Phox2b/Atoh1}$ neurons, a homogenous cellular lineage sharing a developmental history of expression of several transcription factor (Egr2, Phox2b, Atoh1, Lbx1) to evaluate its role in respiratory adaptation to exercise.*

b. Involvement in exercise hyperpnea

The pF is crucial for generating the respiratory rhythm, and for the modulation of the rhythm in response to metabolic changes, thereby placing this structure as a prime candidate to mediate respiratory changes during an increase metabolic drive like exercise. Indeed, several lines of evidences suggest its implication, albeit mostly through indirect observations. First, a study used *ex vivo* preparations of brainstem still attached to the lumbar spinal cord in neonatal rats, and monitored respiratory frequency recorded on the cervical motor nerve C4 as previously presented (see Chapter 1.II.3.b., (Le Gal et al., 2014). The authors show that empiric pharmacological activation of the locomotor CPG in the lumbar spinal cord, in charge of generating a rhythmic and patterned activation of locomotor muscles during movement (see more details in Chapter 3.II.4.), triggers an increase in respiratory frequency recorded on C4. Interestingly, broad lesions of the pF region suppressed the ability for locomotor CPG-driven respiratory increase. Furthermore, patch clamp recordings showed that pF neurons are depolarized during activation of the locomotor CPG, further suggesting that it integrates locomotor signals from the spinal cord. However, the implication of a direct connectivity from the spinal locomotor CPG to the pF was not demonstrated in this study, and the exact identity of pF neurons (apart from the potential expression of *Phox2b*) remains to be elucidated. Second, virally driven inhibition of *Phox2b* pF neurons (albeit also the nearby catecholaminergic C1 neurons) was shown to greatly impact the capacity of adult rats to run for a long distance on a treadmill, suggesting that *Phox2b* neurons in the broad region of the pF are involved in exercise performance (Korsak et al., 2018). However, the implication of this region in mediating exercise hyperpnea in running animals was not addressed. Third, c-fos experiments (i.e., a marker for neuronal activity) showed that *Phox2b* pF neurons are activated by an acute treadmill exercise in rats (Barna et al., 2014). Finally, activation of the hypothalamus in rats (Parker and Sinnamon, 1983), a region that could correspond to the diencephalic locomotor region (DLR), a region that initiates the movement (see more details Chapter 3.II.1.), activates pF neurons and increases respiratory frequency and amplitude (Fortuna et al., 2009). However, hypothalamic stimulation did not trigger locomotion, so the functional significance of this effect remains elusive.

3. The lateral parabrachial/kölliker-fuse nuclei (lPB/KF)

a. A multisensory integrator

The lPB/KF is implicated in respiratory phase transition (Dutschmann and Herbert, 2006; Mörschel and Dutschmann, 2009). The lPB/KF receives principal inputs from the NTS (Herbert et al., 1990) and the dorsal horn of the spinal cord (Cordero-Erausquin et al., 2009; Cameron et al., 2015), and projects to numerous forebrain structures including the amygdala, hypothalamus, cortex and thalamus. Thus, the lPB/KF relays multiple sensory information about respiratory and cardiovascular function and also about nociception, pain, and temperature (Jiang et al., 2004; Davern, 2014; Barik et al., 2018; Palmiter, 2018; Chiang et al., 2019). Interestingly, lPB/KF was shown to coordinate stereotyped responses such as jumping in response to noxious stimuli like heat (Barik et al., 2018). In addition, the lPB/KF receives direct projection from cervical spinal neurons involved in coordinating fore- and hindlimbs (Ruder et al., 2016), although its exact role has not been addressed in this study. Altogether, an emerging view is that the lPB/KF is a multisensory integrative center for peripheral and central stimuli that relays information to forebrain areas to elaborate an adaptive response, and might do so during to exercise.

b. Involvement in exercise hyperpnea

The possible implication of the lPB/KF in mediating respiratory responses to exercise has been investigated in juvenile and neonatal rats (Potts et al., 2005; Giraudin et al., 2012). We saw previously (see Chapter 1.II.2.) that stimulation of lumbar and cervical afferences, that normally arise from contracted locomotor muscles, can trigger an inspiratory burst. Interestingly, lesion or ablation of the lPB/KF abolishes this respiratory response, suggesting that the lPB/KF serves as a pontine relay for transmission of peripheral spinal information to respiratory generating circuits in the brainstem. The transmission from the lumbar spinal cord was shown to require a spinal relay at the cervical level of the spinal cord (Giraudin et al., 2012). The authors argue that peripheral information from contracted muscles is integrated in the lPB/KF to synchronize respiratory and locomotor rhythm. We saw previously in Chapter 1.I.5 that the evidences for a strict temporal synchronization between breathes and strides are poorly documented across species. While a phase-locking of respiratory and locomotor rhythms can occur, it is far from clear that it is a mandatory requirement in all species. In addition, this has never been investigated in rodents and part of my work will address this issue in mice (see Paper 1, (Hérent et al., 2020)). In any case, while the functional significance of the ascending drive from cervical and lumbar sensory feedback involving the lPB/KF remains unclear, the lPB/KF is nonetheless a key structure that receive proprioceptive information from the spinal cord, which might be important to relay sensorimotor signals to respiratory centers during exercise.

Chapter 3: Control of locomotion and candidate neurons

Locomotion is a vital motor behavior allowing animals to move from place to place to hunt for preys, escape predators, find a mate or a suitable habitat. Depending on the species, locomotion can refer to different ambulatory modes: swimming, flying, crawling, over-ground walking, running, or hopping. Although the act of locomotion seems simple, it is a rather complex and sophisticated behavior that relies on the concerted activation and coordination of body and limb muscles. Locomotor movements are driven by planning and initiation centers in the brain and the precise rhythmic and patterned muscle activation is generated in the spinal cord.

In this third chapter, I will describe the general aspects of the locomotor behavior in mammals, focusing on limbed locomotion in quadrupeds. In addition, I will document the central and peripheral neuronal structures essential for locomotor control, with emphasis on locomotor neurons candidates to mediate respiratory adaptation during running exercise.

I. Generalities on locomotor control

1. Locomotor movements: cycle and gait

To move in their environment, mammals use a succession of locomotor cycles (or strides) for each limb and alternate between stance and swing phases. During the **stance** phase, the limb is extended and in contact with the ground to carry the body weight and provide propulsive forces. During the **swing** phase, the limb is flexed and lifted off the ground forward (footlift) until it bounces back on the ground (footfall), to start a new stance phase. Thus, a complete locomotor cycle or stride is comprised between two consecutive footfalls of one given limb (Figure 3.1) (Pearson, 1976; Hughes and Jacobs, 1979; Purves et al., 2001; Ismail et al., 2019).

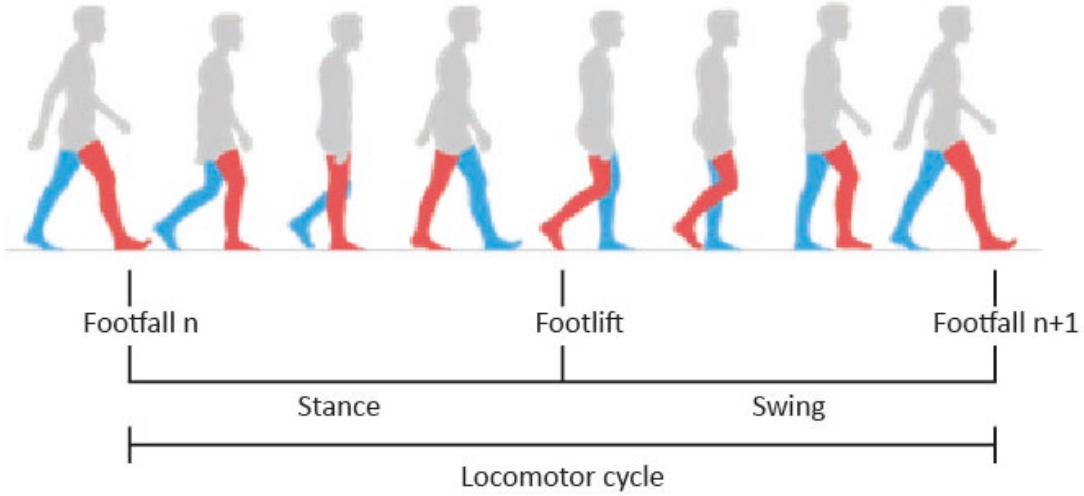

Figure 3.1. The locomotor cycle. Schematics of a human walking. One locomotor cycle is defined between two consecutive footfalls (n, n+1) and includes a swing and a stance phase. The swing phase starts when the foot is lifted off the ground (footlift). Adapted from https://www.kinesis.ie/gait/.

In mammals, locomotor strides are mainly achieved through the precise recruitment of rhythmic and temporally-organized contraction of flexor and extensor muscles from different joints (Grillner, 2011). The control of extensor and flexor muscles within a limb needs to be activated in a precise sequence, often referred to as a "pattern", to avoid contraction of antagonist muscles. To put it simply, flexor muscles are recruited mostly during the swing, and extensor muscles during the stance. To move faster, the locomotor cycle duration can be decreased, notably owing to a reduction in the duration of the stance phase. Indeed, extensor muscles are increasingly recruited as displacement speed augments (Figure 3.2A, B) (Grillner, 2011; Mayer et al., 2018). While such adjustments in the step cycle can support a wide range of running speeds, highest displacement speeds are typically associated, in most quadrupedal mammals, with a switch of gait, i.e., the adoption of a different sequence of interlimb coordination.

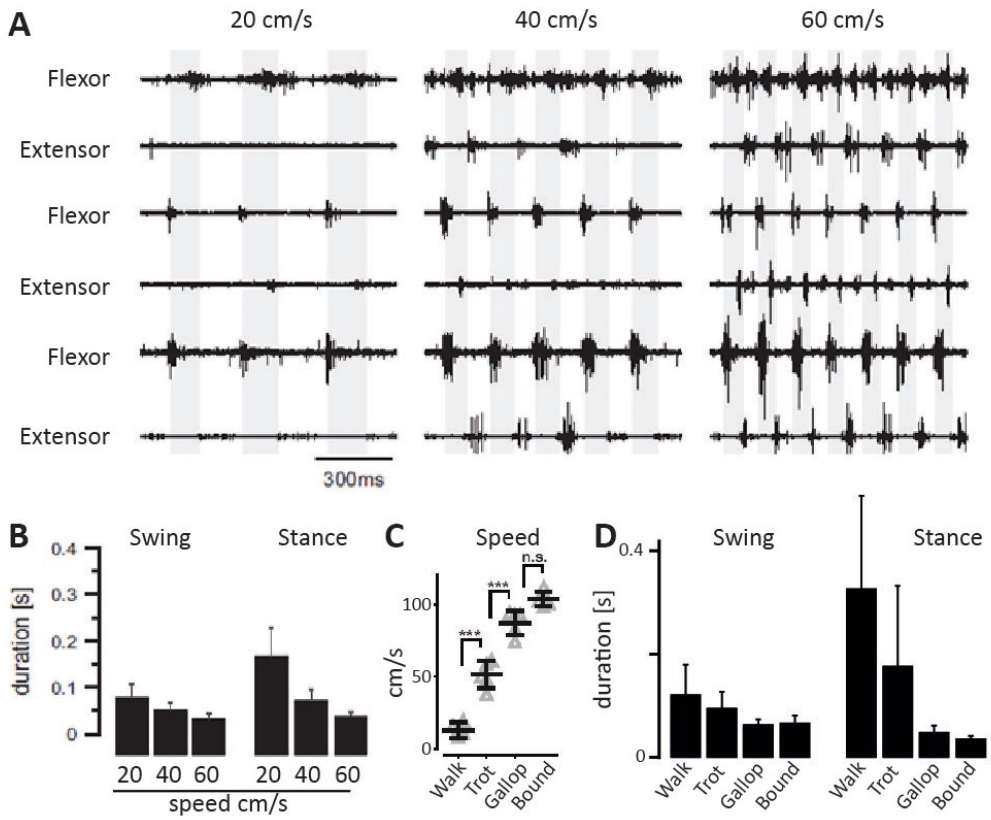

Figure 3.2. Speed dependent recruitment of muscles and gaits. (A) Flexor and extensor muscle activities in mice running at 20 (left), 40 (middle) and 60 cm/s (right). Shaded areas indicate swing phases. Note that locomotor muscles are recruited in a speed dependent fashion, especially extensors. **(B)** Bar-graphs illustrating swing and stance durations at the same running speeds. Note that to increase speed, the stance phase, mostly depending on extensor muscle activities, is highly decreased. **A** and **B** are adapted from Mayer et al. (2018). **(C)** Graph illustrating locomotor speed for each gait in mice. Note the relation between gait and locomotor speed. Adapted from Bellardita and Kiehn (2015). **(D)** Bar-graphs illustrating swing and stance durations for each gait. Note that shifting to higher gaits requires a strong decrease of the stance duration. Adapted from Lemieux et al. (2016).

Mammals show a variety of interlimb coordination patterns, named gaits, which are linked to different speed ranges (Bellardita and Kiehn, 2015; Lemieux et al., 2016; Frigon, 2017). This allows the efficient expression of running behaviors ranging from low-speed exploration to high-speed escape. Quadrupeds display four-leg coordination patterns, divided into four major gaits: walk, trot, gallop and bound (Dagg, 1973). Elegant studies analyzed the kinematics of these different gaits in mice on a catwalk and treadmill (Figure 3.2C, D) (Bellardita and Kiehn, 2015; Lemieux et al., 2016). In Bellardita and Kiehn (2015), **walking** is defined as a slow (10 cm/s) alternating gait where at least three feet are in contact with the ground simultaneously and homologous pair of limbs on the left and left right sides are moving in alternation. **Trotting** is characterized as a fast (between about 15 to 60 cm/s) alternating gait where two feet are touching the ground at the same time and the homologous pair of limbs are also alternating. **Galloping** is defined as a medium- to high-speed (up to 90 cm/s) semi-synchronous gait where left and right hindlimbs are mostly synchronized while left and right forelimbs are alternating. **Bounding** is defined as a high-speed (100 cm/s and beyond) synchronous gait where both homologous fore- and hindlimbs are synchronized. *We will see later that these distinct gaits might be encoded centrally by dedicated microcircuits in supraspinal (see Chapter 3.II.2.a.) and spinal locomotor centers (see Chapter 3.II.4.a.).*

2. Neural bases of locomotor control

The complex intra- and interlimb coordination of limb movements illustrates the complexity of the underlying neuronal organization. Indeed, the locomotor act involves a remarkably conserved neuronal organization amongst vertebrates based on three levels of control extending from the forebrain to the spinal cord (Figure 3.3). The first level is the selection and initiation of locomotor behavior. The **basal ganglia**, located in the forebrain, are the dominating selection system for the execution of planned movements like volitional exploratory or goal-directed locomotion and depends on inputs from cortical areas, thalamus and the dopaminergic system (Kiehn and Dougherty, 2013; Kiehn, 2016; Ferreira-Pinto et al., 2018). The basal ganglia project back to the thalamus and also to key locomotor centers in the diencephalon and the mesencephalon: the **diencephalic locomotor region** (DLR) (Orlovsky, 1969) and the **mesencephalic locomotor region** (MLR) (Shik et al., 1966). The DLR and MLR are thought to mediate locomotor initiation as they have been initially identified in cats as able to initiate locomotor movements and to control locomotor speed and gaits, even without the cortex. The initiating command signal is funneled to long-range projection neurons in the brainstem reticular formation, including neurons that directly project to the spinal cord, i.e., **reticulospinal** (RS) **neurons**. RS neurons therefore provide the final descending signal to the spinal cord to gate (initiate, maintain, and arrest) and modulate locomotion. RS neurons not only relay initiating signals from the MLR and DLR but may also relay external and internal sensory information (Kim et al., 2017; Brownstone and Chopek, 2018). The signal from RS neurons is transmitted to specialized ventral spinal executive circuits, often referred to as a "central pattern generator" (or CPG, (Kjaerulff and Kiehn, 1996; Kiehn, 2006, 2016; Grillner and El Manira, 2020). The **spinal CPG** is in charge of generating the rhythmic and patterned activation of multiple body and limb muscles. Locomotor information is also conveyed from the cerebellum directly or indirectly to the spinal cord to maintain posture, modulate descending pathways signals and regulate motor and spatial learning (Morton and Bastian, 2004; Helleringer et al., 2018; Muzzu et al., 2018; Darmohray et al., 2019; Sathyamurthy et al., 2020). Proprioceptive feedback from contracted

muscles also regulate ongoing activity by projection to the spinal CPG (Lam and Pearson, 2002). Ascending signals from the spinal cord provide sensory and motor information to supraspinal locomotor regions.

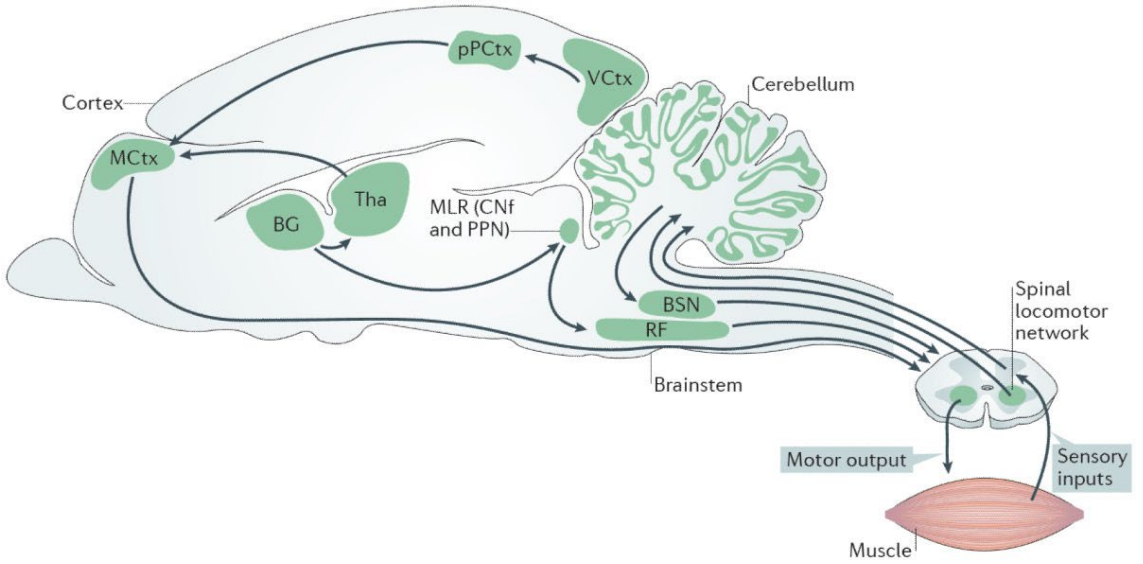

Figure 3.3. Location of essential neurons for locomotor control. The behavior is selected primarily by the basal ganglia (GB) in interaction with thalamocortical areas (Tha, MCtx). The mesencephalic locomotor region (MLR) is contacted by the BG and is the prime initiator of locomotion. The MLR projects to the brainstem reticular formation (RF) including reticulospinal neurons. Brainstem reticulospinal neurons then transmit the locomotor signal to the spinal locomotor network which drives the contraction of dedicated muscles. Once the movement is engaged, sensory inputs from the periphery send feedback to the spinal locomotor network and the cerebellum to modulate descending pathways. *VCtx, Visuomotor cortex. pPCtx, posterior parietal cortex. MCtx, Motor cortex. Tha, Thalamus. CNf, Cuneiform nucleus. PPN, Pedunculopontine nucleus. BSN, Vestibular and rubrospinal brainstem nuclei.* Adapted from Kiehn (2016).

The central command theory stipulates that signals from any of the above locomotor circuits could directly modulate respiratory activity at the onset and during exercise but importantly also prior to exercise. Locomotor neurons candidate for mediating exercise hyperpnea will be detailed in the following section.

II. Candidate locomotor neurons for mediating exercise hyperpnea

1. The diencephalic locomotor region (DLR)

a. Locomotor initiation and control of speed and gaits

The DLR has been identified physiologically by broad stimulations of regions in proximity of the subthalamic nucleus able to trigger a well-controlled locomotion in cats and rats from walk to gallop, depending on the stimulation intensity (Orlovsky, 1969; Parker and Sinnamon, 1983). However, its anatomical location is still debated and remains obscure in mammals. In lampreys,

which share strong similarities with the mammalian locomotor system (Robertson et al., 2014), the DLR is located in the ventral thalamus – a region analogous to the lateral hypothalamus in mammals – and its activation elicits bouts of swimming (El Manira et al., 1997; Ménard and Grillner, 2008). Interestingly, although the DLR connects to the MLR, the MLR is not required to elicit a DLR-induced locomotion, suggesting that the locomotor command from the DLR might be a parallel system for locomotor control (Orlovsky, 1969; Shik et al., 1969) that could be used in different behavioral contexts (Grillner et al., 1997). Therefore, the DLR might play a key role in running exercise by initiating the movement and controlling locomotor speed and gaits.

b. Involvement in exercise hyperpnea

Some lines of evidence have suggested that the DLR might mediate breathing changes during exercise (see Chapter 1.II.3.a., (Eldridge et al., 1981; DiMarco et al., 1983; Waldrop et al., 1988)). Indeed, electrical or pharmacological activation of the DLR in decorticate cats (i.e., without cortex) triggers locomotion and is associated with respiratory and cardiovascular changes during the movement (Eldridge et al., 1981; 1985; DiMarco et al., 1983). Importantly, these changes take place prior to, and also without, any movement (i.e., in curarized animals). This suggests that a central command starting from the DLR might control autonomic changes including exercise hyperpnea in parallel of, or in synergy with, locomotion. While the DLR is clearly a good candidate to mediate exercise hyperpnea, its exact localization and precise cell types are yet to be specified in other mammals, like mice, to ascertain its implication.

2. The mesencephalic locomotor region (MLR)

a. Locomotor initiation and control of speed and gaits

A highly conserved structure amongst vertebrates

The MLR has received much more attention over the years - see for review (Le Ray et al., 2011; Ryczko and Dubuc, 2013). Shik et al. (1969) showed that low MLR stimulation initiates and maintains slow locomotor patterns in decerebrated cats. As the stimulation strength increased, higher speed locomotion is produced, and the animals shift gait. Interestingly, the MLR has been documented in all investigated species from lampreys to mammals and can trigger all types of locomotion, i.e., from swimming to walking and running, and controls locomotor speed and gait (Shik et al., 1966; Skinner and Garcia-Rill, 1984; Sirota et al., 2000; Ryczko et al., 2016; Caggiano et al., 2018; Josset et al., 2018). Interestingly, investigations in humans using mental simulation of exercise and functional magnetic resonance imaging showed that a region corresponding to the anatomical location of the MLR is activated when subjects are “mentally walking” (Jahn et al., 2008; Karachi et al., 2010). When the intensity of the simulated effort is upgraded to “running”, the activation of the MLR intensifies. In addition, the MLR has become a prime target of deep brain stimulations to alleviate some motor deficits of Parkinson patients and Parkinson animal models (Moro et al., 2009; Pereira et al., 2011; Thevathasan et al., 2011; Goetz et al., 2019; Lau et al., 2019). Therefore, the MLR is a highly conserved structure amongst vertebrates and most likely in humans as well.

The glutamatergic MLR is sufficient to elicit a graded locomotion

Using electrical or chemical mapping of the MLR, sites able to elicit locomotion were located in a broad region comprising the **cuneiform nucleus** (CnF) and the **pedunculopontine nucleus** (PPN) (Shik et al., 1969; Skinner and Garcia-Rill, 1984; Sirota et al., 2000; Takakusaki et

al., 2003), although some studies showed variable results (Takakusaki et al., 2016). Indeed, CnF and PPN contain intermingled glutamatergic and GABAergic neurons, with additional cholinergic neurons in the PPN (Figure 3.4A) (Martinez-Gonzalez et al., 2011), making it challenging to further dissect the cellular and functional identity in the MLR. To resolve this, an elegant study manipulated the different subtypes of the MLR using optogenetics tools in mice (Roseberry et al., 2016). They found that the sole activation of glutamatergic MLR neurons could elicit a graded locomotion, whereas inhibition of the same cells caused animals to decelerate and stop ongoing locomotion (Figure 3.4). This demonstrated that the glutamatergic MLR is sufficient to elicit locomotion in a graded fashion and necessary for spontaneous locomotion. However, it was not clear at the time if the glutamatergic MLR included the CnF and/or PPN.

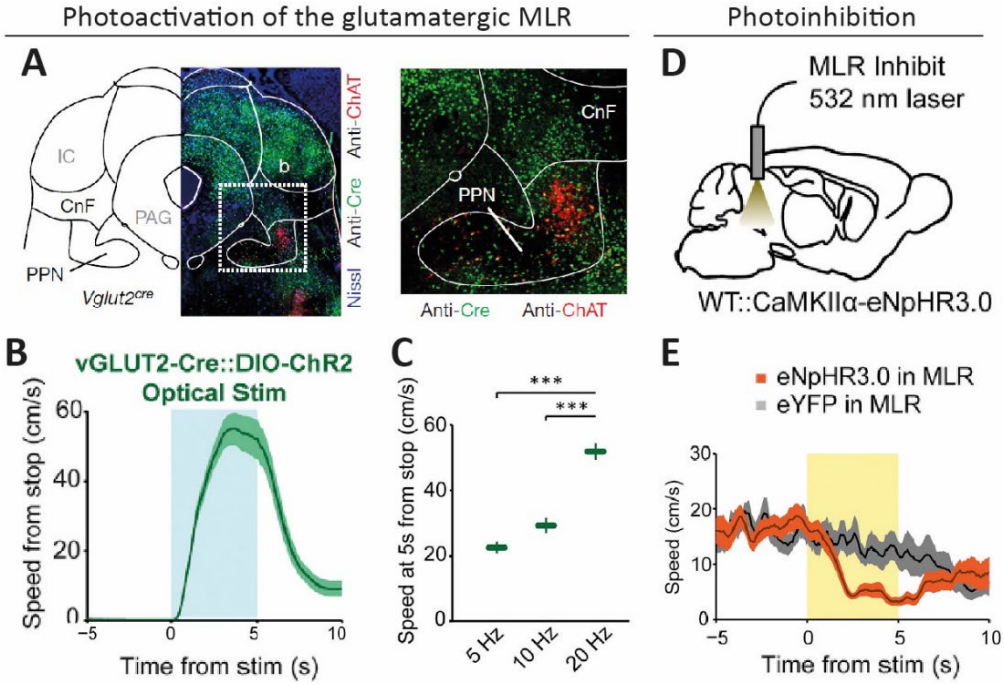

Figure 3.4. Glutamatergic MLR neurons are necessary and sufficient to initiate and control locomotor speed. (A-C) Photoactivation of the glutamatergic MLR. **(A)** Coronal view of the MLR comprising the cuneiform (CnF) and pedunculopontine (PPN) nuclei. Glutamatergic neurons are in green (Cre) in the CnF and the PPN, while cholinergic neurons are in red (ChAt) in the PPN. Adapted from Caggiano et al. (2018). *PAG, periaqueductal grey. IC, inferior colliculus.* **(B)** Photostimulation of the glutamatergic MLR (blue rectangle) from stationary state initiates locomotion. **(C)** Locomotor speeds evoked by MLR stimulation are dependent on the stimulation frequency. **(D-E)** Photoinhibition of the glutamatergic MLR. **(E)** Sagittal view of the MLR inhibition procedure. **(E)** Inhibition of the glutamatergic MLR (yellow rectangle) from running state decreases and stops ongoing locomotion (orange line) as compared to control mice (grey line). Adapted from Roseberry et al. (2016).

<u>The glutamatergic CnF encodes locomotor speeds and gaits, especially high-speed running</u>

Later elegant studies used optogenetics and chemogenic tools in mice to activate either the glutamatergic CnF or PPN (Caggiano et al., 2018; Josset et al., 2018; Dautan et al., 2020). All three studies show that, glutamatergic CnF optoactivation always initiate robust full-body

locomotion at short latencies, from slow alternating speed to fast synchronous gaits depending on the stimulation frequency. Silencing these cells greatly impaired mice ability to engage in high-speed locomotion. In contrast, the exact role of the glutamatergic PPN requires further investigations. Indeed, Caggiano et al. (2018) show that, photoactivation of the glutamatergic PPN can elicit, with longer latencies (~1s), only the slow alternating speeds that are associated with exploratory behavior. Other studies have found that activation of the glutamatergic PPN decreases and arrests ongoing locomotion (Josset et al., 2018; Dautan et al., 2020). These discrepancies might owe to a wide heterogeneity in the electrophysiological properties of glutamatergic PPN cells as compared to the CnF (Caggiano et al., 2018; Dautan et al., 2020).

Interestingly, the glutamatergic PPN receives strong inputs from the basal ganglia, and sensory and motor-related regions of the medulla. In contrast, the CnF receives few inputs from the basal ganglia but is strongly targeted by the colliculi and the periaqueductal gray (PAG) (Figure 3.5) (Caggiano et al., 2018). Both CnF and PPN projects to the brainstem reticular formation where reticulospinal neurons that directly project to the spinal cord reside (see next section).

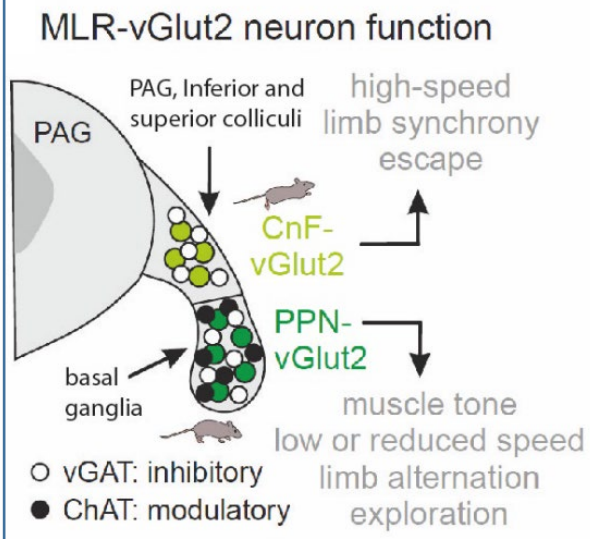

Figure 3.5. Dual control of locomotion by the glutamatergic MLR. Glutamatergic cuneiform nucleus (CnF) neurons (light green) receive inputs from the periaqueductal grey (PAG) and the colliculi and mediate all locomotor speed including high-speed escape behaviors. The glutamatergic pedunculopontine nucleus PPN (dark green) receives strong inputs from the basal ganglia. It is not clear whether it mediates low-speed exploratory-like behavior or solely reduces the speed of ongoing locomotion. Both CnF and PPN comprise inhibitory neurons (vGAT, white), the PPN also contains cholinergic neurons (ChAt, black). Adapted from Ferreira-Pinto et al. (2018).

Taken together these data reinforce the idea of a dual locomotor command in the glutamatergic MLR: **1**) a CnF-mediated fast locomotion to orchestrate all locomotor regimes, especially fast running and escape-like behaviors selected by limbic structures and **2**) a PPN-mediated specifically tuned for low or reduced locomotion relevant during exploratory-like behavior selected by the basal ganglia (Figure 3.5) (Ferreira-Pinto et al., 2018).

b. Involvement in exercise hyperpnea

The MLR, and in particular the glutamatergic CnF in mice, is undoubtedly the initiator command for orchestrating locomotion. Some line of evidences suggested that the MLR can also mediate exercise hyperpnea (see Chapters 1.II.3.a. and 2.II.1.b., (DiMarco et al., 1983; Eldridge et al., 1985; Kawahara et al., 1989; Gariepy et al., 2012)). First in humans, we saw that mental stimulation is associated with MLR activation. Interestingly, mental stimulation also induces respiratory and cardiovascular changes (Tobin et al., 1986; Decety et al., 1991; Thornton et al., 2001), which could suggest a possible implication of the MLR. Secondly in cats, stimulation of the

MLR leads to respiratory and cardiovascular increase that could occur during locomotor episodes but also prior to the movement (Eldridge et al., 1985). Thirdly in lampreys, MLR stimulation also increases respiratory output and importantly projects directly to respiratory centers, and in particular the presumed homologue of the preBötC, the inspiratory generator in mice (Gariepy et al., 2012). Altogether, these data suggest that the MLR integrates and transforms locomotor signals into multifunctional outputs that might control locomotion and autonomic responses in parallel, including breathing. In addition, the MLR encodes the upcoming locomotor action and is therefore in a prime position to regulate breathing prior to, at the onset, and throughout locomotor episodes. However, the exact MLR subcomponent (CnF and/or PPN) involved and its exact neuronal cell types are not documented in mice. Also, the connectivity from the MLR to the preBötC as well as the genetic identity of targeted preBötC cells are yet to be characterized. And we will endeavor to resolve these issues in mice which provide an amazing understanding of the neuronal bases for locomotor and respiratory control and cutting-edge tools to manipulate and trace circuits with synaptic specificity (see Paper 2). In particular in mice, the glutamatergic CnF encodes especially high-speed locomotion (Caggiano et al., 2018; Josset et al., 2018; Dautan et al., 2020), and therefore likely mirrors the intensity of the upcoming effort. Thus, the glutamatergic CnF is a key candidate to mediate exercise hyperpnea. Accordingly, in mice, the generation of inspiratory rhythm relies on glutamatergic preBötC neurons (see Chapter 2.II.1. (Smith et al., 1991; Gray et al., 2001; Tan et al., 2008; Bouvier et al., 2010)), key candidates to receive locomotor signals from the CnF.

3. The reticulospinal neurons (RS)

a. Motor command tuning

RS neurons in the reticular formation can directly or indirectly influence interneurons and motoneurons activity in the spinal locomotor CPG (Lemon, 2008; Brownstone and Chopek, 2018), through excitatory descending commands, especially glutamatergic, serotonergic and dopaminergic (Liu and Jordan, 2005; Kiehn, 2006; Jordan et al., 2008; Hagglund et al., 2010). RS neurons are essential substrates in locomotor control as they convey various information from locomotor centers, but also from other brain and cerebellar areas, to the spinal locomotor CPG to initiate, modulate or terminate its activity. In contrast with studies on the DLR and the MLR, electrical stimulations in the reticular formation based on localization failed to reveal consistent behaviors, presumably owing to the presence of diverse cell-types with little spatial organization (Ferreira-Pinto et al., 2018). Studies in mice have started to disentangle the diversity of locomotor repertoires using developmental genetics and viral tracings combined with discrete manipulation of specific cell types. Corroborating this, broad optogenetic activation of glutamatergic RS neurons in the brainstem established their critical role for initiating locomotion (Hagglund et al., 2010). Later studies used more restricted activation of glutamatergic subsets and further show that the lateral paragigantocellular nucleus (LPGi), located in the caudal brainstem, can elicit locomotion and control the speed (Capelli et al., 2017). Interestingly, combining photoactivation of the MLR with ablation of the glutamatergic LPGi greatly impaired high-speed locomotion without perturbation of the exploratory low-speed locomotion. In addition, the LPGi is preferentially targeted by the CnF subcomponent of the MLR, suggesting that engagement in high-speed locomotion relies on the specific recruitment of the CnF-LPGi pathway (Figure 3.6A, B) (Capelli et al., 2017). This also suggests that the MLR-driven low-speed control is mediated by another neuronal groups, probably in the brainstem, yet to be uncovered. The same study shows

that inhibitory neurons in the LPGi halt ongoing locomotion, highlighting that the diversity of cell types and function of one RS pathway in initiating, or on the contrary arresting, locomotion cannot accurately be predicted by the positioning of the neuronal somata in crudely defined anatomical areas, nor even by its neurotransmitter. Indeed, Bouvier et al. (2015) uncovered the surprising role of a glutamatergic neuronal population, located in the rostral gigantocellular (Gi) nucleus, and expressing *Chox10* (**V2a neurons**). Unexpectedly, bilateral photoactivation of the V2a Gi neurons halted ongoing locomotion, while silencing these cells enhanced mobility (Figure 3.6C). V2a neurons project to inhibitory interneurons in the ventro-lumbar spinal cord, which likely mediate the locomotor arrest. It was however not clear at the time in what behavioral context this locomotor break would take place. Therefore, the study was continued in the lab and my PhD contributed to it, although without direct relation to exercise hyperpnea (see Paper 3, Annex 1, (Usseglio et al., 2020)). In short, we show that distinct subsets of V2a RS neurons project to specific spinal segments and control different motor behaviors: **1**) a lumbar-projecting subset devoted to the control of locomotor speed and break and **2**) a premotor cervical-projecting subset that specifically mediates head orientation. Interestingly, none of these V2a subsets receive inputs from the MLR. Instead, the most abundant source of inputs was seen in the superior colliculus. Altogether this work demonstrates that the arrest of locomotion driven by V2a RS neurons is not related to an MLR-driven modality, but is rather linked with orienting movements. The work also highlights the need to consider functional diversity within RS neurons, even within cells that share the same genetic identity.

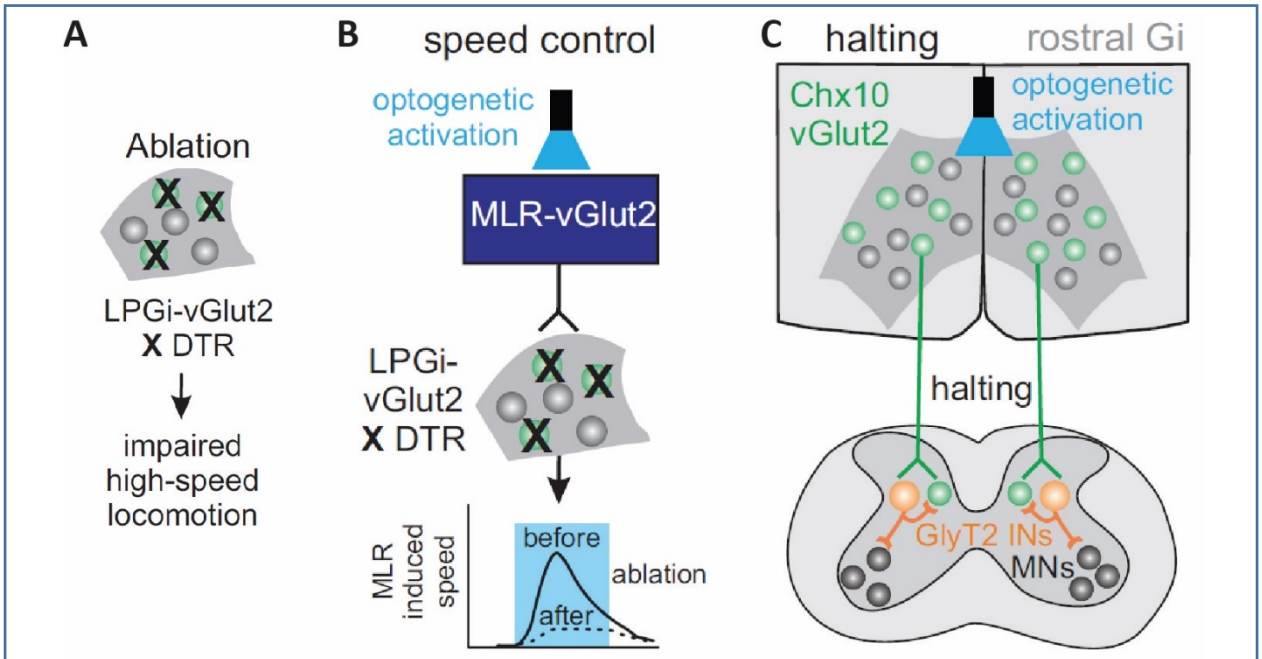

Figure 3.6. Brainstem glutamatergic reticulospinal neurons conveying locomotor stop and go signals. (A) Ablation of the glutamatergic lateral paragigantocellular nucleus (LPGi) impairs high-speed locomotion without affecting low-speed locomotion and **(B)** blunts the speed of locomotion triggered by glutamatergic MLR stimulation. **(C)** Bilateral photoactivation of the glutamatergic V2a neurons, expressing *Chox10*, halts ongoing locomotion by targeting inhibitory spinal circuits. Adapted from Ferreira-Pinto et al. (2018).

b. Involvement in exercise hyperpnea

RS neurons relay crucial information about the upcoming locomotor movement and could also mediate breathing changes prior to and during ongoing movement. Because of their close proximity to respiratory centers, they might also integrate information on other functions like breathing, albeit very few evidences are available. On that note, V2a brainstem neurons were shown to directly project to the preBötC and to be essential to promote stable breathing activity at birth (Crone et al., 2012). It is however not known if such respiratory-related V2a brainstem neurons are preserved in the adult and whether they overlap with the locomotor and orienting-related ones described above (Paper 3, Annex 1**,** (Usseglio et al., 2020)).

4. The spinal locomotor CPG

a. Locomotor rhythm and pattern generation

Locomotor movements are complex and based on rhythmic and coordinated activation of several muscles across many joints by dedicated spinal CPGs. Hindlimbs locomotion is controlled by spinal circuits in the lumbar spinal cord, while forelimbs movements are driven by cervical spinal circuits. The lumbar locomotor CPG has received a lot of attention over the years and appears to be very much conserved amongst vertebrates - see for review (Kiehn, 2006; Frigon, 2017; Grillner and El Manira, 2020) - and likely in humans (Minassian et al., 2017; Klarner and Zehr, 2018). Like for investigating the respiratory rhythm, reduced *ex vivo* preparations were extensively used to isolate the spinal cord circuits and study their organization, function and development (Smith and Feldman, 1987; Branchereau et al., 2000; Clarac et al., 2004). To mimic the activation by descending RS neurons, absent in such preparations, spinal circuits have been classically activated by bath-application of glutamate, serotonin, and dopamine agonists onto the spinal cord, combined with electrophysiological recordings of the 2nd (L2) and 5th (L5) lumbar motor nerves. Notably, activities induced on the L2 flexor- and L5 extensor-like roots resemble the locomotor pattern of gaits *in vivo* like walking and trotting, i.e., alternation between flexor and extensor (ipsilateral L2 and L5), and between left and right (bilateral L2 or L5) (Kiehn, 2006; Goulding, 2009). These activities are therefore referred to as "locomotor-like" activities. Based on this type of experiment, the rhythmogenic core of the locomotor CPG was shown to be restricted to the ventral part of the spinal cord and distributed along the lumbar segments, with the most rhythmogenic capacity in the rostral lumbar segments (L1-L3) (Cazalets et al., 1995; Kjaerulff and Kiehn, 1996). The locomotor CPG harbors key microcircuits that are sufficient to generate a well-coordinated movement: **1**) rhythm generating circuits, **2**) left and right interlimb coordination circuits and **3**) ipsilateral flexor and extensor intralimb coordination circuits – see for review (Kiehn, 2006, 2016). Work with electrophysiology and mouse genetics have provided insights into the identity and function of specialized groups of spinal neurons and allowed to link genetically defined neuronal population to a specific locomotor behavior.

<u>Rhythm generating circuits:</u> Rhythm-generating neurons should be able to conditionally initiate and control the frequency of locomotion. Optogenetic activation or inactivation experiments identified excitatory spinal neurons (i.e., glutamatergic in mice) as necessary and sufficient to generate locomotor rhythm (Kiehn et al., 2008; Hagglund et al., 2010; Hagglund et al., 2013). To date, the only signatures identified for locomotor rhythm neurons are the expression of the

transcription factors *Shox2* (short stature homeobox protein 2) (Dougherty et al., 2013) and *HB9* (basic helix–loop–helix domain containing, class B, 9) (Wilson et al., 2005; Caldeira et al., 2017). Other contributing neurons are yet to be documented. To this day, it is therefore not obvious that locomotor rhythm generation may rely on a prominent, single type of neurons (such as V0 neurons in the preBötC).

Left and right interlimb coordination circuits that encode gaits: The coordination of muscle activities on the left and right side is essential to execute the repertoire of quadrupedal gaits in mammals. Alternation or synchronization of pairs of limbs relies on commissural neurons (CN) whose axons cross the midline. Genetic ablation of types of CN provided insight into the mechanisms underlying left and right coordination and the encoding of gaits. A large proportion of CN in the ventral spinal cord are V0 *Dbx1* neurons subdivided in two populations: excitatory $V0_V$ and inhibitory $V0_D$. Ablation of the V0 population as a whole leads to a disruption of alternating locomotor-like bursting *ex vivo*, and bound becomes the default and only possible gait *in vivo* (Figure 3.7) (Lanuza et al., 2004; Talpalar et al., 2013). However, animals in which only the $V0_V$ are deleted can engage in every gait except trot (Talpalar et al., 2013). Altogether this elegant study shows that the combination of $V0_D$ and $V0_V$ CN encodes alternating gaits (walk and trot), while non-V0 CN encode the synchronous gait bound. Gallop is proposed to rely on a combination of V0 and non-V0 populations. Also, the loss of V2a spinal neurons also disrupts left and right coordination at high trotting speeds, highlighting that V2a neurons can influence gait selection, in a speed dependent manner (Crone et al., 2009).

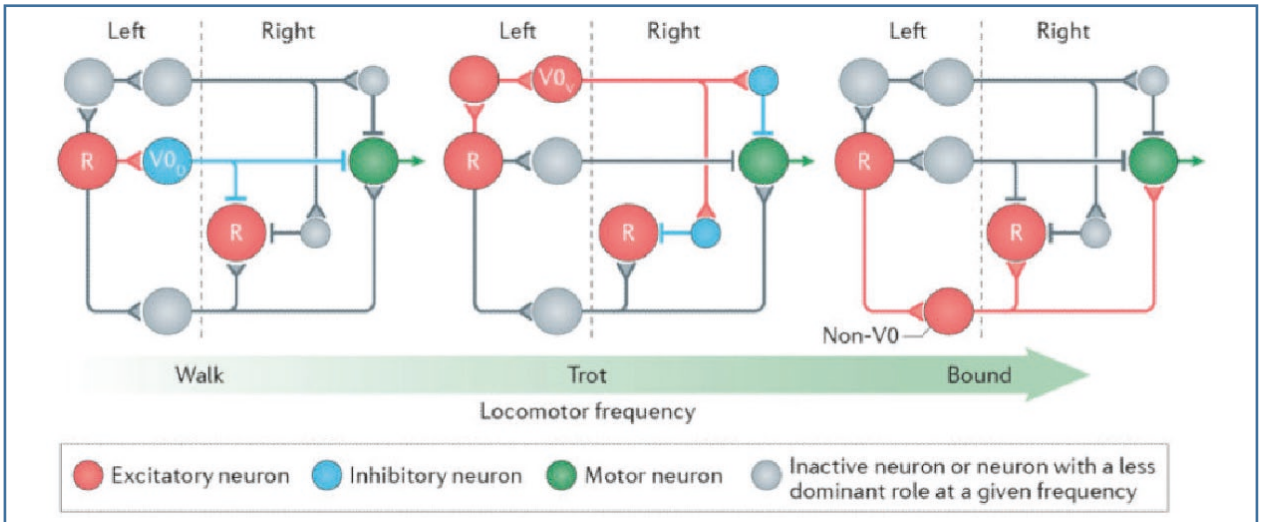

Figure 3.7. Speed dependent recruitment of spinal locomotor circuits controls left-right coordination and encodes gaits. V0 commissural interneurons are subdivided into two populations: inhibitory $V0_D$ and excitatory $V0_V$. Excitatory neurons are in red, inhibitory neurons are in blue, and motor neurons are in green. (Left) At low alternating speeds, $V0_D$ neurons provide inhibition to contralateral motor neurons and excitatory locomotor networks, resulting in walk. (Middle) At higher alternating speeds, $V0_V$ neurons provide excitation to contralateral inhibitory locomotor networks, resulting in trot. (Right) At high-speed locomotor speeds, non-V0 neurons provide excitation to motor neurons and excitatory locomotor networks, resulting in bound. Adapted from Kiehn (2016).

Interestingly, axon guidance and associated molecules play a crucial role in the wiring of spinal neurons by directing the axon of commissural neurons during development (Chédotal, 2019). During my PhD, I have worked on a collaborative project which touched upon the role of the scaffold molecule afadin, expressed at the spinal midline during development (see Paper 4, Annex 2, (Skarlatou et al., 2020)). We found that ablation of afadin from the motor neuron progenitor zone in the developing spinal cord leads to a striking hopping phenotype *in vivo*, and a disruption of left and right coordination in *ex vivo* spinal cord preparations. Afadin ablation does not alter the development of motoneurons, instead, it disrupts the expression of axon guidance molecules at the midline, causing ectopic and aberrant contralateral wiring of several types of spinal interneuron's axons, including V0 and V2a interneurons. This shows that guidance molecules are crucial for the correct laterality in wiring spinal circuits and coordination of key locomotor features.

Ipsilateral flexor and extensor intralimb coordination circuits: Flexor and extensor components of locomotor network are reciprocally connected through ipsilateral inhibitory neurons, notably through inhibitory Ia interneurons, activated by stretch-sensitive proprioceptive muscle spindles (Ia) (Talpalar et al., 2011; Kiehn, 2016). Genetic ablation of both V1 and V2b inhibitory interneurons, expressing respectively *En1* (engrailed homeobox 1) and *GATA2* (GATA binding protein 2), leads to a shift from alternating to synchronous flexor-extensor pattern (i.e., without left-right disruption) (Zhang et al., 2014).

b. Involvement in exercise hyperpnea

We saw that the locomotor CPG harbors complex microcircuits that play key roles in the execution of the rhythmic and patterned locomotor output. Interestingly, supraspinal centers that control the activity of the locomotor CPG receive ascending projections in return about the state of locomotor networks, to adapt ongoing movements to the environment. In particular, the ventral spino-cerebellar and spino-reticulo-cerebellar tracts convey information about the activity of locomotor interneurons activity (Buchanan and Einum, 2008). For example, during locomotor-like activities in rats and lampreys, reticulospinal neurons are rhythmically activated in phase with the locomotor cycle (Dubuc and Grillner, 1989; Oueghlani et al., 2018). Therefore, the locomotor CPG sends ascending efference copies to supraspinal regions involved in locomotion, but also regions related to other motor behaviors. Indeed, ascending projection to brainstem extraocular motoneurons have been shown to ensure gaze stabilization during swimming in tadpoles (Lambert et al., 2012; Straka et al., 2018). Therefore, besides being highly specialized in generating and coordinating locomotor movements, the locomotor CPG also relays critical information to other non-locomotor structures and possibly autonomic centers that are essential to survival, like breathing. Importantly, the CPG encodes the ongoing locomotor speed and gaits (Talpalar and Kiehn, 2010) and is therefore in an advantageous position to mirror the intensity of the effort and mediate respiratory adjustments according to the engaged locomotor program. Interestingly, a spinal ascending efference copy has been shown to upregulate respiration in *ex vivo* brainstem-spinal cord preparations of neonatal rodents (see Chapter 1.II.3.b., (Le Gal et al., 2014; Le Gal et al., 2020)). Importantly, the authors show that this effect does not require synaptic relays in the spinal cord and is rather direct to the brainstem (Le Gal et al., 2014). Also, glutamatergic ascending spinal neurons are thought to mediate this ascending drive (Le Gal et al., 2020). Interestingly, using a specific lesion, the authors show that lumbar-

induced upregulation of respiration seems to require the integrity of the parafacial respiratory region (pF, see Chapter 2.II.2.). We stated previously that a clear characterization of the pF based on genetics and common lineage is needed to avoid further confusion regarding the number of structures at play in the "parafacial region". Therefore, the exact implication and identity of the pF in integrating locomotor signals from the lumbar CPG needs to be more precisely defined, using the outstanding genetic tools available in mice.

5. The spinal peripheral feedback

a. Sensorimotor integration

Although spinal circuits can produce precise and well-organized movements without any sensory inputs, sensorimotor interactions are essential to create an adaptive locomotion to a real environment (Pearson, 2004; Rossignol et al., 2006; Akay et al., 2014). During movement, the locomotor CPG receives sensory information through proprioceptive afferences activated by muscle contractions. In *ex vivo* neonatal reduced brainstem-spinal cord preparations, low threshold stimulation of dorsal nerve roots, that convey proprioceptive signal to the CPG, can even induce episodes of locomotor-like activities (Whelan et al., 2000; Morin and Viala, 2002). Transition from stance (extension) to swing (flexion) is influenced by proprioceptive feedback. When animals increase their speed, the duration of the step cycle decreases due to a reduction of the stance phase duration, mainly mediated by the activity of extensor muscles (Roy et al., 1991). In walking mice, extensor muscles are recruited in a speed-dependent manner (see Chapter 3.I.1., (Mayer et al., 2018)). Acute removal of proprioceptive sensory feedback from the stretch-sensitive muscle spindles (type Ia/II) prevents mice from walking at higher speed. Activation of muscle spindles is thus essential to regulate the strength and amplitude of extensor muscles activity to transition to the swing phase (Mayer et al., 2018). In addition, force-sensitive Golgi tendons organs (type Ib) provide excitation to extensors during the stance phase to increase extension. Once the limb unloads, the excitation decreases and the limb transitions to the swing phase (Conway et al., 1987; Duysens et al., 2000). Peripheral feedback can therefore influence locomotor phase transition, reinforce ongoing activity, and correct the movement according to perturbations in the environment. In addition, interneurons in the dorsal horn also integrate sensory information about noxious, thermal, and mechanical external stimuli (Cordero-Erausquin et al., 2016; Koch et al., 2018). Proprioceptive feedbacks can reach supraspinal structures directly or indirectly through a spinal relay, including reticulospinal neurons, while cutaneous afferences reach the dorsal horn, including laminae I known to send direct afferences to brainstem regions (Rossignol et al., 2006; Koch et al., 2018).

b. Evidences for parallel mediation of respiration

Some evidence point to the implication of proprioceptive inputs in regulating respiratory rhythm. Indeed, electrical stimulation of proprioceptive afferences from the lumbar spinal cord, in *ex vivo* preparations of neonatal and juvenile rats, can reset the respiratory rhythm (see Chapter 1.II.2., (Morin and Viala, 2002; Potts et al., 2005; Giraudin et al., 2012)). The authors argue that this ascending pathway might help coordinating respiratory and locomotor rhythms in walking/running animals, although as discussed previously (see Chapter 1.I.5.), only few studies have actually studied the existence of a temporal synchronization (cycle-to-cycle analysis) of breaths to strides during actual running (Iscoe, 1981; Bramble and Carrier, 1983; Lafortuna et al., 1996). This was in fact never examined in rodents. In any case, this ascending sensory feedback-

driven respiratory resetting was shown to require at least two relays: one in the cervical spinal cord, and one in the pons, i.e., the lateral parabrachial/Kölliker-fuse nuclei (lPB/KF) (Potts et al., 2005; Giraudin et al., 2012). Interestingly, the lPB/KF is a direct target of cervical interneurons (Ruder et al., 2016) and is essential for the transition between inspiratory and expiratory phases, notably through direct projection to the preBötC that generates inspiration (Mörschel and Dutschmann, 2009; Palmiter, 2018; Yang et al., 2020a). While the exact functional significance of this pathway remains unclear, the sensory afferences are nonetheless candidates to send locomotor-related signals to respiratory centers.

RESULTS Chapter 1 – Paper 1

RESEARCH ARTICLE

Absent phasing of respiratory and locomotor rhythms in running mice

Coralie Hérent[1], Séverine Diem[1], Gilles Fortin[2], Julien Bouvier[1]*

[1]Université Paris-Saclay, CNRS, Institut des Neurosciences Paris-Saclay, Gif-sur-Yvette, France; [2]Institut de Biologie de l'École Normale Supérieure (IBENS), École Normale Supérieure, CNRS, INSERM, PSL Research University, Paris, France

Abstract Examining whether and how the rhythms of limb and breathing movements interact is highly informative about the mechanistic origin of hyperpnoea during running exercise. However, studies have failed to reveal regularities. In particular, whether breathing frequency is inherently proportional to limb velocity and imposed by a synchronization of breaths to strides is still unclear. Here, we examined respiratory changes during running in the resourceful mouse model. We show that, for a wide range of trotting speeds on a treadmill, respiratory rate increases to a fixed and stable value irrespective of trotting velocities. Respiratory rate was yet further increased during escape-like running and most particularly at gallop. However, we found no temporal coordination of breaths to strides at any speed, intensity, or gait. Our work thus highlights that exercise hyperpnoea can operate, at least in mice and in the presently examined running regimes, without phasic constraints from limb movements.

Introduction

The versatile adaptability of breathing to changes in the environment or behavioral state is vital. Probably, the most striking example is the augmentation of ventilation at the transition from rest to running exercise to match the augmented energetic demand (***Bramble and Carrier, 1983***; ***Mateika and Duffin, 1995***; ***Gariépy et al., 2010***). The hyperpnoea during running is principally supported by an increased respiratory rate which underscores an upregulation of the respiratory rhythm generator in the brainstem (***Del Negro et al., 2018***). While examining the dynamic interactions between respiratory and locomotor movements should inform on the origin and nature of the activatory signal, studies have failed to reveal regularities. Despite this, a common postulate is that respiratory frequency is entrained by that of locomotor movements, through inertial oscillations of the viscera and/or by proprioceptive signals from the limbs impacting the respiratory generator (***Iscoe and Polosa, 1976***; ***Bramble and Carrier, 1983***; ***Baudinette et al., 1987***; ***Alexander, 1993***; ***Morin and Viala, 2002***; ***Potts et al., 2005***; ***Giraudin et al., 2012***).

Two alleged signatures of hyperpnoea to running exercise have in particular fueled this model. Firstly, breathing augmentation during running is often considered to be inherently proportional to the velocity of repetitive limb movements (***Bechbache and Duffin, 1977***; ***Eldridge et al., 1981***; ***DiMarco et al., 1983***; ***Casey et al., 1987***). Yet, opposite findings have also been reported (***Kay et al., 1975***), as well as increased respiratory rates during mental imagery of exercise, that is without actual movements (***Thornton et al., 2001***). Secondly, and this is probably the most controversial aspect, the temporal coordination of breaths to strides (often referred to as the 'locomotor-respiratory coupling' or LRC), is commonly highlighted as a conserved feature of hyperpnoea to exercise (***Bechbache and Duffin, 1977***; ***Bramble and Carrier, 1983***; ***Alexander, 1993***; ***Corio et al., 1993***; ***Mateika and Duffin, 1995***; ***Lafortuna et al., 1996***; ***Boggs, 2002***). However, studies in human participants reported a strong heterogeneity in LRC between individuals, from a constant degree of coupling to no coupling at all (***Kay et al., 1975***; ***Bernasconi and Kohl, 1993***; ***Daley et al., 2013***;

***For correspondence:** julien.bouvier@cnrs.fr

Competing interests: The authors declare that no competing interests exist.

Funding: See page 17

Received: 08 August 2020
Accepted: 20 November 2020
Published: 01 December 2020

Reviewing editor: Jeffrey C Smith, National Institute of Neurological Disorders and Stroke, United States

Stickford et al., 2015). The LRC may also be favored by auditory cues (*Bernasconi and Kohl, 1993*) or by experience (*Bramble and Carrier, 1983*), arguing for the contribution of multiple factors including external stimuli and training. In quadrupeds, the fewer studies available, essentially on running performant species including rabbits, dogs, cats, and horses (*Bramble and Carrier, 1983*; *DiMarco et al., 1983*; *Corio et al., 1993*; *Lafortuna et al., 1996*), again revealed various degrees and ratios of locomotor-respiratory coordination, and raised the possibility that faster running gaits (i.e. gallop) may impose a stronger coupling. Therefore, a major source of confound about the coordination of locomotor and respiratory rhythms may owe to the variety of species examined thus far, and to the attendant variability in ambulatory modes and in the contributions of pre-determined (i.e. hardwired) versus secondary (i.e. sensory, volitional, acquired through experience) factors. Another source of confound probably lies in the distinct indicators used across studies to report the coordination between respiratory and locomotor rhythms (see Discussion). Therefore, while the above respiratory-locomotor interactions *can* occur, it is thus far from clear that they are an obligatory feature of hyperpnoea to exercise and are the manifestation of pre-determined circuits that impose on respiratory frequency that of the locomotor movements.

Laboratory mice have become the premier model for investigating complex integrated tasks including adaptive locomotor and respiratory control (*Benarroch, 2007*; *Bouvier et al., 2010*; *Ramanantsoa et al., 2011*; *Talpalar et al., 2013*; *Bouvier et al., 2015*; *Ruffault et al., 2015*; *Kiehn, 2016*; *Del Negro et al., 2018*; *Usseglio et al., 2020*) with promising benefits for human health (*Amiel et al., 2003*; *Benarroch et al., 2003*; *Lavezzi and Matturri, 2008*). Mice also stand as a good model for investigating the physiological basis and benefits of running exercise (*Lerman et al., 2002*; *Lancel et al., 2003*; *Sartori et al., 2020*). Furthermore, by being housed and raised in a standardized manner across laboratories, mice should give access to the hardwired manifestation of hyperpnoea to exercise, that is with minimal influence of volitional control, variations in external stimuli, or prior experience. Finally, mice benefit from a large array of 'Omics' toolboxes that allow the manipulation of signals, cell types and neural circuit activity combined to quantitative measurements of behaviors. However, the dynamics of hyperpnoea to exercise had yet to be characterized in this resourceful species, to pave the way for hypothesis-driven investigations of its cellular and circuit underpinnings. To this aim, we developed a novel method for monitoring inspiratory activity chronically, which we combined with video-tracking of the four limbs during unrestrained running on a motorized treadmill operating at different speeds. We reveal that inspiratory frequency augments during trotting by about twofolds to a fixed and stable set point value, irrespective of trotting velocities and of inclination. Yet, respiratory rate was further enhanced during escape running, and most significantly at gallop. We also demonstrate the absence at all of temporal coordination of breaths to strides at any speed, intensity, or gait. Our work therefore highlights a hardwired mechanism that discretely sets respiratory frequency independently of limb movements but in line with the engaged locomotor program.

Results

Chronic electromyographic recordings of diaphragmatic activity in running mice

Examining whether and how the rhythms of limb and breathing movements interact in mice requires to access breathing parameters in freely moving conditions. As an alternative to measuring ventilation by whole body plethysmography (WBP [*DeLorme and Moss, 2002*]) which is hardly compatible with displacement movements, or to the constraining use of air-tight chambers (*Tsuchiya et al., 2012*), we extended to mice the use of electromyography (EMG) recordings of the diaphragm (*Fat-Chun Tony Chang and Harper, 1989*; *Shafford et al., 2006*), the main inspiratory muscle. For this, we placed two steel wires within the peritoneum to superficially contact the diaphragm, that is without passing through the muscle itself (*Figure 1A,B*; see Materials and methods for details). Upon full recovery, we first placed EMG-implanted animals in a customized WBP chamber and confirmed that diaphragmatic neurograms correlate with the rising phase (i.e. inspiration) of the plethysmography signal, an estimate of the respiratory volume (*Figure 1C*). We used the alternating phases of activity and inactivity of diaphragmatic EMG to define respectively inspiration and expiration and to measure their durations (inspiratory time Ti; expiratory time Te; *Figure 1D*). The cycle-to-cycle interval

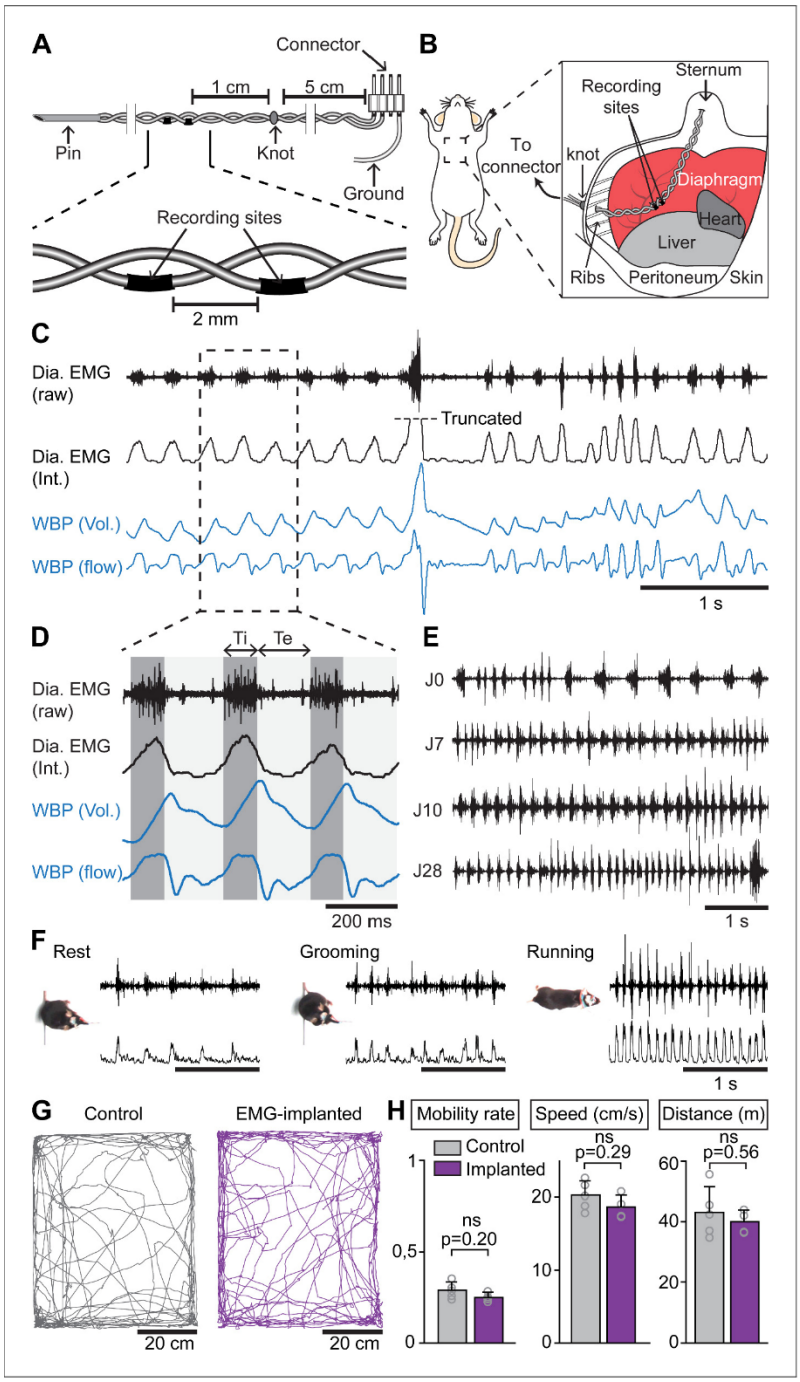

Figure 1. Chronic electromyographic recordings of the diaphragm to monitor inspiration in freely moving mice. (**A, B**) Schematics of the EMG recording electrodes and of the diaphragm implantation. (**C**) Simultaneous diaphragm EMG recordings (raw and integrated traces in black) and whole-body plethysmography (WBP, volume and flow, in blue) showing that the diaphragm neurogram estimates inspiratory flow. (**D**) Enlarged view of three

Figure 1 continued on next page

Figure 1 continued

inspiratory bursts highlighting the following respiratory parameters: inspiratory time (Ti) defined as a bout of diaphragm activity, and expiratory time (Te) as the silent period between bouts. (**E**) Diaphragm activity recorded on the day of the surgery (J0) and at 7, 10, and 28 days post-surgery (representative of four mice). (**F**) Raw and integrated diaphragm neurograms in an open field test during rest, grooming and spontaneous running showing preserved recording quality in spite of movements. (**G**) Locomotor trajectories of one representative non-implanted mouse (gray) and one representative EMG-implanted mouse (purple) for 10 min in the open field. (**H**) Bar-graphs showing the mean ± SD mobility rate, locomotor speed during mobility and total distance traveled in control (n = 5) and EMG-implanted mice (n = 4). p values in (**H**) are obtained from Mann-Whitney *U* tests and considered not significant when p>0.05.

The online version of this article includes the following source data for figure 1:

Source data 1. Locomotor parameters in the open field.

(Ti+Te) was used to obtain the instantaneous frequency of each inspiratory burst, leading to respiratory rate. The peak amplitude of integrated EMG signals appeared as an estimate of inspiratory flow obtained as the first derivative of plethysmographic signal (***Figure 1C,D***). Additionally, these measurements could be repeated over up to 28 days post-surgery without signal degradation (***Figure 1E***). Importantly, and in contrast to WBP, our EMG recordings provide stable inspiratory activity independently of the animal's displacement movements and can therefore be performed in freely behaving mice (***Figure 1F***). Finally, implanted and connected animals behaved similarly as non-operated mice in an open field arena (***Figure 1G,H***) indicating that the implantation did not alter the animal's ability to move spontaneously nor induced pain.

Breathing frequency augments independently of displacement speed during treadmill trotting

The most-common gait used by mice for running is the trot, characterized by simultaneous forward movements of the diagonal limb pairs and alternation of homologous limb pairs (***Bellardita and Kiehn, 2015***; ***Lemieux et al., 2016***). At trot, variations in step frequency allow to cover a wide range of displacement speeds (***Bellardita and Kiehn, 2015***; ***Mayer et al., 2018***). To examine how breathing frequency changes at different regimes of trot, we placed EMG-implanted animals on the belt of a motorized treadmill. We selected four representative speeds (15, 25, 40, and 50 cm/s) that cover most of the range achieved at trot (***Bellardita and Kiehn, 2015***; ***Lemieux et al., 2016***) and are accessible without prior training or aversive motivation (***Fernando et al., 1993***). Displacement speeds below 15 cm/s were not analyzed since they are typically manifested by intermittent bouts of walking interleaved with non-exercise behaviors, notably whisking and sniffing that also mobilize the respiratory apparatus and would be a source of confound.

When the animals engaged in stable running, that is their displacement speed was in phase with that of the treadmill, their respiratory rate (collected during the first 1.5 min) was increased but, surprisingly, independently of the running speed. Indeed, respiratory frequency increased by 245% at 15 cm/s, *225*% at 25 cm/s, *233*% at 40 cm/s, and by *226*% at 50 cm/s, without significant difference between the four speeds (***Figure 2A–B***). The increase in respiratory frequency from baseline was associated with a decrease of both Ti and Te (***Figure 2C,D***). Additionally, the amplitude of integrated EMG bursts was significantly higher during running than rest, but still without clear relation with speed (***Figure 2E***). *To examine the impact of a longer run*, and exclude an effect of acute stress during the first minutes after starting the treadmill, *animals were challenged* to a continuous 10-min run at 40 cm/s, the highest speed maintainable without prior training. We found the respiratory frequency to be stable throughout the period (***Figure 2—figure supplement 1***). *Next*, to examine the impact of workload onto breathing changes, mice were submitted to the same running speeds on a treadmill with a 10% incline (***Gardiner et al., 1982***; ***Gillis and Biewener, 2002***, ***Figure 2F–J***). We found that changes in respiratory parameters were overall similar to the values obtained on the level treadmill and were still independent of running speed (***Figure 2G–J***). These experiments altogether show that, during trotting on a treadmill in mice, respiratory rate increases to a fixed set point value that is independent of the animal's displacement speed. Furthermore, running on a 10% inclined treadmill did not further enhance breathing rate, suggesting little influence of the exercise grade.

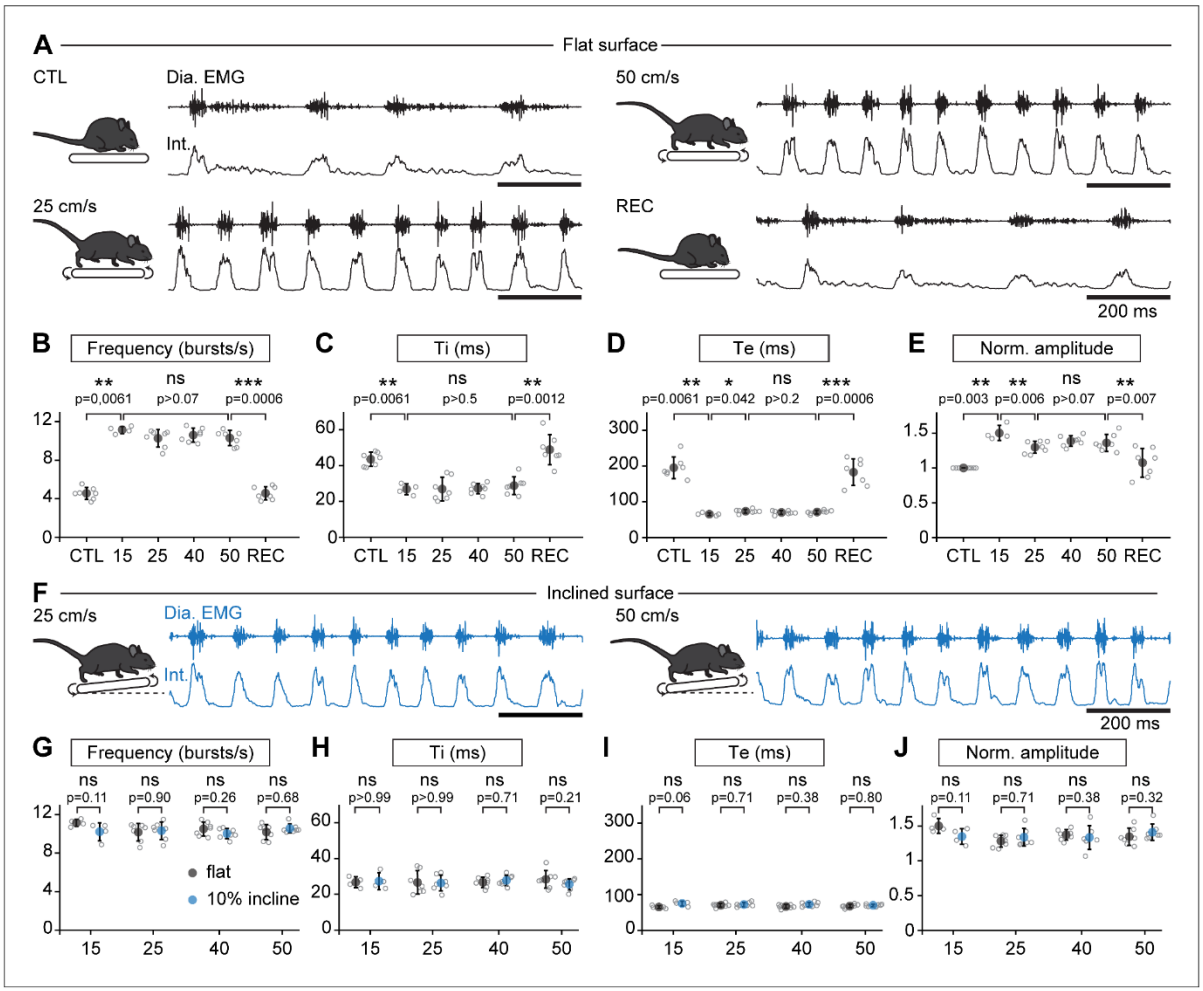

Figure 2. Breathing rate augments during trotting independently of limb velocity or surface inclination. (**A**) Diaphragm activity recordings in control condition (CTL), trotting at 25 and 50 cm/s and during recovery after the run (REC). Raw (Dia. EMG) and integrated (Int.) signals are illustrated in each condition. (**B–E**) Analysis of respiratory parameters in control condition, and during trot at 15, 25, 40, and 50 cm/s, and during recovery: frequency (**B**), inspiratory (Ti, **C**) and expiratory (Te, **D**) times and normalized amplitude (**E**). Data are mean ± SD from n = 7 mice per condition for all speeds except at 15 cm/s (n = 4) where three animals had unstable running and were discarded. p values indicated are obtained from Mann-Whitney *U* tests and considered not significant (ns) when p>0.05. (**F**) Raw (Dia. EMG) and integrated (Int.) diaphragmatic activity recordings during trot at 25 and 50 cm/s on a treadmill with 10% incline. (**G–J**) Similar analyses as in (**B–E**) during running on the inclined treadmill (blue) compared to the values on the flat treadmill (black). p values indicated are obtained from Mann-Whitney *U* tests and considered not significant when p>0.05. See ***Figure 2—figure supplement 1*** for a similar analysis during a 10-min run.

The online version of this article includes the following source data and figure supplement(s) for figure 2:

Source data 1. Respiratory parameters on the flat (B–E) and inclined (G–J) treadmill.

Figure supplement 1. Respiratory changes during a prolonged treadmill running.

Figure supplement 1—source data 1. Respiratory parameters (panels B, C).

Breaths are not temporally synchronized to strides during treadmill trotting

While our observations above suggest that the respiratory rhythm can operate without constraints from locomotor movements, a temporal coordination between breaths and strides could occur at

specific regimes (*Lafortuna et al., 1996*). To examine this, each limb was tracked using DeepLabCut (*Mathis et al., 2018*; *Mathis and Mathis, 2020*, *Figure 3A–B*, see Materials and methods) and their coordinates were used to register the time of footfall as well as the stance and the swing phases that define the locomotor cycle (*Bellardita and Kiehn, 2015*, *Figure 3C*). We then expressed the onset of individual inspiratory bursts within the locomotor cycle as a phase value (ΦInsp) from 0 (preceding footfall, FF_{n-1}) to 1 (footfall, $FF_{n,}$ *Figure 3C*). We then reported ΦInsp values of at least 35 consecutive breaths for one representative animal, as well as the mean concentration of phases for each animal, on a circular diagram (*Kjaerulff and Kiehn, 1996*, see Materials and methods). During trotting on the level treadmill, we found that inspiratory bursts could occur at any moment of the locomotor cycle, regardless of the limb considered as a reference. Indeed, ΦInsp values were evenly distributed across a circular plot diagram (*Figure 3D*, black marks on the outer circle are for one representative animal) resulting in non-oriented mean phase values (colored dots within the inner circle, one color dot per animal). Consequently, ΦInsp values collected from all animals were evenly distributed across the entire locomotor cycle (*Figure 3D*, bar-graphs). These observations were consistent at both the lowest (15 cm/s), intermediate (25 cm/s) and fastest (50 cm/s) trotting speeds accessible on the treadmill (*Figure 3D*), as well as with a 10% incline (*Figure 3E*). We found similar results when mice were challenged to a 10-min run (*Figure 3—figure supplement 1*). Furthermore, correlating diaphragmatic activity with either the forelimb or hindlimb resulted in a flat cross-correlogram (*Figure 3—figure supplement 2*), confirming the absence of common modulation between breaths and strides, even at a higher ratio. Altogether, these data demonstrate that respiratory rate increases without any phasing of breaths to locomotor movements, at least at the most common regimes of trot accessible without training and aversive conditioning on treadmill.

Breathes are not temporally correlated to strides at higher displacement speeds, including at gallop, in a linear corridor

While the conditions examined above on the treadmill cover a large range of the displacement speeds in mice, these animals can engage into even faster regimes (*Bellardita and Kiehn, 2015*; *Lemieux et al., 2016*). Furthermore, at these most demanding displacement speeds, mice can, like other quadrupeds, increase step frequency further using a galloping gait defined by synchronized movements of the left and right hindlimbs and alternating movements of the left and right forelimbs (*Heglund and Taylor, 1988*; *Bellardita and Kiehn, 2015*; *Caggiano et al., 2018*; *Josset et al., 2018*). We hence investigated how breathing rate adjusts at these faster running regimes, including gallop, in mice. To be engaged in these regimes without resorting to aversive to conditioning on a treadmill, EMG-implanted animals were placed in a linear corridor and a brief air puff was applied to the back of the animal (*Caggiano et al., 2018*). This could engage the animals in either of few bouts of trot, at an average displacement speed of 72 ± 9 cm/s (*Figure 4A,B*), or in a few bouts of gallop at 98 ± 11 cm/s (*Figure 4D,E*). When trot was evoked, respiratory frequency increased by 247% from baseline, to a value slightly higher than at 50 cm/s on the treadmill (*Figure 4G*). However, analyzing the temporal coupling of breathes to strides using the same methods as above revealed that breath onsets were again evenly distributed across the locomotor cycle regardless of the limb considered (*Figure 4C*). When the air puff instead evoked a few bouts of gallop (*Figure 4D,E*), we found that the respiratory frequency was increased by 314% from baseline to a value significantly higher than that measured during trot in both the treadmill and the corridor (*Figure 4G*). This respiratory frequency increase owed to a further decrease in Ti and Te (*Figure 4H,I*), and the amplitude of inspiratory bursts was also increased compared to trotting values on the treadmill (*Figure 4J*).

During gallop, the 'hopping-like' movements of the hindlimbs impose a stronger constraint on the visceral mass that may act as a piston mechanism (*Baudinette et al., 1987*; *Alexander, 1993*; *Bramble and Jenkins, 1993*) assisting in producing respiratory airflow. Therefore a constrained occurrence of diaphragmatic movements to a specific phase of the locomotor cycle may be preferred, since possibly most advantageous, at this gait (*Baudinette et al., 1987*; *Lafortuna et al., 1996*; *Boggs, 2002*). We thus examined whether gallop favored a temporal coupling of breaths to strides in mice using the same analytic methods as for trot. Our data however show that, similar to the trot conditions, breath onsets during gallop were evenly distributed across the locomotor cycle, whether defined using the alternating forelimbs or the left-right synchronized hindlimbs (*Figure 4E, F*).

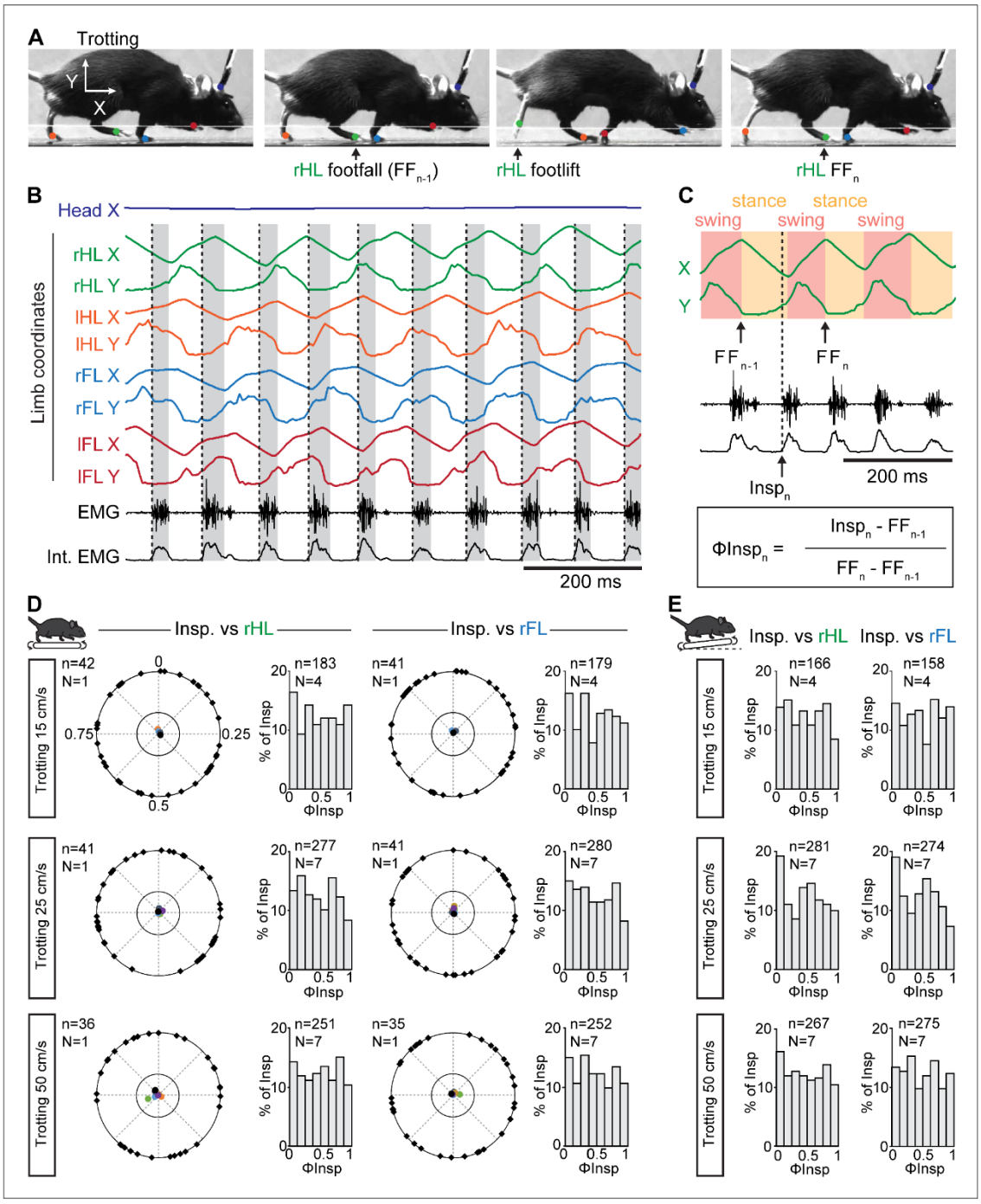

Figure 3. Breaths are not temporally-synchronized to strides during trotting on a treadmill. (**A**) Side views of one representative trotting mouse on a flat treadmill. The four limbs and the head were tracked and color-labeled: right hindlimb (rHL, green), left hindlimb (lHL, orange), right forelimb (rFL, blue), left forelimb (lFL, red) and head (dark blue). One complete rHL locomotor cycle is shown, between two consecutive footfalls (FF$_{n-1}$ and FF$_n$). (**B**) Horizontal (X) and vertical (Y) coordinates of the tracked limbs as well as raw (EMG) and integrated (Int. EMG) diaphragmatic neurograms, during stable

Figure 3 continued on next page

Figure 3 continued

trot. Dotted black lines indicate the onsets of inspiratory bursts and shaded rectangles highlight inspiratory times. (**C**) Enlarged view of locomotor cycles of the rHL showing the swing and stance phases. The occurrences of inspiratory bursts ($Insp_n$) within the locomotor cycle are expressed as a phase value ($\Phi Insp_n$) from 0 (FF_{n-1}) to 1 (FF_n). (**D**) Circular plots diagrams showing the phase-relationship between individual inspiratory bursts and the indicated reference limb for one representative animal trotting at 15, 25, and 50 cm/s on a flat treadmill. Black diamonds on the outer circle indicate the phase of n individual inspirations. The black dot indicates the mean orientation vector for that animal and the colored dots indicate the mean orientation vector of 3 (at 15 cm/s) or 6 (at 25 and 50 cm/s) other animals. The positioning of these mean values within the inner circle illustrates the absence of a significantly oriented phase preference ($R < 0.3$, with R being the concentration of phase values around the mean as defined in ***Kjaerulff and Kiehn, 1996***). Bar-graphs to the right are distribution histograms of the phases of inspiratory bursts and the same reference limb for all n events from N animals. (**E**) Phase distribution histograms between inspiratory bursts and the indicated reference limb for all n events from N animals running at 15, 25, or 50 cm/s on the inclined treadmill. Note that inspiratory bursts in (**D**) and (**E**) are evenly distributed across the entire locomotor cycle in each condition and that distribution histograms do not show a phase-preference. See also ***Figure 3—figure supplement 1*** for a similar analysis during a 10-min run, and ***Figure 3—figure supplement 2*** for cross-correlograms between inspiratory and limb activity.
The online version of this article includes the following source data and figure supplement(s) for figure 3:

Source data 1. Circular plots for the flat treadmill conditions (panel D).
Source data 2. Distribution histograms for both the flat and inclined treadmill (panels D and E).
Figure supplement 1. Correlation of breaths to strides during prolonged treadmill running.
Figure supplement 1—source data 1. Circular plots.
Figure supplement 1—source data 2. Distribution histograms.
Figure supplement 2. Example cross-correlations of breathing and locomotor rhythms showing no common modulation.

Altogether, these results indicate that the respiratory frequency increase is more pronounced when mice engage in faster running regimes associated with escape, and particularly at gallop. However, even at these regimes, breaths are not temporally coordinated to strides.

Prior training does not favor a temporal synchronization of breaths to strides

Since the coordination between breathing and stride rhythms may increase as a function of experience level (***Bramble and Carrier, 1983***), we next reasoned that some degree of locomotor respiratory synchronization may be acquired through training. Therefore, three animals underwent a 8 week training consisting in (1) free access to a running wheel in the cage, a paradigm that suffices to have multiple benefits typically associated with exercise, including enhanced locomotor learning and skills, changes in synaptic and axonal function and anti-inflammatory actions (***Lancel et al., 2003***; ***Parachikova et al., 2008***; ***Li and Spitzer, 2020***) and (2) daily training on the treadmill, also shown to improve motor skill learning through enhanced synaptic and axonal function (***Chen et al., 2019***, ***Figure 5***). Animals were then implanted with EMG electrodes and challenged to treadmill running on a level or inclined treadmill as well as to the air puff driven gallop as performed above. We observed similar changes in breathing frequency and burst amplitude as in untrained mice (data not shown), and importantly, we found that the onsets of inspiratory bursts were still evenly distributed across the locomotor cycle with no phase preference for any animal and in any condition (***Figure 5B–D***). Altogether, these experiments and cycle-to-cycle correlation analyses demonstrate that respiratory frequency in mice increases without breaths being temporally synchronized to locomotor movements, regardless of locomotor speed, grade, gait, or prior training.

Discussion

We provide here the first examination of breathing changes and of the coordination of breaths with strides during running in the resourceful mouse model. This was made possible by a unique method for implanting EMG electrodes on the diaphragm combined with limb video tracking. Contrary to WBP, this allows repetitive, long duration and artifact-free recordings of inspiratory activity during locomotor displacements. Furthermore, our method eliminates the need to use an air-tight chamber for measuring breathing during exercise (***Tsuchiya et al., 2012***), and is thus compatible with a variety of laboratory environments including large open fields (***Figure 1***), standard treadmills (***Figures 2*** and ***3***), and corridors (***Figure 4***). Our method was designed to specifically monitor inspiratory activity, the only breathing phase (i) maintained throughout the rest/activity cycle (expiration is passive at

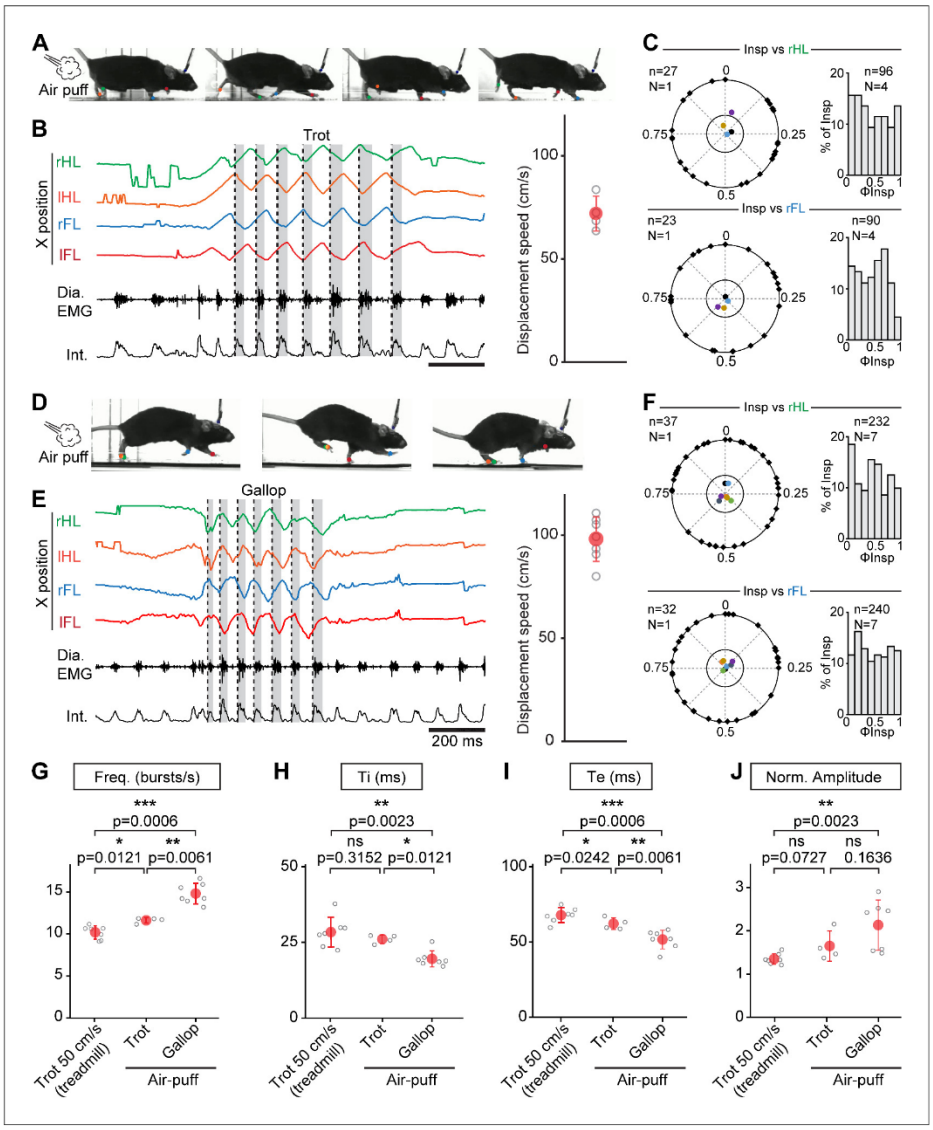

Figure 4. Further augmentation of breathing rate yet without temporal correlation of breaths to strides during escape running, including at gallop. (**A**) Side views of one representative mouse during air puff induced trot where right and left hindlimbs (rHL, green; lHL, orange) and forelimbs (rFL, blue; lFL, red) are alternating. (**B**) Changes in the horizontal (X) axis of the limbs over time as well as raw (Dia. EMG) and integrated (Int.) diaphragmatic neurograms are shown before and during four cycles of trot induced by air puff. Dotted black lines indicate the onsets of inspiratory bursts and shaded areas highlight inspiratory times. On the limb coordinates, rapid deflections before the onset of movement are occasional failures in detecting the paws at rest. The graph to the right shows the average running speed of each animal (gray open circles) and the mean ± SD across animals (in red) during air puff induced trot. (**C**) Circular plots showing the phase-relationship between n inspiratory bursts and the indicated reference limb for one representative animal (black diamonds on the outer circle). The black dot indicates the mean orientation vector for that animal and the colored dots indicate the mean orientation vector for three other animals. The positioning of these mean values within or close to the inner circle illustrates the absence of a significantly oriented phase preference (R < 0.3, with R being the concentration of phase values around the mean as defined in ***Kjaerulff and Kiehn, 1996***). Bar-graphs to the right are distribution histograms of the phases of inspiratory bursts and the same reference limb for all n events from N = 4 animals. (**D–F**) Same representation as (**A–C**) during air puff induced gallop where right and left hindlimbs are now synchronized and right and left forelimbs are alternating. The average displacement speed of the animals at gallop (98 ± 11 cm/s) is significantly higher than at trot (72 ± 8 cm/s, p=0.0121, Mann-Whitney *U* test). Circular plots and distribution histograms are obtained from N = 7 animals. (**G–J**) Changes in respiratory frequency

Figure 4 continued on next page

Figure 4 continued

(G), inspiratory (Ti, H) and expiratory (Te, I) times and normalized amplitude (J) between trot at 50 cm/s on the treadmill, and air puff induced trot and gallop. Note that breathing rate is most significantly increased at gallop. Data are presented as mean ± SD (trot treadmill: N = 7 mice; trot air puff: N = 4 mice; gallop air puff N = 7 mice) and p values indicated are obtained from Mann-Whitney *U* tests.
The online version of this article includes the following source data for figure 4:

Source data 1. Circular plots (panels C and F).
Source data 2. Distribution histograms (panels C and F).
Source data 3. Respiratory parameters (panels G–J).

rest) and (ii) with a known pacing origin - the preBötzinger complex, the main respiratory rhythm generator (***Ausborn et al., 2018***; ***Del Negro et al., 2018***). Therefore, diaphragm EMGs constitute an accurate readout of the temporal organization of sequences of neuronal activity in executive inspiratory circuits. Compared to implanted nasal probes (***Kurnikova et al., 2017***) our EMG approach allows a sampling of respiratory activity with much higher temporal resolution. It thus constitutes a timely addition to the toolbox for studying the adaptive control of breathing.

The dynamics of respiratory changes observed during acute running exercise in laboratory mice, housed and raised in a standardized manner across laboratories, make it possible to draw up an outline of the hardwired interactions between respiration and locomotion, that is with minimal contribution of conditioning or prior experience. Through that, it will help future hypothesis-driven attempts to identify the long-sought physiological, likely neuronal, substrate for hyperpnoea to exercise (***Mateika and Duffin, 1995***; ***Gariépy et al., 2010***; ***Paterson, 2014***). On that matter, one major finding of our work is the absence at all of a temporal locking of breaths to strides in both naive and trained mice. These findings were first observed during treadmill running up to 50 cm/s, which represent the comfortable speed of volitional running in this species. As previously reported (***Fernando et al., 1993***), we could not engage animals at higher running speeds on the treadmill without prior training with electric shocks, but we also investigated the coordination of breaths to strides during over-ground running in a linear corridor. There, animals engage to higher displacement speeds at trot (72 cm/s on average) and utilize gallop for the fastest displacements (98 cm/s), as previously reported (***Bellardita and Kiehn, 2015***; ***Lemieux et al., 2016***). Yet, no breath-to-stride temporal locking was seen at these regimes either. Although we may not have covered the most extreme speeds in this species (***Lemieux et al., 2016***), our work argues that a synchronization of breaths to strides is not a typical feature of respiratory hyperpnoea during running in mice. This lack of coordination should be discussed thoroughly since its existence has been alleged in all species. It must be stressed, however, that the indicator that is most typically used, the 'locomotor respiratory coupling' (or LRC), has a very ambiguous interpretation. In many instances, it only reports the frequency ratio between the two movements, that is locomotor events per respiratory events (***Bechbache and Duffin, 1977***; ***Bramble and Carrier, 1983***; ***Paterson et al., 1986***; ***Corio et al., 1993***). There, the terms 1:1 'coupling' or 'entrainment' therefore refer to the locomotor frequency being, on average, not statistically different to that of breathing. It however says nothing about the phasing of both movements on a cycle-to-cycle basis as performed here. Closest studies are those measuring the 'LRC ratio', the 'degree of LRC', or the 'LRC %', that is the percentage of inspirations starting in the same phase of the step cycle. The distinction between the two measurements is clearly illustrated in the investigation of ***Lafortuna et al., 1996***. This study reported that at all running speeds, horses adopt a breathing frequency that is systematically equal to that of the limbs. Yet, the temporal locking of breathes to strides is only intermittent at trot and becomes more frequent at gallop. Similarly in running cats, respiratory frequency is half that of locomotion but with only little common modulation between diaphragmatic and quadriceps activities (***Iscoe, 1981***). Pertinent breaths-to-strides analyses are more common in humans but reveal a strong heterogeneity between individuals, from a constant degree of cycle-to-cycle coupling to no coupling at all (***Kay et al., 1975***; ***Bernasconi and Kohl, 1993***; ***Daley et al., 2013***; ***Stickford et al., 2015***). Therefore, it is often far from clear, especially in animal studies, to which of the above parameters (ratio of frequencies or actual synchronous events) the typical 1:1, or 2:1 'coupling' or 'entrainment' refers to. Making the distinction is yet important when thinking on the neuronal substrates of exercise hyperpnoea. For a temporal locking of breaths and strides, a synchronizing neural command needs to be

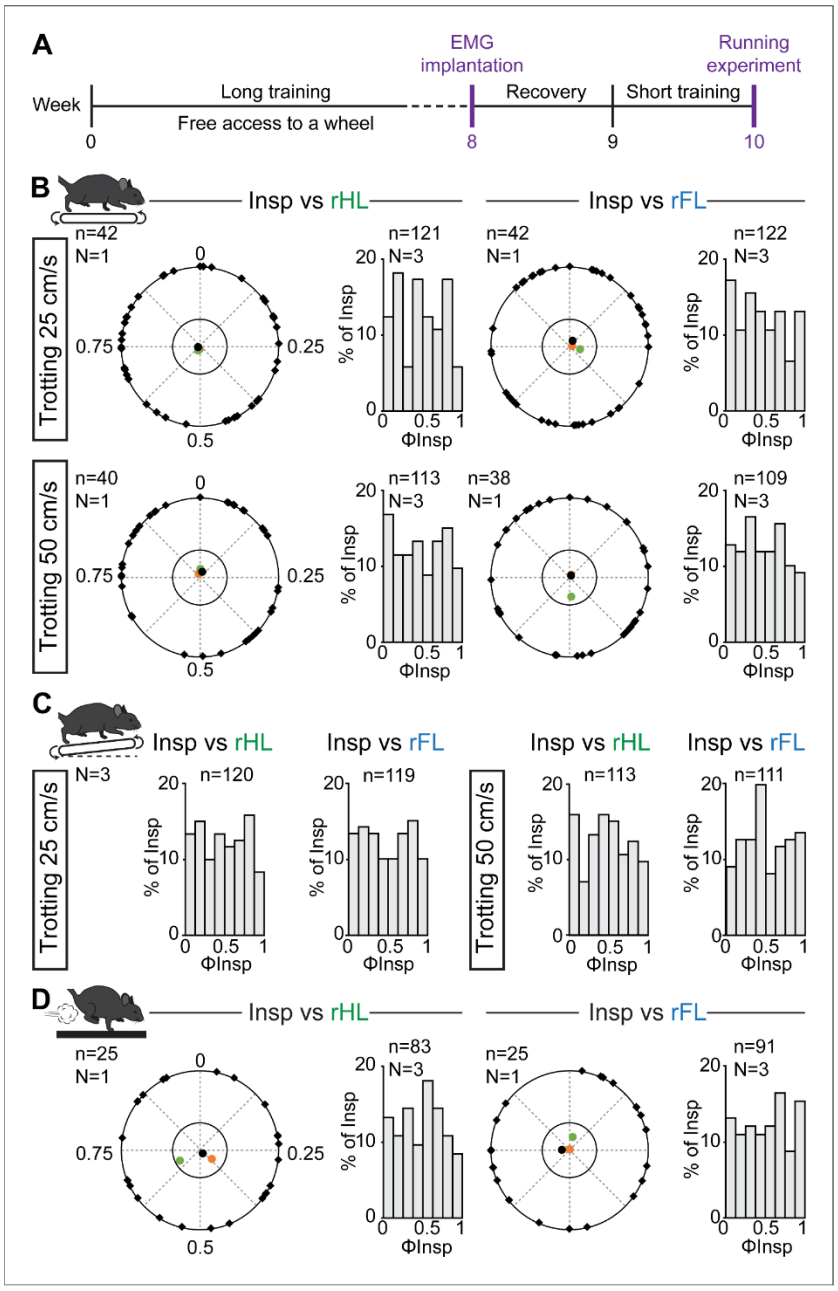

Figure 5. Respiratory changes during running in trained mice and phase-relationship analysis between breaths and strides. (**A**) Experimental timeline. Mice were trained for 8 weeks before being implanted for EMG recordings of the diaphragm. (**B**) Circular plots showing the phase-relationship between inspiratory bursts and the indicated reference limb for one representative animal trotting at 25 (top) and 50 cm/s (bottom). Black diamonds on the outer circle indicate the phase of n individual inspirations. The black dot indicates the mean orientation vector for that animal and the colored dots the mean orientation vector of two other animals. The positioning of these mean values within the inner circle illustrates the absence of a significantly-oriented phase preference ($R < 0.3$, with R being the concentration of phase values around the mean as defined in ***Kjaerulff and Kiehn, 1996***). Bar-graphs to

Figure 5 continued on next page

Figure 5 continued

the right are distribution histograms of the phases of inspiratory bursts and the same reference limb for all n events from three animals. (**C**) Phase distribution histograms between inspiratory bursts and the indicated reference limb for all n events from three animals running at 25 (left) or 50 cm/s (right) on the inclined treadmill. (**D**) Circular plot showing the phase-relationship between inspiratory bursts and the indicated limb for one representative trained animal during gallop. Black diamonds on the outer circle indicate the phase of n individual inspirations. The black circle indicates the mean orientation vector for that animal and the colored circles the mean orientation vector of two other animals. To the right are phase distribution histograms between inspiratory bursts and the same reference limb for all n events from three animals. Note that all inspiratory bursts are evenly distributed across the entire locomotor cycle in all conditions.
The online version of this article includes the following source data for figure 5:

Source data 1. Circular plots (panels B and D).
Source data 2. Distribution histograms (panels B–D).

produced from either active respiratory or the locomotor networks and be fed onto respectively the locomotor or respiratory networks. Admittedly, the complete absence of synchronization of breaths to strides we report here in selected contexts in the C57BL/6J mouse strain does not ascertain that synchronization *never* occurs in mice. One should notably acknowledge that exercise capacity varies among mouse strains, and in between individuals within a strain (***Lerman et al., 2002***; ***Meek et al., 2009***). The C57BL/6J line used here having relatively low endurance exercise capacity (***Avila et al., 2017***) it would be interesting to know if FVB/NJ and SWR/J mice with high endurance exercise capacity present comparable, or distinct, adaptive variations. It would also be very informative to examine the impact of longer running sessions, and/or more intense training, for instance until exhaustion (***Avila et al., 2017***) and during sustained gallop. That being said, our findings in multiple running contexts, and the ambiguities raised above from other species make it unlikely that breaths/strides synchronization constitutes a hardwired and obligatory component of respiratory adaptation to running exercise in quadrupeds. Therefore, the implication of phasic signals (i.e. from sensory feedbacks or visceral oscillations) may be a complementary, rather than obligatory, mechanism of exercise hyperpnoea. This possibility is also supported by the persistence of a normal ventilatory response to exercise following the removal of peripheral signals in animal models (***Eldridge et al., 1981***; ***Eldridge et al., 1985***) and human subjects (***Fernandes et al., 1990***).

Our data instead favors the quest, at least in mice and during slow-to-moderate trotting speeds on the treadmill, of a primary mechanism that sets respiratory frequency independently of the locomotor cycle and even independently of the velocity of limb movements. Indeed, at running speeds between 15 and 50 cm/s, respiratory rate increased in a step-like manner by about twofolds from rest, and was stably maintained thereafter throughout the running period, irrespective of trotting velocities and regardless of difference in height of the route. This is reminiscent of the respiratory changes previously documented during swimming in the lamprey (***Gravel et al., 2007***) but contrasts, at first glance, with the proportional increase of respiration to limb velocity observed in human participants (***Bechbache and Duffin, 1977***; ***DiMarco et al., 1983***; ***Casey et al., 1987***) (but see ***Kay et al., 1975*** for contradictory findings). It also raises the question of how mice cope with the increased metabolic demand associated with faster running and inclined route (***Heglund and Taylor, 1988***). In fact, it is likely that increased ventilation during running exercise may also operate through increased tidal volume (***Leith, 1976***). However, while our noticing of increased amplitude of diaphragm EMG signals during exercise denotes increased inspiratory muscular efforts and is compatible with increased tidal volume, our method cannot monitor further augmentations of respiratory airflows if supported by additional muscles. Accessory respiratory muscles in particular are active during high ventilatory demand such as exercise to expand and stabilize the chest wall (***Sieck and Gransee, 2012***). We therefore cannot exclude that, even at a stable respiratory frequency, additional muscles can be mobilized as displacement speed and effort intensity increase, to adjust ventilatory volumes on the fly and thereby help maintain respiratory homeostasis. Further experiments utilizing targeted recordings of accessory muscles (***Romer et al., 2017***) will be needed to evaluate this directly. Our data nonetheless demonstrate that any putative adjustments in volume not accessed here do not constrain the duration of the respiratory cycle, which remains constant over a

large range of displacement speeds. In the same line, the switch from passive to active expiration, a candidate signature of exercise hyperpnoea, mobilizes abdominal expiratory muscles (**Abdala et al., 2009**). This was only reflected in our data by manifest shortenings of expirations (Te), especially at gallop. Targeted recordings of expiratory abdominal muscles will be needed to ascertain it.

Interestingly, we found that respiratory rates increased further when animals engaged into the fastest, escape-like, running regimes in a linear corridor (**Figure 4**). Admittedly, our results cannot discriminate whether such higher respiratory rates compared to the treadmill situation reflect the higher displacement speeds or owe to the different protocol employed (air puff stimulus). This nevertheless indicates that the respiratory rhythm generator was not operating at maximal frequency regime during treadmill trotting but rather at a fixed frequency set point. Importantly, the strongest increase in respiratory frequency was seen when animals engaged into gallop, instead of trot, following the air puff. We therefore propose that efficient breathing adaptation to exercise may include, at least in mice, distinct dedicated behavior-dependent solutions. The transition from rest to moderate exercise could engage a default 'exercise' breathing at a fixed frequency set point compatible with a range of energetic demands corresponding to ritualistic territorial and explorative tasks and their share of uncertain evolutions (change of speed, of slope, etc...). There, the mobilization of other respiratory muscles may support on-the-fly adjustments of respiratory volumes. The engagement into faster displacement speeds, typically associated with escape behaviors, appears to operate through a further increase of respiratory frequency and, possibly, active expiration.

The mechanisms by which the breathing frequency is set, and those allowing transiting from it will need to be investigated. A bulk of evidence indicates that transitions from walk, to trot and gallop are controlled by specific circuits in the brainstem centers for locomotor initiation (**Bachmann et al., 2013**; **Caggiano et al., 2018**; **Josset et al., 2018**) and in the executive centers of the spinal cord (**Andersson et al., 2012**; **Talpalar et al., 2013**; **Bellardita and Kiehn, 2015**; **Skarlatou et al., 2020**). Therefore, it is likely that a direct modulation of the brainstem respiratory generator by a neuronal drive of central origin, that is from the brainstem and/or spinal locomotor centers, may trigger respiratory frequency increase during exercise (**Eldridge et al., 1981**; **Eldridge et al., 1985**; **Gariépy et al., 2012**; **Le Gal et al., 2014**; **Paterson, 2014**). Immediate concerns would be to identify candidate trigger neurons, as well as their partners in the respiratory centers. This should be achievable using selective interventional manipulations of locomotor and respiratory neuronal types, now both well-defined and accessible with molecular and genetic markers, viral tracers, and dedicated transgenic mice lines (**Bouvier et al., 2010**; **Talpalar et al., 2013**; **Ruffault et al., 2015**; **Kiehn, 2016**; **Del Negro et al., 2018**; **Skarlatou et al., 2020**).

Materials and methods

Key resources table

Reagent type (species) or resource	Designation	Source or reference	Identifiers	Additional information
Strain strain background *Mus musculus*	C57BL/6J	Janvier Labs	IMSR Cat# JAX:000664, RRID:IMSR_JAX:000664	https://www.janvier-labs.com/en/fiche_produit/c57bl-6jrj_mouse/
Software, algorithm	Labscribe NI	iWorxs		https://www.iworx.com/products/biomedical-engineering/labscribeni/
Software, algorithm	Clampfit (pCLAMP 11)	Molecular Devices	RRID:SCR_011323	https://www.moleculardevices.com/products/axon-patch-clamp-system/acquisition-and-analysis-software/pclamp-software-suite#Resources
Software, algorithm	Deeplabcut	Mathis Lab		http://www.mousemotorlab.org/deeplabcut
Software, algorithm	ToxTrac	**Rodriguez et al., 2017**		https://sourceforge.net/projects/toxtrac/
Software, algorithm	GraphPad Prism 7		RRID:SCR_002798	https://www.graphpad.com/
Software, algorithm	2nd Look	IO Industries		https://shop.ioindustries.com/products/2ndlook

Animals

All experiments were conducted in accordance with EU directive 2010/63/EU and approved by the local ethical committee (authorization 2020–022410231878). Experiments were performed on C57BL/6J mice of either sex, aged 3 months at the time of the EMG implantation and obtained from Janvier Labs (Le Genest-Saint-Isle, France). All animals were group-housed in plastic breeding cages with free access to food and water, in controlled temperature conditions and exposed to a conventional 12 hr light/dark cycle. Animals were managed by qualified personnel and efforts were made to avoid suffering and minimize the number of animals.

Housing and training protocol

Mice were divided in two groups: untrained mice housed in normal environments, and trained mice that had free access to a running-wheel in the cage. Furthermore, trained mice were exercised daily, from the age of 1 month, for 8 consecutive weeks (see ***Figure 5A***) on a custom-made motorized treadmill with adjustable speed range (Scop Pro, France, belt dimensions: 6 cm x 30 cm). Each training session consisted in placing the animals on the stationary treadmill with no incline for 5 min, before they were engaged for a total of 15 min of running at three distinct speeds (25, 40, and 50 cm/s, 5 min at each speed). Mice could rest for 5 min after running before being placed back in their cage. A week after the EMG implantation, both groups were exercised daily for a week using a similar paradigm but for 1 min at each speed. This step was crucial to obtain stable running animals during experimental sessions. Only animals determined to be good runners based on their ability to run without reluctance were included in this study.

Diaphragm EMG recordings

Fabrication of EMG electrodes

The protocol was inspired by previous work (***Pearson et al., 2005***). The electrodes were made of Teflon-coated insulated steel wires with an outside diameter of 0.14 mm (A-M systems, ref 793200). For each animal, a 12 cm pair of electrodes was prepared as follows (***Figure 1A***). Two wires were lightly twisted together, and a knot was placed 5 cm from one end. At 1 cm from the knot, the Teflon insulation was stripped over 1 mm from each wire so that the two bared regions were separated by about 2 mm. The ends of the two wires were soldered to a miniature dissecting pin. The free ends of the electrodes, as well as a 5 cm ground wire, were soldered to a micro connector (Antelec). Nail polish and an insulation sleeve were used to insulate the wires at the connector.

Surgical implantation of EMG electrodes in the diaphragm

To implant the diaphragm, 3-month-old animals were anaesthetized using isoflurane (4% at 1 L/min for induction and 2% at 0.2 L/min for maintenance), placed in a stereotaxic frame (Kopf) and hydrated by a subcutaneous injection of saline solution (0.9%). Their temperature was maintained at 36˚C with a feedback-controlled heating pad. This step was crucial to ensure post-surgery survival. The skull was exposed and processed to secure the micro connector using dental cement (Tetric Evofow). The ground wire was inserted under the neck's skin and the twisted electrodes were tunneled towards the right part of the animal guided by a 10-cm silicon tube of 2 mm inner diameter. The animal was then placed in supine position, the peritoneum was opened horizontally under the sternum, extending laterally to the ribs, and the silicon tube containing the electrodes was pulled through the opening. The sternum was clamped and lifted upwards to expose the diaphragm. A piece of stretched sterile parafilm was placed on the upper part of the liver to avoid friction during movement of the animal and to prevent conjunctive tissue formation at the recording sites. The miniature dissecting pin was pushed through the right floating ribs. The pin was then inserted through the sternum, leaving the bare part of the wires in superficial contact with the diaphragm (***Figure 1B***). The position of the electrodes was secured on both sides of the floating ribs and sternum using dental cement. The pin was removed by cutting above the secured wires. The peritoneum and abdominal openings were sutured and a head bar was placed on the cemented skull to facilitate animal's handling when connecting and disconnecting EMG cables during behavioral sessions. Buprenorphine (0.025 mg/kg) was administered subcutaneously for analgesia at the end of the surgery and animals were observed daily following the surgery.

Behavioral experiments

Upon a full week of recovery, implanted animals were connected with custom light-weight cables to an AC amplifier (BMA-400, CWE Inc) and neurograms were filtered (high-pass: 100 Hz, low-pass: 10 KHz), collected at 10 kHz using a National Instruments Acquisition card (USB-6211) and live-integrated using the LabScribe NI software (iWorxs).

Plethysmography recordings

Four unrestrained implanted animals were connected to the AC amplifier and placed inside a hermetic whole-body plethysmography chamber (***Ruffault et al., 2015***), customized to allow the passage of the EMG cable. Respiratory volume and diaphragm EMG activity were recorded simultaneously over a period of 10 min using the LabScribe NI software. Respiratory volume was derived to obtain the respiratory flow (***Figure 1C,D***).

Open field experiments

For analyzing changes in global locomotor activity, control or implanted and connected animals were placed, one at a time, in a custom open field arena (opaque PVC, 60 × 70 cm) without prior habituation and filmed from above during 10 min at 20 frames/s using a CMOS camera (Jai GO-5000-C-USB). The open-source software ToxTrac (***Rodriguez et al., 2017***) was used for automated tracking of the animal's position over time. Following geometric calibration, the following parameters were extracted for each mice (***Figure 1H***): the mobility rate defined as the percent of time that the animal spent moving above 7.5 cm/s, the average mobility speed defined as the average speed of the animal during mobility (i.e. above 7.5 cm/s) and the total distance travelled per 10 min recording. Within each category (i.e. control or EMG-implanted) a grand-mean ± SD across mice was then calculated to produce histograms.

Running experiments

We used a custom-built treadmill (Scop Pro, France) whose speed was remotely adjusted using a USB servo controller (Maestro Polulu). Implanted untrained (n = 7) and trained (n = 3) animals followed the same running experiments while recording breathing changes. First, we evaluated breathing changes during running at trot, without or with incline. For each speed, the protocol was as follows. Animals were first placed on the stationary treadmill to monitor basal respiration. Animals were then challenged to trot at the lowest speed (15 cm/s) for 1.5 min followed by a 5-min break. The treadmill was then inclined with a 10% slope and animals exercised at the same speed for 1.5 min. This sequence was repeated for the three other speeds (25, 40, and 50 cm/s) with 5 min of rest between trials. At the end of the running experiment, a breathing recovery period was recorded. We also recorded breathing changes throughout a continuous 10 min exercise at 40 cm/s on the motorized treadmill for n = 2 untrained and n = 2 trained animals. Since faster running speeds typically associated with escape cannot be achieved on the treadmill without aversive conditioning (***Fernando et al., 1993***), we resorted to air puff induced escape in a linear corridor (80 × 10 cm) as previously described (***Talpalar et al., 2013***; ***Caggiano et al., 2018***). Trials were classified as trot or gallop based on the alternation (trot) or synchronization (gallop) of the hindlimbs. The test was repeated, with several minutes of rest between trials, until enough bouts (around 20) were acquired.

During running sessions, animals were filmed from the side at 200 fps and 0.5 ms exposure time using a CMOS camera (Jai GO-2400-USB) and images were streamed to a hard disk using the 2nd LOOK software (IO Industries). The start of the EMG recordings was hardware-triggered by the start of the video-recordings using the frame exposure output of the video camera, so that the two recordings are synchronized.

Automated analysis of limb movements

To track limb movements during running, we used DeepLabCut (version 2.1.5.2, ***Mathis et al., 2018***, see ***Figures 3,4***). We manually labeled the positions of the head and the 4 paws from 50 frames of each video. We then used 95% of the labeled frames to train the network using a ResNet-50-based neural network with default parameters for three training iterations. We validated with two shuffles and found that the test error for trot experiments was: 3.33 pixels and the train error: 2.37 pixels (image size: 1344 × 301). Similarly, we trained the network for gallop condition using a

ResNet-50-based neural network with default parameters for one training iteration. We validated with two shuffles and found that the test error was: 3.43 pixels and the train error: 2.43 pixels (image size: 1936 × 230). These networks were then used to analyze videos from similar experimental settings. X and Y coordinates from the head and the four limbs were then extracted and interpolated to 10 kHz to match the EMG recordings. The latter were exported from LabScribe to Clampfit (Molecular Devices), and both sets of signals were merged in a single file, before being processed offline in Clampfit.

Quantifications and statistics

The instantaneous frequency and amplitude of respiratory bursts were detected using the threshold search in Clampfit from stable trotting moments, that is when the animal's speed was in phase with the treadmill, inferred by the absence of changes in head's horizontal coordinates. Instantaneous respiratory frequency was measured for a total duration of 6 s, thus encompassing around 60 cycles. These measurements were either done using two to three windows taken at any stable moment of the 1.5-min run (excluding the first 20 s to exclude possible stress-induced changes when the treadmill is just engaged), and averaged to give the value for each animal. For the analysis of longer runs (***Figure 2—figure supplement 1***), similar measurements were done at 5 and 10 min of continuous running. Inspiratory time (Ti) was defined as the duration of the diaphragmatic burst and the expiratory time (Te) as the silent period in between bursts as illustrated in ***Figure 1D***. Respiratory amplitude change was normalized and expressed as a percent of the control amplitude before running started. Values for respiratory bursts (frequency, Ti, Te and amplitude) were expressed as mean ± SD across n animals. Statistical differences between means were analyzed using Mann-Whitney *U* tests (GraphPad Prism 9) and changes were considered as not significant (ns) when $p>0.05$ and as significant when $p<0.05$. Significance was reported as * when $0.05 < p < 0.01$, ** when $0.01 < p < 0.001$ and as *** when $p<0.001$. All p values are declared in figures.

The temporal coordination of breaths to strides was represented with circular statistics, imprinted from numerous studies having investigated the cycle-to-cycle correlations of motor activities (***Kjaerulff and Kiehn, 1996***; ***Talpalar et al., 2013***; ***Skarlatou et al., 2020***). The phase of each individual inspiratory burst within the locomotor cycle (ΦInsp, at least 35 bursts on the treadmill and at least 20 for the air puff context) is represented as the position, from 0 to 1, of the black diamond marks on the outer circle (see ***Figure 3C***; ***Figure 3D***). For each animal, we also computed the mean phase of consecutive inspiratory bursts and represented it as a colored dot (the mean phases of different animals are in different colors). The distance R of the mean phase to the center of the circle indicates the concentration of individual phase values around the mean, as established by ***Kjaerulff and Kiehn, 1996***. If inspiratory and locomotor movements are temporally correlated, then individual phase values will be concentrated around a preferred phase value (for instance 0 or 1, at the top of the circle, if the two motor activities were temporally locked). The mean value would then be positioned at a significant distance from the center. Conversely, if inspiratory and locomotor movements are not coupled, individual phases will be evenly distributed across the circle. Consequently, the mean phase value will be at a short distance from the diagram center, illustrating the dispersion of values around the mean. The inner circles of the circular diagrams depict the threshold for mean phase values to be considered significantly oriented ($R < 0.3$) as commonly done (***Kjaerulff and Kiehn, 1996***; ***Talpalar et al., 2013***; ***Skarlatou et al., 2020***). Circular plots were obtained using a custom macro in Excel. Auto and cross-correlograms (***Figure 3—figure supplement 2***) were computed in Clampfit for one representative animal during stable epochs of running, inferred by the absence of changes in head's horizontal coordinates.

Acknowledgements

This work was funded by an Agence Nationale de la Recherche grant to JB (ANR-17-CE16-0027) and supported by CNRS, Université Paris-Saclay and NeuroPSI. CH holds doctoral fellowships from Région Ile-de-France and Fondation pour la Recherche Médicale. We thank the animal facility for housing animals, Edwin Gatier and Anthony Renard for help with DeepLabCut and Aurélie Heuzé for lab management and help with animals.

Additional information

Funding

Funder	Grant reference number	Author
Agence Nationale de la Recherche	ANR-17-CE16-0027	Julien Bouvier
Fondation pour la Recherche Médicale	Doctoral fellowship	Coralie Hérent
Région Ile-de-France	Doctoral fellowship	Coralie Hérent
University of Paris-Saclay		Julien Bouvier
Centre National de la Recherche Scientifique		Julien Bouvier
NeuroPSI		Julien Bouvier

The funders had no role in study design, data collection and interpretation, or the decision to submit the work for publication.

Author contributions

Coralie Hérent, Conceptualization, Formal analysis, Investigation, Methodology, Writing - review and editing; Séverine Diem, Formal analysis, Investigation, Methodology; Gilles Fortin, Conceptualization, Writing - review and editing; Julien Bouvier, Conceptualization, Formal analysis, Supervision, Funding acquisition, Methodology, Writing - original draft, Project administration, Writing - review and editing

Author ORCIDs

Coralie Hérent https://orcid.org/0000-0002-8472-5097
Gilles Fortin https://orcid.org/0000-0002-2123-8603
Julien Bouvier https://orcid.org/0000-0002-1307-4426

Ethics

Animal experimentation: All experiments were conducted in accordance with EU directive 2010/63/EU and approved by the local ethical committee (authorization 2020-022410231878). Animals were managed by qualified personnel and every effort was made to minimize suffering and reduce the number of animals.

Decision letter and Author response

Decision letter https://doi.org/10.7554/eLife.61919.sa1
Author response https://doi.org/10.7554/eLife.61919.sa2

Additional files

Supplementary files

- Transparent reporting form

Data availability

All data generated or analysed during this study are included in the manuscript and supporting files. Source data files have been provided for all figures.

References

Abdala AP, Rybak IA, Smith JC, Paton JF. 2009. Abdominal expiratory activity in the rat brainstem-spinal cord in situ: patterns, origins and implications for respiratory rhythm generation. *The Journal of Physiology* **587**:3539–3559. DOI: https://doi.org/10.1113/jphysiol.2008.167502, PMID: 19491247

Alexander RM. 1993. Breathing while trotting. *Science* **262**:196–197. DOI: https://doi.org/10.1126/science.8211137, PMID: 8211137

Amiel J, Laudier B, Attié-Bitach T, Trang H, de Pontual L, Gener B, Trochet D, Etchevers H, Ray P, Simonneau M, Vekemans M, Munnich A, Gaultier C, Lyonnet S. 2003. Polyalanine expansion and frameshift mutations of the paired-like homeobox gene PHOX2B in congenital central hypoventilation syndrome. *Nature Genetics* **33**:459–461. DOI: https://doi.org/10.1038/ng1130, PMID: 12640453

Andersson LS, Larhammar M, Memic F, Wootz H, Schwochow D, Rubin CJ, Patra K, Arnason T, Wellbring L, Hjälm G, Imsland F, Petersen JL, McCue ME, Mickelson JR, Cothran G, Ahituv N, Roepstorff L, Mikko S, Vallstedt A, Lindgren G, et al. 2012. Mutations in DMRT3 affect locomotion in horses and spinal circuit function in mice. *Nature* **488**:642–646. DOI: https://doi.org/10.1038/nature11399, PMID: 22932389

Ausborn J, Koizumi H, Barnett WH, John TT, Zhang R, Molkov YI, Smith JC, Rybak IA. 2018. Organization of the core respiratory network: insights from optogenetic and modeling studies. *PLOS Computational Biology* **14**:e1006148. DOI: https://doi.org/10.1371/journal.pcbi.1006148, PMID: 29698394

Avila JJ, Kim SK, Massett MP. 2017. Differences in exercise capacity and responses to training in 24 inbred mouse strains. *Frontiers in Physiology* **8**:974. DOI: https://doi.org/10.3389/fphys.2017.00974, PMID: 29249981

Bachmann LC, Matis A, Lindau NT, Felder P, Gullo M, Schwab ME. 2013. Deep brain stimulation of the midbrain locomotor region improves paretic hindlimb function after spinal cord injury in rats. *Science Translational Medicine* **5**:208ra146. DOI: https://doi.org/10.1126/scitranslmed.3005972, PMID: 24154600

Baudinette RV, Gannon BJ, Runciman WB, Wells S, Love JB. 1987. Do cardiorespiratory frequencies show entrainment with hopping in the tammar wallaby? *The Journal of Experimental Biology* **129**:251–263. PMID: 3585241

Bechbache RR, Duffin J. 1977. The entrainment of breathing frequency by exercise rhythm. *The Journal of Physiology* **272**:553–561. DOI: https://doi.org/10.1113/jphysiol.1977.sp012059, PMID: 592202

Bellardita C, Kiehn O. 2015. Phenotypic characterization of speed-associated gait changes in mice reveals modular organization of locomotor networks. *Current Biology* **25**:1426–1436. DOI: https://doi.org/10.1016/j.cub.2015.04.005, PMID: 25959968

Benarroch EE, Schmeichel AM, Low PA, Parisi JE. 2003. Depletion of ventromedullary NK-1 receptor-immunoreactive neurons in multiple system atrophy. *Brain* **126**:2183–2190. DOI: https://doi.org/10.1093/brain/awg220, PMID: 12902309

Benarroch EE. 2007. Brainstem respiratory control: substrates of respiratory failure of multiple system atrophy. *Movement Disorders* **22**:155–161. DOI: https://doi.org/10.1002/mds.21236, PMID: 17133520

Bernasconi P, Kohl J. 1993. Analysis of co-ordination between breathing and exercise rhythms in man. *The Journal of Physiology* **471**:693–706. DOI: https://doi.org/10.1113/jphysiol.1993.sp019923, PMID: 8120830

Boggs DF. 2002. Interactions between locomotion and ventilation in tetrapods. *Comparative Biochemistry and Physiology Part A: Molecular & Integrative Physiology* **133**:269–288. DOI: https://doi.org/10.1016/S1095-6433(02)00160-5

Bouvier J, Thoby-Brisson M, Renier N, Dubreuil V, Ericson J, Champagnat J, Pierani A, Chédotal A, Fortin G. 2010. Hindbrain interneurons and axon guidance signaling critical for breathing. *Nature Neuroscience* **13**:1066–1074. DOI: https://doi.org/10.1038/nn.2622

Bouvier J, Caggiano V, Leiras R, Caldeira V, Bellardita C, Balueva K, Fuchs A, Kiehn O. 2015. Descending command neurons in the brainstem that halt locomotion. *Cell* **163**:1191–1203. DOI: https://doi.org/10.1016/j.cell.2015.10.074, PMID: 26590422

Bramble DM, Carrier DR. 1983. Running and breathing in mammals. *Science* **219**:251–256. DOI: https://doi.org/10.1126/science.6849136, PMID: 6849136

Bramble DM, Jenkins FA. 1993. Mammalian locomotor-respiratory integration: implications for diaphragmatic and pulmonary design. *Science* **262**:235–240. DOI: https://doi.org/10.1126/science.8211141, PMID: 8211141

Caggiano V, Leiras R, Goñi-Erro H, Masini D, Bellardita C, Bouvier J, Caldeira V, Fisone G, Kiehn O. 2018. Midbrain circuits that set locomotor speed and gait selection. *Nature* **553**:455–460. DOI: https://doi.org/10.1038/nature25448, PMID: 29342142

Casey K, Duffin J, Kelsey CJ, McAvoy GV. 1987. The effect of treadmill speed on ventilation at the start of exercise in man. *The Journal of Physiology* **391**:13–24. DOI: https://doi.org/10.1113/jphysiol.1987.sp016722, PMID: 3127577

Chen K, Zheng Y, Wei JA, Ouyang H, Huang X, Zhang F, Lai CSW, Ren C, So KF, Zhang L. 2019. Exercise training improves motor skill learning via selective activation of mTOR. *Science Advances* **5**:eaaw1888. DOI: https://doi.org/10.1126/sciadv.aaw1888, PMID: 31281888

Corio M, Palisses R, Viala D. 1993. Origin of the central entrainment of respiration by locomotion facilitated by MK 801 in the decerebrate rabbit. *Experimental Brain Research* **95**:84–90. DOI: https://doi.org/10.1007/BF00229657, PMID: 8405255

Daley MA, Bramble DM, Carrier DR. 2013. Impact loading and locomotor-respiratory coordination significantly influence breathing dynamics in running humans. *PLOS ONE* **8**:e70752. DOI: https://doi.org/10.1371/journal.pone.0070752, PMID: 23950997

Del Negro CA, Funk GD, Feldman JL. 2018. Breathing matters. *Nature Reviews Neuroscience* **19**:351–367. DOI: https://doi.org/10.1038/s41583-018-0003-6, PMID: 29740175

DeLorme MP, Moss OR. 2002. Pulmonary function assessment by whole-body plethysmography in restrained versus unrestrained mice. *Journal of Pharmacological and Toxicological Methods* **47**:1–10. DOI: https://doi.org/10.1016/S1056-8719(02)00191-0, PMID: 12387933

DiMarco AF, Romaniuk JR, Von Euler C, Yamamoto Y. 1983. Immediate changes in ventilation and respiratory pattern associated with onset and cessation of locomotion in the cat. *The Journal of Physiology* **343**:1–16. DOI: https://doi.org/10.1113/jphysiol.1983.sp014878, PMID: 6644612

Eldridge FL, Millhorn DE, Waldrop TG. 1981. Exercise hyperpnea and locomotion: parallel activation from the hypothalamus. *Science* **211**:844–846. DOI: https://doi.org/10.1126/science.7466362, PMID: 7466362

Eldridge FL, Millhorn DE, Kiley JP, Waldrop TG. 1985. Stimulation by central command of locomotion, respiration and circulation during exercise. *Respiration Physiology* **59**:313–337. DOI: https://doi.org/10.1016/0034-5687(85)90136-7, PMID: 3992065

Fat-Chun Tony Chang , Harper RM. 1989. A procedure for chronic recording of diaphragmatic electromyographic activity. *Brain Research Bulletin* **22**:561–563. DOI: https://doi.org/10.1016/0361-9230(89)90112-3

Fernandes A, Galbo H, Kjaer M, Mitchell JH, Secher NH, Thomas SN. 1990. Cardiovascular and ventilatory responses to dynamic exercise during epidural anaesthesia in man. *The Journal of Physiology* **420**:281–293. DOI: https://doi.org/10.1113/jphysiol.1990.sp017912, PMID: 2324985

Fernando P, Bonen A, Hoffman-Goetz L. 1993. Predicting submaximal oxygen consumption during treadmill running in mice. *Canadian Journal of Physiology and Pharmacology* **71**:854–857. DOI: https://doi.org/10.1139/y93-128, PMID: 8143245

Gardiner KR, Gardiner PF, Edgerton VR. 1982. Guinea pig soleus and gastrocnemius electromyograms at varying speeds, grades, and loads. *Journal of Applied Physiology* **52**:451–457. DOI: https://doi.org/10.1152/jappl.1982.52.2.451, PMID: 7061299

Gariépy JF, Missaghi K, Dubuc R. 2010. The interactions between locomotion and respiration. *Progress in Brain Research* **187**:173–188. DOI: https://doi.org/10.1016/B978-0-444-53613-6.00012-5, PMID: 21111208

Gariépy JF, Missaghi K, Chevallier S, Chartré S, Robert M, Auclair F, Lund JP, Dubuc R. 2012. Specific neural substrate linking respiration to locomotion. *PNAS* **109**:E84–E92. DOI: https://doi.org/10.1073/pnas.1113002109, PMID: 22160700

Gillis GB, Biewener AA. 2002. Effects of surface grade on proximal hindlimb muscle strain and activation during rat locomotion. *Journal of Applied Physiology* **93**:1731–1743. DOI: https://doi.org/10.1152/japplphysiol.00489.2002, PMID: 12381761

Giraudin A, Le Bon-Jégo M, Cabirol MJ, Simmers J, Morin D. 2012. Spinal and pontine relay pathways mediating respiratory rhythm entrainment by limb proprioceptive inputs in the neonatal rat. *Journal of Neuroscience* **32**:11841–11853. DOI: https://doi.org/10.1523/JNEUROSCI.0360-12.2012, PMID: 22915125

Gravel J, Brocard F, Gariépy JF, Lund JP, Dubuc R. 2007. Modulation of respiratory activity by locomotion in lampreys. *Neuroscience* **144**:1120–1132. DOI: https://doi.org/10.1016/j.neuroscience.2006.10.019, PMID: 17137720

Heglund NC, Taylor CR. 1988. Speed, stride frequency and energy cost per stride: how do they change with body size and gait? . *The Journal of Experimental Biology* **138**:301–318. PMID: 3193059

Iscoe S. 1981. Respiratory and stepping frequencies in conscious exercising cats. *Journal of Applied Physiology* **51**:835–839. DOI: https://doi.org/10.1152/jappl.1981.51.4.835, PMID: 7298426

Iscoe S, Polosa C. 1976. Synchronization of respiratory frequency by somatic afferent stimulation. *Journal of Applied Physiology* **40**:138–148. DOI: https://doi.org/10.1152/jappl.1976.40.2.138, PMID: 1248992

Josset N, Roussel M, Lemieux M, Lafrance-Zoubga D, Rastqar A, Bretzner F. 2018. Distinct contributions of mesencephalic locomotor region nuclei to locomotor control in the freely behaving mouse. *Current Biology* **28**:884–901. DOI: https://doi.org/10.1016/j.cub.2018.02.007, PMID: 29526593

Kay JD, Petersen ES, Vejby-Christensen H. 1975. Breathing in man during steady-state exercise on the bicycle at two pedalling frequencies, and during treadmill walking. *The Journal of Physiology* **251**:645–656. DOI: https://doi.org/10.1113/jphysiol.1975.sp011113, PMID: 1185678

Kiehn O. 2016. Decoding the organization of spinal circuits that control locomotion. *Nature Reviews Neuroscience* **17**:224–238. DOI: https://doi.org/10.1038/nrn.2016.9, PMID: 26935168

Kjaerulff O, Kiehn O. 1996. Distribution of networks generating and coordinating locomotor activity in the neonatal rat spinal cord *in* vitro: a lesion study. *The Journal of Neuroscience* **16**:5777–5794. PMID: 8795632

Kurnikova A, Moore JD, Liao SM, Deschênes M, Kleinfeld D. 2017. Coordination of orofacial motor actions into exploratory behavior by rat. *Current Biology* **27**:688–696. DOI: https://doi.org/10.1016/j.cub.2017.01.013, PMID: 28216320

Lafortuna CL, Reinach E, Saibene F. 1996. The effects of locomotor-respiratory coupling on the pattern of breathing in horses. *The Journal of Physiology* **492 (Pt 2**:587–596. DOI: https://doi.org/10.1113/jphysiol.1996.sp021331, PMID: 9019552

Lancel M, Droste SK, Sommer S, Reul JM. 2003. Influence of regular voluntary exercise on spontaneous and social stress-affected sleep in mice. *European Journal of Neuroscience* **17**:2171–2179. DOI: https://doi.org/10.1046/j.1460-9568.2003.02658.x, PMID: 12786984

Lavezzi AM, Matturri L. 2008. Functional neuroanatomy of the human pre-Bötzinger complex with particular reference to sudden unexplained perinatal and infant death. *Neuropathology* **28**:10–16. DOI: https://doi.org/10.1111/j.1440-1789.2007.00824.x

Le Gal JP, Juvin L, Cardoit L, Thoby-Brisson M, Morin D. 2014. Remote control of respiratory neural network by spinal locomotor generators. *PLOS ONE* **9**:e89670. DOI: https://doi.org/10.1371/journal.pone.0089670, PMID: 24586951

Leith DE. 1976. Comparative mammalian respiratory mechanics. *The Physiologist* **19**:485–510. DOI: https://doi.org/10.1016/0034-5687(82)90069-X, PMID: 996118

Lemieux M, Josset N, Roussel M, Couraud S, Bretzner F. 2016. Speed-Dependent modulation of the locomotor behavior in adult mice reveals attractor and transitional gaits. *Frontiers in Neuroscience* **10**:42. DOI: https://doi.org/10.3389/fnins.2016.00042, PMID: 26941592

Lerman I, Harrison BC, Freeman K, Hewett TE, Allen DL, Robbins J, Leinwand LA. 2002. Genetic variability in forced and voluntary endurance exercise performance in seven inbred mouse strains. *Journal of Applied Physiology* **92**:2245–2255. DOI: https://doi.org/10.1152/japplphysiol.01045.2001, PMID: 12015333

Li HQ, Spitzer NC. 2020. Exercise enhances motor skill learning by neurotransmitter switching in the adult midbrain. *Nature Communications* **11**:2195. DOI: https://doi.org/10.1038/s41467-020-16053-7, PMID: 32366867

Mateika JH, Duffin J. 1995. A review of the control of breathing during exercise. *European Journal of Applied Physiology and Occupational Physiology* **71**:1–27. DOI: https://doi.org/10.1007/BF00511228, PMID: 7556128

Mathis A, Mamidanna P, Cury KM, Abe T, Murthy VN, Mathis MW, Bethge M. 2018. DeepLabCut: markerless pose estimation of user-defined body parts with deep learning. *Nature Neuroscience* **21**:1281–1289. DOI: https://doi.org/10.1038/s41593-018-0209-y, PMID: 30127430

Mathis MW, Mathis A. 2020. Deep learning tools for the measurement of animal behavior in neuroscience. *Current Opinion in Neurobiology* **60**:1–11. DOI: https://doi.org/10.1016/j.conb.2019.10.008, PMID: 31791006

Mayer WP, Murray AJ, Brenner-Morton S, Jessell TM, Tourtellotte WG, Akay T. 2018. Role of muscle spindle feedback in regulating muscle activity strength during walking at different speed in mice. *Journal of Neurophysiology* **120**:2484–2497. DOI: https://doi.org/10.1152/jn.00250.2018, PMID: 30133381

Meek TH, Lonquich BP, Hannon RM, Garland T. 2009. Endurance capacity of mice selectively bred for high voluntary wheel running. *Journal of Experimental Biology* **212**:2908–2917. DOI: https://doi.org/10.1242/jeb.028886

Morin D, Viala D. 2002. Coordinations of locomotor and respiratory rhythms *in* vitro are critically dependent on hindlimb sensory inputs. *The Journal of Neuroscience* **22**:4756–4765. DOI: https://doi.org/10.1523/JNEUROSCI.22-11-04756.2002, PMID: 12040083

Parachikova A, Nichol KE, Cotman CW. 2008. Short-term exercise in aged Tg2576 mice alters neuroinflammation and improves cognition. *Neurobiology of Disease* **30**:121–129. DOI: https://doi.org/10.1016/j.nbd.2007.12.008, PMID: 18258444

Paterson DJ, Wood GA, Morton AR, Henstridge JD. 1986. The entrainment of ventilation frequency to exercise rhythm. *European Journal of Applied Physiology and Occupational Physiology* **55**:530–537. DOI: https://doi.org/10.1007/BF00421649, PMID: 3769910

Paterson DJ. 2014. Defining the neurocircuitry of exercise hyperpnoea. *The Journal of Physiology* **592**:433–444. DOI: https://doi.org/10.1113/jphysiol.2013.261586, PMID: 23918772

Pearson KG, Acharya H, Fouad K. 2005. A new electrode configuration for recording electromyographic activity in behaving mice. *Journal of Neuroscience Methods* **148**:36–42. DOI: https://doi.org/10.1016/j.jneumeth.2005.04.006, PMID: 15908013

Potts JT, Rybak IA, Paton JF. 2005. Respiratory rhythm entrainment by somatic afferent stimulation. *Journal of Neuroscience* **25**:1965–1978. DOI: https://doi.org/10.1523/JNEUROSCI.3881-04.2005, PMID: 15728836

Ramanantsoa N, Hirsch MR, Thoby-Brisson M, Dubreuil V, Bouvier J, Ruffault PL, Matrot B, Fortin G, Brunet JF, Gallego J, Goridis C. 2011. Breathing without CO(2) chemosensitivity in conditional Phox2b mutants. *Journal of Neuroscience* **31**:12880–12888. DOI: https://doi.org/10.1523/JNEUROSCI.1721-11.2011, PMID: 21900566

Rodriguez A, Zhang H, Klaminder J, Brodin T, Andersson M. 2017. ToxId: an efficient algorithm to solve occlusions when tracking multiple animals. *Scientific Reports* **7**:14774. DOI: https://doi.org/10.1038/s41598-017-15104-2, PMID: 29116122

Romer SH, Seedle K, Turner SM, Li J, Baccei ML, Crone SA. 2017. Accessory respiratory muscles enhance ventilation in ALS model mice and are activated by excitatory V2a neurons. *Experimental Neurology* **287**:192–204. DOI: https://doi.org/10.1016/j.expneurol.2016.05.033, PMID: 27456268

Ruffault P-L, D'Autréaux F, Hayes JA, Nomaksteinsky M, Autran S, Fujiyama T, Hoshino M, Hägglund M, Kiehn O, Brunet J-F, Fortin G, Goridis C. 2015. The retrotrapezoid nucleus neurons expressing Atoh1 and Phox2b are essential for the respiratory response to CO2. *eLife* **4**:e07051. DOI: https://doi.org/10.7554/eLife.07051

Sartori CR, Pagliusi M, Bonet IJM, Tambeli CH, Parada CA. 2020. Running wheel exercise induces therapeutic and preventive effects on inflammatory stimulus-induced persistent hyperalgesia in mice. *PLOS ONE* **15**:e0240115. DOI: https://doi.org/10.1371/journal.pone.0240115, PMID: 33048957

Shafford HL, Strittmatter RR, Schadt JC. 2006. A novel electrode design for chronic recording of electromyographic activity. *Journal of Neuroscience Methods* **156**:228–230. DOI: https://doi.org/10.1016/j.jneumeth.2006.03.009, PMID: 16621006

Sieck GC, Gransee HM. 2012. *Respiratory Muscles: Structure Function & Regulation*. Morgan & Claypool Life Sciences. DOI: https://doi.org/10.4199/C00057ED1V01Y2012ISP034

Skarlatou S, Hérent C, Toscano E, Mendes CS, Bouvier J, Zampieri N. 2020. Afadin signaling at the spinal neuroepithelium regulates central canal formation and gait selection. *Cell Reports* **31**:107741. DOI: https://doi.org/10.1016/j.celrep.2020.107741, PMID: 32521266

Stickford AS, Stickford JL, Tanner DA, Stager JM, Chapman RF. 2015. Runners maintain locomotor-respiratory coupling following isocapnic voluntary hyperpnea to task failure. *European Journal of Applied Physiology* **115**: 2395–2405. DOI: https://doi.org/10.1007/s00421-015-3220-y, PMID: 26194932

Talpalar AE, Bouvier J, Borgius L, Fortin G, Pierani A, Kiehn O. 2013. Dual-mode operation of neuronal networks involved in left-right alternation. *Nature* **500**:85–88. DOI: https://doi.org/10.1038/nature12286, PMID: 23812590

Thornton JM, Guz A, Murphy K, Griffith AR, Pedersen DL, Kardos A, Leff A, Adams L, Casadei B, Paterson DJ. 2001. Identification of higher brain centres that may encode the cardiorespiratory response to exercise in humans. *The Journal of Physiology* **533**:823–836. DOI: https://doi.org/10.1111/j.1469-7793.2001.00823.x, PMID: 11410638

Tsuchiya N, Iwase M, Izumizaki M, Homma I. 2012. Dopaminergic modulation of exercise hyperpnoea via D(2) receptors in mice. *Experimental Physiology* **97**:228–238. DOI: https://doi.org/10.1113/expphysiol.2011.062703, PMID: 22041981

Usseglio G, Gatier E, Heuzé A, Hérent C, Bouvier J. 2020. Control of orienting movements and locomotion by Projection-Defined subsets of brainstem V2a neurons. *Current Biology* **1**:14. DOI: https://doi.org/10.1016/j.cub.2020.09.014

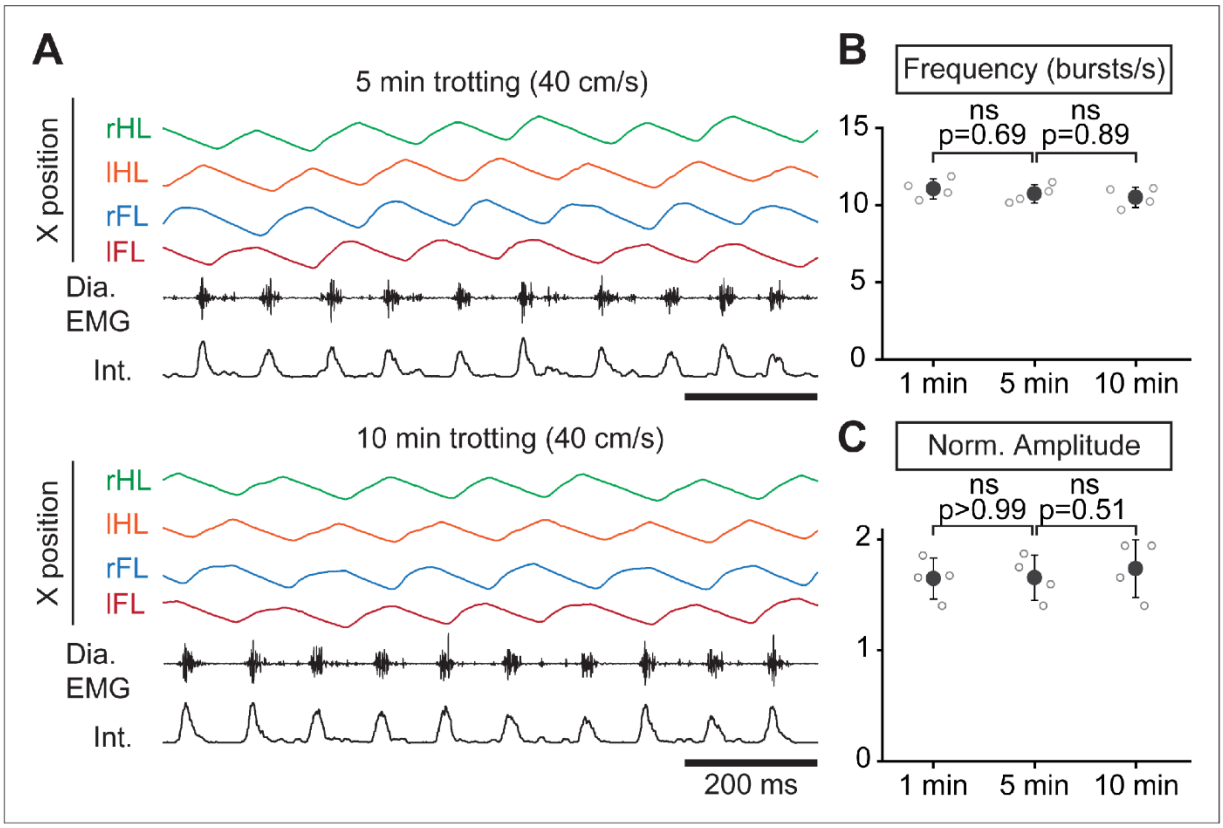

Figure 2—figure supplement 1. Respiratory changes during a prolonged treadmill running. (**A**) Changes in the horizontal (X) axis of the right hindlimb (rHL, green), left hindlimb (lHL, orange), right forelimb (rFL, blue) and left forelimb (lFL, red) over time, as well as raw (Dia. EMG) and integrated (Int.) diaphragmatic neurograms, after 5 and 10 min of continuous running at 40 cm/s on the level treadmill. (**B–C**) Analyses of respiratory parameters changes after 1, 5, and 10 min of running at 40 cm/s on the level treadmill: frequency (**B**) and normalized amplitude (**C**). Note that respiratory parameters were stable throughout the 10-min run. Data are presented as mean ± SD from n = 4 mice and p values indicated are obtained from Mann-Whitney *U* tests and considered not significant (ns) when p>0.05.

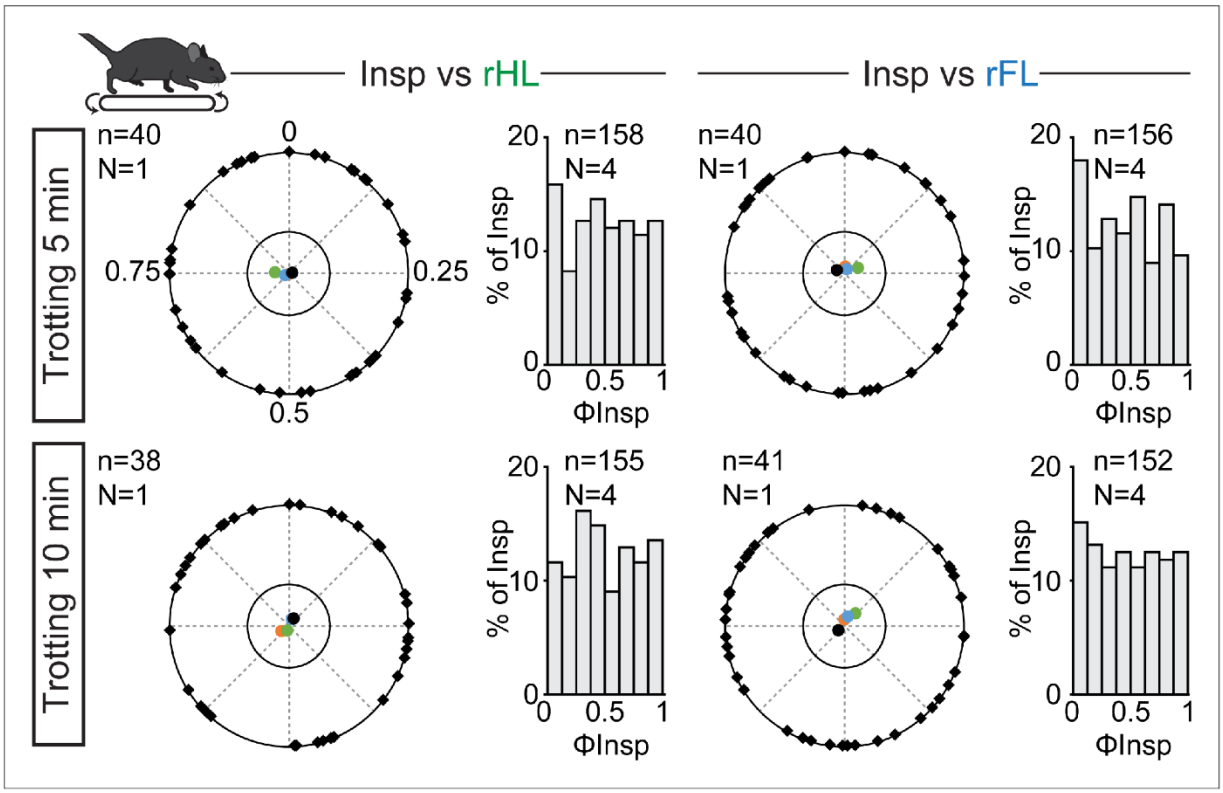

Figure 3—figure supplement 1. Correlation of breaths to strides during prolonged treadmill running. Circular plots showing the phase-relationship between inspiratory bursts and the indicated reference limb for one representative animal trotting continuously for 5 (top) or 10 min (bottom). Black diamonds on the outer circle indicate the phase of n individual inspirations. The black dot indicates the mean orientation vector for that animal and the colored dots the mean orientation vector of three other animals (each in a specific color). The positioning of these mean values within the inner circle illustrates the absence of a significantly-oriented phase preference ($R < 0.3$, with R being the concentration of phase values around the mean as defined in ***Kjaerulff and Kiehn, 1996***). To the right of the circular plots are phase distribution histograms between inspiratory bursts and the same reference limb for all n events from four animals. Note that all inspiratory bursts are evenly distributed across the entire locomotor cycle in each condition.

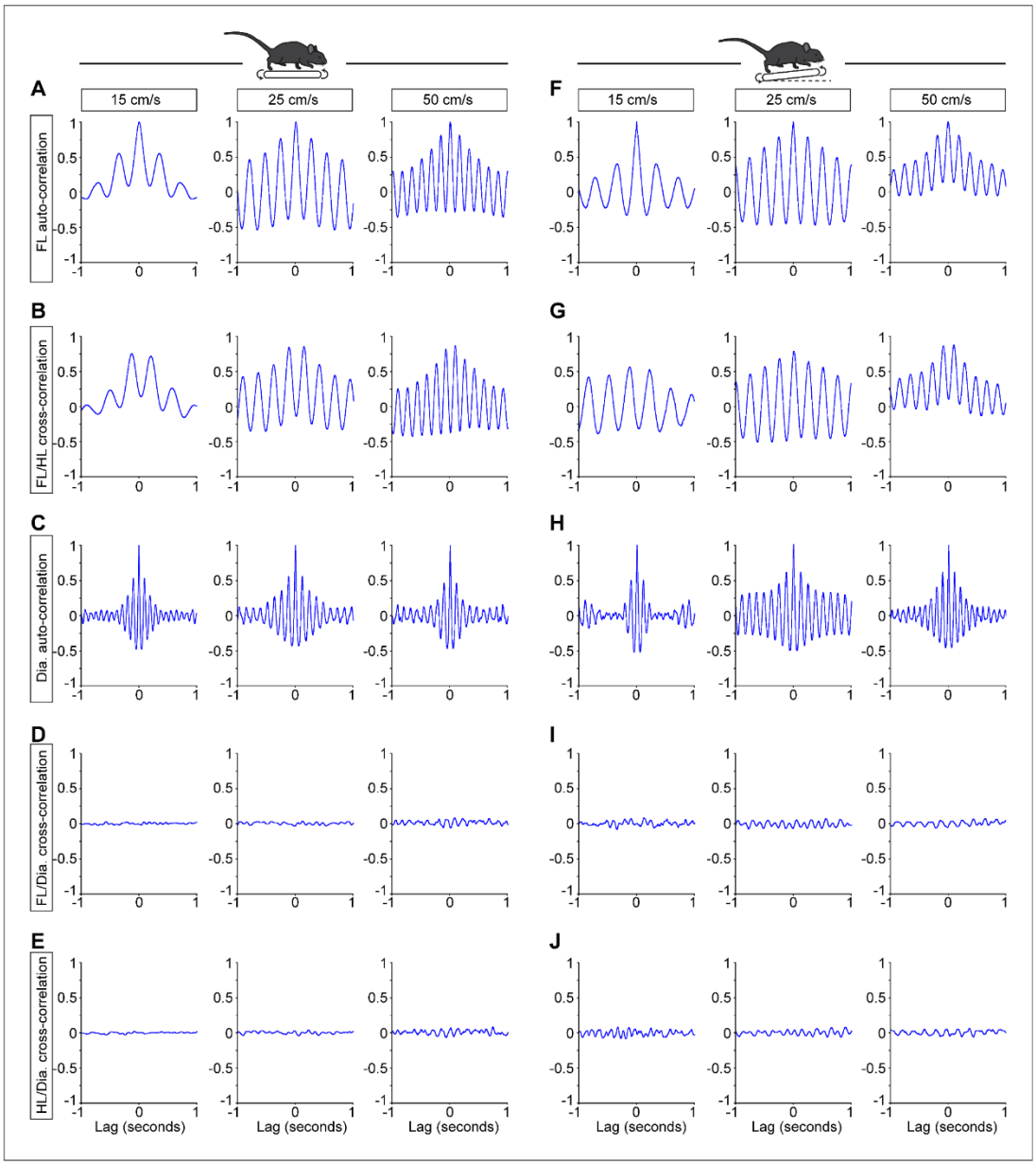

Figure 3—figure supplement 2. Example cross-correlations of breathing and locomotor rhythms showing no common modulation. (**A–E**) Correlograms during stable trotting at 15, 25, and 50 cm/s on a level treadmill for one representative animal, with a lag of 1 s. For the limbs, the horizontal coordinates were used (see ***Figure 3***). For the diaphragm (Dia.) the integrated EMG activity was used. Data are presented as the correlation function estimate (from −1 to 1) at each lag (in s). (**A**) Auto-correlogram of the right forelimb showing the regularity of the rhythm and the increase step cycle as the treadmill speed increases. (**B**) Cross-correlogram of the homolateral forelimb and hindlimb showing their alternating activity. (**C**) Auto-correlogram of the integrated diaphragmatic activity showing the regularity of the rhythm and the comparable frequency at the different treadmill speeds. (**D**) Cross-correlogram of the forelimb movements and diaphragmatic EMG activity, showing no common modulation at all tested speeds. (**E**) Cross-correlogram of the hindlimb movements and diaphragmatic EMG activity, showing no common modulation at all tested speeds. (**F–I**) Similar representations for the same animal trotting on a 10% inclined treadmill, showing no common modulation between locomotor and respiratory rhythms at all tested speeds.

RESULTS Chapter 2 – Paper 2

Distinct neuronal drives from locomotor circuits upregulate breathing rate during running exercise

Coralie Hérent[1], Séverine Diem[1], Gilles Fortin[2] and Julien Bouvier[1]

[1]Université Paris-Saclay, CNRS
Institut des Neurosciences Paris-Saclay
91190, Gif-sur-Yvette,
France.

[2] Institut de Biologie de l'École Normale Supérieure (IBENS),
École Normale Supérieure, CNRS, INSERM, PSL Research University,
75005 Paris,
France

Abstract

While respiratory adaptation to exercise is compulsory to cope with metabolic supply to, and necessary clearing of metabolic waste from, body tissues, the neural apparatus at stake remains poorly identified. Using viral tracing, *ex vivo* and *in vivo* optogenetic and chemogenetic interference strategies in mice, we unravel interactive locomotor and respiratory networks' nodes that mediate respiratory rate increase accompanying a running exercise. We show that the mesencephalic locomotor region (MLR) and the lumbar spinal locomotor pattern generator (lumbar CPG) that respectively initiate and execute the locomotor behavior access the respiratory network through distinct entry points. The MLR directly projects onto the preBötzinger complex (preBötC) that paces breathing and can trigger moderate increase of respiratory frequency, prior to, or even in the absence of locomotion. In contrast, the lumbar CPG projects onto the retrotrapezoid nucleus (RTN) that in turn contacts the preBötC to enforce, during effective locomotion, higher respiratory frequencies commensurate to locomotor velocity. These data expand, on the one hand, the functional implications of the MLR beyond locomotor initiation to *bona fide* respiratory modulation and on the other hand, the adaptive respiratory ambitions of the RTN beyond chemoception to "locomotor-ception".

Introduction

Breathing is a vital behavior which must combine extreme robustness with continuous adaptability. One striking example is the abrupt augmentation of ventilation at the transition from rest to running in order to maintain homeostasis in spite of increased metabolic demand (DiMarco et al., 1983; Duffin and Bechbache, 1983; Mateika and Duffin, 1995). This "exercise hyperpnoea" is manifested by an increase in both respiratory frequency and volume. It has long been proposed that its main trigger, at least for acute exercise, is of neuronal nature, i.e., relies on activatory signals from locomotor effectors or circuits impacting onto the respiratory generator in the brainstem (Mateika and Duffin, 1995; Gariepy et al., 2010; Duffin, 2014; Paterson, 2014). However, the underlying cells and circuits are not fully elucidated.

We recently uncovered that running hyperpnoea can, at least in mice but very likely in all quadrupeds, occur without temporal synchronization of breathes to strides (Hérent et al., 2020). This, together with the ventilatory response seen in men during mental simulation of exercise (Tobin et al., 1986; Decety et al., 1991; Decety et al., 1993) or in the absence of peripheral signals (Fernandes et al., 1990), highlights that the main neuronal trigger of exercise hyperpnoea is of central, rather than peripheral, origin. Of particular interest are therefore brain regions that command or execute locomotor movements and could provide a parallel drive to respiratory centers (Eldridge et al., 1981; Eldridge et al., 1985). The mesencephalic locomotor region (MLR) in the dorsal midbrain is considered the main site of locomotor initiation throughout the animal kingdom (Shik et al., 1966; Le Ray et al., 2011; Ryczko et al., 2016) and possibly humans (Jahn et al., 2008). Stimulation of the MLR, and particularly its cuneiform nucleus (CnF) component, engages forward locomotion at a speed that is commensurate to the intensity of the stimulus (Bachmann et al., 2013; Roseberry et al., 2016; Caggiano et al., 2018; Josset et al., 2018), making it a candidate neuronal driver and encoder of running intensity. The possibility that the MLR may provide a parallel activation of respiratory centers is suggested by work in the lamprey (Gariepy et al., 2012), an ancestral vertebrate specie, but this has yet not been investigated in terrestrial mammals. Another central drive to respiratory centers may originate in the circuits of spinal cord that elaborate the locomotor rhythm and coordinate the motor output during ongoing locomotor movements, often referred to as "Central Pattern Generator" or CPG (Grillner, 2006; Kiehn, 2016; Grillner and El Manira, 2020). Indeed, pharmacological activation of the lumbar enlargement, where the hindlimb CPG circuit resides, can upregulate the frequency of respiratory-like activities on *ex-vivo* preparations from neonatal rats (Le Gal et al., 2014; Le Gal et al., 2020). While this is suggestive of ascending projections to respiratory centers, the underlying circuit and its functionality during running has not been documented.

Another gap of knowledge resides in the identification of the respiratory neurons targeted by descending (i.e., MLR) or ascending (i.e., from the CPG) locomotor drives. In mammals, the respiratory

rhythm is paced by a confined cluster of neurons in the ventromedial medulla, the pre-Bötzinger complex (preBötC, (Smith et al., 1991; Del Negro et al., 2018)). Direct activation or inactivation of preBötC glutamatergic neurons respectively increases, or reduces and even arrests, respiratory rate (Tan et al., 2008; Alsahafi et al., 2015; Cui et al., 2016; Vann et al., 2018). The preBötC receives inputs from several brain areas including the midbrain (Yang et al., 2020) and, in the lamprey, MLR neurons were shown to contact a presumed homologue of the preBötC (Mutolo et al., 2010; Gariepy et al., 2012). This makes the preBötC a candidate for promptly entraining respiration during exercise in mammals. More rostrally, an area collectively referred to as the parafacial respiratory region may be another candidate of respiratory regulation during metabolic challenges including effort. In particular in this region, non-catecholaminergic *Phox2b*-expressing neurons (defining the Retrotrapezoid Nucleus, RTN) are well-known for their capacity to rapidly upregulate respiratory rate in the context of central chemoception (Abbott et al., 2009; Abbott et al., 2011). They might also support active expiration which is thought to accompany exercise (Ainsworth et al., 1989; Iscoe, 1998; Abraham et al., 2002). *Phox2b*-positive neurons in the parafacial region have been shown to be activated during running (Barna et al., 2012, 2014), during locomotor-like activity on *ex vivo* neonatal rat preparations (Le Gal et al., 2014), and their chemogenetic silencing limits exercise capacity in running rats (Korsak et al., 2018).

Here we sought to investigate the central circuits interfacing locomotor and respiratory centers in the resourceful mouse model. We found the existence of both a feed-forward drive from the MLR, and of an ascending drive from the locomotor CPG of the lumbar spinal cord. Remarkably, the MLR is capable of upregulating breathing rate even before the initiation of actual limb movements. We further uncovered that the two systems have rapid access to respiratory rhythm generation mechanisms albeit through two different synaptic schemes. The MLR directly projects to the preBötC, but not to the parafacial respiratory region, while the lumbar spinal cord targets the RTN which in turns contacts the preBötC. Our work therefore demonstrates two central drives that may underlie breathing adaptability during running and their synaptic nodes in the respiratory central network.

Results

Glutamatergic CnF neurons project to the preBötC

We first examined whether locomotor promoting MLR neurons in mice, as the case in the lamprey (Gariepy et al., 2012), contact neuronal groups involved in respiratory rhythm generation. The MLR contains two major subdivisions, the cuneiform nucleus (CnF) containing glutamatergic (Glut+) neurons, and the pedunculopontine nucleus (PPN) containing both glutamatergic and cholinergic neurons (Roseberry et al., 2016; Caggiano et al., 2018; Josset et al., 2018). Since locomotor initiation is mostly attributed to the former, we traced the projections of CnF neurons by unilateral stereotaxic injections of a Cre-dependent Adeno Associated Virus (AAV) coding the fluorescent protein eYFP in *vGlut2-IRES-Cre* adult mice (Vong et al., 2011) (Figure 1A-F, Figure S1). Abundant eYFP-positive fibers were detected in the preBötC, defined as located ventrally to the nucleus ambiguous, containing SST-positive neurons and between antero-posterior levels -7.3 and -6.7 from bregma (Stornetta et al., 2003; Tan et al., 2008). These projections were found bilaterally with an ipsilateral predominance (Figure 1C, D). In contrast, projections were very sparse ventral to the facial motor nucleus (7N) in the parafacial respiratory area (pF, between antero-posterior levels -6.5 and -5.7 from Bregma, Figure 1E, F). We also observed CnF projections to the lateral parabrachial nucleus (lPB, Figure S1B, C) and to the nucleus of the tractus solitarius (NTS, Figure S1D, E). To verify that CnF neurons synaptically target preBötC neurons, we made use of a genetically restricted two-virus approach (Kim et al., 2016) to reveal preBötC putative inputs anatomically. Functional

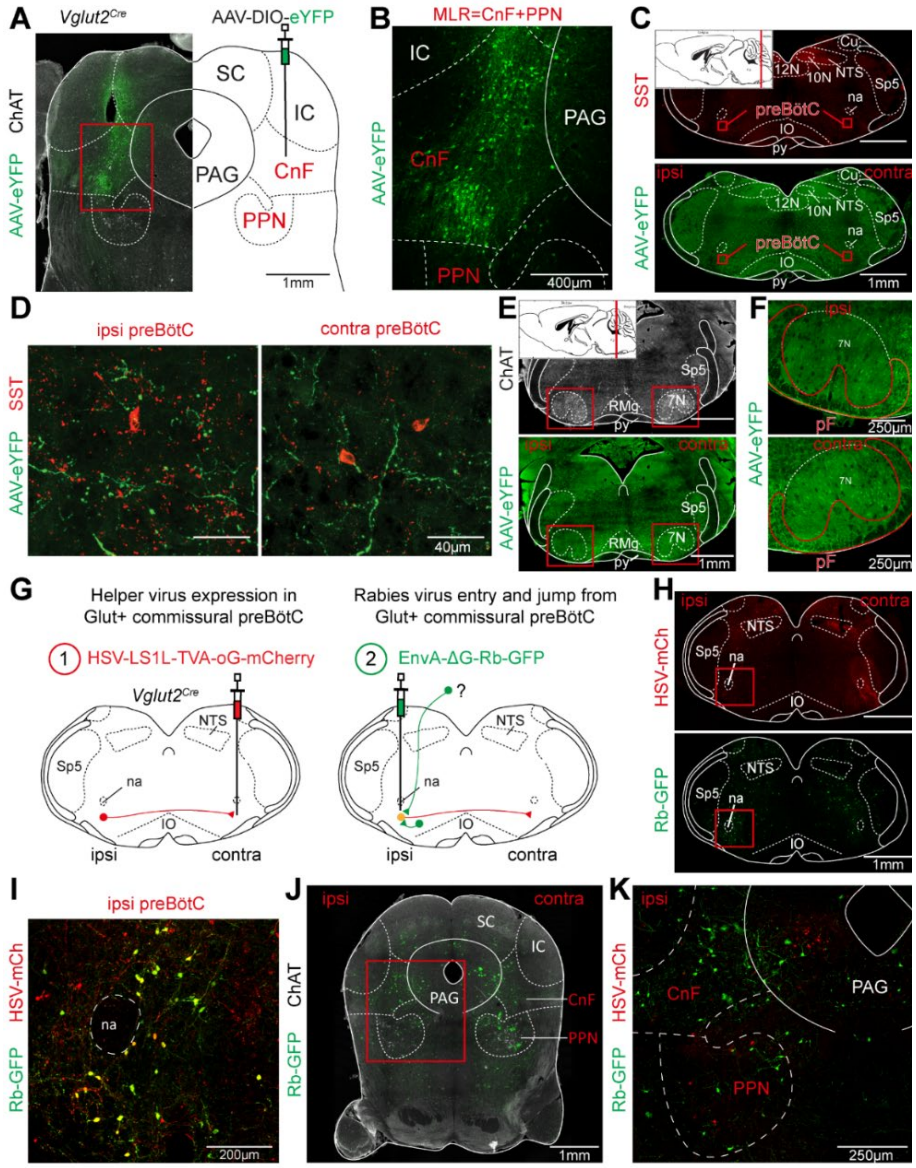

Figure 1: Glutamatergic CnF neurons contact the preBötC. (A-B) Transfection of the glutamatergic CnF. **(A)** Low magnification at the level of the injection site, showing the glutamatergic CnF transfected with an AAV-DIO-eYFP on a cholinergic staining background (ChAT, delineating the PPN) in a *Vglut2*^{Cre} mouse. **(B)** Magnification of the area framed in red in **A**. **(C)** Low magnification at the preBötC level. Top, somatostatin staining (SST, top) is used to locate anatomically the preBötC. Bottom, CnF projections. **(D)** High magnifications of the ipsi- and contralateral preBötC framed in red in **C** and identified by SST. Note that the CnF projects to both sides, although prominently on the side ipsilateral to the injection. **(E)** Low magnification at the parafacial respiratory region (pF) level. Top, cholinergic staining (ChAT). Bottom, CnF projections. **(F)** High magnifications of the ipsi- and contralateral areas framed in red in **E**. The pF is delineated in red close to the facial motor nucleus (7N). Note that the CnF projects very little to both pF. **(G)** Approach used for revealing presynaptic cells of the commissural glutamatergic preBötC in a *Vglut2*^{Cre} mouse line. See text for details. Starter cells appear yellow while presynaptic cells are green. **(H)** Low magnifications at the preBötC level showing HSV-infected cells (top) and Rb-infected cells (bottom). **(I)** High magnification of the ipsilateral preBötC area framed in red in **H**. Starter cells are yellow (HSV-mCherry^{+} and Rb-GFP^{+}). **(J)** Low magnification at the MLR (CnF + PPN) level showing presynaptic cells (Rb-GFP) on a ChAT background. **(K)** Magnification of the area framed in red in **J**. Note the presence of presynaptic cells in the CnF and some in the PPN. *Abbreviations used in all figures: CnF, Cuneiform nucleus. PPN, Pedunculopontine nucleus. SC, Superior colliculus. IC, Inferior colliculus. PAG, Periaqueductal gray. MLR, Mesencephalic locomotor region. Cu, Cuneate nucleus. 12N, Hypoglossal nucleus. 10N, Vagus motor nucleus. NTS, Nucleus tractus solitarius. Sp5, Spinal trigeminal nucleus, interpolar. na, Nucleus ambiguous. preBötC, preBötzinger complex. IO, Inferior olive. py, Pyramidal tract. RMg, Raphe magnus nucleus. 7N, facial motor nucleus. pF, Parafacial respiratory region*

preBötC neurons can be efficiently delineated as glutamatergic (Glut+) neurons with commissural projections (Koshiya and Smith, 1999; Bouvier et al., 2010). We therefore drove the expression of the TVA receptor and the rabies protein G using a retrogradely transported Cre-dependent Herpes Simplex Virus (HSV (Neve et al., 2005; Reinhard et al., 2019)) injected in the preBötC on one side. Seven days later, a G-deleted and EnvA-pseudotyped rabies (Rb) virus coding mCherry was injected in the preBötC on the other side (Figure 1G). As demonstrated previously, this leads to the expression of the Rb virus in projection-defined neuronal somata (Usseglio et al., 2020), here commissural Glut+ neurons of the preBötC, and, from these starter cells, to its trans-neuronal spread to upstream neurons (Figure 1H, K). Trans-neuronally labelled neurons, i.e., expressing only the Rb-driven fluorophore, were detected in the Cn-F and PPN nuclei bilaterally (Figure 1J, K). Putative inputs to Glut+ preBötC neurons were also detected in the contralateral preBötC, the periaqueductal grey, the superior colliculus and the NTS, and only few cells were detected in the parafacial respiratory region on either side (Figure 1H, J, Figure S1G-J). Altogether, these converging anterograde and retrograde tracings collectively demonstrate that Glut+ MLR neurons make direct contact with candidate respiratory rhythm generating neurons in the preBötC, but not in the parafacial respiratory region.

Glutamatergic CnF neurons modulate inspiratory rhythm generation mechanisms

We next aimed at verifying the functionality of Glut+ MLR neurons to the preBötC. One hallmark of photo-activating preBötC neurons is an altered timing of the subsequent respiratory motor burst that depends on the time of light onset within the respiratory cycle (Cui et al., 2016; Baertsch et al., 2018). To evaluate the capacity of MLR neurons to reproduce this, we virally delivered the Channelrhodopsin 2 (ChR2) in the CnF on one side (AAV-DIO-ChR2-eYFP) of *Vglut2-Cre* mice, and implanted an optic fiber over the MLR on the same side (Figure 2A). Breathing cycles were measured in awake adult animals with whole body plethysmography (WBP, (DeLorme and Moss, 2002), Figure 2B) while short single-pulse (50 ms) photo-activations were randomly delivered during the respiratory cycle. We calculated the resultant phase shift, expressed as the perturbed cycle duration over the control cycle duration as done previously ((Cui et al., 2016; Baertsch et al., 2018), Figure 2C). A phase shift <1 (perturbed cycle duration lower than the control one) indicates a shortening of the respiratory cycle, a phase shift >1 (perturbed cycle duration higher than the control one) indicates a lengthening, and a phase shift equal to 1 (perturbed cycle duration equal to the control one) indicates no effect. We found that unilateral photo-stimulation of CnF neurons elicited an ectopic inspiratory burst and shortened the respiratory cycle (Figure 2C) but that this effect was dependent on the timing of light-activation during the respiratory cycle. Specifically, the most significant cycle shortening was seen when delivering light pulses during early expiration (phase: 0.5-0.6, phase shift: 0.77 ± 0.12, $p<0.0001$ Figure 2D). In contrast, the effect was only minimal when photo-stimulations were delivered in late expiration. Intriguingly, a shortening, albeit to a lesser extent, was also noted on the three subsequent respiratory cycles (Figure S2A-D). To ascertain that this modulation of respiratory rhythm generation owes to direct projections of Glut+ CnF neurons to the preBötC, we next aimed at photo-activating ChR2-expressing fibers in the preBötC following the delivery of the ChR2 virus in the CnF (Figure 2E). This led to a similar phase-dependent shortening of the respiratory cycle, with a maximal shortening observed when light-activations are delivered in early expiration (phase: 0.5-0.6; phase shift: 0.73 ± 0.15, $p<0.0001$, Figure 2F, G). This effect disappeared after the 2nd subsequent respiratory cycle (θ+3, Figure S2E-H). Overall, this indicates that Glut+ MLR neurons, through their direct projections to the preBötC, can trigger a phase-dependent resetting of the respiratory cycle, highlighting an excitatory modulation of inspiratory burst generation mechanisms.

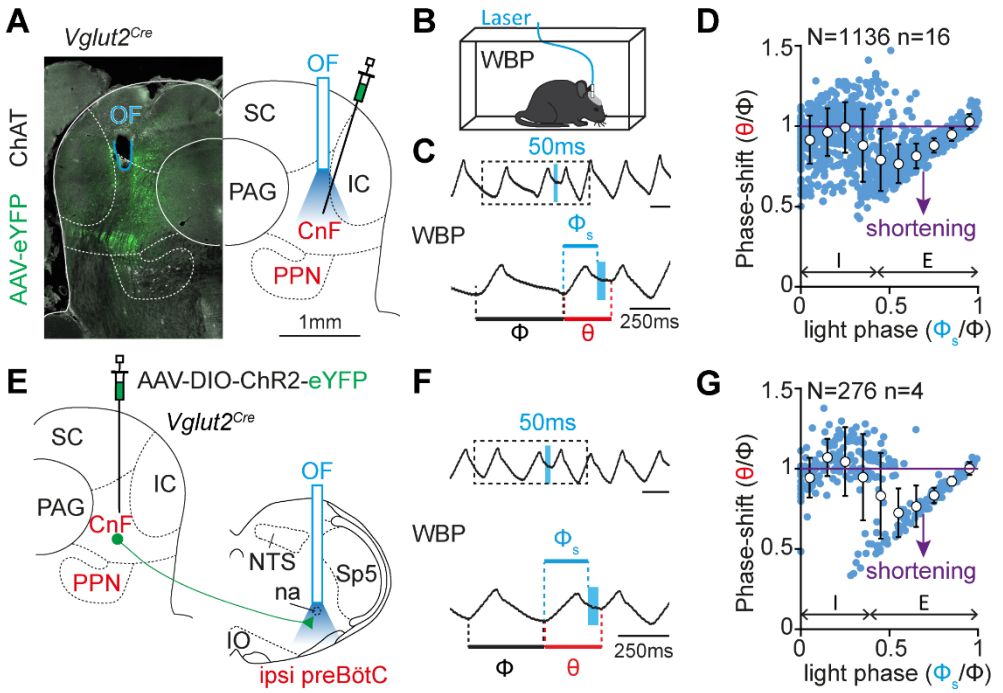

Figure 2: Photoactivation of the Glut+ CnF impacts respiratory rhythm generation through direct projections to the preBötC. (A) Photoactivation of the glutamatergic CnF. **(A)** Left, low magnification at the level of the injection and optic fiber (OF, blue) implantation sites, showing glutamatergic CnF neurons transfected with an AAV-DIO-ChR2-eYFP on a cholinergic staining background (ChAT, delineating the PPN) in a *Vglut2^{Cre}* mouse. **(B)** Setup for recording breathing movements using a whole-body plethysmography chamber (WBP) while the animal is connected to a laser. **(C)** WBP recordings of respiratory cycles while a 50 ms stimulation of the glutamatergic CnF (blue rectangles) is applied. Top, one example of the stimulation occurring during the expiratory phase of one respiratory cycle. Note that the stimulation precipitates a new cycle. Bottom, magnification of the top trace showing parameters used in **D**: the perturbed cycle (θ, red), the control cycle (ϕ, black) and the light cycle (ϕ_s, blue). **(D)** Plot of the phase-shift (perturbed cycle normalized to the control cycle: θ/ϕ) as a function of the light phase (light cycle normalized to the control cycle: ϕ_s/ϕ). Inspiration (I) and expiration (E) mean durations are annotated on the graph. A shortening of the perturbed cycle occurs when values are under 1 (purple line). Note that the perturbed cycle is shortened when the light pulse occurs in the expiratory part of the respiratory cycle. N=1136 random trials, n=16 mice. **(E)** Schematics of the injection identical to **A** in the CnF and optic fiber implantation in the preBötC ipsilateral to the injection. **(F-G)** Same as in **C-D** using photostimulation of the CnF fibers in the preBötC area. Note the similar effect as in **C-D**. N=276 random trials, n=4 mice. *See Figure 1 for abbreviations of brain structures.*

Glutamatergic CnF neurons modulate breathing in synergy with locomotion

Through their access to rhythm generating neurons in the preBötC, Glut+ MLR neurons might be capable of upregulating breathing frequency in synergy with locomotor initiation. To access respiratory parameters during vigorous displacement movements, we made use of our recently developed method for chronic electromyographic (EMG) recordings of the diaphragm, the main inspiratory muscle (Hérent et al., 2020). Animals were thus made to express ChR2 in Glut+ CnF neurons, EMG-implanted and placed in a linear corridor. Light was delivered in trains of 1 s duration at increasing pulse frequencies when animals were stationary at one end of the corridor (Figure 3A). Animals were filmed from the side and their displacement speed computed using markerless video-tracking (Mathis et al., 2018) as performed previously (Hérent et al., 2020). In line with numerous studies (Roseberry et al., 2016; Caggiano et al., 2018; Josset et al., 2018), we found that light-activation of Glut+ CnF neurons at 15 Hz or more engage animals in forward locomotion, and that higher stimulation frequencies impose faster regimes, increase the occurrence of left-right synchronous gaits, and shorten the latency between light onset and locomotor

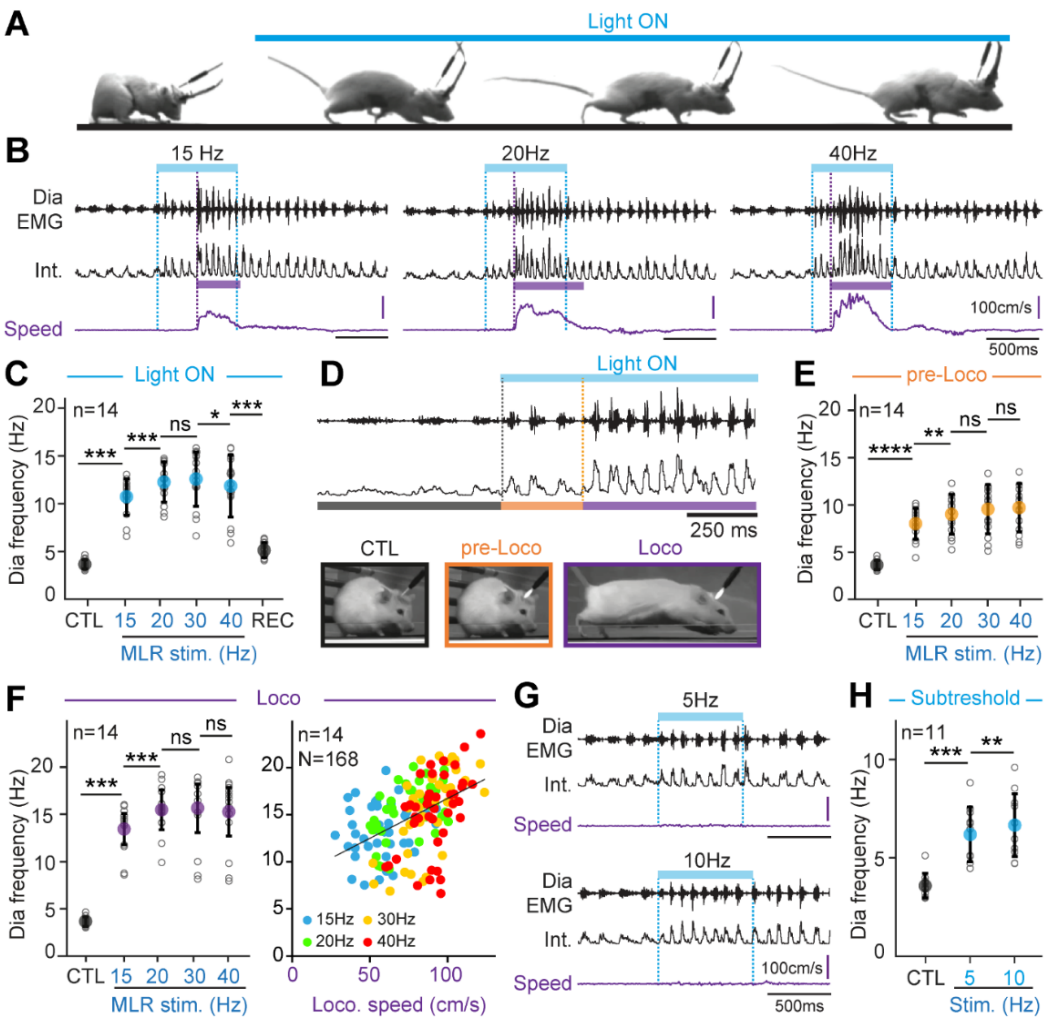

Figure 3: Glut+ CnF neurons upregulate breathing in synergy with locomotor episodes, and even in the absence of movement. (A) Snapshots from one animal showing that photostimulation of the glutamatergic CnF (blue bar) can trigger running. **(B)** Example traces from one representative animal during CnF photostimulation at 15, 20 Hz and 40 Hz. Raw neurogram of the diaphragm (Dia EMG), integrated EMG signal (Int.) and locomotor speed (Speed, purple) of the animal are presented for each stimulation frequency. The onset and offset (dotted blue lines), and duration of the light stimulation (blue bar) are highlighted, as well as the onset (dotted purple line) and duration of the locomotor episode (purple bar). **(C)** Graph showing the diaphragm frequency in resting condition (CTL), during 1 s CnF stimulation frequencies (15-20-30-40 Hz) and in recovery (REC) in n=14 mice. **(D)** Top, example traces from one animal showing raw and integrated diaphragm EMG signals. The resting condition is depicted by a gray bar (CTL). The 1 s CnF photostimulation (top blue bar) is divided in two conditions: "pre-Loco" (orange bar) characterized by the absence of movement, and "Loco" (purple bar) when the animal engages in running. Note that the diaphragm frequency increases prior to ("pre-Loco"), and during ("Loco") the locomotor episode. Bottom, snapshots showing the state of one representative animal in the 3 illustrated conditions. **(E)** Characterization of the respiratory changes during the "pre-Loco" condition. Graph showing the diaphragm frequency during control (CTL) and CnF stimulations at 15, 20, 30 and 40 Hz. Note that the diaphragm frequency increases until a plateau at 20 Hz in n=14 mice. **(F)** Left, same representation as in **E** during the "Loco" condition. The diaphragm frequency increases dramatically during the movement and reaches a plateau at 20 Hz in n=14 mice. Right, color plot showing the diaphragm frequency in relation to the locomotor speed. Each stimulation frequency is color coded. Note that the diaphragm frequency somewhat correlates with the speed (linear regression, black line, R^2=0.22). N=168 trials, n=14 mice. **(G)** Example traces from one representative animal during CnF subthreshold photostimulation at 5 and 10 Hz. The onset and offset of the CnF stimulation are represented with blue dotted lines. Note that subthreshold CnF stimulations do not trigger a locomotor episode, yet breathing frequency is increased. **(H)** Graph showing the diaphragm frequency in control (CTL) and during subthreshold CnF stimulation (5-10 Hz). Note that the diaphragm frequency increases during subthreshold stimulations in the absence of movement in n=11 mice. Data in all graphs are mean ± SD. Wilcoxon matched-pairs tests are used to compare conditions. ns, not significant. *, p<0.05. **, p<0.01. ***, p<0.001. ****, p<0.0001.

initiation (Figure S3A-D). Importantly, in trials that effectively engage forward locomotion, we observed an increased respiratory rate (Figure 3B, C). In what we consider a remarkable observation, during CnF photo-activations, respiratory rate increased in a two-step sequential manner. In a first step, that we term the "pre-loco" phase, a modest increase was seen immediately at light onset but before the first locomotor movements (i.e., during the latency between light onset and the initiation of locomotion, Figure 3D). The mean respiratory rate during this "pre-loco" phase was found significantly higher than baseline but was not correlated to the CnF stimulation frequency nor to the displacement speed eventually adopted by the animal (Figure 3E). In a second step, when the animal effectively engage in locomotion ("loco" phase) the average respiratory rate was further augmented (Figure 3D, F). There, respiratory rate was still not strongly dependent on stimulation frequency, however it was partly proportional to the actual displacement speed (R^2 = 0.23, Figure 3F). This likely reflects the variability of locomotor velocities at a given stimulation frequency (Figure S3B). Altogether, these results indicate that respiratory frequency during CnF-evoked locomotion is 1) upregulated immediately at light onset and before the initiation of locomotion, and 2) further upregulated during actual locomotion in a somewhat speed-dependent manner.

These data suggest that Glut+ CnF neurons can modulate respiratory activity independently of their action on limb movements, in line with what was reported in the lamprey (Gariepy et al., 2012). To demonstrate this further, we reduced the intensity of photo-stimulations by bringing down the frequency of light pulses onto CnF Glut+ neurons to 5 and 10 Hz at which locomotion initiation failed (Figure 3G, Figure S3B). We found that, in spite of absent locomotor movements, the respiratory frequency could indeed be significantly increased from baseline (CTL 3.6 ± 0.6 bursts/s; 5 Hz: 6.2 ± 1.4; 10 Hz: 6.7 ± 1.6 bursts/s, Figure 3H). These values are in keeping with those reached above during the "pre-loco" phase. Altogether, these analyses demonstrate that i) Glut+ CnF neurons can upregulate breathing before, or even in the absence of, locomotor movements, ii) during CnF-evoked locomotion, the highest increase in breathing rate from rest occurs when actual locomotor movements are engaged, and iii) respiratory frequency increases during the "loco" phase are partly proportional to the displacement speed.

The spinal locomotor circuits project to the parafacial respiratory region.

From the above observation we reasoned that the engagement in actual locomotor movements may be associated with a stronger activating drive onto respiratory centers which could originate in executive lumbar locomotor circuits. We thus examined the ascending projections to the brainstem of glutamatergic lumbar neurons that are essential in the regulation of locomotor speed (Kjaerulff and Kiehn, 1996; Hagglund et al., 2010; Hagglund et al., 2013; Talpalar et al., 2013). To do so, we injected a Cre-dependent AAV-eYFP vector bilaterally in the ventral laminae of the 2nd lumbar segment (L2) of adult *Vglut2-Cre* animals (Figure 4A, B) and examined projections in the brainstem reticular formation. In contrast to the anterograde tracings from the CnF, this revealed very few, if any, eYFP-positive fibers in the anatomical area of the preBötC (Figure 4C, D) but their abundant presence in the parafacial respiratory region, defined as layers of neurons ventral and medial to the facial motor nucleus (Figure 4E, F). Ascending projections were also detected in the lateral parabrachial nucleus, the NTS and the lateral reticular nucleus (LRt, Figure S4A-C). To discriminate passing fibers from putative synaptic contacts, we performed similar spinal injections this time with a high-titer AAV coding the Cre recombinase (AAV1-Syn-Cre, (Zingg et al., 2017)), on wild-type mice. This vector has been previously shown to be transported anterogradely down the axon and to enable expression of the Cre-recombinase in postsynaptic target neurons that then are amenable to visualization through Cre-dependent transgene expression. We therefore injected, one week after the first viral injection a Cre-dependent AAV-eYFP vector in the parafacial respiratory region by stereotaxy. This led to numerous eYFP-expressing cells (Figure 4G, H). Since this region does not project to the lumbar spinal cord (Figure S4D, E), the Cre-dependent labelling cannot owe to spurious retrograde

transport of the AAV1-Syn-Cre virus. Therefore, ascending spinal projections synaptically target the parafacial respiratory region.

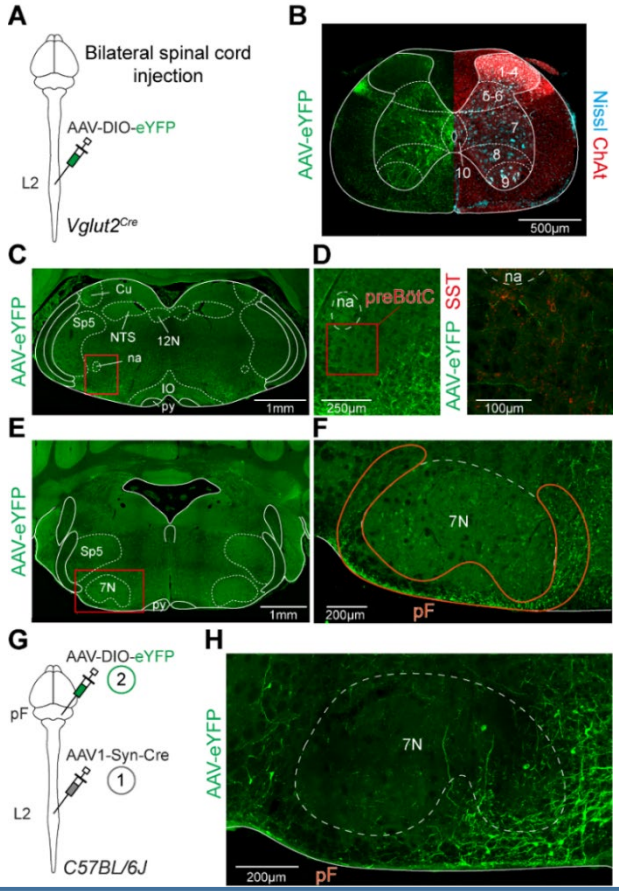

Figure 4: Ventral glutamatergic lumbar neurons contact the parafacial respiratory region. (A) An AAV-DIO-eYFP was injected in the 2nd lumbar spinal segment (L2) in a *Vglut2*^{Cre} mouse line. **(B)** Low magnification of the spinal cord, at the level of the injection site, showing glutamatergic ventral eYFP^{+} interneurons restricted to ventral laminae, delineated using Nissl and ChAT staining. **(C)** Low magnification at the level of the preBötC showing anterograde projections from the spinal cord. **(D)** Left, magnification of the red rectangle in **C**. The preBötC area is highlighted in red. Note the absence of projections from the spinal cord. Right, high magnification of the preBötC area identified by somatostatin staining (SST). **(E)** Low magnification showing spinal projections at the level of the parafacial respiratory region (pF). **(F)** Magnification of the red rectangle in **E**. Note the eYFP^{+} green projections from the spinal cord in the pF region. **(G-H)** Trans-neuronal anterograde tracing from the lumbar ventral spinal cord. **(G)** Schematics of the bilateral injection of an AAV1-Syn-Cre in L2 and an AAV-DIO-eYFP in the pF in a *C57BL/6J* mouse. **(H)** High magnification at the level of the pF, showing post-synaptic neurons. *Cu, Cuneate nucleus. 12N, Hypoglossal nucleus. See Figure 1 for abbreviations of brain structures.*

Lumbar locomotor circuits upregulate breathing through the RTN$^{Phox2b/Atoh1}$ *ex vivo*.

To investigate functionally the possibility that lumbar locomotor circuits can upregulate breathing, we used the *ex vivo* isolated brainstem/spinal cord preparation from neonatal mouse. Although long-used for monitoring locomotor (Kjaerulff and Kiehn, 1996; Bouvier et al., 2015) or respiratory-like (Bouvier et al., 2010; Ramanantsoa et al., 2011b) activities, monitoring both simultaneously using pharmacological activation of the lumbar CPG had only been achieved on neonatal rat preparations (Le Gal et al., 2014; Le Gal et al., 2020). We adapted the method to neonatal mice and used a split-bath allowing independent pharmacological manipulation of the brainstem and spinal cord superfused by artificial-cerebrospinal fluid (a-CSF, see methods). In these conditions, we recorded respiratory-like activity recorded on the 4th cervical root and locomotor-like activity on the 2nd lumbar ventral rootlet (Figure 5A, B).

When both the brainstem and spinal cord were superfused with their respective control a-CSF solution, the frequency of respiratory-like activities was found to be very variable across animals, ranging from 2.5 to 8.3 bursts/min, with an average of 4.3 ± 1.6 bursts/min. Bath-application of the neuroactive substances N-methyl-D-aspartate (NMDA) and serotonin (5-HT) in the spinal cord compartment evoked locomotor-like activities associated with an increased frequency of the respiratory-like activity (7.2 ± 3.6 bursts/min, 162 ± 30 % of baseline, Figure 5B, C). Reminiscent of what we observed in freely running mice (Hérent et al., 2020), we found that respiratory- and locomotor-like activities were not temporally synchronized (data not shown). To rule out drug leakage from the spinal compartment we first verified that this frequency increase of respiratory-like activities was abolished following a cervical trans-section of the medulla (Figure S5A-C). We also examined respiratory changes following the engagement of locomotor-like activities by targeted optogenetic activations of lumbar excitatory neurons (*Vglut2-*

Cre;floxedChR2), in the absence of NMDA and 5-HT (Hagglund et al., 2010; Hagglund et al., 2013; Le Gal et al., 2020). In this optogenetic paradigm, the frequency of inspiratory activity was increased similarly to the pharmacological-induced locomotion (170 ± 38 % from baseline, Figure S5D-F). Altogether, these experiments indicate that the lumbar spinal segments containing the locomotor CPG exert an excitatory effect on respiratory activity.

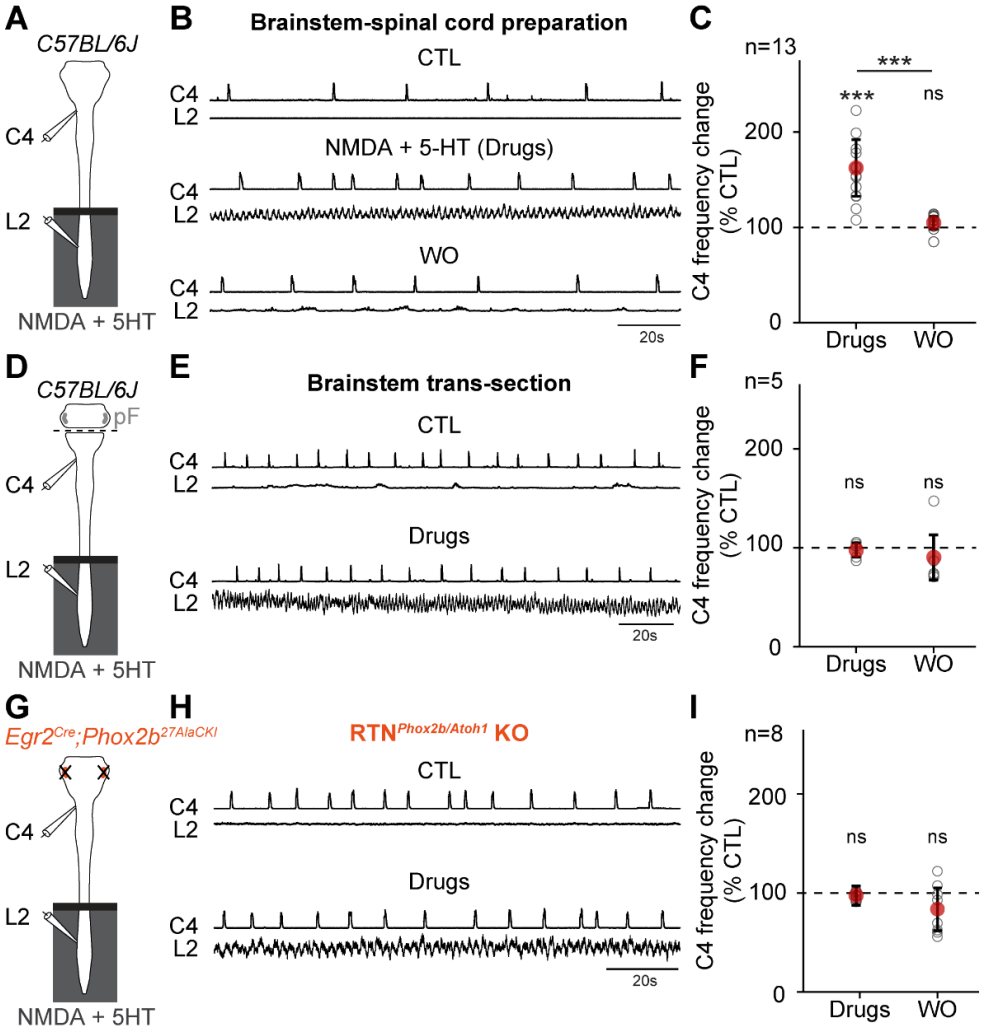

Figure 5: Activation of the lumbar spinal cord increases the frequency of in inspiratory-like frequencies *ex vivo*, which requires the RTN$^{Phox2b/Atoh1}$. (A) Schematics of an isolated *ex vivo* brainstem-spinal cord preparation from *C57BL/6J* neonates (1-2 days), continuously superfused with oxygenated artificial cerebrospinal fluid (aCSF). Respiratory- and locomotor-like activities are recorded using suction electrodes on the 4th cervical (C4) and the 2nd lumbar (L2) motor nerve roots, respectively. The preparation is separated in two compartments using a Vaseline barrier (black bar) to allow the lumbar spinal cord to be superfused with control aCSF of drugs-enriched aCSF (NMDA and 5-HT, gray rectangle). **(B)** Recordings of C4 and L2 activities of one representative animal before (CTL), during (Drugs) and after (WO) perfusion of NMDA and 5-HT in the lumbar spinal cord compartment. Note that perfusion of locomotor drugs in the lumbar spinal cord triggers locomotor-like activity on L2 and elicits a concomitant increase in C4 respiratory frequency. **(C)** Graph showing C4 frequency change normalized to the control condition (CTL) during drug-induced locomotor-like activity (Drugs) and during drugs washout (WO) in n=13 mice. **(D-F)** Similar experiments as in **A-C** but a brainstem trans-section was performed to physically remove the parafacial respiratory region (pF) from the preparations. Note the absence of increase in C4 respiratory frequency during drugs perfusion in n=5 mice. **(G-I)** Similar experiments as in **A-C** were performed in *Egr2^{Cre};Phox2b^{27AlaCKI}* mouse line to genetically delete RTN neurons having co-expressed *Phox2b* and *Atoh1* (i.e., the RTN$^{Phox2b/Atoh1}$). Note that the elimination of the RTN$^{Phox2b/Atoh1}$ is sufficient to abolish the drug induced-C4 frequency increase in n=8 mice. Data in all graphs are mean ± SD. Wilcoxon matched-pairs tests are used to compare conditions. ns, not significant. ***, p<0.001.

Since our anatomical observations place the parafacial respiratory region as a candidate target of ascending pathways from the spinal cord, we next addressed the functional contribution of this region. In a first set of experiments, we eliminated physically the parafacial respiratory region by a complete trans-section below the facial motor nucleus (Figure 5D). Respiratory-like activities persisted on the 4th cervical root, but pharmacological activation of lumbar circuits was no longer capable of significantly upregulating their frequency (Figure 5E, F). In a second set of experiments, we examined specifically the contribution of RTN neurons in the parafacial region (Abbott et al., 2009; Abbott et al., 2011). For this we made use of the fact that RTN neurons relevant for modulating respiratory rhythm generation, at least in the context of central chemoception, are i) best identified by their combined history of expression of the transcription factors *Phox2b* and *Atoh1* during embryogenesis (thereafter RTN$^{Phox2b/Atoh1}$ neurons, (Ramanantsoa et al., 2011b; Ruffault et al., 2015)) and ii) can be deleted when expressing a mutated allele of PHOX2B (*Phox2b*^{27Ala}) in rhombomeres 3 and 5 (*Egr2-cre;Phox2b*^{27AlaCKI} mutants, Figure S5G, H, (Ramanantsoa et al., 2011b; Ruffault et al., 2015)). We thus generated RTN mutant pups and recorded respiratory- and locomotor-like activities as above. Preparations showed persistent inspiratory-like activity on the C4 root, but pharmacological activation of lumbar circuits was no longer capable of significantly upregulating its frequency (Figure 5G-I). These experiments altogether highlight the capacity of spinal lumbar circuits to upregulate respiratory-like activities through RTN$^{Phox2b/Atoh1}$ neurons in the parafacial respiratory region.

Silencing RTN$^{Phox2b/Atoh1}$ neurons reduces respiratory increase during running exercise *in vivo*

The importance of RTN$^{Phox2b/Atoh1}$ neurons revealed above on *ex vivo* neonatal preparations prompted to address their contribution to respiratory activity during running in behaving adult mice. For this, we used the *Atoh1-FRTCre;Phox2b-Flpo* intersectional background, i.e., in which Cre-expression from the *Atoh1* locus is conditional to Flpo expression driven by the *Phox2b* locus (Ruffault et al., 2015), and injected in the parafacial region bilaterally a Cre-dependent AAV coding the inhibitory DREADD receptor hM4Di (Figure 6A, B). Three weeks later, animals underwent the chronic implantation of diaphragmatic EMG electrodes (Hérent et al., 2020). Inspiratory frequency was then measured before, and 2-3 h after, the administration of the DREADD ligand Clozapine-N-Oxide (CNO, 10 mg/Kg) while animals were at rest or running at a set frequency on a motorized treadmill.

At rest, we found that CNO administration had no significant effect on the mean inspiratory frequency (Figure 6C, D), supporting previous findings that the RTN only minimally contributes to setting the baseline breathing rate (Korsak et al., 2018). When animals were made to run for 1.5 min at a velocity of 40 cm/s set by the treadmill, they presented with augmented respiratory frequency (from 3.85 ± 0.2 bursts/s at rest to 10.4 ± 1.1 bursts/s, which represents a 271 % increase, Figure 6E, F). We have recently reported that this value is characteristic of running mice on a treadmill, regardless of the trotting speed (Hérent et al., 2020). Following CNO administration, while animals were still capable to run at 40 cm/s for 1.5 min, their breathing rate was significantly reduced when compared to controls (8.4 ± 1.2 bursts/s, which represents a 227 % augmentation from rest, Figure 6E, F). Administration of saline in hM4Di-injected mice, or CNO on wild-type mice did not significantly reduce breathing rate (Figure S6). These experiments altogether indicate that the activity of RTN$^{Phox2b/Atoh1}$ neurons is required for setting the adapted ventilatory frequency during running exercise.

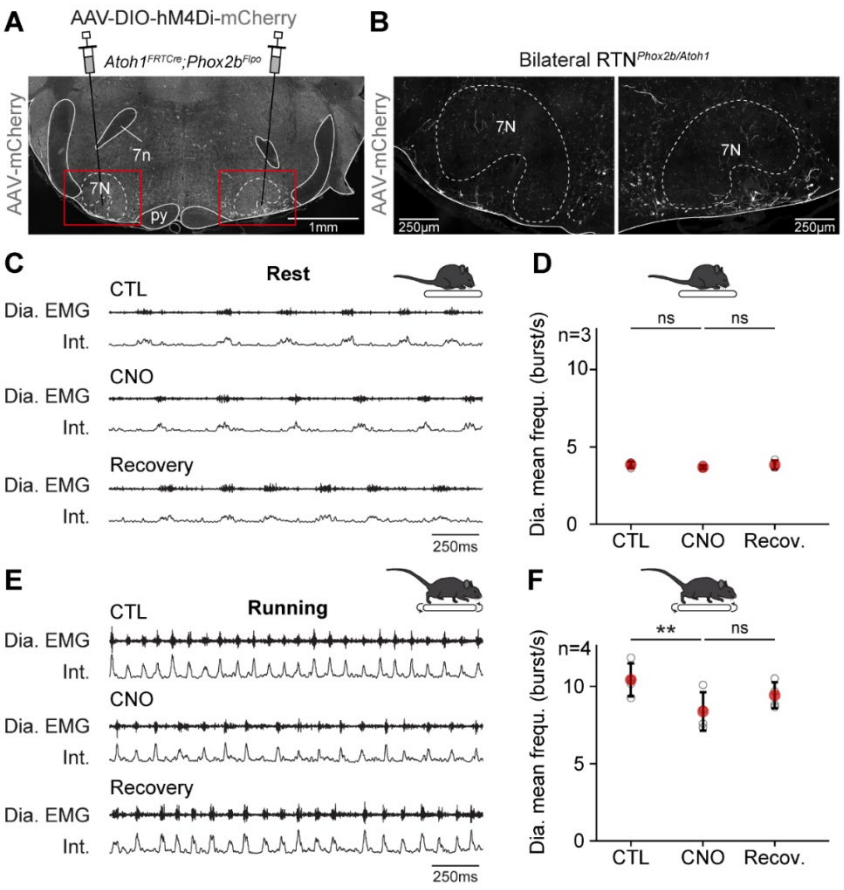

Figure 6: Chemical silencing of the RTN$^{Phox2b/Atoh1}$ impairs running-induced increase in respiratory frequency. (A) Low magnification at the level of the injection site, showing the bilateral RTN$^{Phox2b/Atoh1}$ neurons transfected with an AAV-DIO-hM4Di-mCherry in an *Atoh1^{FRTCre};Phox2b^{Flpo}* mouse line. **(B)** High magnifications of the bilateral transfected RTN$^{Phox2b/Atoh1}$ cells (red rectangles in **A**). **(C)** Raw (Dia. EMG) and integrated (Int.) recordings of the diaphragm activity of one representative animal at rest before (CTL), during (CNO) and after (Recovery) intraperitoneal injection of the agonist CNO (10 mg/kg). **(D)** Graph showing the diaphragm mean frequency change before (CTL), during (CNO) and after (Recov.) injection of CNO in n=3 mice at rest. Note that silencing the RTN$^{Phox2b/Atoh1}$ does not alter breathing frequency at rest. **(E, F)** Similar representations as in **C**, **D** in n=4 mice running on a treadmill. Note the reduction in diaphragm frequency during CNO injection. Data in all graphs are mean ± SD. Paired t-test and Wilcoxon matched-pairs test are used to compare conditions in **D** and **F,** respectively. ns, not significant. **, p<0.01. *7n, Facial nerve. See Figure 1 for all other abbreviations.*

RTN$^{Phox2b/Atoh1}$ neurons project to the preBötC generator

The reduced breathing rate following the silencing of RTN$^{Phox2b/Atoh1}$ neurons suggests that this genetically defined neuronal subset may have access to the main inspiratory generator, the preBötC. While the parafacial region was previously shown to send axonal projections to the ventral respiratory column and possibly the preBötC (Smith et al., 1989; Li et al., 2016), this had not been determined for RTN$^{Phox2b/Atoh1}$ neurons. We therefore injected, in the parafacial region using the *Atoh1-FRTCre;Phox2b-FlpO* mouse background a Cre-dependent AAV vector coding a synaptic eYFP (AAV-DIO-syn-eYFP, Figure 7A). We found eYFP puncta, i.e., putative synaptic contacts, in the preBötC (Figure 7B) as well as in other respiratory-related nuclei, including the lateral parabrachial nucleus, the ventral respiratory group and the NTS (Figure S7A-G). To demonstrate functionally the capacity RTN$^{Phox2b/Atoh1}$ neurons to directly modulate rhythm generation mechanisms in the preBötC, we delivered the ChR2 unilaterally in the parafacial area and examined respiratory responses to short single-pulse (50 ms) photo-activations with the same analytic tools described earlier for CnF activations (Figure 7C-D). We found that unilateral photo-stimulation of

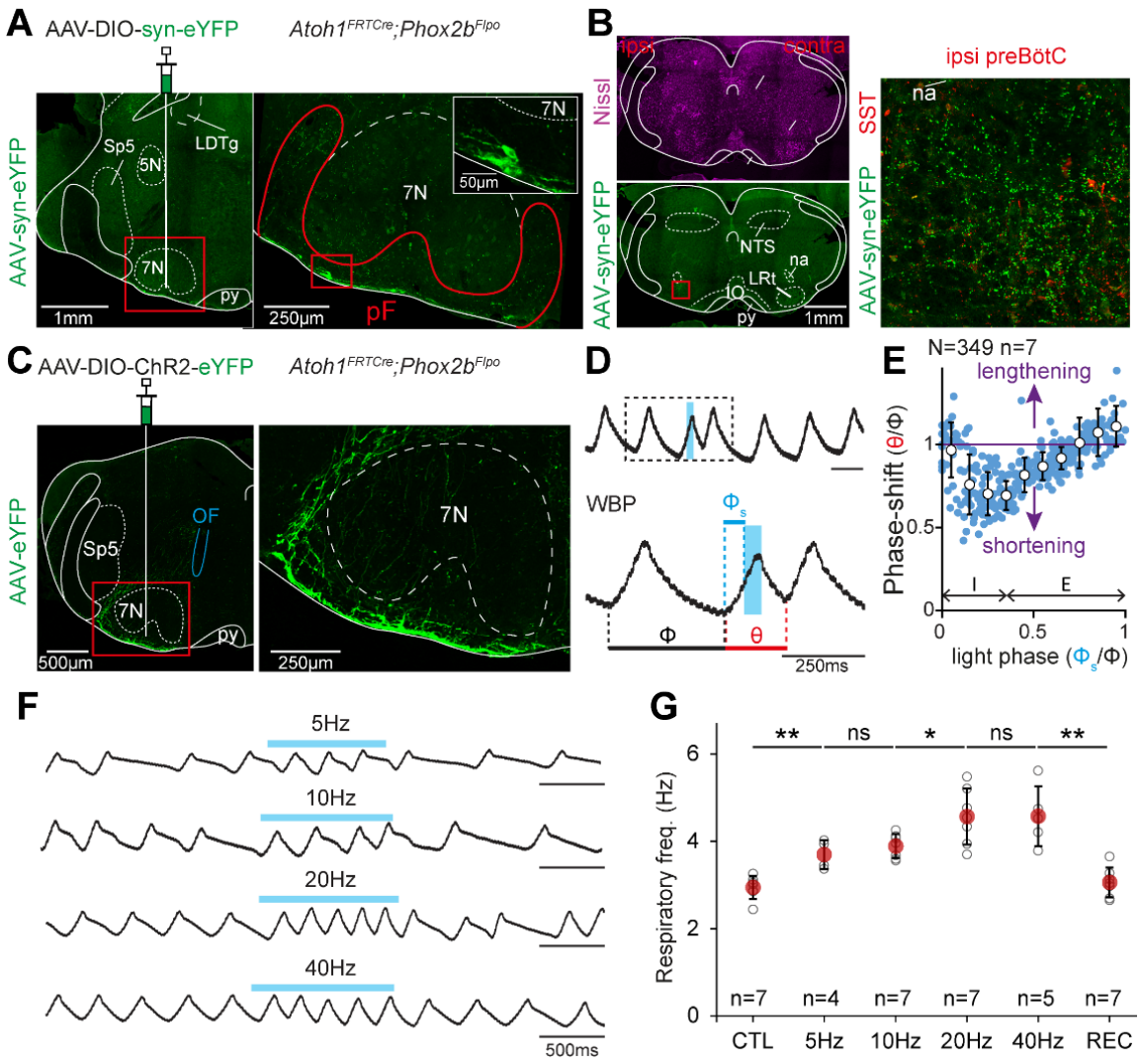

Figure 7: The RTN$^{Phox2b/Atoh1}$ contacts the preBötC and impacts respiratory rhythm generation. (A) Left, low magnification at the level of the parafacial respiratory region (pF), showing RTN$^{Phox2b/Atoh1}$ neurons transfected with an AAV-DIO-syn-eYFP in an *Atoh1^{FRTCre};Phox2b^{Flpo}* mouse. Right, high magnification of the infected RTN$^{Phox2b/Atoh1}$ (red rectangle in the left picture). Top right, Magnification of the area framed in red, showing the syn-eYFP^{+} infected cells. **(B)** Left, low magnification at the preBötC level. Top, Nissl staining. Bottom, localization of the syn-eYFP^{+} putative synapses. Right, high magnification of the putative synapses from the RTN$^{Phox2b/Atoh1}$ in the preBötC, identified by somatostatin staining (SST). Note the abundant putative synapses in the ipsilateral preBötC. **(C)** Left, low magnification at the level of the injection site an optic fiber implantation (OF, blue), showing the RTN$^{Phox2b/Atoh1}$ neurons transfected with an AAV-DIO-ChR2-eYFP in an *Atoh1^{FRTCre};Phox2b^{Flpo}* mouse. Right, magnification of the infected RTN$^{Phox2b/Atoh1}$ (red rectangle in the left picture), showing the eYFP^{+} cells. **(D)** Whole body plethysmography (WBP) recordings of respiratory cycles while a 50 ms pulse stimulation of the RTN$^{Phox2b/Atoh1}$ (blue rectangles) is applied. Top, one example of the light pulse occurring during the inspiratory phase of one respiratory cycle. Note that the light pulse precipitates a new cycle. Bottom, magnification of the top trace showing parameters used in **E**: the perturbed cycle (θ, red), the control cycle (ϕ, black) and the light cycle (ϕ_s, blue). **(E)** Plot of the phase-shift (perturbed cycle normalized to the control cycle: θ/ϕ) as a function of the light phase (light cycle normalized to the control cycle: ϕ_s/ϕ). Inspiration (I) and expiration (E) mean durations are annotated on the graph. A shortening of the perturbed cycle happens when values are under 1 (purple line) and a lengthening occurs when values are over 1. Note that the perturbed cycle shortening starts in inspiration. Also, the perturbed cycle is lengthened at the end of expiration. N=349 random trials, n=7 mice. **(F)** Whole body plethysmography recordings at different RTN$^{Phox2b/Atoh1}$ stimulation frequencies (5-10-20-40 Hz, blue bars). **(G)** Graph showing the respiratory frequency change before (CTL), during (5-40 Hz) and after (REC) RTN$^{Phox2b/Atoh1}$ stimulations. Data are mean ± SD. Mann-Whitney U-tests are used to compare conditions. ns, not significant. *, p<0.05. **, p<0.01. *LDTg, Lateral dorsal tegmentum. 5N, Trigeminal motor nucleus. See Figure 1 for all other abbreviations.*

RTN$^{Phox2b/Atoh1}$ neurons could elicit an ectopic inspiratory burst and shorten the respiratory cycle. However, when compared to CnF photostimulation, shortenings of the respiratory peaked earlier during the inspiration phase (phase 0.2-0.3 and 0.3-0.4, phase shift: 0.70 ± 0.13 and 0.69 ± 0.09, p<0.0001 Figure 7D, E) and, contrary to the CnF, stimulation of the RTN during late expiration caused a significant lengthening of the respiratory cycle (phases 0.9-1, phase shift: 1.11 ± 0.12, p=0.0004). Again, as expected from access to the preBötC rhythm generator, a clear resetting of the rhythm ensued without effect on the period of subsequent cycle following the stimulus (Figure S7H-K). Finally, 1 s pulsed-light stimulations of the RTN$^{Phox2b/Atoh1}$ neurons resulted in significant augmentations of respiratory frequency during the stimulus (Figure 7F-G). Altogether, these results demonstrate that the genetically defined subset of RTN neurons co-expressing *Phox2b* and *Atoh1* can upregulate respiratory rate through direct projections to the preBötC. Interestingly, the phase-dependent shortening (in inspiration) and lengthening (in late expiration) observed from RTN stimulations are reminiscent of those reported when photo-stimulating inhibitory preBötC neurons (Baertsch et al., 2018). This suggests that RTN$^{Phox2b/Atoh1}$ and CnF locomotor-related drives may also differ by their targeting of a distinct balance of excitatory versus inhibitory preBötC neurons.

Discussion

A neuronal substrate for hyperpnea during running has long been proposed but its underlying cells and circuits had remained speculative. We uncover here two systems by which the central locomotor network can enable respiratory rate to be augmented in relation to running activity. On the one hand, we demonstrate the capacity of the MLR subnucleus CnF, a conserved locomotor controller across the vertebrate phylum (Shik et al., 1969; Dubuc et al., 2008; Le Ray et al., 2011; Bachmann et al., 2013; Roseberry et al., 2016; Caggiano et al., 2018; Josset et al., 2018), to upregulate breathing. On the other hand, we also demonstrate that the lumbar enlargement of the spinal cord, containing the hindlimb CPG, also acts as a potent upregulator of breathing rate. Using cell-type specific circuit tracing, we further characterize both locomotor drives by identifying their distinct neuronal targets in the respiratory network.

Multiple locomotor drives set respiratory rhythm frequency

One intriguing feature we observed with CnF stimulations is that respiratory rate is upregulated before the engagement of effective locomotor movements, or for stimulations intensities that are below the threshold for locomotor initiation. This may reflect that the CnF has direct access to the inspiratory rhythm generator (Figures 1, 2), while its action on the limb controller requires the crossing of multiple synapses, including onto reticulospinal neurons (Jordan et al., 2008; Capelli et al., 2017; Caggiano et al., 2018), as manifested by the typical 100 to 300 ms latency from light onset to locomotor movements. The regulation of breathing from the CnF in the absence of locomotor movements may bear physiological relevance as an anticipatory mechanism to the planned motor action. In the lamprey, spontaneous swimming bouts are preceded by a marked increase in respiratory frequency, an effect that may incriminate the MLR (Gravel et al., 2007; Gariepy et al., 2012). Men informed of an upcoming exercise also show increased ventilation and cardiovascular responses before movement onset, albeit less drastically than during the actual movements (Krogh and Lindhard, 1913; Tobin et al., 1986; Green et al., 2007), reminiscent of the “pre-loco” phase resulting here from CnF stimulations (Figure 3). The mere mental imagination of performing exercise also suffices to increase breathing rate (Decety et al., 1991; Decety et al., 1993; Thornton et al., 2001; Williamson et al., 2001). Interestingly, the CnF subcomponent of the MLR is associated with escape-like fast regime running, rather than exploratory locomotion (Caggiano et al., 2018; Josset et al., 2018) and may be part of a larger command system for defensive behaviors in the broad sense (Mitchell et al., 1988a; Depoortere et al., 1990; Korte et al., 1992; Ryczko and Dubuc, 2013). It may therefore bear output connectivities allowing to engage a composite response with both cardiovascular (Mitchell et al., 1988b; Korte et al., 1992), respiratory (this study and (Gariepy et al., 2012)), and if needed, locomotor components. A higher threshold and longer latency for the latter would ensure sufficient

priming of relevant autonomic respiratory and cardiovascular controls. Interestingly, data in the lamprey indicate that locomotor and respiratory centers are not contacted by the same individual MLR neurons with branched collaterals but rather by distinct subtypes (Gariepy et al., 2012). Pending an equivalent examination in mice, it is possible that the MLR may, similarly to other descending motor pathways (Sathyamurthy et al., 2020; Usseglio et al., 2020) host projection-defined subsets that each control one trait of a multi-faceted adaptive response.

We also report the existence of a respiratory-modulatory drive from the lumbar spinal segments that contains the hindlimb locomotor circuits supporting ongoing locomotion (Kiehn, 2016). Such an ascending drive, previously suggested in rats (Le Gal et al., 2014; Le Gal et al., 2020) is demonstrated here in mice by local pharmacological (Figure 5) or optogenetic (Figure S5) activations of the lumbar enlargement on reduced preparations *ex vivo.* Indeed in these, the absence of the MLR and of peripheral structures, as well as the experimental control of the extracellular solution allows to isolate the functional contribution of a spinal ascending drive from descending, peripheral feedbacks and central chemoceptive ones. Since the activity of the spinal locomotor circuits is proportional to locomotor speed (Talpalar and Kiehn, 2010), it is possible that this ascending drive continuously informs supra-spinal structures including respiratory centers (this study, see also (Le Gal et al., 2014)) on the state of ongoing locomotion. We thus propose that active locomotor executive circuits are, at least partly, causal to the further increase of respiratory rate seen when animals engage in locomotion (i.e., the "loco" phase) following CnF stimulations. In support of this, we show *ex vivo* that respiratory-like activity rates are no longer upregulated by engagement of locomotor-like activity after elimination of the RTN $^{Phox2b/Atoh1}$ (Figure 5). However, acute silencing of the RTN $^{Phox2b/Atoh1}$ neurons *in vivo* reduces, but does not completely prevent, the capacity to accelerate breathing during treadmill running (Figure 6). This could owe to the relative efficiency of the chemogenetic inhibition strategy (i.e., variable levels of expression of DREADDS receptors in transfected neurons) only partially reducing neuronal activity. Alternatively, the residual respiratory increase may reflect persistent activity of CnF neurons, and therefore of excitatory drive on the preBötC, during a running episode (Caggiano et al., 2018). This leaves open the possibility that, during ongoing running, the two locomotor drives, i.e., from the CnF and the lumbar spinal cord, may synergize to set the respiratory frequency.

Our results also do not speak to the possible involvement of other central locomotor descending pathways (Jordan et al., 2008) whose contribution will remain to be investigated. However, the absent phasing between respiratory and locomotor drives or movements reported previously during treadmill running (Hérent et al., 2020) together with the persistence of a normal ventilatory response to exercise following the removal of peripheral signals in multiple species (Eldridge et al., 1981; Eldridge et al., 1985; Fernandes et al., 1990), make it very unlikely that phasing signals arising from proprioceptive limb afferences or sensory modalities reporting visceral oscillations are important components of the respiratory adaptation to exercise.

Different respiratory nodes integrate distinct locomotor drives

Another intriguing observation is that the two revealed locomotor drives target different nuclei in the rhythm generating respiratory network. The CnF connects to the preBötC, the main site of inspiratory rhythm generation (Smith et al., 1991; Del Negro et al., 2018), while the lumbar CPG rather contacts the parafacial respiratory region, and possibly the RTN$^{Phox2b/Atoh1}$ previously implicated in central chemoception (Abbott et al., 2009; Abbott et al., 2011; Ramanantsoa et al., 2011a; Ruffault et al., 2015). For the former, the connectivity is first demonstrated anatomically by the detection of anterograde fibers and a trans-neuronal labelling approach initiated from preBötC neurons (Figure 1). Transposing this trans-neuronal strategy to RTN$^{Phox2b/Atoh1}$ neurons however led to no labelling aside the starter cells. This inconclusive result may owe to the suboptimal expression of the rabies glycoprotein with our intersectional background, or to synaptic connections onto the RTN being more refractory to rabies transfer. Therefore, while our anterograde labelling from the CnF only showed little projections in the parafacial respiratory region, in line with other reports (Caggiano et al., 2018), we cannot firmly exclude some contacts especially

if remote from neuronal somata. Regarding the identity of the preBötC neurons targeted by the CnF, our analysis advocate for outputs onto glutamatergic neurons, considered as the essential drivers of inspiratory rhythm (Cui et al., 2016; Del Negro et al., 2018). First, CnF neurons are detected when initiating a trans-neuronal labelling from glutamatergic preBötC neurons. Secondly, the capacity of short CnF photo-stimulations to shorten the respiratory cycle when delivered at a specific time within the respiratory cycle (Figure 2) are reminiscent to that observed when directly stimulating glutamatergic preBötC neurons collectively (Baertsch et al., 2018) or the *Dbx1*-expressing V0 subset (Cui et al., 2016, Baertsch et al., 2018), the main rhythmogenic candidates (Bouvier et al., 2010; Gray et al., 2010). Since *Dbx1* expression is, similar to most transcription factors used to delineate cardinal neuronal classes (Jessell, 2000), downregulated in the adult (Pierani et al., 2001), dedicated strategies to prolong the *Dbx1* conditionality will be needed to confirm the identity of targeted preBötC neurons in adult mice (Pivetta et al., 2014).

In contrast, we found that ascending projections from the lumbar spinal cord were virtually absent in the preBötC but were dense in the parafacial respiratory region (Figure 4) in an area compatible with that of the RTN. The synaptic nature of these projections was ascertained using an AAV vector that has the capacity to deliver the Cre recombinase to post-synaptic partners (Figure 4G, H, (Zingg et al., 2017)). The functionality of these ascending projections and the identity of their neuronal targets were evaluated here by loss of function experiments. Specifically, certainly the best defined RTN neurons are those characterized by a history of co-expression of *Phox2b* and *Atoh1* (Ramanantsoa et al., 2011b; Ruffault et al., 2015). Remarkably, the selective demise of RTN$^{Phox2b/Atoh1}$ neurons totally abolished the acceleration of respiratory-like activities associated with pharmacological activation of the lumbar spinal cord, *ex vivo* (Figure 5). Therefore, while other parafacial respiratory neurons as well as neighboring adrenergic C1 neurons (Abbott et al., 2011; Guyenet et al., 2013) may also be targeted by the locomotor spinal circuits, the RTN$^{Phox2b/Atoh1}$ subset may be the prominent integrator of the ascending locomotor drive, at least for the setting of respiratory frequency. As discussed above, that their silencing *in vivo* only reduces, but does not completely prevent, the capacity of breathing to accelerate during running (Figure 6) could reflect a too partial reduction of neuronal activity or the additive effect of concomitant spinal cord and CnF drives. Finally, our results indicate that the capacity of RTN$^{Phox2b/Atoh1}$ neurons to upregulate breathing frequency may be supported by their direct projections to the preBötC (Figure 7).

Limitations

While our work reveals important features of respiratory regulation in the mouse model, and highlights some of its constituent cellular actors, others remain to be investigated. Our results notably do not speak to the identity of spinal neurons that support the ascending drive. Spinal V2a neurons (i.e., *Chx10*-expressing) stood as key candidates, by virtue of their glutamatergic nature and involvement in rhythm generation (Dougherty and Kiehn, 2010a, b; Dougherty et al., 2013). However, we previously found that only the cervical V2a neurons project to the brainstem (Usseglio et al., 2020) but not the lumbar ones (data not shown). V0$_V$ and V3 spinal interneurons, expressing respectively *Evx1* and *Sim1*, should next be considered. In the same line, while our anatomical and functional investigations demonstrate that both the CnF and the RTN$^{Phox2b/Atoh1}$ project to the preBötC, the exact identity of targeted neurons remains to be elucidated. Intriguingly however, we observed that the capacity of RTN$^{Phox2b/Atoh1}$ stimulations to trigger an ectopic inspiratory burst is more efficient in inspiration while that of the CnF in early expiration (compare Figure 2D, G with Figure 7E). Furthermore, a significant lengthening of the respiratory cycle is observed when photo-activations are delivered in late expiration to the RTN$^{Phox2b/Atoh1}$, but not to the CnF. This permissive action in inspiration and the lengthening in expiration recalls what others have reported when specifically activating inhibitory, but not excitatory, preBötC neurons (Baertsch et al., 2018). This leaves open the possibility that the RTN$^{Phox2b/Atoh1}$ and the CnF might preferentially target different cell-types in the preBötC: inhibitory neurons for the former, and glutamatergic ones for the latter. Note that such a RTN bias towards contacting inhibitory preBötC neurons could explain its absent labeling following retrograde trans-neuronal tracing using preBötC glutamatergic neurons as entry points (Figure 1G-I, Figure S1I, J). Although our data are compatible with such a working model, the proposed connectivity will need

to be investigated directly by future work. Finally, while changes in breathing frequency are a major substrate of increased minute ventilation, further adjustments can be achieved by changes in tidal volume. Admittedly, our diaphragmatic EMG recordings only reliably report the former. It would therefore be important to measure additional respiratory parameters and/or accessory respiratory muscles that can support changes in tidal volume (Sieck and Gransee, 2012) in response to targeted activations of the CnF, the RTN$^{Phox2b/Atoh1}$, and the lumbar spinal cord. This might underscore specific actions of each modality on different traits of respiratory rhythm and pattern formation.

Material and methods

Mice

C57BL/6J wild-type mice were obtained by Janvier Labs (Le Genest-Saint-Isle, France). VGlut2-IRES-Cre animals (therefafter *Vglut2-Cre*, (Vong et al., 2011) and *Ai32(RCL-ChR2(H134R)/EYFP) (*thereafter *floxedChR2, (*Madisen et al., 2012*)*) were obtained from Jackson Laboratories. To manipulate *Phox2b/Atoh1*-expressing RTN neurons we used the following mouse lines: *Egr2-Cre* (Voiculescu et al., 2000) crossed with *Phox2b*^{27AlaCKI} (Ramanantsoa et al., 2011b) and *Atoh1-FRTCre;Phox2b-Flpo* (Ruffault et al., 2015) mouse lines. Animals were group-housed with free access to food and water in controlled temperature conditions and exposed to a conventional 12-h light/dark cycle. Experiments were performed on animals of either sex, aged 2 to 3 months at the time of first injection. All procedures were approved by the French Ethical Committee (authorization 2020-022410231878) and conducted in accordance with EU Directive 2010/63/EU. All efforts were made to reduce animal suffering and minimize the number of animals.

Viruses used

For anterograde tracing and photostimulation of the CnF and its projection in the preBötC, we used a Cre-dependent AAV9-Ef1a-DIO-hChR2(E123T/T159C)-eYFP (Addgene #35509, titer 7.7e12vp/ml (Mattis et al., 2011)) unilaterally in the CnF (70 to 100 nL). For anterograde tracing from the lumbar spinal cord, the same virus was injected bilaterally (600-750 nL each side) in the lumbar segment, and for RTN$^{Phox2b/Atoh1}$ photostimulation, the injection was unilateral (350-400 nL). For reversible silencing of RTN$^{Phox2b/Atoh1}$ neurons we used bilateral injections (400 nL each side) of an AAV8.2-hEF1a-DIO-hM4Di-mCherry-WPRE obtained from Dr. Rachael Neve (Gene Delivery Technology Core, Massachusetts General Hospital, USA, titer: 5.6e12). For transsynaptic labelling of inputs onto preBötC neurons, we used 500 nL of a HSV1-hEF1a-LS1L-TVA950-T2A-rabiesOG-IRES-mCherry obtained from Dr. Rachael Neve (Gene Delivery Technology Core, Massachusetts General Hospital, USA), and 200 nL of EnvA-ΔG-rabies-GFP obtained by the GT3 core (Salk Institute, USA, titer: 9.59e9vp/ml). For anterograde transsynaptic tracing, we used injection of the AAV2/1-hSyn-Cre-WPRE-hGH (UPenn Vector Core, titer: 6.68e13 vg/ml (Zingg et al., 2017)) bilaterally in the spinal cord (600-750 nL each side) and AAV-DJ-EF1-DI-hChR2(E123T/T159C)-p2A-eYFP-WPRE (Karl Deisseroth, Addgene # 35509, titer: 0.7.8e12 vg/ml) bilaterally in the RTN (300 nL). For anterograde synaptic tracing from the RTN$^{Phox2b/Atoh1}$ we used a unilateral injection (350-500 nL) of an AAV8.2-hEF1a-DIO-synaptophysin-eYFP obtained from Dr. Rachael Neve (Gene Delivery Technology Core, Massachusetts General Hospital, USA, titer: 5.4e12).

Surgical procedures

Injections and implants in the brainstem

Animals were anesthetized with isoflurane throughout the surgery (4 % at 1 L/min for induction and 2 % at 0.2 L/min for maintenance). Buprenorphine (0,025mg/kg) was administered subcutaneously for analgesia before the surgery. The temperature of the mice was maintained at 36 °C with a feedback-controlled heating pad. Anesthetized animals were placed on a stereotaxic frame (Kopf) and the skull was exposed. Viral vectors were delivered using a pulled glass pipette connected to a syringe pump (Legato 130, KD Scientific, customized by Phymep, France). The infusion flow was set to 100 nL/min. Coordinates

(in mm) used to target CnF neurons (Figures 1-3) were: 4.4 caudal to bregma, 1.3 lateral, and 2.8 from the skull surface. RTN$^{Phox2b/Atoh1}$ neurons were targeted unilaterally (Figure 7) or bilaterally (Figures 4, 6) by the following coordinates: 5.6 caudal to bregma, 1.25 lateral, and 0.2 above the ventral surface. Sequential bilateral injection in the preBötC (Figure 1) were performed at the following coordinates: -6.5 from bregma, 1.25 lateral, and 0.5 above the ventral surface. After the injection, the pipette was held in place for 5 to 10 min before being slowly retracted. For optogenetic activations of the CnF, the CnF fibers in the preBötC and the RTN$^{Phox2b/Atoh1}$, a 200 µm core 0.39 NA optic fiber (Thorlabs) connected to a 1.25 mm diameter ferrule (Thorlabs) was implanted 0.4 mm above the injected site (CnF, Figures 2-3), as well as 1.5 mm (preBötC, Figure 2) and 1 mm (RTN$^{Phox2b/Atoh1}$, Figure 7) above the ventral surface. Optic fibers were secured to the skull with dental cement (Tetric Evoflow). Animals were followed daily after the surgery.

Injections in the spinal cord

Animals were anesthetized as described above and spinal injections were performed as previously done (Bouvier et al., 2015; Usseglio et al., 2020). A 2 cm incision of the skin was performed dorsally on anesthetized animals and the exposed spinal column was fixed with two holders on the left and right sides to a stereotaxic frame to minimize movements. Vertebral spinous processes were used as landmarks to target specific segments (Harrison et al., 2013). A small incision of the ligamentum Flavum allowed access to the spinal cord. A pulled glass pipette connected to a motorized syringe pump injector (Legato 130, KD Scientific, customized by Phymep, France) was positioned into the ventromedial area of the 2nd lumbar segment (L2, between the 11th and 12th vertebral body) using the following coordinates (in mm) : 0.35 laterally from the dorsal artery and 0.8 depth from the dorsal surface. This lateral positioning ensures that the injection pipette does not pass through the lateral funiculus where ascending and descending axons travel. For CTB experiments, we injected on each side of the spinal cord 600-750 nL of Cholera Toxin B (CTB)-AF647 conjugate (ThermoFisher Scientific Cat #: C-34778) diluted at 0.5 % in sterile water (Figure S4D, E). After each injection, the pipette was held in place for 5 to 10 min before being slowly retracted. The skin was sutured, and animals were followed daily after the surgery. All animals recovered without motor impairments.

Diaphragm EMG recordings

The protocol was described previously (Hérent et al., 2020). In brief, a 12 cm pair of electrodes was prepared from Teflon-coated insulated steel wires with an outside diameter of 0.14 mm (A-M systems, ref 793200). Two wires were lightly twisted together, and a knot was placed 5 cm from one end. At 1 cm from the knot, the Teflon insulation was stripped over 1 mm from each wire so that the two bared regions were separated by about 2 mm. The ends of the two wires were soldered to a miniature dissecting pin. The free ends of the electrodes, as well as a 5 cm ground wire, were soldered to a micro connector (Antelec). Nail polish was used to insulate the wires at the connector.

To implant the diaphragm as previously reported (Hérent et al., 2020), animals were anaesthetized placed in a stereotaxic frame and hydrated by a subcutaneous injection of saline solution (0.9 %). Their temperature was maintained at 36 °C with a feedback-controlled heating pad. This step was crucial to ensure post-surgery survival. The skull was exposed and processed to secure the micro connector using dental cement (Tetric Evofow). The ground wire was inserted under the neck's skin and the twisted electrodes were tunneled towards the right part of the animal guided by a 10 cm silicon tube of 2 mm inner diameter. The animal was then placed in supine position, the peritoneum was opened horizontally under the sternum, extending laterally to the ribs, and the silicon tube containing the electrodes was pulled through the opening. The sternum was clamped and lifted upwards to expose the diaphragm. A piece of stretched sterile parafilm was placed on the upper part of the liver to avoid friction during movement of the animal and to prevent conjunctive tissue formation at the recording sites. The miniature dissecting pin was pushed through the right floating ribs. The pin was then inserted through the sternum, leaving the bare part of the wires in superficial contact with the diaphragm. The position of the electrodes was secured on both sides of the floating ribs and sternum using dental cement. The pin was removed by cutting above the secured wires. The peritoneum and abdominal openings were sutured, and a head bar

was placed on the cemented skull to facilitate animal's handling when connecting and disconnecting EMG cables during behavioral sessions. Buprenorphine (0.025 mg/kg) was administered subcutaneously for analgesia at the end of the surgery and animals were observed daily following the surgery and treated with Buprenorphine if needed.

Histology

Adult mice were anesthetized with Euthasol Vet (140 mg/kg) and perfused with 4 % paraformaldehyde (PFA) in 1 X Phosphate Buffered Saline (PBS). Brains and spinal cords were dissected out and fixed overnight in 4 % PFA at 4 °C. After fixation, tissues were rinsed in 1X PBS. Brain and spinal cord were cryoprotected overnight at 4 °C, respectively in 16 % and 20 % of sucrose in PBS. Tissues were rapidly cryo-embedded in OCT mounting medium and sectioned at 30 µm using a cryostat. Sections were blocked in a solution of 1 X Tris Buffered Saline (TBS), 5 % normal donkey serum and 1 % Triton X-100. The primary antibodies, carried out 48 hours at 4 °C, were: goat anti-ChAt (1:500, ref: AB144P, Merck Millipore), chicken anti-GFP (1:500, ref: 1020, Aves Labs), rabbit anti-RFP (1:500, ref: 600-401-379, Rockland), rabbit anti-SST (1:500, ref: T-4103, BMA Biomedicals), and sheep anti-TH (1:500, ref: AB1542, Merck Millipore). Primary antibodies were detected after 2 hours of incubation at room temperature with appropriate secondary antibodies coupled to Alexa-Fluor 488, 647, Cy-3 or Cy-5 (1:500, Jackson ImmunoResearch). Sections were counterstained with a fluorescent Nissl stain (NeuroTrace 435/445 blue, ref: N21479, 1:200 or NeuroTrace 640/660 deep-red, ref: N21483, 1:1000, Thermo Fisher Scientific) and mounted in Prolong Diamond Antifade Montant (P36970, Thermo Fisher Scientific) or Ibidi Mounting Medium (50001, Ibidi). Sections were acquired with a Leica TCS SP8 confocal microscope (imaging platform of the NeuroPSI Institute, Gif-sur-Yvette, France) with 10 x and 25 x objectives.

The preBötC was defined as located ventrally to the cholinergic ChAT^{+} neurons of the nucleus ambiguous (na) where somatostatin^{+} (SST) neurons are detected ((Stornetta et al., 2003), Figure 1C-D, corresponding to areas from 7.3 to 6.7 mm caudal to bregma). The parafacial respiratory region (pF) was defined as immediately ventral, ventro-median and ventro-lateral to the facial motor neurons ((Guyenet and Mulkey, 2010), Figure 1E-F, corresponding to areas from 6.5 to 5.7 mm caudal to bregma).

Behavioral experiments

Optogenetic activations

Behavioral experiments started 4 to 5 weeks after the viral injection. Implanted animals were connected to a laser source (473 nm DPSS system, LaserGlow Technologies, Toronto, Canada) through a mating sleeve (Thorlabs). The laser was triggered by the output of a National Instruments interface (NI-USB 6211) and the timings of light activations were delivered using the NI MAX software. For CnF or RTN$^{Phox2b/Atoh1}$ long photostimulation, light was delivered in trains of pulses of 20 ms (5 to 30 Hz) and of 15 ms (40 Hz) frequency for a duration of 1 s. Each frequency stimulation was repeated three times with several minutes of rest between trials. We used the minimal laser power sufficient to evoke a response, which was measured to be between 5-12 mW at the fiber tip using a power meter (PM100USB with S120C silicon power head, Thorlabs) to restrict photo-activations unilaterally (Stujenske et al., 2015), prevent heat, and exclude an unintentional silencing by over-activation. For randomized short light-pulses, 50 ms light stimulations (50-70 pulses/experiment) were applied randomly in the respiratory cycle.

Plethysmography recordings

To analyze the effect of short photo-activations of the CnF and CnF fibers in the preBötC (Figure 2), or the RTN$^{Phox2b/Atoh1}$ (Figure 7) on burst timing, ChR2-injected animals were placed inside a hermetic whole-body plethysmography (WBP) chamber (Ruffault et al., 2015), customized to allow the passage of the optical patch-cord, four weeks after viral injection. The plethysmography signal was recorded over a period of 10 min using the LabScribe NI software (iWorxs).

Locomotion in a linear runway

Four to five weeks following the injection of the ChR2-expressing virus in the CnF, animals were implanted with a diaphragm EMG as explained previously (Figure 3). One week following EMG implantation, animals were placed in a linear corridor (80 x 10 cm), and familiarized for 1 h/day for 3 days, prior to the experiments. Implanted animals were filmed from the side at 200 fps and 0.5 ms exposure time using a CMOS camera (Jai GO-2400-USB) and images were streamed to a hard disk using the 2nd LOOK software (IO Industries). The start of the EMG recordings was hardware-triggered by the start of the video-recordings using the frame exposure output of the video camera, so that the two recordings are synchronized. When animals were immobile at one end of the corridor and the respiration was stable, we delivered CnF optogenetic activations with frequencies ranging from 5 to 40 Hz. For each frequency, the stimulation was repeated three times with several minutes of rest between trials.

Chemogenetic silencing and treadmill experiment

Three weeks following the injection of the hM4Di virus in the RTN$^{Phox2b/Atoh1}$, animals were implanted for diaphragm EMG recordings as explained above (Figure 6). Non-injected C57BL/6J mice were also implanted as controls to test for CNO side effects. One week following EMG implantation, implanted animals were familiarized on a stationary custom-made motorized treadmill with adjustable speed range (Scop Pro, France, belt dimensions: 6 cm x 30 cm) for 30 min/day for 3 days, prior to the experiments. In addition, implanted animals were exercised during this time for a total of 5 min at 40 cm/s each day. This step was crucial to obtain stable running animals during experimental sessions. Mice could rest for 5 min after running before being placed back in their cage. Following this short training, implanted mice were connected with custom light-weight cables to an AC amplifier (BMA-400, CWE Inc.) and neurograms were filtered (high-pass: 100 Hz, low-pass: 10 kHz), collected at 10 kHz using a National Instruments acquisition card (USB-6211) and live-integrated using the LabScribe NI software. Animals were first placed on the stationary treadmill to monitor basal respiration. Animals were then challenged to trot at 40 cm/s for 1.5 min before being administered intraperitoneally with CNO (Enzo Life science, cat #: BML-NS105-0005, 10 mg/kg) or saline (0.9 %). Animals were placed again on the treadmill with the same paradigm 2-3 h and 5 h after CNO or saline administration to measure respiration in resting and running conditions. During experiments, animals were filmed from the side in the same way as above to monitor the stability of running episodes.

Ex vivo brainstem-spinal cord experiments

Pups aged 1-2 days were used in all experiments. The pups were anaesthetized with isoflurane, decerebrated and the brainstem still attached to the spinal cord was dissected and isolated in ice-cold artificial-cerebrospinal fluid (a-CSF) solution that contained (in mM): 111 NaCl, 3 KCl, 25 $NaHCO_3$, 1.25 $MgSO_4$, 1.1 KH_2PO_4, 2.5 $CaCl_2$ and 11 D-Glucose, and oxygenated in 95 % O_2, 5 %CO_2 to obtain a pH of 7.4. Isolated brainstem-spinal cords were transferred into a recording chamber and pinned to a Sylgard 184 resin. Preparations were partitioned in two compartments at the level of lower thoracic segments (11th thoracic, T11) using a Vaseline wall, to restrict bath application of locomotor drugs on the lumbar spinal cord (Figure 5). The lumbar compartment was continuously perfused with the above a-CSF solution while the rostral compartment containing the brainstem was superfused with an a-CSF containing (in mM): 111 NaCl, 8 KCl, 25 $NaHCO_3$, 3.7 $MgSO_4$, 1.1 KH_2PO_4, 1.25 $CaCl_2$ and 30 D-Glucose. All recordings were done at room temperature (22-25 °C) after allowing 30 min of resting period after the dissection. Respiratory- and locomotor-like activities were recorded respectively on the 4th cervical (C4) and the 2nd lumbar (L2) ventral rootlets using extracellular suction glass pipettes (120F-10, Harvard Apparatus). Drug-evoked locomotor-like activities were induced by bath-applying 10-14 µM of N-methyl-D-aspartate (NMDA, Tocris) and serotonin (5-HT, Sigma-Aldrich) (Figure 5) or using blue light on the lumbar spinal cord of ChR2-expressing pups (*Vglut2cre;floxedChR2*, Figure S5). Signals were collected and band-passed filtered at 100 Hz to 1 kHz with an AC amplifier (Model 1700, A-M Systems) and live-integrated (Neurolog, Digitimer) with a time constant of 100 ms (C4) and 200 ms (L2). Signals were sampled using Clampex 11 (Molecular Devices) at 5

kHz. To control for locomotor drugs leakage, some preparations were transected at the level of the cervical spinal cord (Figure S5A-C). For brainstem trans-section experiments, the rostral part of the brainstem containing the parafacial respiratory region was physically removed (Figure 5D-F). *Egr2-Cre;Phox2b^{27AlaCKI}* pups were used to genetically eliminate RTN$^{Phox2b/Atoh1}$ neurons ((Ramanantsoa et al., 2011b; Ruffault et al., 2015), Figure 5G-I).

Quantifications and statistical analysis

Phase-shift analysis

We measured the duration of the respiratory cycle containing the light stimulus (perturbed cycle, θ) and the previous respiratory cycle (control cycle, ϕ, Figures 2, 7). One respiratory cycle was defined as from the onset of inspiration to the subsequent inspiratory onset. The stimulated cycle ϕ_S was defined as from the onset of the perturbed cycle to the onset of the light pulse. The perturbed cycle θ was defined as from the onset of the inspiration prior to the light stimulation to the onset of the subsequent inspiration. The phase-shift was calculated as the ratio of the perturbed cycle divided by the control cycle (θ/ϕ). The light phase was defined as the ratio of the stimulated cycle divided by the control cycle (ϕ_S/ϕ). The phase-shift was then plotted against the light phase for all N events from n animals. The number of events (N) and animals (n) are assigned in the corresponding figures for all tested condition (CnF, CnF fibers in the preBötC, and RTN$^{Phox2b/Atoh1}$ stimulation). In addition, the average phase-shift was plotted against the average light phase in bins (1/10) as mean ± SD. Inspiratory time (I) was measured, averaged for each animal and a grand average was calculated and annotated in the corresponding figures for all tested condition. Expiratory time (E) was calculated from respiratory cycle and inspiratory (I) times.

Locomotor parameters analysis

To track the mouse displacement and measure its speed, we used DeepLabCut (version 2.1.5.2, (Mathis et al., 2018)) and manually labelled the positions of the head from 50 frames of each video. We then used 95 % of the labelled frames to train the network using a ResNet-50-based neural network with default parameters for 3 training iterations. This network was then used to analyze videos from similar experimental settings. For treadmill experiments, the head X coordinate was used as a control for running stability on the treadmill. For CnF stimulations on the corridor, the head X coordinate was used to calculate the animal's speed s_x using the gradient over time.

$$\overrightarrow{s_x} = \frac{\partial \vec{x}}{\partial t}, \vec{x}\ being\ the\ displacement\ of\ the\ head\ along\ the\ x\ axis$$

Head X coordinate (treadmill) and calculated speed (corridor) were then exported to Clampfit (Molecular Devices) and interpolated to 10 kHz to match the acquisition frame rate of diaphragmatic EMG recordings. Both sets of signals (head X and diaphragm, or speed and diaphragm) were merged in single files, before being processed offline in Clampfit. The animal's instantaneous speed is illustrated in Figure 3. The mean speed, defined from the onset of the movement to the end of the photostimulation, was then calculated using the statistic function in Clampfit for each CnF stimulation (5 to 40 Hz). All values were averaged across trials (3 trials/animal) for each animal, and a grand mean ± SD across n animals was calculated per stimulation frequency (5 to 40 Hz, Figure S3B).

For gait analysis during CnF photo-stimulations (15 to 40 Hz), we manually annotated the paw of a reference hindlimb (ipsilateral) and registered the timings of footfalls (when the paw first touches the floor). Each reference locomotor cycle was then defined as the duration from one footfall (ipsi_FF$_n$) to the next (ipsi_FF$_{n+1}$). The time of occurrence of the contralateral hindlimb footfall within the reference locomotor cycle was annotated manually (contra_FF) and the synchronicity rate was then computed as follows:

$$synchronicity\ rate = \frac{t_{contra\_\mathrm{FF}} - t_{\mathrm{ipsi\_FFn}}}{t_{\mathrm{ipsi\_FFn+1}} - t_{\mathrm{ipsi\_FFn}}}$$

A custom MATLAB script was then used to categorize synchronized (synchronicity rate $\in$[0, 0.25[$\cup$[0.75, 1]) or alternated (synchronicity rate $\in$[0.25, 0.75[) ipsi- and contralateral hindlimb steps.

Synchronicity rates were averaged across animals (3 trials/animal) and a grand mean ± SD across n animals was calculated per stimulation frequency (15 to 40 Hz, Figure S3C).

Locomotor latencies were defined as the duration from the onset of the CnF stimulation to the onset of movement for each CnF stimulations. All values were averaged across trials (3 trials/animal) and a grand mean ± SD across n animals was calculated per stimulation frequency (15 to 40 Hz, Figure S3D).

In vivo respiratory changes analysis

To analyze breathing changes to CnF (EMG recordings, Figure 3) and RTN$^{Phox2b/Atoh1}$ (WBP recordings, Figure 7) photo-stimulation, instantaneous diaphragm frequencies were detected over a 1 s window, using the threshold search in Clampfit before (CTL), during (Light) and directly after (REC) the light stimulation for all frequencies (5 to 40 Hz). For CnF stimulations that triggered locomotor episodes (15-40 Hz), the recovery period was measured as soon as the animal returned to immobility. Respiratory changes detected from the onset of the light stimulus to the onset of the movement were categorized as during the "pre-Loco" phase (Figure 3D, E). Those detected from the onset of the movement to the offset of the light stimulus were categorized as during the "Loco" phase (Figure 3D, F). All values were averaged across animals (3 trials/animal) and a grand mean ± SD across n animals was calculated per stimulation frequency.

For treadmill exercise (Figure 6), the mean diaphragm frequency was analyzed prior to exercise (resting condition) and from stable trotting moments, i.e., when the animal's speed was in phase with the treadmill, inferred by the absence of changes in head's X coordinates (running condition). Instantaneous respiratory frequency was measured for a total duration of 6 s in each condition: before (CTL), during (CNO/saline) and after (REC) administration of either CNO or saline. These measurements were done using 2 to 3 windows taken during resting conditions and at any stable moment of the 1.5 min run (excluding the first 20 s to exclude possible stress-induced changes when the treadmill is just engaged). Measurements were averaged to give the mean value for each animal. Averaged mean values were expressed as mean ± SD across n animals.

Ex vivo respiratory-like activities analysis

For each preparation, instantaneous respiratory-like frequencies were analyzed offline using the threshold search in Clampfit (Molecular Devices) before (CTL), during (Drugs) and after bath application of NMDA and 5-HT (WO) (Figure 5). Respiratory frequency changes during drug and washout conditions were normalized and expressed as a percent of the control. A grand mean ± SD across n animals was calculated.

Statistical Analysis

All data are expressed as mean ± SD. Statistical tests were performed using Prism (GraphPad Prism 7) and are spelled out in the corresponding figure legends, as well as the number of trials (N) and animals (n) used for each experiment. Changes were considered as not significant (ns) when $p>0.05$ and as significant when $p<0.05$. Significance levels are reported as follows: * $p<0.05$, ** $p< 0.01$, *** $p< 0.001$, and **** $p< 0.0001$.

Acknowledgements

This work was funded by Agence Nationale de la Recherche (ANR-15-CE16-013-02 to GF and ANR-17-CE16-0027 to JB) and CNRS, Université Paris-Saclay and by NeuroPSI. CH holds doctoral fellowships from Région Ile-de-France and Fondation pour la Recherche Médicale. We thank Aurélie Heuzé for lab management and genotyping animals, Edwin Gatier for help with DeepLabCut and analytic scripts, JF Brunet for providing animals, and the NeuroPSI animal facility for housing animals.

References

Abbott, S.B., Stornetta, R.L., Coates, M.B., and Guyenet, P.G. (2011). Phox2b-expressing neurons of the parafacial region regulate breathing rate, inspiration, and expiration in conscious rats. J Neurosci *31*, 16410-16422.

Abbott, S.B., Stornetta, R.L., Fortuna, M.G., Depuy, S.D., West, G.H., Harris, T.E., and Guyenet, P.G. (2009). Photostimulation of retrotrapezoid nucleus phox2b-expressing neurons in vivo produces long-lasting activation of breathing in rats. J Neurosci *29*, 5806-5819.

Abraham, K.A., Feingold, H., Fuller, D.D., Jenkins, M., Mateika, J.H., and Fregosi, R.F. (2002). Respiratory-related activation of human abdominal muscles during exercise. J Physiol *541*, 653-663.
Ainsworth, D.M., Smith, C.A., Eicker, S.W., Henderson, K.S., and Dempsey, J.A. (1989). The effects of locomotion on respiratory muscle activity in the awake dog. Respir Physiol *78*, 145-162.
Alsahafi, Z., Dickson, C.T., and Pagliardini, S. (2015). Optogenetic excitation of preBötzinger complex neurons potently drives inspiratory activity in vivo. J Physiol *593*, 3673-3692.
Bachmann, L.C., Matis, A., Lindau, N.T., Felder, P., Gullo, M., and Schwab, M.E. (2013). Deep brain stimulation of the midbrain locomotor region improves paretic hindlimb function after spinal cord injury in rats. Science translational medicine *5*, 208ra146.
Baertsch, N.A., Baertsch, H.C., and Ramirez, J.M. (2018). The interdependence of excitation and inhibition for the control of dynamic breathing rhythms. Nat Commun *9*, 843.
Barna, B.F., Takakura, A.C., and Moreira, T.S. (2012). Pontomedullary and hypothalamic distribution of Fos-like immunoreactive neurons after acute exercise in rats. Neuroscience *212*, 120-130.
Barna, B.F., Takakura, A.C., and Moreira, T.S. (2014). Acute exercise-induced activation of Phox2b-expressing neurons of the retrotrapezoid nucleus in rats may involve the hypothalamus. Neuroscience *258*, 355-363.
Bouvier, J., Caggiano, V., Leiras, R., Caldeira, V., Bellardita, C., Balueva, K., Fuchs, A., and Kiehn, O. (2015). Descending Command Neurons in the Brainstem that Halt Locomotion. Cell *163*, 1191-1203.
Bouvier, J., Thoby-Brisson, M., Renier, N., Dubreuil, V., Ericson, J., Champagnat, J., Pierani, A., Chedotal, A., and Fortin, G. (2010). Hindbrain interneurons and axon guidance signaling critical for breathing. Nat Neurosci *13*, 1066-1074.
Caggiano, V., Leiras, R., Goni-Erro, H., Masini, D., Bellardita, C., Bouvier, J., Caldeira, V., Fisone, G., and Kiehn, O. (2018). Midbrain circuits that set locomotor speed and gait selection. Nature *553*, 455-460.
Capelli, P., Pivetta, C., Soledad Esposito, M., and Arber, S. (2017). Locomotor speed control circuits in the caudal brainstem. Nature.
Cui, Y., Kam, K., Sherman, D., Janczewski, W.A., Zheng, Y., and Feldman, J.L. (2016). Defining preBotzinger Complex Rhythm- and Pattern-Generating Neural Microcircuits In Vivo. Neuron *91*, 602-614.
Decety, J., Jeannerod, M., Durozard, D., and Baverel, G. (1993). Central activation of autonomic effectors during mental simulation of motor actions in man. J Physiol *461*, 549-563.
Decety, J., Jeannerod, M., Germain, M., and Pastene, J. (1991). Vegetative response during imagined movement is proportional to mental effort. Behav Brain Res *42*, 1-5.
Del Negro, C.A., Funk, G.D., and Feldman, J.L. (2018). Breathing matters. Nature reviews *19*, 351-367.
DeLorme, M.P., and Moss, O.R. (2002). Pulmonary function assessment by whole-body plethysmography in restrained versus unrestrained mice. J Pharmacol Toxicol Methods *47*, 1-10.
Depoortere, R., Sandner, G., and Di Scala, G. (1990). Aversion induced by electrical stimulation of the mesencephalic locomotor region in the intact and freely moving rat. Physiol Behav *47*, 561-567.
DiMarco, A.F., Romaniuk, J.R., Von Euler, C., and Yamamoto, Y. (1983). Immediate changes in ventilation and respiratory pattern associated with onset and cessation of locomotion in the cat. J Physiol *343*, 1-16.
Dougherty, K.J., and Kiehn, O. (2010a). Firing and cellular properties of V2a interneurons in the rodent spinal cord. J Neurosci *30*, 24-37.
Dougherty, K.J., and Kiehn, O. (2010b). Functional organization of V2a-related locomotor circuits in the rodent spinal cord. Annals of the New York Academy of Sciences *1198*, 85-93.
Dougherty, K.J., Zagoraiou, L., Satoh, D., Rozani, I., Doobar, S., Arber, S., Jessell, T.M., and Kiehn, O. (2013). Locomotor rhythm generation linked to the output of spinal shox2 excitatory interneurons. Neuron *80*, 920-933.
Dubuc, R., Brocard, F., Antri, M., Fenelon, K., Gariepy, J.F., Smetana, R., Menard, A., Le Ray, D., Viana Di Prisco, G., Pearlstein, E*., et al.* (2008). Initiation of locomotion in lampreys. Brain research reviews *57*, 172-182.
Duffin, J. (2014). The fast exercise drive to breathe. J Physiol *592*, 445-451.
Duffin, J., and Bechbache, R.R. (1983). The changes in ventilation and heart rate at the start of treadmill exercise. Can J Physiol Pharmacol *61*, 120-126.
Eldridge, F.L., Millhorn, D.E., Kiley, J.P., and Waldrop, T.G. (1985). Stimulation by central command of locomotion, respiration and circulation during exercise. Respir Physiol *59*, 313-337.
Eldridge, F.L., Millhorn, D.E., and Waldrop, T.G. (1981). Exercise hyperpnea and locomotion: parallel activation from the hypothalamus. Science *211*, 844-846.
Fernandes, A., Galbo, H., Kjaer, M., Mitchell, J.H., Secher, N.H., and Thomas, S.N. (1990). Cardiovascular and ventilatory responses to dynamic exercise during epidural anaesthesia in man. J Physiol *420*, 281-293.
Gariepy, J.F., Missaghi, K., Chevallier, S., Chartre, S., Robert, M., Auclair, F., Lund, J.P., and Dubuc, R. (2012). Specific neural substrate linking respiration to locomotion. Proc Natl Acad Sci U S A *109*, E84-92.
Gariepy, J.F., Missaghi, K., and Dubuc, R. (2010). The interactions between locomotion and respiration. Prog Brain Res *187*, 173-188.
Gravel, J., Brocard, F., Gariépy, J.F., Lund, J.P., and Dubuc, R. (2007). Modulation of respiratory activity by locomotion in lampreys. Neuroscience *144*, 1120-1132.
Gray, P.A., Hayes, J.A., Ling, G.Y., Llona, I., Tupal, S., Picardo, M.C., Ross, S.E., Hirata, T., Corbin, J.G., Eugenin, J*., et al.* (2010). Developmental origin of preBotzinger complex respiratory neurons. J Neurosci *30*, 14883-14895.
Green, A.L., Wang, S., Purvis, S., Owen, S.L., Bain, P.G., Stein, J.F., Guz, A., Aziz, T.Z., and Paterson, D.J. (2007). Identifying cardiorespiratory neurocircuitry involved in central command during exercise in humans. J Physiol *578*, 605-612.

Grillner, S. (2006). Biological pattern generation: the cellular and computational logic of networks in motion. Neuron *52*, 751-766.
Grillner, S., and El Manira, A. (2020). Current Principles of Motor Control, with Special Reference to Vertebrate Locomotion. Physiological reviews *100*, 271-320.
Guyenet, P.G., and Mulkey, D.K. (2010). Retrotrapezoid nucleus and parafacial respiratory group. Respir Physiol Neurobiol.
Guyenet, P.G., Stornetta, R.L., Bochorishvili, G., Depuy, S.D., Burke, P.G., and Abbott, S.B. (2013). C1 neurons: the body's EMTs. American journal of physiology *305*, R187-204.
Hagglund, M., Borgius, L., Dougherty, K.J., and Kiehn, O. (2010). Activation of groups of excitatory neurons in the mammalian spinal cord or hindbrain evokes locomotion. Nat Neurosci *13*, 246-253.
Hagglund, M., Dougherty, K.J., Borgius, L., Itohara, S., Iwasato, T., and Kiehn, O. (2013). Optogenetic dissection reveals multiple rhythmogenic modules underlying locomotion. Proc Natl Acad Sci U S A.
Harrison, M., O'Brien, A., Adams, L., Cowin, G., Ruitenberg, M.J., Sengul, G., and Watson, C. (2013). Vertebral landmarks for the identification of spinal cord segments in the mouse. NeuroImage *68*, 22-29.
Hérent, C., Diem, S., Fortin, G., and Bouvier, J. (2020). Absent phasing of respiratory and locomotor rhythms in running mice. Elife *9*.
Iscoe, S. (1998). Control of abdominal muscles. Progress in neurobiology *56*, 433-506.
Jahn, K., Deutschländer, A., Stephan, T., Kalla, R., Wiesmann, M., Strupp, M., and Brandt, T. (2008). Imaging human supraspinal locomotor centers in brainstem and cerebellum. NeuroImage *39*, 786-792.
Jessell, T.M. (2000). Neuronal specification in the spinal cord: inductive signals and transcriptional codes. Nature reviews *1*, 20-29.
Jordan, L.M., Liu, J., Hedlund, P.B., Akay, T., and Pearson, K.G. (2008). Descending command systems for the initiation of locomotion in mammals. Brain research reviews *57*, 183-191.
Josset, N., Roussel, M., Lemieux, M., Lafrance-Zoubga, D., Rastqar, A., and Bretzner, F. (2018). Distinct Contributions of Mesencephalic Locomotor Region Nuclei to Locomotor Control in the Freely Behaving Mouse. Curr Biol *28*, 884-901 e883.
Kiehn, O. (2016). Decoding the organization of spinal circuits that control locomotion. Nature reviews *17*, 224-238.
Kim, E.J., Jacobs, M.W., Ito-Cole, T., and Callaway, E.M. (2016). Improved Monosynaptic Neural Circuit Tracing Using Engineered Rabies Virus Glycoproteins. Cell Rep.
Kjaerulff, O., and Kiehn, O. (1996). Distribution of networks generating and coordinating locomotor activity in the neonatal rat spinal cord in vitro: a lesion study. J Neurosci *16*, 5777-5794.
Korsak, A., Sheikhbahaei, S., Machhada, A., Gourine, A.V., and Huckstepp, R.T.R. (2018). The Role Of Parafacial Neurons In The Control Of Breathing During Exercise. Scientific reports *8*, 400.
Korte, S.M., Jaarsma, D., Luiten, P.G., and Bohus, B. (1992). Mesencephalic cuneiform nucleus and its ascending and descending projections serve stress-related cardiovascular responses in the rat. Journal of the autonomic nervous system *41*, 157-176.
Koshiya, N., and Smith, J.C. (1999). Neuronal pacemaker for breathing visualized in vitro. Nature *400*, 360-363.
Krogh, A., and Lindhard, J. (1913). The regulation of respiration and circulation during the initial stages of muscular work. J Physiol *47*, 112-136.
Le Gal, J.P., Colnot, E., Cardoit, L., Bacque-Cazenave, J., Thoby-Brisson, M., Juvin, L., and Morin, D. (2020). Modulation of respiratory network activity by forelimb and hindlimb locomotor generators. Eur J Neurosci.
Le Gal, J.P., Juvin, L., Cardoit, L., Thoby-Brisson, M., and Morin, D. (2014). Remote control of respiratory neural network by spinal locomotor generators. PLoS One *9*, e89670.
Le Ray, D., Juvin, L., Ryczko, D., and Dubuc, R. (2011). Chapter 4--supraspinal control of locomotion: the mesencephalic locomotor region. Prog Brain Res *188*, 51-70.
Li, P., Janczewski, W.A., Yackle, K., Kam, K., Pagliardini, S., Krasnow, M.A., and Feldman, J.L. (2016). The peptidergic control circuit for sighing. Nature.
Madisen, L., Mao, T., Koch, H., Zhuo, J.M., Berenyi, A., Fujisawa, S., Hsu, Y.W., Garcia, A.J., 3rd, Gu, X., Zanella, S.*, et al.* (2012). A toolbox of Cre-dependent optogenetic transgenic mice for light-induced activation and silencing. Nat Neurosci *15*, 793-802.
Mateika, J.H., and Duffin, J. (1995). A review of the control of breathing during exercise. Eur J Appl Physiol Occup Physiol *71*, 1-27.
Mathis, A., Mamidanna, P., Cury, K.M., Abe, T., Murthy, V.N., Mathis, M.W., and Bethge, M. (2018). DeepLabCut: markerless pose estimation of user-defined body parts with deep learning. Nat Neurosci *21*, 1281-1289.
Mattis, J., Tye, K.M., Ferenczi, E.A., Ramakrishnan, C., O'Shea, D.J., Prakash, R., Gunaydin, L.A., Hyun, M., Fenno, L.E., Gradinaru, V.*, et al.* (2011). Principles for applying optogenetic tools derived from direct comparative analysis of microbial opsins. Nature methods *9*, 159-172.
Mitchell, I.J., Dean, P., and Redgrave, P. (1988a). The projection from superior colliculus to cuneiform area in the rat. II. Defence-like responses to stimulation with glutamate in cuneiform nucleus and surrounding structures. Experimental brain research Experimentelle Hirnforschung *72*, 626-639.
Mitchell, I.J., Redgrave, P., and Dean, P. (1988b). Plasticity of behavioural response to repeated injection of glutamate in cuneiform area of rat. Brain research *460*, 394-397.
Mutolo, D., Bongianni, F., Cinelli, E., and Pantaleo, T. (2010). Role of Neurokinin Receptors and Ionic Mechanisms Within the Respiratory Network of the Lamprey. Neuroscience.
Neve, R.L., Neve, K.A., Nestler, E.J., and Carlezon, W.A., Jr. (2005). Use of herpes virus amplicon vectors to study brain disorders. Biotechniques *39*, 381-391.
Paterson, D.J. (2014). Defining the neurocircuitry of exercise hyperpnoea. J Physiol *592*, 433-444.

Pierani, A., Moran-Rivard, L., Sunshine, M.J., Littman, D.R., Goulding, M., and Jessell, T.M. (2001). Control of interneuron fate in the developing spinal cord by the progenitor homeodomain protein Dbx1. Neuron *29*, 367-384.
Pivetta, C., Esposito, M.S., Sigrist, M., and Arber, S. (2014). Motor-circuit communication matrix from spinal cord to brainstem neurons revealed by developmental origin. Cell *156*, 537-548.
Ramanantsoa, N., Hirsch, M.R., Thoby-Brisson, M., Dubreuil, V., Bouvier, J., Ruffault, P.L., Matrot, B., Fortin, G., Brunet, J.F., Gallego, J.*, et al.* (2011a). Breathing without CO(2) chemosensitivity in conditional Phox2b mutants. J Neurosci *31*, 12880-12888.
Ramanantsoa, N., Hirsch, M.R., Thoby-Brisson, M., Dubreuil, V., Bouvier, J., Ruffault, P.L., Matrot, B., Fortin, G., Brunet, J.F., Gallego, J.*, et al.* (2011b). Breathing without CO(2) chemosensitivity in conditional Phox2b mutants. J Neurosci *31*, 12880-12888.
Reinhard, K., Li, C., Do, Q., Burke, E.G., Heynderickx, S., and Farrow, K. (2019). A projection specific logic to sampling visual inputs in mouse superior colliculus. Elife *8*.
Roseberry, T.K., Lee, A.M., Lalive, A.L., Wilbrecht, L., Bonci, A., and Kreitzer, A.C. (2016). Cell-Type-Specific Control of Brainstem Locomotor Circuits by Basal Ganglia. Cell *164*, 526-537.
Ruffault, P.L., D'Autreaux, F., Hayes, J.A., Nomaksteinsky, M., Autran, S., Fujiyama, T., Hoshino, M., Hagglund, M., Kiehn, O., Brunet, J.F.*, et al.* (2015). The retrotrapezoid nucleus neurons expressing Atoh1 and Phox2b are essential for the respiratory response to CO(2). Elife *4*.
Ryczko, D., Auclair, F., Cabelguen, J.M., and Dubuc, R. (2016). The mesencephalic locomotor region sends a bilateral glutamatergic drive to hindbrain reticulospinal neurons in a tetrapod. J Comp Neurol *524*, 1361-1383.
Ryczko, D., and Dubuc, R. (2013). The multifunctional mesencephalic locomotor region. Curr Pharm Des *19*, 4448-4470.
Sathyamurthy, A., Barik, A., Dobrott, C.I., Matson, K.J.E., Stoica, S., Pursley, R., Chesler, A.T., and Levine, A.J. (2020). Cerebellospinal Neurons Regulate Motor Performance and Motor Learning. Cell Rep *31*, 107595.
Shik, M.L., Severin, F.V., and Orlovskii, G.N. (1966). [Control of walking and running by means of electric stimulation of the midbrain]. Biofizika *11*, 659-666.
Shik, M.L., Severin, F.V., and Orlovsky, G.N. (1969). Control of walking and running by means of electrical stimulation of the mesencephalon. Electroencephalography and clinical neurophysiology *26*, 549.
Sieck, G.C., and Gransee, H.M. (2012). Respiratory Muscles: Structure. Function & Regulation,. Morgan & Claypool Life Sciences.
Smith, J.C., Ellenberger, H.H., Ballanyi, K., Richter, D.W., and Feldman, J.L. (1991). Pre-Botzinger complex: a brainstem region that may generate respiratory rhythm in mammals. Science *254*, 726-729.
Smith, J.C., Morrison, D.E., Ellenberger, H.H., Otto, M.R., and Feldman, J.L. (1989). Brainstem projections to the major respiratory neuron populations in the medulla of the cat. J Comp Neurol *281*, 69-96.
Stornetta, R.L., Rosin, D.L., Wang, H., Sevigny, C.P., Weston, M.C., and Guyenet, P.G. (2003). A group of glutamatergic interneurons expressing high levels of both neurokinin-1 receptors and somatostatin identifies the region of the pre-Botzinger complex. J Comp Neurol *455*, 499-512.
Stujenske, J.M., Spellman, T., and Gordon, J.A. (2015). Modeling the Spatiotemporal Dynamics of Light and Heat Propagation for In Vivo Optogenetics. Cell Rep *12*, 525-534.
Talpalar, A.E., Bouvier, J., Borgius, L., Fortin, G., Pierani, A., and Kiehn, O. (2013). Dual-mode operation of neuronal networks involved in left-right alternation. Nature.
Talpalar, A.E., and Kiehn, O. (2010). Glutamatergic mechanisms for speed control and network operation in the rodent locomotor CpG. Frontiers in neural circuits *4*.
Tan, W., Janczewski, W.A., Yang, P., Shao, X.M., Callaway, E.M., and Feldman, J.L. (2008). Silencing preBotzinger complex somatostatin-expressing neurons induces persistent apnea in awake rat. Nat Neurosci *11*, 538-540.
Thornton, J.M., Guz, A., Murphy, K., Griffith, A.R., Pedersen, D.L., Kardos, A., Leff, A., Adams, L., Casadei, B., and Paterson, D.J. (2001). Identification of higher brain centres that may encode the cardiorespiratory response to exercise in humans. J Physiol *533*, 823-836.
Tobin, M.J., Perez, W., Guenther, S.M., D'Alonzo, G., and Dantzker, D.R. (1986). Breathing pattern and metabolic behavior during anticipation of exercise. J Appl Physiol (1985) *60*, 1306-1312.
Usseglio, G., Gatier, E., Heuzé, A., Hérent, C., and Bouvier, J. (2020). Control of Orienting Movements and Locomotion by Projection-Defined Subsets of Brainstem V2a Neurons. Curr Biol.
Vann, N.C., Pham, F.D., Dorst, K.E., and Del Negro, C.A. (2018). Dbx1 Pre-Bötzinger Complex Interneurons Comprise the Core Inspiratory Oscillator for Breathing in Unanesthetized Adult Mice. eNeuro *5*.
Voiculescu, O., Charnay, P., and Schneider-Maunoury, S. (2000). Expression pattern of a Krox-20/Cre knock-in allele in the developing hindbrain, bones, and peripheral nervous system. Genesis *26*, 123-126.
Vong, L., Ye, C., Yang, Z., Choi, B., Chua, S., Jr., and Lowell, B.B. (2011). Leptin action on GABAergic neurons prevents obesity and reduces inhibitory tone to POMC neurons. Neuron *71*, 142-154.
Williamson, J.W., McColl, R., Mathews, D., Mitchell, J.H., Raven, P.B., and Morgan, W.P. (2001). Hypnotic manipulation of effort sense during dynamic exercise: cardiovascular responses and brain activation. J Appl Physiol (1985) *90*, 1392-1399.
Yang, C.F., Kim, E.J., Callaway, E.M., and Feldman, J.L. (2020). Monosynaptic Projections to Excitatory and Inhibitory preBötzinger Complex Neurons. Front Neuroanat *14*, 58.
Zingg, B., Chou, X.L., Zhang, Z.G., Mesik, L., Liang, F., Tao, H.W., and Zhang, L.I. (2017). AAV-Mediated Anterograde Transsynaptic Tagging: Mapping Corticocollicular Input-Defined Neural Pathways for Defense Behaviors. Neuron *93*, 33-47.

Supplemental figures

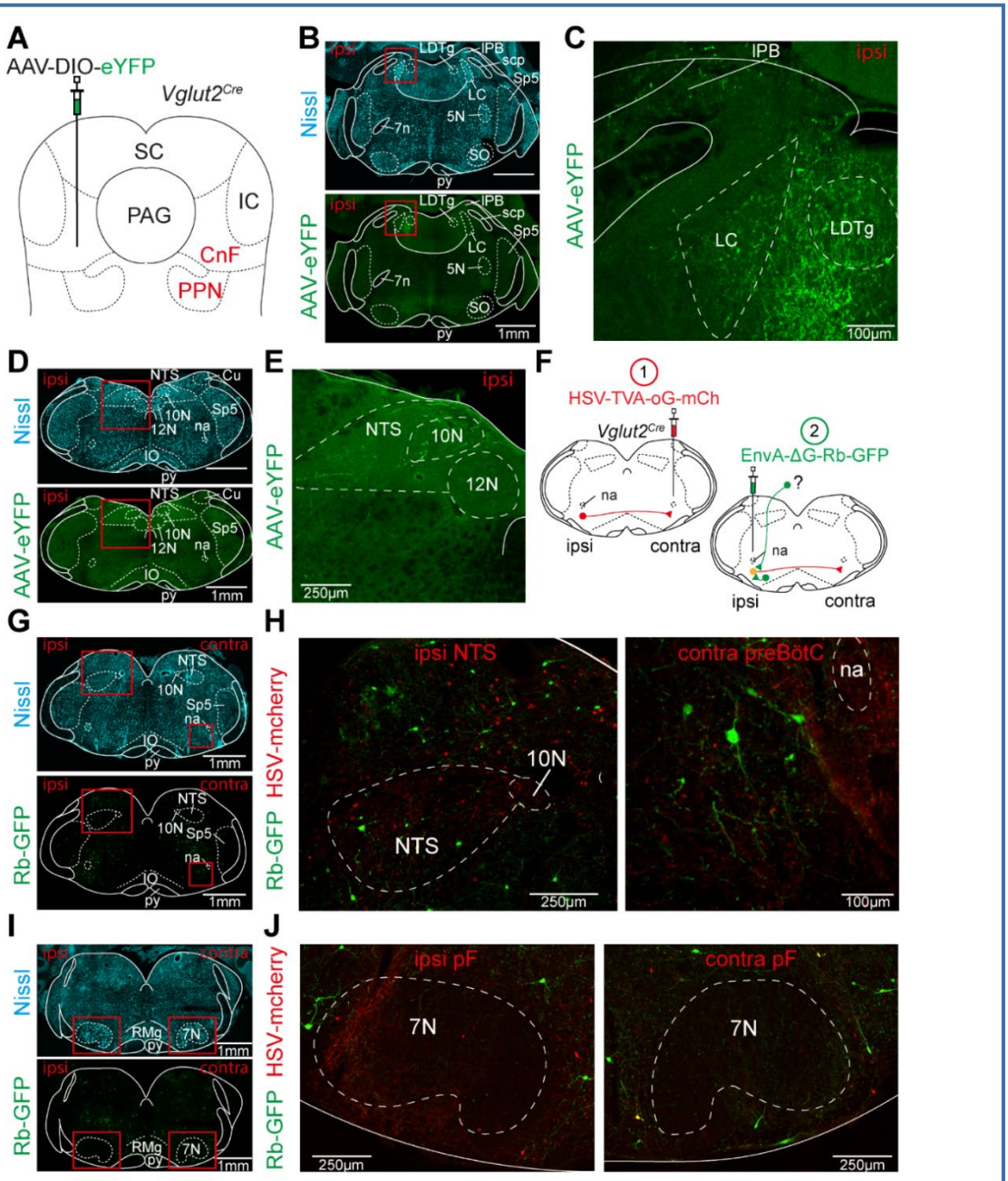

Figure S1: Outputs of the glutamatergic CnF and inputs onto the glutamatergic preBötC. (A) Schematics of the unilateral injection in the glutamatergic CnF with an AAV-DIO-eYFP in a *Vglut2*^{Cre} mouse line. **(B)** Low magnifications at the level of the lateral parabrachial nucleus (IPB). Top, Nissl staining. Bottom, glutamatergic CnF projections. **(C)** Magnification of the area framed in red in **B**, showing CnF projections. **(D)** Low magnifications at the level of the nucleus tractus solitarius (NTS). Top, Nissl staining. Bottom, glutamatergic CnF projections. **(E)** Magnification of the area framed in red in **D**, showing the CnF projections. **(F)** Approach used for revealing presynaptic cells of the commissural glutamatergic preBötC in a *Vglut2*^{Cre} mouse line. See text for details. Starter cells appear yellow while presynaptic cells are green. **(G)** Low magnifications at the preBötC and NTS level. Top, Nissl staining. Bottom, Rb-infected cells. **(H)** Magnifications of the ipsilateral NTS (left) and contralateral preBötC (right) framed in red in **G**, showing HSV-mCherry^{+} and Rb-GFP^{+} cells. **(I)** Low magnifications at the parafacial respiratory region (pF) level. Top, Nissl staining. Bottom, Rb-infected cells. **(J)** Magnification of the bilateral pF framed in red in **I**, showing HSV-mCherry^{+} and Rb-GFP^{+} cells. Note the few presynaptic cells in the pF. *See Figure 1 for all abbreviations.*

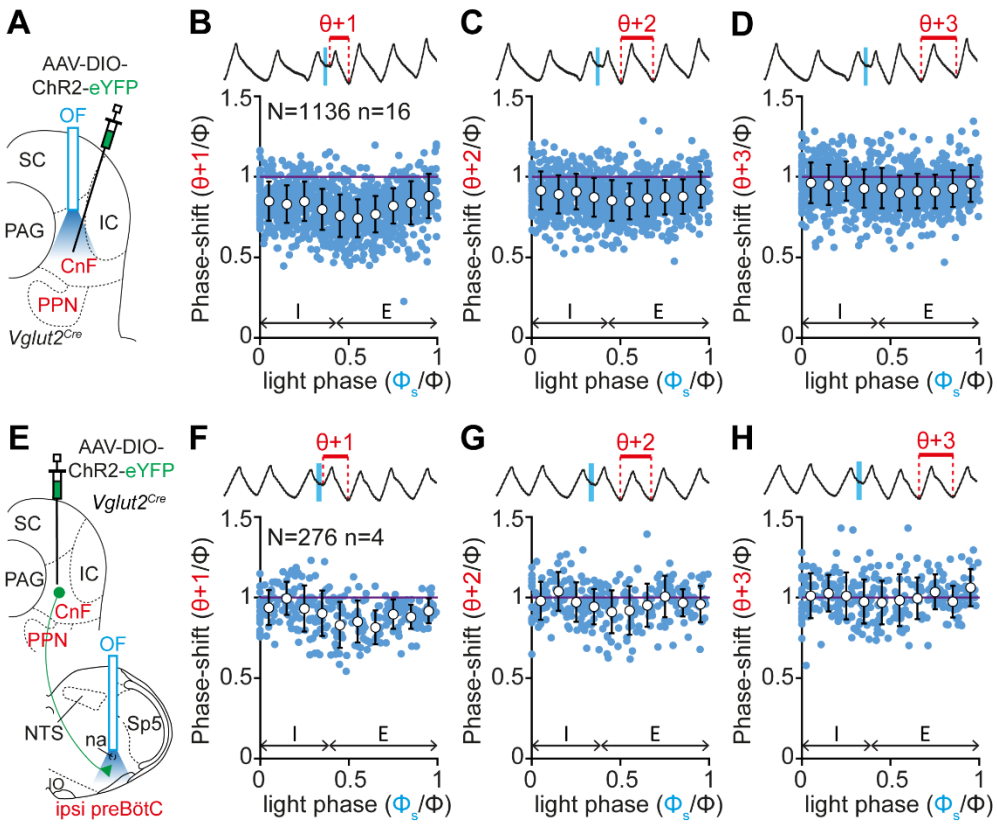

Figure S2: Temporal impact of photoactivation of the glutamatergic CnF and its projection in the preBötC area on respiratory cycles following the light-perturbed cycle. (A) Schematics of the viral injection (AAV-DIO-ChR2-eYFP) and optic fiber implantation (OF) to photoactivate the glutamatergic CnF in a *Vglut2*^{Cre} mouse line. **(B)** Top, whole body plethysmography (WBP) recordings of respiratory cycles while a 50 ms pulse stimulation (blue rectangle) is applied. The cycle n+1 following the perturbed cycle is annotated on the trace (θ+1, red). Bottom, plot of the phase-shift (perturbed cycle n+1 normalized to the control cycle: θ+1/ϕ) as a function of the light phase (light cycle normalized to the control cycle: ϕ_s/ϕ). Inspiration (I) and expiration (E) mean durations are annotated on the graph. A shortening of the perturbed cycle happens when values are under 1 (purple line). N=1136 random trials, n=16 mice. **(C, D)** Similar representations for cycles n+2 (θ+2) and n+3 (θ+3). **(E)** Schematics of the injection identical to **A** in the CnF and fiber implantation in the preBötC ipsilateral to the injection (OF). **(F-H)** Similar representations as (**B-D**). N=276 random trials, n=4 mice. *See Figure 1 for all abbreviations.*

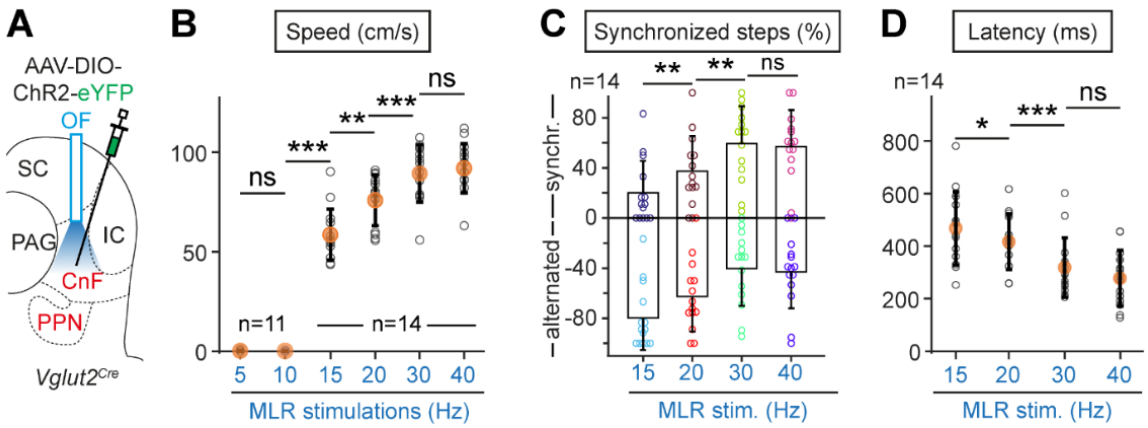

Figure S3: Glutamatergic CnF control of locomotor parameters. (A) Schematics of the viral injection (AAV-DIO-ChR2-eYFP) and optic fiber implantation (OF) to photoactivate the glutamatergic CnF in a *Vglut2^{Cre}* mouse line. **(B)** Graph showing the speed of the animal during CnF stimulation frequencies (5-40 Hz). Note that the locomotor speed reaches a plateau at 30 Hz. 5-10 Hz, n=11 mice; 15-40 Hz, n=14 mice. **(C)** Bar-graph showing the percent of hindlimb synchronized steps during CnF stimulation frequencies (15-40 Hz) in n=14 mice. Negative and positive values indicate respectively alternated and synchronized (synchr.) steps. **(D)** Graph showing the onset of locomotion latency during CnF stimulation frequencies (15-40 Hz) in n=14 mice. Data in all graphs are mean ± SD. Wilcoxon matched-pairs tests are used to compare conditions. ns, not significant. *, p<0.05. **, p<0.01. ***, p<0.001. *See Figure 1 for all abbreviations.*

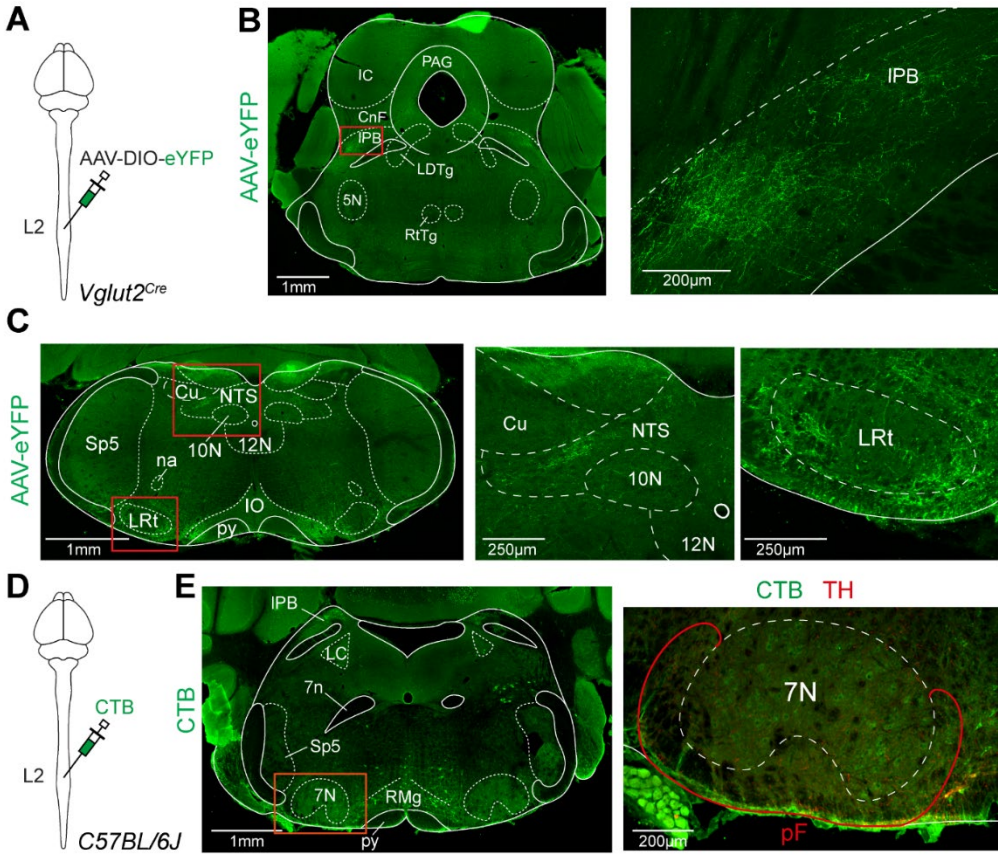

Figure S4: Outputs of the glutamatergic lumbar spinal cord to other respiratory nuclei and control of AAV1-Syn-Cre spinal injection. (A) Schematics of the bilateral injection of an AAV-DIO-eYFP in the 2nd lumbar spinal segment (L2) in a *Vglut2*^{Cre} mouse line. **(B)** Left, low magnification at the level of the lateral parabrachial nucleus (lPB), showing spinal projections. Right, magnification of the red rectangle in the left picture showing green projections in the lPB. **(C)** Left, low magnification at the level of the nucleus tractus solitarius (NTS) and lateral reticular nucleus (LRt), showing spinal projections. Middle and right, magnifications of the red rectangles in the left picture showing green projections in the NTS and the LRt. **(D)** Schematics of the bilateral injection of Cholera toxin B (CTB) in L2 in a *C57BL/6J* mouse line. CTB is used as a retrograde marker. **(E)** Left, low magnification at the level of the parafacial respiratory region (pF), showing spinal projections. Right, high magnification of the red rectangle in the left picture, showing spinal projections (AAV-eYFP) and catecholaminergic neurons (tyrosine hydroxylase, TH). Note that the pF does not project to the L2 lumbar spinal cord. *See Figure 1 for all abbreviations.*

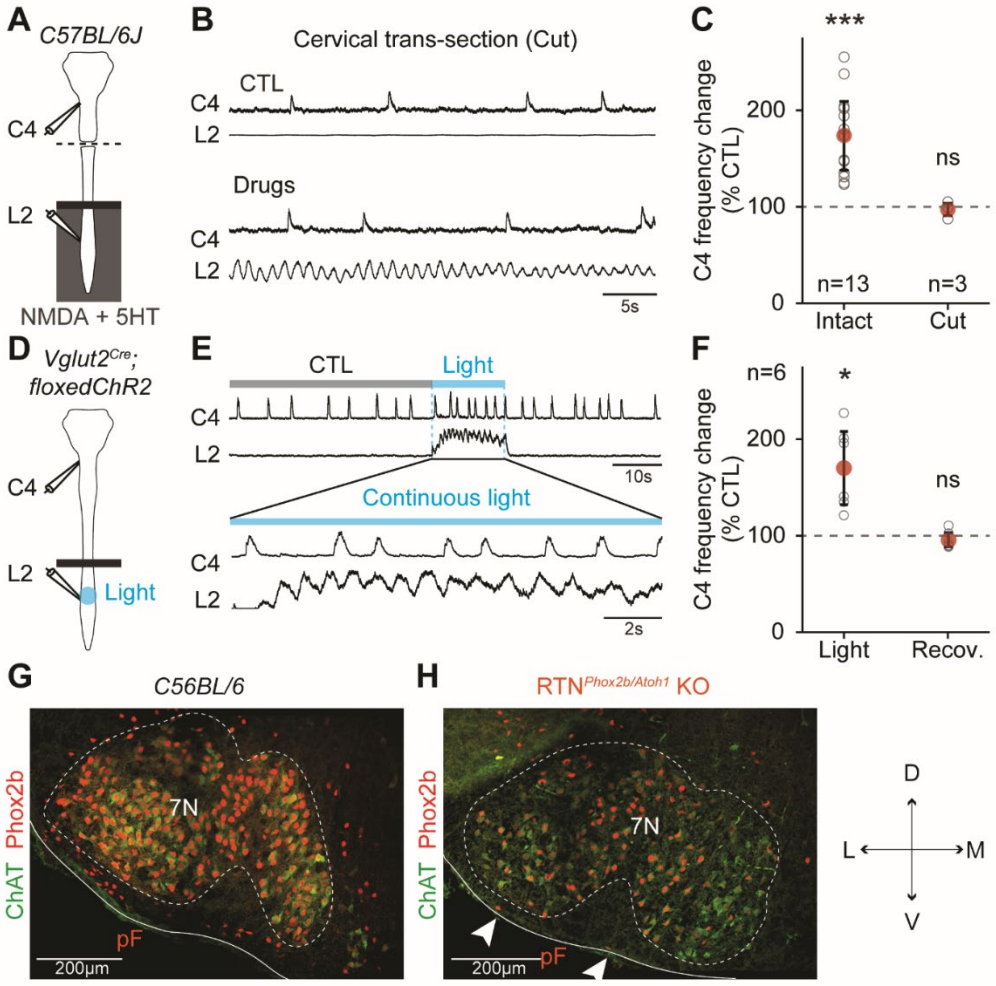

Figure S5: *Ex vivo* control experiments, *ex vivo* photoactivation of the glutamatergic lumbar spinal generator and anatomy of RTN$^{Phox2b/Atoh1}$ KO neonatal mice. (A) Schematics of the isolated *ex vivo* brainstem-spinal cord preparation from *C57BL/6J* neonates (see Figure 5). Preparations are cut at the cervical level. **(B)** Recordings of respiratory- (C4) and locomotor-like (L2) activities of one representative animal before (CTL) and during perfusion of NMDA and 5-HT in the lumbar spinal cord compartment (Drugs, gray rectangle in **A**). Note the absence of the drug induced-C4 frequency increase during the drugs perfusion when the spinal cord is transected. **(C)** Graph showing C4 frequency change normalized to the control condition (CTL) during drug-induced locomotor-like activity in intact (Intact, n=13 mice) and transected (Cut, n=3 mice) preparations. **(D)** Similar preparations in *Vglut2^{Cre};floxedChR2* mice. Light stimulations are applied on the lumbar cord (blue circle). **(E)** Recordings of C4 and L2 activities of one representative animal. Top, representative traces before (CTL, gray line), during (Light, blue line) and after 15 s light stimulation. Bottom, magnification of the top traces during the light stimulation. **(F)** Graph showing C4 frequency change normalized to the control condition (CTL) during light-induced locomotor-like activity (Light) and during recovery (Recov.) in n=6 preparations. Data in all graphs are mean ± SD. Wilcoxon matched-pairs tests are used to compare conditions. ns, not significant. *, p<0.05. ***, p<0.001. **(G-H)** High magnifications of the parafacial respiratory region (pF) in wild-type (**G**, *C57BL/6J*) and *Egr2^{Cre};Phox2b^{27AlaCKI}* (**H**, RTN$^{Phox2b/Atoh1}$ KO) neonatal mice, showing Phox2b and ChAt staining. Orientations are depicted on the right. Note the almost complete loss of Phox2b^{+} pF cells in **H**. *See Figure 1 for all abbreviations.*

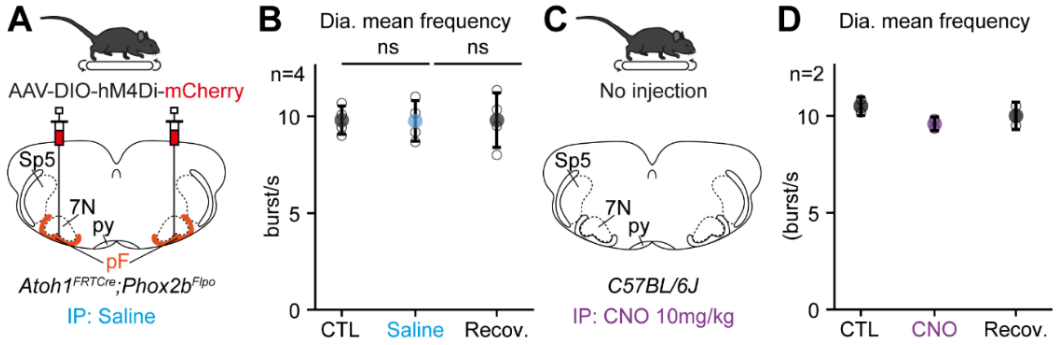

Figure S6: Control for RTN$^{Phox2b/Atoh1}$ chemogenic silencing experiments. (A) Schematics of the bilateral injection in the parafacial respiratory region (pF) to transfect RTN$^{Phox2b/Atoh1}$ cells with an AAV-DIO-hM4Di-mCherry in an *Atoh1*^{FRTCre}*;Phox2b*^{Flpo} mouse line. Injected mice were challenged to run on the treadmill before, during and after intraperitoneal (IP) injection of saline solution. **(B)** Graph showing the diaphragm mean frequency change before (CTL), during (Saline) and after (Recov.) saline injection in n=4 mice. Note that saline injection does not alter mice capacity to increase diaphragm frequency during running. Paired t-test is used to compare conditions. ns, not significant. **(C)** Schematics of the experiment. Non-injected *C57BL/6J* mice were challenged to run on the treadmill before, during and after IP injection of CNO (10 mg/kg). **(D)** Graph showing the diaphragm mean frequency change before (CTL), during (CNO) and after (Recov.) CNO IP injection in n=2 mice. Data in all graphs are mean ± SD. *See Figure 1 for all abbreviations.*

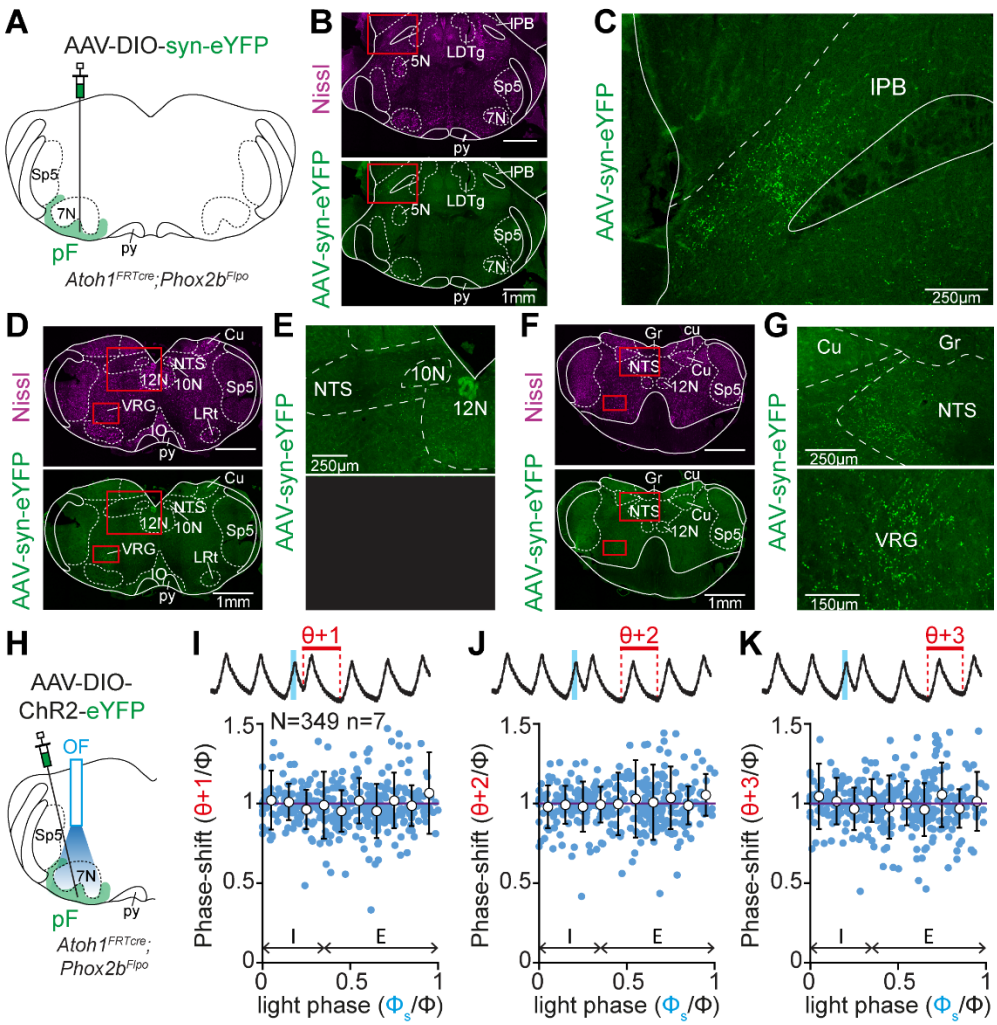

Figure S7: Outputs of the RTN$^{Phox2b/Atoh1}$ to other respiratory nuclei and extended data on RTN$^{Phox2b/Atoh1}$ photostimulation. (A) Schematics of the unilateral injection of an AAV-DIO-syn-eYFP in the parafacial respiratory region (pF) to transfect RTN$^{Phox2b/Atoh1}$ neurons in an *Atoh1^{FRTCre};Phox2b^{Flpo}* mouse line. **(B)** Low magnification at the level of the lateral parabrachial nucleus (lPB). Top, Nissl staining. Bottom, synapses from the RTN$^{Phox2b/Atoh1}$. **(C)** Magnification of the synapses from the RTN$^{Phox2b/Atoh1}$ in the lPB (red rectangle in **B**). Note that the RTN$^{Phox2b/Atoh1}$ projects to the lPB. **(D)** Low magnification at the level of the nucleus tractus solitarius (NTS) and ventral respiratory group (VRG). Top, Nissl staining. Bottom, synapses from the RTN$^{Phox2b/Atoh1}$. **(E)** Magnification of the synapses from the RTN$^{Phox2b/Atoh1}$ in the NTS (top red rectangle in **B**) and in the VRG (bottom red rectangle in **B**). Note that the RTN$^{Phox2b/Atoh1}$ projects to the VRG. **(F-G)** Same representations but at a more caudal level. Note the RTN$^{Phox2b/Atoh1}$ projects to the caudal NTS and VRG. **(H)** Schematics of the unilateral injection of an AAV-DIO-ChR2-eYFP in the RTN$^{Phox2b/Atoh1}$ in an *Atoh1^{FRTCre};Phox2b^{Flpo}*mouse line. **(I)** Top, whole body plethysmography recordings of respiratory cycles while a 50 ms stimulation (blue rectangle) is applied. The cycle n+1 following the perturbed cycle is annotated on the trace (θ+1). Bottom, plot of the phase-shift (perturbed cycle n+1 normalized to the control cycle: θ+1/ϕ) as a function of the light phase (light cycle normalized to the control cycle: ϕ_s/ϕ). Inspiration (I) and expiration (E) mean durations are annotated on the graph. A shortening of the perturbed cycle happens when values are under 1 (purple line). N=349 random trials, n=7 mice. **(J, K)** Similar representations for cycles n+2 (θ+2) and n+3 (θ+3). *Gr, Gracile nucleus. cu, cuneate fasciculus. See Figure 1 for all other abbreviations.*

DISCUSSION AND PERSPECTIVES

My PhD investigated integrative neurophysiology in motor systems. The work aimed at unravelling some key features between motor systems that support an accurate and timely control of behavior, crucial for animal survival.

A major part of my work has focused on one major example of crucial interaction between two, otherwise independent, motor behaviors: locomotion (running exercise) and breathing, and more precisely the influence of running exercise on breathing. Our study is the first to provide a precise examination of respiratory parameters changes as well as the temporal coordination of breaths to strides in mice. We first examined whether and how running exercise impacts breathing in mice (**Paper 1** (Hérent et al., 2020)). We demonstrate that immediate and sustained increase in respiratory rate during running is as an obligatory feature of exercise hyperpnea in mice. Also, we found that hyperpnea to exercise in mice is not dependent on limb velocity *per se*, but rather seems to depend on the locomotor context (treadmill vs overground run) or the engaged behavior (exploratory- vs escape-like behaviors). Importantly, we show, at least in mice, that the temporal synchronization of breaths to strides is not a hardwired component of exercise hyperpnea. Overall, this suggests that exercise hyperpnea 1) depends on a trigger signal at the onset and throughout exercise, 2) requires gait- or context-dependent specific signals to modulate the frequency, and 3) lacks phasic locomotor signals from sensory feedbacks or internal visceral oscillations, which would impose a synchronization of the two central commands. Therefore, we next looked for the neuronal, likely central, substrates in the locomotor and respiratory networks that would mediate exercise hyperpnea in the resourceful mouse model (**Paper 2**). We found the existence of at least two distinct central locomotor drives, targeting different respiratory centers, that modulate breathing in relation to running exercise. One descending excitatory drive from the prime locomotor center for initiation – the dorsal part of the MLR, the CnF – directly contacts the principal inspiratory generator – the preBötC – and can upregulate breathing prior to, and even in the absence of, locomotor movements. Another drive is excitatory and ascending from the lumbar executive circuits – the locomotor CPG – onto the expiratory generator – the parafacial respiratory region – and modulates breathing during ongoing locomotion.

1. Breakdown of the locomotor-respiratory phase-locking dogma

When searching through the literature during my PhD, a long-standing dogma stated that respiratory events are temporally phase-locked to locomotor movements in all species, even more so at the fastest speeds or gaits like gallop as compared to slower alternating gaits (Iscoe, 1981; Bramble and Carrier, 1983; Lafortuna et al., 1996; Simons, 1999; Boggs, 2002). Our study in running mice clearly demonstrates that breaths are never phase-locked to strides at any tested speeds from 15 to 50 cm/s, gaits (trot and gallop), and with or without incline. We should acknowledge that the analysis did not covered all possible speeds in running mice (Lemieux et al., 2016). However, further analyses on CnF stimulations experiments *in vivo*, which provided a complementary sample of triggered locomotor speeds ranging from 40 to 120 cm/s, will shortly settle this caveat. In any case, we already examined a wide range of trot as well as the fastest gait in mice (gallop) in two different locomotor contexts (treadmill and overground locomotion) and

behaviors (exploratory- and escape-like running). At first glance, our results seem to be contradicting previous work. As discussed in Chapter 1.1.5. and Paper 1 (Hérent et al., 2020), the strict temporal occurrence of breaths within the same part of the stride cycle has only been sparsely investigated (Iscoe, 1981; Bramble and Carrier, 1983; Bernasconi and Kohl, 1993; Lafortuna et al., 1996; Simons, 1999), yet it was assumed to exist in all species (Boggs, 2002; Stickford and Stickford, 2014). This assumption led researchers to consider the existence of phase-locking, notably in rodents, when searching for neuronal substrates of running hyperpnea (Morin and Viala, 2002; Giraudin et al., 2012). Pertinent cycle-to-cycle analysis studies, as done in this work, are therefore of the utmost importance when searching for the neuronal mechanisms responsible for phase-locking breaths to strides. Studies using clear cycle-to-cycle analysis however revealed heterogeneity between individuals from a constant degree of coupling to no coupling at all (Bramble and Carrier, 1983; Bernasconi and Kohl, 1993; Daley et al., 2013). In addition, large differences were reported between experienced and unexperienced runners (Bramble and Carrier, 1983). While experienced runners presented a tight phase locking, subjects with little to no serious running experience showed little to no tendency to temporally synchronize breaths and strides. Our results in trained mice, given free access to a running wheel combined with a 15 min daily training run on the treadmill, show that prior training does not lead to a temporal phase-locking in our conditions. Importantly, this does not mean that a temporal synchronization never occurs in mice. One should probably also take into consideration genetic variations in mice that affect on the one hand, exercise performance (Avila et al., 2017) and on the other hand, proper breathing (Tankersley et al., 1998; Menuet et al., 2011) with therefore possible incidence on adaptation of the latter to the former. Further experiments will be needed to ascertain the total absence of temporal synchronization in mice for example in running-performant mouse lines (Avila et al., 2017), by testing longer and more intense daily treadmill training sessions (Multon et al., 2003; Park et al., 2010) or even investigate other ambulatory modes like swimming which differ in sensory feedback contribution (Akay et al., 2014).

Altogether, we propose that the temporal synchronization of respiratory and locomotor movements is not a mandatory requirement to sustain aerobic exercise, at least in mice. We also stress the importance of pertinent cycle-to-cycle analysis to avoid ambiguous results which led to the assumption of evolutionary convergence across species. Based on this assumption, periodic signals from sensory feedbacks (and/or from the viscera) were investigated and proposed to drive the phasing of respirations to locomotor movements (Iscoe and Polosa, 1976; Bramble and Carrier, 1983; Palisses et al., 1988; Potts et al., 2005), even in rodents (Morin and Viala, 2002; Giraudin et al., 2012). Based on our results and the discrepancies in the literature, we however propose that phasic locomotor sensory or visceral signals are not hardwired mechanisms of exercise hyperpnea, although their contribution in other mechanisms cannot be excluded. Our results are otherwise is in accordance with studies showing an increase in ventilation in anticipation of, or prior to, exercise, during a mental exercise, or after removal of peripheral feedbacks (Butler and Woakes, 1980; Eldridge et al., 1981; Eldridge et al., 1985; Tobin et al., 1986; Fernandes et al., 1990; Decety et al., 1991; Decety et al., 1993; Thornton et al., 2001; Gariepy et al., 2012).

2. Hardwired features of exercise hyperpnea

Our study in mice confirms that an immediate (and sustained) increase in ventilation is an obligatory component of exercise hyperpnea, as observed by others in swimming lampreys

(Gravel et al., 2007), running cats (Eldridge et al., 1981; Eldridge et al., 1985) and running humans (Mateika and Duffin, 1995). Therefore, this fast and reliable respiratory feature seems preserved across vertebrates which highly suggests the involvement of shared behavioral and neuronal programming relevant for survival. We notably revealed two central neuronal pathways that could encode this feature in mice and might be conserved across species. This will be discussed later.

Exercise hyperpnea is classically described as dependent on the exercise speed and hence presumed to inherently depend on limb velocity in humans (Dejours et al., 1959; Duffin and Bechbache, 1983; Casey et al., 1987; Mateika and Duffin, 1995; Wells et al., 2007) as well as horses (Honda, 1985; Robinson, 1985), albeit little was known for other species. Our work revealed that the respiratory frequency and amplitude increase is not proportional to the locomotor speed or height in running mice, even for a wide range of trotting speeds on the treadmill. These results contrast at first glance with previous studies but corroborate with other work in lamprey and human (Kay et al., 1975; Berry et al., 1985; Gravel et al., 2007). One explanation could come from the method used to record respiratory activity through diaphragm inspiratory activity. Although the diaphragm rate is a great indicator of the preBötC-mediated inspiratory frequency, the diaphragm amplitude does not reflect the actual volume of the lungs. Indeed, additional respiratory muscles, i.e., expiratory and inspiratory accessory muscles, are typically recruited during an increased energetic demand like exercise to expand the rib cage further (Abraham et al., 2002; Sieck and Gransee, 2012; Aliverti, 2016). Therefore, even if respiratory frequency remains stable, the sequential recruitment of additional muscles, not accessed in this work, might increase the total volume of the lungs. It would be interesting to record the activity from these muscles to evaluate this. Others have already developed specific recordings, albeit in resting or anesthetized rodents (Pagliardini et al., 2011; Romer et al., 2017). In any case, even if these muscles are recruited during treadmill exercise, they do not impact on the frequency of inspirations in our study.

Some studies in human running on a treadmill suggested that respiratory variables are not dependent on the speed of repetitive leg movements but rather are tightly related to the metabolic demand (Kay et al., 1975; Berry et al., 1985). Thus, it is also possible that in our context of low to moderate exploratory-like exercise, the metabolic demand does not require a proportional increase in breathing frequency to maintain homeostasis. Interestingly, when mice engage in higher speeds or a higher gait (i.e., gallop) in a corridor, whether it is triggered by an air-puff (**Paper 1**, (Hérent et al., 2020)) or CnF stimulations (**Paper 2**), breathing frequency increases further than during treadmill sessions. Interestingly, CnF-driven increase in breathing was not highly dependent on the engaged locomotor speed but was significantly different at the lowest stimulation frequencies used (15-20 Hz). These results could reflect a difference in metabolic demands between two distinct locomotor contexts. In addition, during air puff-induced gallop, we found a reduction in the expiratory time (Te) which likely reflects the mobilization of active expiration. Further targeted recordings of abdominal muscles will be needed to ascertain this. Altogether, we propose that breathing parameters, rather than being dependent on the exercise speed, are modulated according to the behavioral context animals are engaged in. In a context of exploration, a fixe and stable increase in breathing would suffice to meet the energetic demand, while an escape-like locomotor context would require a further increase in breathing

through both increased breathing rate and the possible recruitment of active expiration. Interestingly, exploration and escape behaviors are encoded by supraspinal initiation centers (Capelli et al., 2017; Caggiano et al., 2018; Josset et al., 2018) and spinal executive circuits (Talpalar et al., 2013; Bellardita and Kiehn, 2015). Therefore, and in line with others, we propose that the sequential increase in breathing according to the locomotor context in mice might directly be mediated by central connections from key locomotor circuits to respiratory centers (Eldridge et al., 1985; Gariepy et al., 2012; Le Gal et al., 2014; Paterson, 2014; Le Gal et al., 2020).

3. Distinct locomotor circuits modulate breathing during exercise

A bulk of evidence points to a central connectivity as the major activatory signal for exercise hyperpnea, but only few neuronal substrates were actually identified. Our study in mice revealed that the brainstem control of respiration during exercise is mediated by, at least, two distinct locomotor drives.

We first show that the glutamatergic CnF component of the MLR, in addition to triggering running, upregulates breathing frequencies even before the movement begins (2.5 folds from resting conditions), and also when stimulations of the CnF do not trigger any movements (1.8 folds from resting conditions). This demonstrates that the glutamatergic CnF can modulate breathing independently from the activation of the locomotor CPG controlling limb movements, or of muscular sensory feedbacks. Similar results were found in MLR-stimulated cats and lampreys, suggesting an evolutionary convergence for the role of the MLR in respiratory adjustments (DiMarco et al., 1983; Eldridge et al., 1985; Gariepy et al., 2012). In cats, stimulation of the MLR also increases heart rate (Eldridge et al., 1985). Interestingly, breathing increase actually precedes spontaneous locomotor episodes in swimming lamprey, flying geese, and running cat, as well as a concomitant cardiovascular response (Butler and Woakes, 1980; Eldridge et al., 1985; Gariepy et al., 2012). And in humans, the mere anticipation or mental simulation of exercise suffices to increase breathing and heart rate (Tobin et al., 1986; Decety et al., 1991; Decety et al., 1993; Thornton et al., 2001). Therefore, one can speculate that this movement-independent upregulation of breathing by the CnF might help anticipating drastic metabolic changes that come with exercise, by priming respiratory and cardiovascular centers. Interestingly, the MLR is activated during a simulated exercise in a speed-dependent manner in humans (Jahn et al., 2008; Karachi et al., 2010), and its dorsal component the CnF (investigated in this study) encodes escape-like running speeds in mice through key inputs from limbic structures (Caggiano et al., 2018; Josset et al., 2018; Dautan et al., 2020). Therefore, the MLR might serve as a multifunctional key integrator to pilot autonomic responses associated with defensive behaviors, like respiratory and cardiovascular adjustments, before the planned movement is executed (Ryczko and Dubuc, 2013). Circuit wise, the same CnF neurons could be activated at different thresholds to activate autonomic responses without movement, or different neurons might target in parallel autonomic and locomotor centers. However, our work did not address this issue. The study in lampreys advocates for the latter possibility by showing segregated sets of MLR neurons directly contacting either respiratory- or locomotor-related circuits (Gariepy et al., 2012). Further investigations are needed in mice to ascertain this, using projection-based transsynaptic tracings from targeted respiratory and locomotor neurons directly targeted by the CnF (Pivetta et al., 2014; Ruder et al., 2016) as also used in Paper 3 (Annex 1, (Usseglio et al., 2020)).

Our results in mice further show that, upon CnF stimulations, the strongest increase in breathing rate occurs at the onset and throughout running episodes (about 4-fold from resting conditions), which is about 1.6-fold greater than prior to the movement. This suggests the existence of an additional drive from the spinal executive circuits, possibly from the locomotor CPG itself, polysynaptically contacted by the CnF through reticulospinal neurons (Grillner, 2003; Kiehn, 2006, 2016; Capelli et al., 2017; Caggiano et al., 2018). Indeed, we demonstrate that the sole activation of the lumbar locomotor CPG, in *ex vivo* neonatal brainstem-spinal cord preparations lacking the CnF and sensory afferences, was sufficient to increase respiratory-like activities significantly, as shown by others in neonatal rats (Morin and Viala, 2002; Le Gal et al., 2014; Le Gal et al., 2020). Interestingly, the lumbar CPG also encodes locomotor speeds and gaits (Lanuza et al., 2004; Crone et al., 2009; Talpalar and Kiehn, 2010; Bellardita and Kiehn, 2015) and could therefore provide key information about the locomotor state. Indeed, spinal CPGs have been shown to send ascending signals, i.e., efference copies, to locomotor supraspinal regions (Dubuc and Grillner, 1989; Matsushita, 1999; Fedirchuk et al., 2013; Stecina et al., 2013; Pivetta et al., 2014; Oueghlani et al., 2018) to adapt the locomotor command to ongoing movements, but also to regions related to other motor behaviors. For example, to maintain stable visual processing while moving, i.e., gaze stabilization, intrinsic feedforward spinal copies are sent directly to brainstem extraocular motoneurons to ensure visual acuity in swimming tadpoles (Lambert et al., 2012; Straka et al., 2018). Therefore, besides being highly specialized in generating and coordinating locomotor movements, we propose that the locomotor CPG also relays multifunctional information regarding ongoing movements to update rapidly and coordinate other motor behaviors like breathing, and possibly others autonomic centers that are essential to survival.

An unresolved question regards the identity of the spinal locomotor neurons that send the ascending drive. Importantly, we show that the glutamatergic lumbar CPG is required and sufficient to upregulate respiratory-like frequencies in *ex vivo* preparations and directly projects to respiratory centers in the brainstem (see next section). Within the spinal cord, different glutamatergic ventral subtypes have been previously shown to project directly to the brainstem. For example, V2a cervical interneurons (expressing *Chox10*) have been shown, by us (Paper 3, Annex 1, (Usseglio et al., 2020)) and others, to send ascending projections to the brainstem (Azim et al., 2014; Pivetta et al., 2014), and lumbar V2a are involved in the speed-dependent gait selection (Crone et al., 2008; Crone et al., 2009). However, anterograde tracing revealed that the V2a lumbar neurons do not project to the supraspinal regions (data not shown and (Azim et al., 2014)). Further experiments should therefore be designed to look for an ascending drive from other, non-V2a, classes of ventro-lumbar glutamatergic interneurons. For example, cervical V3 interneurons (expressing *Sim1*) project to the brainstem (Pivetta et al., 2014), and lumbar V3 interneurons mediate left and right coordination and might partly be involved in rhythm generation (Zhang et al., 2008; Kiehn, 2016). Other key lumbar subtypes might send efference copies to the brainstem, notably non-V2a *Shox2* (Dougherty et al., 2013) and *HB9* interneurons (Caldeira et al., 2017), involved in rhythm generation and the control of locomotor speeds, or interneurons mediating left/right interlimb coordination and controlling locomotor gaits, like $V0_V$ (expressing *Evx1,* (Talpalar et al., 2013; Bellardita and Kiehn, 2015)).

4. Distinct respiratory neurons integrate different locomotor drives

Our study revealed that the locomotor drives presented above upregulate breathing through distinct respiratory targets in the respiratory CPG.

The fact that CnF-mediated breathing increase can be separated from the movement suggests that the CnF might target brainstem respiratory centers independently or prior to the movement. Using anterograde tracing, we show that the glutamatergic CnF directly contacts the inspiratory generator, the preBötC (Smith et al., 1991; Feldman and Del Negro, 2006; Del Negro et al., 2018). A recent study has revealed brain presynaptic inputs onto a subset of glutamatergic preBötC neurons expressing somatostatin (Yang et al., 2020b). The CnF was not documented as a presynaptic region, although it was not clear from the figures whether no presynaptic cells were present in the CnF or if it was simply overlooked. As previously shown in the lab, a large subset of glutamatergic preBötC neurons expresses the transcription factor *Dbx1* and constitutes the core circuit for generating inspiratory rhythm (Bouvier et al., 2010). In addition, a large fraction of glutamatergic and commissural preBötC neurons are *Dbx1* and are crucial to synchronize the rhythm (Bouvier et al., 2010; Wu et al., 2017). Unfortunately, the expression of *Dbx1* is downregulated in the adult (Pierani et al., 2001), precluding the use of classic Cre-dependent viral tools to trace from these genetically defined cells. To overcome this issue, we used retrograde transsynaptic viral tools from the preBötC sharing the glutamatergic and commissural identity. We reveal that the CnF directly contacts the glutamatergic and commissural preBötC, key candidate for generating and synchronizing inspiration (Thoby-Brisson et al., 2005; Bouvier et al., 2010; Wu et al., 2017). Importantly, we revealed that short stimulations of the glutamatergic CnF fibers in the preBötC can directly modify the timing of respiratory bursts in a phase dependent manner (phase-shift), especially during the expiratory phase. This suggests that the excitatory CnF has access to inspiratory rhythm generation mechanisms in the preBötC, possibly via glutamatergic neurons (Funk et al., 1993; Gray et al., 2001). Interestingly, the phase dependent shift we observed from activating the CnF terminals in the PreBötC, predominant in the expiratory phase, resembles the effect of short pulse stimulations applied directly onto *Dbx1*-derived preBötC neurons, in anesthetized mice (Cui et al., 2016; Baertsch et al., 2018). Therefore, we hypothesize that the glutamatergic CnF might directly contact the *Dbx1*-derived inspiratory rhythmogenic circuits. Future experiments should ascertain this hypothesis and further dissect the exact genetic identity of targeted preBötC cells. We should take advantage of available tools to label preBötC *Dbx1*-derived neurons up to adulthood (*Dbx1*^{ERT2Cre} crossed with a floxed reporter line, (Kottick et al., 2017)), trace from glutamatergic flippase-expressing CnF neurons (*Vglut2*^{Flpo} mouse line, JAX #030212) using Flpo-dependent AAVs, and searched for putative boutons onto *Dbx1*-expressing preBötC neurons. Alternatively, presynaptic partners of *Dbx1*-expressing preBötC neurons could be transsynaptically traced in a dedicated genetic background where the transient *Dbx1*^{Cre} conditionality can be replaced by a permanent Flpo conditionality through Cre-recombination of a flippase expressing floxed allele (*LsL-TauFlpo*^{INLA}, (Pivetta et al., 2014)).

In contrast with the CnF-mediated drive, our anterograde tracing demonstrates that the glutamatergic ventro-lumbar spinal cord does not target the preBötC but rather contacts directly the other essential oscillator of the respiratory CPG, the parafacial respiratory region (pF) implicated in the modulation of the respiratory rhythm (Guyenet and Mulkey, 2010; Del Negro et al., 2018; Pisanski and Pagliardini, 2019). Anterograde transsynaptic tracing from the lumbar

spinal cells revealed that postsynaptic cells in the pF are mostly located ventral and median to the facial motor nucleus, corroborating our anterograde tracing.

I should note that the definition of the pF is very confusing in the literature owing to its presumed implication in multiple functional tasks that rest on non-overlapping anatomical locations and variable molecular identities that too rare efforts have attempted to crisscross. Many studies have imputed distinct functions (inspiratory generation, chemoception and conditional expiratory generation) depending on its developmental stage (embryonic, perinatal, juvenile, adult), anatomical locations (ventro-median, ventro-lateral edges of the facial motor nucleus, or lack thereof), neurotransmitter identity (glutamatergic, non-catecholaminergic), peptidergic (Galanin (Stornetta et al., 2009), Neuromedin B (Shi et al., 2017)) and genetic identity (mainly *Phox2b*). For example, the rhythmogenic parafacial respiratory group (pFRG), coupled to the preBötC, drives inspiration at embryonic and perinatal stages, expresses *Phox2b* and retains its rhythmicity in later stages (Onimaru et al., 1987; Mulkey et al., 2004; Onimaru 2008). The parafacial respiratory region (pF) that conditionally generates expiration at juvenile and adult stages, is presumably located in the ventro-lateral part of the facial motor nucleus in anatomical overlap with the pFRG while its genetic identity is not well defined (Abbott et al., 2009; Marina et al., 2010; Pagliardini et al., 2011; Del Negro et al., 2018). The chemosensitive parafacial area termed RTN retains its function from perinatal to adult stages, is presumably located in the ventro-medial part of the facial motor nucleus and expresses *Phox2b* but in adults its neurons are tonically active and not rhythmically active (Mulkey et al., 2004; Stornetta et al., 2006; Guyenet and Bayliss, 2015; Guyenet et al., 2016). Finally, several interventional studies targeting parafacial neurons using their *Phox2b* signatures will not discriminate RTN neurons from nearby C1 adrenergic neurons regulating cardiovascular function. These examples illustrate the necessity today to replace sheer anatomical boundaries based on cytoarchitectonic criteria by a delineation of brain areas integrating precise molecular identity of resident neurons. Presumably, this will help dissecting specific neurons with dedicated executive implications whose molecular mappings will eventually unveil the intermixing granulosity. Finally, in direct interest to my work, the lumbar spinal cord projects mostly to the ventro-median part of the pF which overlaps with the location of *Phox2b* chemosensitive neurons of the RTN (Stornetta et al., 2006; Huckstepp et al., 2015; Del Negro et al., 2018).

Consequently, in my work, I resorted to investigate the role, in the parafacial area, of the RTN chemosensitive center defined, notably by elegant studies in the lab, as hosting neurons having combined histories of expression of *Egr2*, *Phox2b, Atoh1, Lbx1,* and *vGlut2* and that importantly can be selectively accessed through a *Phox2b/Atoh1* intersectional genetic strategy (Ramanantsoa et al., 2011; Ruffault et al., 2015). In line with that, we used the genetic mutation (*Egr2*^{Cre}*; Phox2b*^{27AlaCKI}) that specifically leads to the demise of *Atoh1/Phox2b* RTN cells during development (Ruffault et al., 2015). Remarkably, we show that this genotype leads to abrogation of the respiratory increase triggered by pharmacological activation the locomotor CPG, in *ex vivo* neonatal preparations. This result is in accordance with a previous study in neonatal rat that used broad lesion of the pF without proper genetic identification (Le Gal et al., 2014). Hence, we demonstrate the implication of RTN$^{Phox2b/Atoh1}$ cells in mediating lumbar CPG-induced increase in breathing. Corroborating this, we show that silencing RTN$^{Phox2b/Atoh1}$ neurons in adult mice greatly reduced exercise hyperpnea during treadmill exercise. This together demonstrates that the activity of RTN neurons is upregulated by locomotor activity and establishes the RTN as a "locomotor-ceptive" respiratory center, i.e., a structure hosting neurons whose activity is

changed during a locomotor challenge (locomotor-sensitive) and whose change of activity will be reflected in an adaptive change of respiration (locomotor-ceptive). Interestingly, silencing the *Phox2b*-expressing pF (and neighboring C1 cells), using chemogenic tools, was previously shown to markedly reduce exercise capacity, inferred by the total distance rats were able to cover until a point of exhaustion (Korsak et al., 2018). Jointly, this argues for a role of the pF expressing *Phox2b*, and likely *Atoh1*, in maintaining an optimal increased respiratory response during exercise and determines exercise performance by integrating locomotor signals from the locomotor CPG. It is therefore striking that the same structure may take part in the upregulation of respiratory rates through a seemingly continuous implication that may sequentially first rely on its locomotor-ceptive role (at a time when exquisite sensitivity to blood CO_2 has no object), and possibly later, on combined locomotor-ceptive and chemoceptive roles when the oxygen supply takes priority over the need to keep CO_2 constant as the metabolic cost of locomotion rises.

Admittedly, we should acknowledge a potential underestimation of the effect of silencing the RTN$^{Phox2b/Atoh1}$ on exercise hyperpnea in our chemogenetic silencing experiments. Indeed, *Atoh1/Phox2b* cells might express different levels of the Gi-coupled DREADD receptor (hM4Di) leading to varied efficiency from cells to cells. Also, the method used to deliver the agonist CNO by intraperitoneal injection might not be optimal. Indeed, in our work on V2a neurons (Paper 3, Annex 1, (Usseglio et al., 2020)), we used intracranial injections of CNO directly onto hM4Di-expressing cells in the gigantocellular nucleus, as intraperitoneal CNO injections were less effective. However, our experiments during running require the implantation of diaphragm EMG which entails to cover the skull with cement and thus precludes subsequent intracranial injections. However, intracranial CNO injections can be directed by prior implantation of a cannula (Mahler et al., 2014; Stachniak et al., 2014; Lichtenberg et al., 2017) and further experiments should implement this approach to ensure maximum efficiency.

One important caveat of this work is that, although our results 1) ascertain a direct synaptic connectivity from the locomotor CPG to the pF (anterograde tracing and anterograde transsynaptic tracings) and 2) demonstrate the implication of the RTN$^{Phox2b/Atoh1}$ (elimination or silencing), they do not establish a direct connectivity from the lumbar CPG onto the genetically defined RTN$^{Phox2b/Atoh1}$. Efforts were made to trace presynaptic cells of the RTN$^{Phox2b/Atoh1}$. However, every attempt during my PhD, although successfully revealed starter cells, has failed to reveal their presynaptic neurons (data not shown). Even attempts using the *Vglut2*^{Cre} line, otherwise effective in presynaptic tracing from the preBötC, were unsuccessful. Thus, synaptic inputs onto the RTN$^{Phox2b/Atoh1}$, and more broadly onto the pF, seem refractory to rabies-mediated transsynaptic jump, which could come from a difference in synaptic strength (i.e., number of contacts on pF cells) or location of synapses onto these neurons (Callaway and Luo, 2015), as compared to structures successfully traced in the lab (preBötC in this study, and V2a neurons in Paper 3, Annex 1, (Usseglio et al., 2020)).

We next thought to understand how the RTN$^{Phox2b/Atoh1}$ integrates locomotor inputs to produce an adaptive respiratory response during exercise. Our results show that the RTN$^{Phox2b/Atoh1}$ directly projects to the inspiratory generator the preBötC and mediates an increase in breathing once photoactivated. Therefore, the downregulation of breathing observed during running on the treadmill might be explained by the silencing of the direct inputs onto the preBötC. Interestingly, we found that short activations of the RTN$^{Phox2b/Atoh1}$ trigger a reduction of the perturbed respiratory cycle with the maximum effect starting earlier that CnF-mediated phase

shift, in inspiration. We also observed a lengthening of perturbed cycle at the end of expiration which was not observed following CnF stimulations. This suggests that the RTN$^{Phox2b/Atoh1}$ has access to different rhythm generating mechanisms than the CnF. The inspiratory and late expiratory effects following short pulse stimulations have been documented when stimulating directly inhibitory preBötC neurons in anesthetized mice (Baertsch et al., 2018). In addition, transsynaptic tracings from glutamatergic preBötC neurons revealed few presynaptic cells in the pF. Therefore, we propose that the RTN$^{Phox2b/Atoh1}$ targets different preBötC cell types than those from the CnF, including inhibitory neurons, to add an additional drive to exercise hyperpnea mediated by spinal executive circuits. Further experiments to trace from the inhibitory preBötC should ascertain this.

5. Relative contribution of the two pathways

Our work in mice revealed the implication of at least two distinct locomotor pathways, at the level of the initiation and execution of the movement, able to upregulate breathing in relation to running exercise. We found that each pathway targets different key respiratory neurons in the brainstem. The first drive originates from the glutamatergic CnF which upregulates breathing independently from the movement and sends a descending drive to the glutamatergic preBötC. The second drive originates from the glutamatergic locomotor CPG which increases breathing during locomotion and sends an ascending drive directly to the pF. The genetically defined RTN$^{Phox2b/Atoh1}$ is a key integrator of the ascending spinal locomotor drive and projects to the preBötC. But what is the relative contribution of the two neuronal pathways?

The CnF-mediated respiratory response can occur prior to the movement, suggesting that activation of the locomotor CPG is not necessary to upregulate breathing before exercise. However, the activation of the lumbar CPG triggers an increase in respiration during locomotion in reduced preparations lacking the CnF, suggesting that the drive from the lumbar CPG can operate independently from the CnF. Also, we show that silencing the RTN$^{Phox2b/Atoh1}$ during running reduces, but does not abolish, exercise hyperpnea. This could either suggest a methodological underestimation of the effect discussed previously, or a persistence of the excitatory drive from the CnF during movement, or probably both. Interestingly, recent investigations have shown that CnF neurons are active during the entire photostimulation and during treadmill exercise (Caggiano et al., 2018; Josset et al., 2018). Altogether, this suggests that both pathways might operate in synergy to set respiratory responses both in anticipation (CnF) and during running (CnF + locomotor CPG) to meet with the drastic metabolic changes associated with exercise.

Importantly, our data support the existence of different targets in the preBötC. The CnF directly contacts glutamatergic preBötC neurons while the RTN$^{Phox2b/Atoh1}$ might target a combination of glutamatergic and inhibitory neurons. This is very interesting when looking at the role of excitation and inhibition in generating inspiratory rhythm in the preBötC. Glutamatergic preBötC neurons are necessary and sufficient for rhythmogenesis, albeit the produced rhythm is slow and not so flexible (Smith et al., 1991; Gray et al., 2001; Bouvier et al., 2010; Baertsch et al., 2018), while inhibitory preBötC neurons cannot produce the rhythm *per se* (Janczewski et al., 2013; Sherman et al., 2015; Baertsch et al., 2018). Interestingly, boosting phasic inhibition in the preBötC triggers a reduction of the refractory period for glutamatergic preBötC bursting, which increases excitability of glutamatergic preBötC neurons and triggers rapid breathing (see Chapter

2.II.1., (Baertsch et al., 2018)). In this elegant work the authors added that, as a result of phasic activation of inhibitory preBötC neurons, the "*frequency was increased beyond the maximum possible frequency predicted by the refractory period*". This means that inhibitory preBötC neurons are critical for eliciting a wider range of inspiratory frequencies and granting flexibility over a higher frequency spectrum. Therefore, we advocate for the recruitment of glutamatergic preBötC neurons (possibly *Dbx1-derived*) by the CnF in anticipation and during exercise to upregulate breathing up to a certain point, fixed by intrinsic refractory period of the glutamatergic preBötC. Once the movement is engaged, additional inputs onto inhibitory preBötC neurons from the RTN$^{Phox2b/Atoh1}$, activated by the spinal drive, would allow for a further increase in breathing, which would support flexibility to overcome the metabolic demand that comes with different locomotor contexts.

To ascertain this, further experiments should concentrate on dissociating the action of the locomotor CPG and the CnF during the movement. Some attempts were made in this sense during my PhD (data not shown). In particular, we tried to acutely silence the locomotor CPG using virally driven chemogenic tools in the glutamatergic spinal cord, as well as injecting xylocaine in the spinal cord to block axonal conduction. However, these methods did not work as animals were still able to engage and maintain locomotor activity. This further corroborates the fact the chemogenic silencing of the RTN$^{Phox2b/Atoh1}$ might be underestimating its functional impact on exercise hyperpnea. For ethical reasons, no attempts were made to physically cut the descending locomotor pathways in the spinal cord. Another experiment could take advantage of our brainstem-spinal cord *ex vivo* preparations in which the CnF would be preserved. This approach would allow to activate the CnF/MLR using optogenetics or electrical stimulations and record inspiratory frequency change before and after removal of the spinal cord to assess the relative contribution of the two locomotor drives.

6. Perspectives

Our results do not speak to the possible influence of other neuronal locomotor descending and ascending pathways. For example, the diencephalic locomotor region (DLR), the other presumed locomotor center, is able to initiate and drive graded locomotion in cats, rats, and lampreys (Orlovsky, 1969; Parker and Sinnamon, 1983; El Manira et al., 1997; Ménard and Grillner, 2008), and is required for engagement in spontaneous locomotion (Shik and Orlovsky, 1976). Importantly, electrical or pharmacological activation of the DLR triggers locomotion and is associated with similar respiratory and cardiovascular changes as MLR stimulation, prior to and during the movement (Eldridge et al., 1981; DiMarco et al., 1983; Eldridge et al., 1985). Therefore, we cannot exclude the potential contribution of the DLR in sending a parallel drive directly to respiratory centers, or indirectly through the MLR, in anticipation and during locomotion. However, its exact location and precise cell types are yet to be clearly identified in mammals to address its implication in autonomic responses in running mice.

Another descending drive could also originate from brainstem reticulospinal neurons activated upon MLR-evoked locomotion and directly contacting the locomotor CPG (Gariepy et al., 2012; Juvin et al., 2016; Ryczko et al., 2016; Capelli et al., 2017). In lampreys, activation of reticulospinal neurons seems to precede bouts of swimming (Brocard and Dubuc, 2003; Juvin et al., 2016). Reticulospinal neurons could therefore also be candidates to mediate respiratory changes prior to and during running. In particular, the glutamatergic lateral paragigantocellular nucleus (LPGi), located in the caudal brainstem, has been previously identified as able to initiate

and control locomotor speed in mice (see Chapter 3.II.3., (Capelli et al., 2017)). The LPGi is contacted directly by the MLR, preferentially from the CnF, directly projects to the ventral lumbar cord and its ablation during MLR stimulation greatly impairs high-speed locomotion (Capelli et al., 2017; Caggiano et al., 2018). In addition, the LPGi lies very closely to the preBötC and the pF regions which might be an advantage in relaying fast and precise information about the descending locomotor command. Also, brainstem reticulospinal neurons V2a (expressing *Chox10*) have been shown to promote regular breathing pattern by providing a tonic excitatory drive to the preBötC in neonatal mice (Crone et al., 2012). Whether such connection and function are preserved in the adult and whether they overlap with V2a neurons controlling locomotor- and orienting-related responses (Paper 3, Annex 1, (Usseglio et al., 2020)) remains to be investigated.

Admittedly, we cannot exclude that in addition of the RTN$^{Phox2b/Atoh1}$, the lumbar CPG drive might target other supraspinal respiratory neurons and further contribute to mediate exercise hyperpnea. For example, we show that lumbar spinal neurons project densely to the lateral parabrachial/kölliker-fuse nucleus (lPB/KF), notably involved in facilitating respiratory phase transitions (Dutschmann and Herbert, 2006; Mörschel and Dutschmann, 2009). This region was previously implicated in relaying sensory afferences information to respiratory centers and reset respiratory rhythm in neonatal and juvenile rats (see Chapter 2.II.3.b., (Potts et al., 2005; Giraudin et al., 2012)). In addition, the lPB/KF is contacted by cervical neurons projecting to the lumbar spinal cord, which have been shown as crucial for limb coordination notably in high speed locomotion (Ruder et al., 2016). Therefore, the lPB/KF could convey information from lumbar spinal interneurons and relay locomotor signals about the state of locomotion.

Others ascending pathways from the spinal cord could also provide an additional drive during ongoing locomotion. Indeed, pharmacological activation of the locomotor CPG at the cervical spinal cord level was previously shown to mediate respiratory changes in *ex vivo* brainstem spinal cord preparations of neonatal rats, although in contrast with the lumbar spinal cord, respiratory changes rely on non-glutamatergic cervical neurons (Le Gal et al., 2020). Upon confirmation in mice with specific activation of cervical inhibitory neurons, these cervical efference copies might originate from inhibitory V1 interneurons (expressing *En1*), that project directly to the brainstem (Pivetta et al., 2014). Cervical spinal copies have been previously implicated in reaching and grasping behaviors (Azim et al., 2014) and could therefore mediate breathing changes associated to motor behaviors, beyond locomotion, involving forelimb movement.

7. General conclusion

My work has addressed the neural bases of the interface between breathing and locomotion which are both vital, comparatively simple, and evolutionary conserved behavior in vertebrates. I aimed at identifying the principles by which neuronal circuits interact and orchestrate accurate and timely adapted control of behavior. I sought to understand how the nervous system can modulate a permanent rhythmic activity and pattern adaptive neuronal drives that ensure homeostatic breathing.

On the one hand, by analyzing jointly respiratory and locomotor movements, I proved wrong the assumption that respiratory adaptation to exercise takes place, at least in the preferred mammalian model (mice) used to study motor systems, through a neural architecture enforcing a phasing of respiratory sequences of activity to locomotor ones. On the other hand, my study

clearly highlights that exercise hyperpnea rests on at least two distinct modulatory drives onto the respiratory rhythm generator, one from locomotor initiation (CnF) and one from locomotor execution (lumbar CPG) levels. I uncovered new roles for respiratory and locomotor structures beyond and thus expanding those defining them. On the locomotor side, the CnF is shown to increase respiratory rates before, or even in the absence of locomotion, so that this module critical for locomotor initiation is unexpectedly also a *bona fide* module ensuring respiratory modulation. On the respiratory side, our work expands the adaptive respiratory ambition of the RTN$^{Phox2b/Atoh1}$ from sheer chemoception to "locomotor-ception". Both the CnF directly, and the lumbar CPG through a relay in the RTN$^{Phox2b/Atoh1}$, are shown to target the preBötC. This opens avenues for a comprehensive view of the articulation of these drives onto a distinct balance of excitatory and inhibitory preBötC neurons suggested here to enable flexibility of respiratory frequency adaptation. This work constitutes a contribution to the current advancements in neurobiology whereby multifunctionality of neural circuits is ever more often the rule, than the exception.

ANNEX 1: Paper 3

Article

Current Biology

Control of Orienting Movements and Locomotion by Projection-Defined Subsets of Brainstem V2a Neurons

Graphical Abstract

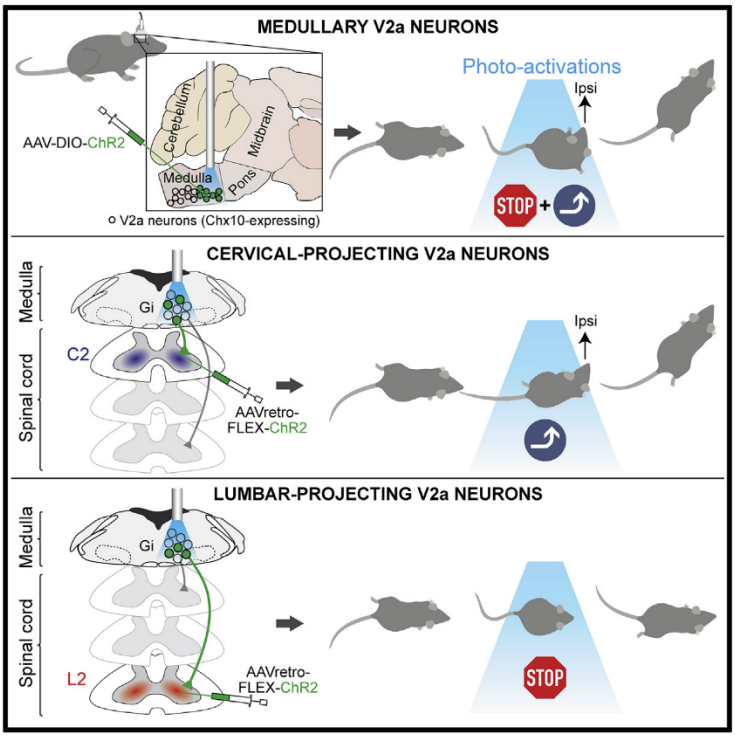

Highlights

- Brainstem V2a neurons control orienting movements, locomotor speed, and trajectory
- Distinct V2a subsets contact the cervical and lumbar spinal segments
- Cervical-projecting V2a neurons govern the head orientation and the path trajectory
- Lumbar-projecting V2a neurons are dedicated to control locomotor velocity

Authors

Giovanni Usseglio, Edwin Gatier, Aurélie Heuzé, Coralie Hérent, Julien Bouvier

Correspondence

julien.bouvier@cnrs.fr

In Brief

Usseglio et al. demonstrate that V2a neurons, a genetically circumscribed class of excitatory reticular neurons, control multiple motor actions linked to orientation. Using viral tracings and circuit optogenetics, they further uncover a modular organization of this neuronal class, with projection-defined subtypes that each support one motor action.

Usseglio et al., 2020, Current Biology *30*, 1–17
December 7, 2020
https://doi.org/10.1016/j.cub.2020.09.014

CellPress

Current Biology

CellPress
OPEN ACCESS

Article

Control of Orienting Movements and Locomotion by Projection-Defined Subsets of Brainstem V2a Neurons

Giovanni Usseglio,[1] Edwin Gatier,[1] Aurélie Heuzé,[1] Coralie Hérent,[1] and Julien Bouvier[1,2,*]
[1]Université Paris-Saclay, CNRS, Institut des Neurosciences Paris-Saclay, 91190 Gif-Sur-Yvette, France
[2]Lead Contact
*Correspondence: julien.bouvier@cnrs.fr
https://doi.org/10.1016/j.cub.2020.09.014

SUMMARY

Spatial orientation requires the execution of lateralized movements and a change in the animal's heading in response to multiple sensory modalities. While much research has focused on the circuits for sensory integration, chiefly to the midbrain superior colliculus (SC), the downstream cells and circuits that engage adequate motor actions have remained elusive. Furthermore, the mechanisms supporting trajectory changes are still speculative. Here, using transneuronal viral tracings in mice, we show that brainstem V2a neurons, a genetically defined subtype of glutamatergic neurons of the reticular formation, receive putative synaptic inputs from the contralateral SC. This makes them a candidate relay of lateralized orienting commands. We next show that unilateral optogenetic activations of brainstem V2a neurons *in vivo* evoked ipsilateral orienting-like responses of the head and the nose tip on stationary mice. When animals are walking, similar stimulations impose a transient locomotor arrest followed by a change of trajectory. Third, we reveal that these distinct motor actions are controlled by dedicated V2a subsets each projecting to a specific spinal cord segment, with at least (1) a lumbar-projecting subset whose unilateral activation specifically controls locomotor speed but neither impacts trajectory nor evokes orienting movements, and (2) a cervical-projecting subset dedicated to head orientation, but not to locomotor speed. Activating the latter subset suffices to steer the animals' directional heading, placing the head orientation as the prime driver of locomotor trajectory. V2a neurons and their modular organization may therefore underlie the orchestration of multiple motor actions during multi-faceted orienting behaviors.

INTRODUCTION

Our capacity to continuously adjust our attention and directional heading in response to internal goals or external stimuli is vital. It supports a large panel of behaviors including spatial navigation, exploration of the environment, feeding, and defense. In order to achieve this, animals mobilize lateralized motor actions that are often tightly coupled. In the animal's reference frame, coordinated movements of the head, the eyes, and in rodents, the orofacial sensors represent the primary mean to displace the visual axis and the sensory apparatus toward a point in space [1–3]. When the animal is on the move, these "strict" orienting responses are accompanied by a change in limb activity to reduce locomotor speed, to allow fixation and exploration of a fixed cue, and/or when needed, to change the path trajectory. How the brain orchestrates these multiple motor actions is still only partly resolved. Additionally, the mechanical substrate for trajectory changes during ongoing locomotion, whether it is head orientation [4–6], an asymmetric descending drive to limb controllers [7, 8], or a combination of both, has remained speculative. Much attention has been given to circuits for sensory integration, mainly to the superior colliculus (SC; reviewed in [9]). This midbrain structure synthesizes inputs from different sensory modalities and controls spatially targeted motion in the large sense, including head-eye responses, orofacial movements, and locomotor trajectory [10–14]. However, the cells and circuits that are downstream of the SC and relay orienting commands to the adequate motor groups have remained elusive.

The reticular formation (RF) of the pons and medulla is well known to control movements and is a candidate relay of orienting commands. First, the output layers of the SC project abundantly to the RF [15, 16]. Second, it hosts the circuits for ocular and orofacial movements [17, 18] as well as reticulospinal (RS) neurons that directly reach the spinal cord [19]. In particular, neck motoneurons of the upper cervical spinal cord that control the head orientation are contacted by RS neurons of the gigantocellular (Gi) reticular nucleus [20–22]. The timing and velocity of hindlimb movements, controlled by the lumbar spinal cord [23, 24], are also critically dependent on descending signals from the Gi and adjacent nuclei [25–28]. Third, left-right unbalanced activation or inhibition of the RF has been linked to head orienting movements [26, 29] and to the steering of swimming in the lamprey [8] and of locomotor-like activities on neonatal rat *in vitro* preparations [7]. However, these investigations did not determine the identity of reticular neurons that are downstream of the SC and mediate orienting responses, or examine their

CellPress
OPEN ACCESS

Current Biology
Article

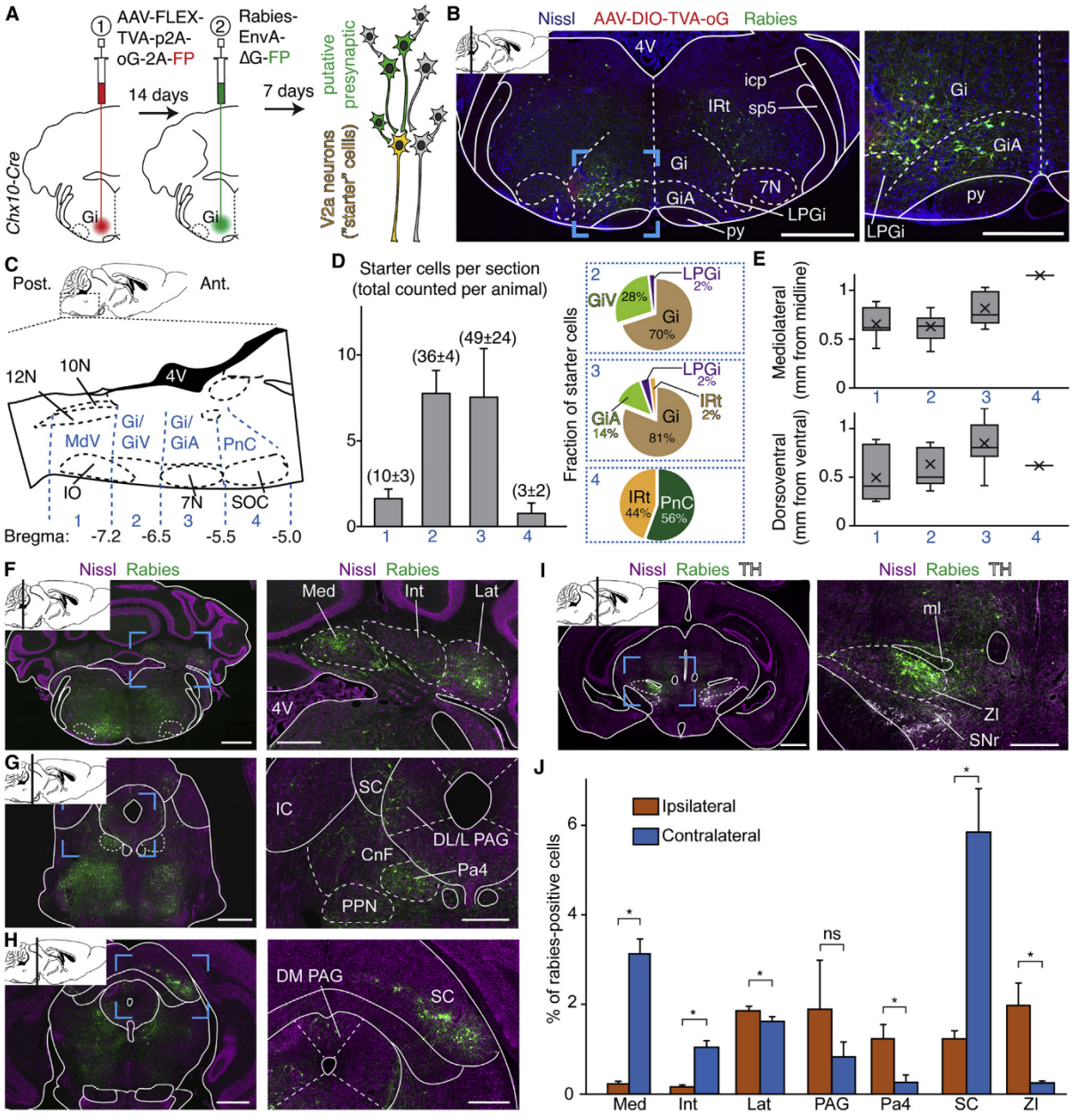

Figure 1. Retrograde Transneuronal Viral Strategy Reveals the Upstream Circuits of V2a Gi Neurons

(A) Schematics of the injection of the helper virus coding TVA and oG (1) and the EnvA-ΔG-rabies (Rb) virus (2) unilaterally in the left Gi of a *Chx10-Cre* adult mouse.

(B) Transverse brainstem section at the level of the injection site showing V2a neurons transfected with the helper virus (red), those co-transfected with the Rb virus ("starter" cells, yellow), and their putative presynaptic partners (Rb only, green), on a Nissl background (blue). Scale bar, 1 mm. Inset to the right is an enlargement of the blue boxed area. Scale bar, 500 μm.

(C) Sagittal schematic of the brainstem indicating the rostrocaudal levels (1 to 4) used for reporting starter cells.

(D) Bar graph showing the average number ± SEM of starter cells per histological section, and in brackets the average total ± SEM per animal, at the 4 rostrocaudal levels (total starter cells counted: 299 from 3 animals; average per animal: 100 ± 29). Pie graphs to the right show the distribution, within rostrocaudal levels 2, 3, and 4, of starter neurons in the indicated subnuclei (in percent of all starter cells at each level, pooled from the 3 animals). All cells at the rostrocaudal level 1 were in the MdV. See STAR Methods for the delineation of brainstem nuclei.

(E) Mediolateral (top, in mm from the midline) and dorsoventral (bottom, in mm from the ventral border) positions of starter cells at each rostrocaudal level (pooled from 299 cells from 3 animals) presented as the mean (crosses) and box-and-whisker plots, which give the median, 25th and 75th percentiles, and range.

(F–I) Transverse sections showing Rb^+ cells (green) at various rostrocaudal locations on a Nissl background (magenta). A tyrosine hydroxylase staining (TH, gray) is added in (I) to identify the SNr. Scale bars, 1 mm and 500 μm (insets).

(legend continued on next page)

implication to trajectory changes during limbed locomotion *in vivo*. Another significant gap of knowledge concerns the possibility for a synergistic control of distinct motor actions by a unique population, or by instead distinct subsets, of reticular neurons. Specifically, movements of the head, orofacial sensors, and locomotor velocity and direction are often tightly coupled [1, 2, 4, 5], and the existence of reticular neurons with branched axonal collaterals [19, 21] raises the possibility for a common control by a unique neuronal population. Yet this remained to be supported experimentally.

Here we investigated the possibility that brainstem V2a neurons, a genetically circumscribed neuronal class defined by the expression of the transcription factor Chx10 [30, 31], may control orienting motor actions. Indeed, they represent a subgroup of excitatory glutamatergic neurons located in the ventral RF, including in the Gi nucleus [32, 33]. Photo-activation of V2a Gi neurons in mice unexpectedly depresses spinal locomotor circuits [34], and this function could participate in steering locomotor trajectory [35]. Second, V2a neurons collectivity send both local and spinal projections [32–36], raising the possibility that this population, or subsets thereof, may drive other motor actions in synergy with limb control. However, these neurons have globally not been incorporated into the framework for studying orientation and nothing is known about their putative diversity.

Using transneuronal viral tracings, we show that V2a Gi neurons receive putative inputs from the contralateral SC, making them candidates for relaying lateralized orienting commands. Next, we found that unilateral photo-activations of V2a Gi neurons both evoked orienting-like motor responses on still animals and can halt and steer the locomotor trajectory when animals are on the move. Finally, and this is a major finding reported here, we reveal distinct functional subsets of V2a RS neurons with at least (1) a lumbar-projecting subset that controls locomotor velocity, but does not impact trajectory even when activated unilaterally, and (2) a cervical-projecting subset dedicated to head orientation and whose activation suffices to steer locomotor trajectory. These findings establish that multiple motor components of orientation are controlled by distinct reticular neurons that share a common genetic identity but that differ in their efferent connectivity. Furthermore, our work argues that the head orientation acts as the prime driver for steering locomotor trajectory.

RESULTS

V2a Gi Neurons Receive Putative Inputs from the Contralateral Superior Colliculus

To address whether V2a Gi neurons are embedded in circuits for orientation, we used a genetically restricted two-virus approach [37] to anatomically reveal their putative inputs (Figure 1A). Specifically, a cre-dependent AAV helper vector (AAV-DIO-TVA-oG-GFP; STAR Methods) was injected unilaterally in the Gi of *Chx10-Cre* adult mice [34, 38, 39], followed by a G-deleted and EnvA-pseudotyped rabies (Rb) virus coding mCherry. We aimed at transfecting V2a neurons unilaterally and located within the intermediate and rostral medullary reticular formation, i.e., rostrocaudal levels that house the Gi and its ventral and alpha parts (GiA/GiV; Figures 1B–1D) where V2a neurons that arrest locomotion are located [34]. Occasional starter cells were found in the adjacent intermediate reticular nucleus (IRt) and the lateral paragigantocellular nucleus (LPGi; Figure 1D), also known to contain V2a neurons [36]. Transneuronally labeled neurons, i.e., expressing only the Rb-driven fluorophore, were detected throughout the brainstem and to a lower extent in the diencephalon. A large proportion of Rb-positive cells was found in the medullary and pontine reticular formations, both ipsilaterally (15% ± 2% of total Rb^+ cells) and contralaterally (15% ± 3%). Aside from this local connectivity, labeling was detected in the deep cerebellar nuclei with various degrees of lateralization (Figures 1F and 1J). In the midbrain, confined labeling was seen in the periaqueductal gray and the mesencephalic reticular formation, notably in what may correspond to the paratrochlear nucleus (Pa4; Figures 1G and 1J). We found no Rb^+ cells in the cuneiform and pedunculopontine nuclei (CnF and PPN; Figure 1G), forming the mesencephalic locomotor region that controls forward locomotion [40, 41]. Importantly, the highest proportion of transneuronally labeled neurons aside from the reticular formation was observed in the SC, predominantly contralaterally (Figures 1H and 1J). Confined labeling was also observed in the zona incerta, mostly ipsilaterally (Figures 1I and 1J). More rostrally, only sparse Rb^+ cells were seen in the somatosensory and motor cortices (data not shown). These experiments indicate that V2a neurons of the Gi and adjacent nuclei are downstream of the SC and may therefore relay lateralized orienting commands.

Activating V2a Gi Neurons Unilaterally Evokes Orienting Motor Responses

To evaluate the capacity of V2a Gi neurons to mediate orienting movements when activated unilaterally, we virally delivered the Channelrhodopsin 2 (ChR2) in the Gi on one side (AAV-DIO-ChR2-eYFP) of *Chx10-Cre* mice and implanted an optic fiber on the same side (Figures 2A and 2B). We confined transfections sites unilaterally and to the rostral medulla, i.e., encompassing the Gi and the adjacent GiA nuclei (Figure S1A), where the strongest inhibitory effect on locomotion was reported [34]. We did not attempt to target smaller contingents (e.g., GiA versus Gi); we will therefore refer to V2a Gi neurons throughout the study.

When light stimulations were delivered unilaterally (500 ms trains of 15 ms pulses at 40 Hz) on stationary mice, the most

(J) Mean percentage ± SEM of Rb^+ cells in a given region over the total amount of Rb^+ cells (n = 3 animals, total cells counted: 8,157; average per animal: 2,719 ± 139). Regions presented are those showing the highest proportions of Rb^+ cells, outside of the RF, which accounted for 15% ± 2% ipsilaterally and 15% ± 3% contralaterally.

4V, fourth ventricle; sp5, spinal trigeminal tract; Gi, gigantocellular reticular nucleus; GiA, gigantocellular reticular nucleus alpha part; GiV, gigantocellular reticular nucleus ventral part; LPGi, lateral paragigantocellular nucleus; IRt, intermediate reticular nucleus; 7N, facial nucleus; py, pyramidal tract; Med, medial (fastigial) nucleus; Int, interposed nucleus; Lat, lateral (dentate) nucleus; IC, inferior colliculus; SC, superior colliculus; LPAG, lateral periaqueductal gray; DLPAG, dorsolateral periaqueductal gray; DMPAG, dorsomedial periaqueductal gray; CnF, cuneiform nucleus; PPN, pedunculopontine nucleus; Pa4, parathroclear nucleus; ml, medial lemniscus; ZI, zona incerta; SNr, substantia nigra pars reticulata.

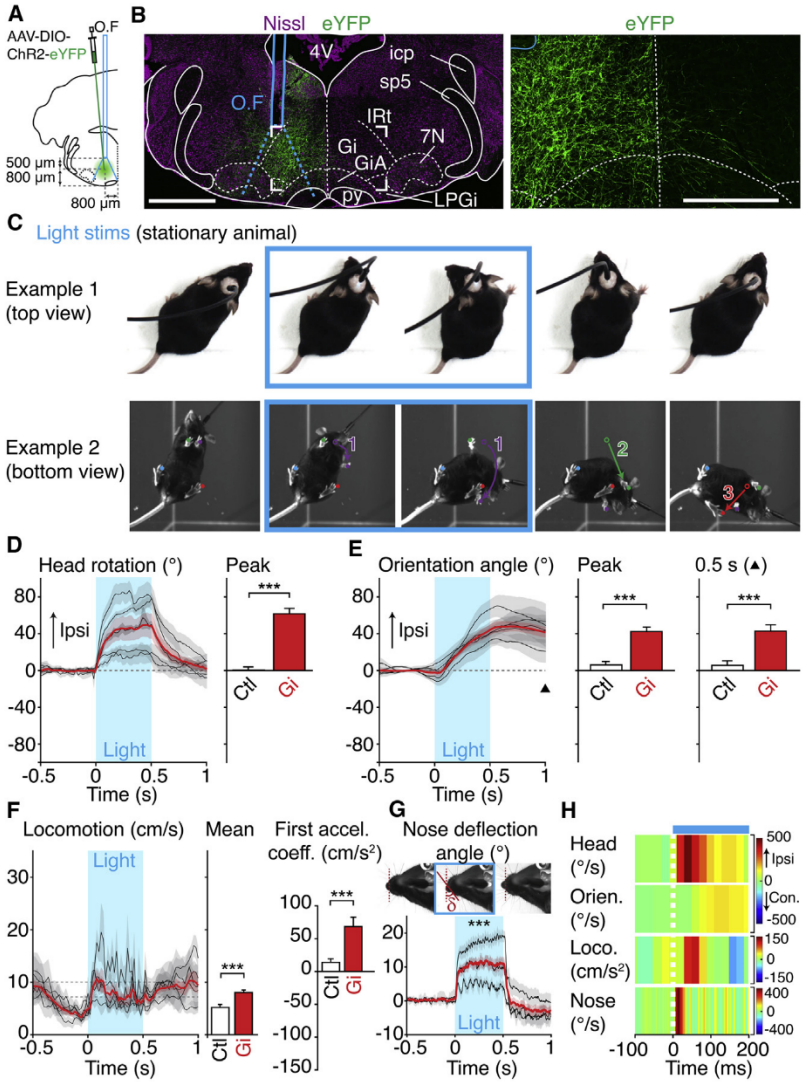

Figure 2. Unilateral Photo-Activations of V2a Gi Neurons Evoke Orienting-like Motor Responses

(A) Experimental strategy for photo-activating V2a Gi neurons. OF, optic fiber. The injection pipette is depicted with an angle for clarity, but the injection was performed without angle.

(B) Left: transverse section at the level of the Gi showing transfected V2a neurons (eYFP, green) on a Nissl background (magenta), the position of the OF, and the theoretical light cone at the fiber tip (dashed blue lines). Scale bar, 1 mm. Right: close-up view over the boxed area showing that transfected neurons are strictly restricted to the ipsilateral side. The vertical dashed line depicts the midline. Scale bar, 500 µm. See also Figure S1A.

(C) Two example snapshots from two animals, showing the typical head yaw rotation and the possible change in orientation evoked by the photo-activation of V2a Gi neurons (15 ms pulses at 40 Hz, for a duration of 500 ms, in blue). On the bottom view, colored numbers indicate the order of limb movements. See also Video S1.

(D–F) Left: mean ± SEM light-evoked changes in head yaw rotation (D), body orientation (E), and locomotor speed (F) for each animal (gray, n = 5 animals, 7 trials each) and across animals (red). The black arrowhead in (E) indicates the time point at 0.5 s after light offset. The dashed zone in (F) indicates the threshold from stationary (<7.5 cm/s) to locomoting (>10 cm/s) conditions. Bar graphs to the right show the mean ± SEM of the peak head rotation during photo-activations (D), the peak change in orientation during photo-activations and the orientation angle 0.5 s after light offset (E), and the mean locomotor speed and the first acceleration coefficient during photo-activations (F) across all trials (Gi, n = 35 trials from 5 mice, 7 trials each) compared with mock trials from control mice (Ctl, n = 44 trials from 4 mice, 11 trials each). ***p < 0.001 (unpaired t test). See also Figure S2 for the calculation of movements and the responses of control mice.

(G) Top: snapshots of one head-fixed animal showing the angular displacement of the snout (δ). Bottom: mean angular deflection ± SEM of the snout normalized to the angle during the same time interval before light onset, for each animal (gray) and across animals (red). ***p < 0.001 (paired t test between mean values 0.5 s before and during the 0.5 s photo-activations, n = 15 trials from 3 mice, 5 trials each).

(H) Color plot showing the first derivative of the above motor parameters from 100 ms before to 200 ms after light onset (the dashed white line indicates light onset). Note the rapid occurrence of nose deflection (peak change at 15 ms), followed by the head rotation (peak change at 40 ms) and the delayed change in body orientation (peak at 140 ms).

striking response was a robust rotation of the head in the yaw axis and a displacement of the body orientation toward the stimulated side (Figures 2C–2E; Video S1; see STAR Methods and Figures S2A–S2D for movement calculations). These movements were not seen in mock trials on injected and implanted wild-type mice (Figures S2E–S2H), which served as the reference for statistical comparisons in freely moving situations throughout this study (bar graphs in Figures 2D–2F). Photo-activations did not engage animals in sustained locomotor activity, but the forelimbs could perform one or two steps to maintain the body orientation with that of the head (Figures 2C and 2F). Following light offset, animals could regain their initial orientation, but in the majority of trials, they remained oriented toward the stimulated side (Figure 2E; compare also examples in Figure 2C and Video S1). Examinations on head-fixed animals revealed that photo-activations also evoked an immediate horizontal deflection of the snout tip toward the stimulated side (Figure 2G), known to accompany head orienting movements [2]. Finally, to examine the relative temporal occurrences of these motor responses, we computed and color-plotted the first derivative of each parameter after light onset (Figure 2H). This revealed that the change in nose positioning peaked first, on average at 15 ms after light onset, rapidly followed by the head rotation (at 40 ms), suggesting that these are the primary

CellPress
OPEN ACCESS

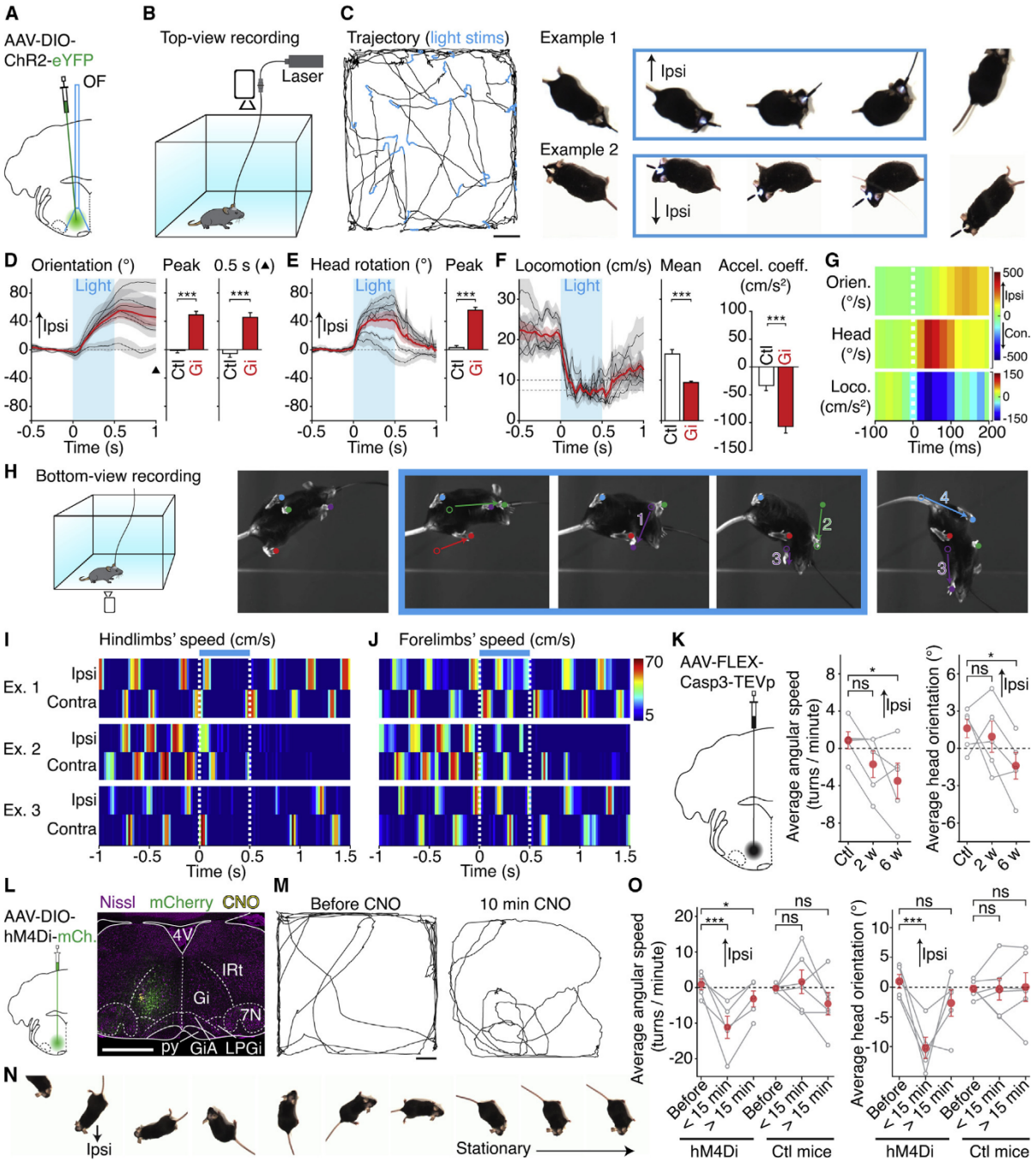

Figure 3. V2a Gi Neurons Control Locomotor Trajectory

(A) Experimental strategy for photo-activating V2a Gi neurons. OF, optic fiber. The injection pipette is depicted with an angle for clarity, but the injection was performed without angle. See also Figure S1A.

(B) Setup for top-view video recordings in an open field.

(C) Left: trajectory of one representative mouse for 3 min showing abrupt photo-evoked directional changes (15 ms pulses at 40 Hz, for a duration of 500 ms, in blue). Scale bar, 10 cm. Right: two example snapshots from two mice showing the typical light-evoked change of locomotor trajectory. See also Video S2.

(D–F) Left: mean ± SEM light-evoked changes in body orientation (D), head yaw rotation (E), and locomotor speed (F) of each animal (gray, n = 6 mice, 8 trials each) and across animals (red). The black arrowhead in (D) indicates the time point at 0.5 s after light offset. The dashed zone in (F) indicates the threshold from stationary (<7.5 cm/s) to locomoting (>10 cm/s) conditions. Bar graphs to the right show the mean ± SEM of the peak change in orientation during photo-activations and the orientation angle 0.5 s after light offset (D), the peak head rotation (E), and the mean locomotor speed and the first acceleration coefficient during

(legend continued on next page)

responses evoked. The change of body orientation occurred later with a peak angular speed at 140 ms. Altogether, these results indicate that activating V2a neurons in the Gi unilaterally evokes known motor components of oriented attention in rodents [2, 14, 42].

Activating V2a Gi Neurons Unilaterally during Locomotion Changes Trajectory

The orienting-like responses described above prompted us to test whether V2a Gi neurons also impact locomotor trajectory when animals are moving. For this, injected and implanted animals were placed in an open field and tracked from above (Figures 3A and 3B) while pulsed light stimulations were delivered during locomotion (i.e., instantaneous speed > 10 cm/s). We observed a striking and pronounced change of locomotor trajectory toward the stimulated side that persisted after light offset (Figures 3C and 3D; Video S2). This orientation change is associated with a rotation of the head (Figures 3C and 3E), reminiscent of the still trials. Additionally, locomotor speed was strongly reduced and animals reached the stationary threshold within 130 ± 30 ms of light onset (Figures 3C and 3F). This progressive locomotor halt, obtained here from strict unilateral activations (Figure S1A), recalls what was reported previously when activating the same cells bilaterally [34]. These motor changes were, however, not seen in, and are thus significantly different from, mock trials in control mice (bar graphs in Figures 3D–3F; see Figures S2I–S2K for responses of control mice). Temporal examination of the evoked motor sequence revealed that the head rotation and the locomotor deceleration occurred first and concomitantly (both peaked at 40 ms), followed by the body orientation (peak at 140 ms; Figure 3G). Manual tracking of the animal's paws showed that, during photo-activations, the hindlimbs terminate the ongoing step before remaining immobile and positioned symmetrically while the forelimbs performed left-right alternating movements toward the stimulated side (Figures 3H–3J; Video S2). When the animals resumed walking after light offset, they did so in the direction pointed by the head. Activating V2a Gi neurons unilaterally during ongoing locomotion therefore imposes a rapid yaw rotation of the head, a bilateral arrest of the hindlimbs, and a displacement of the forelimbs, altogether leading to a change of trajectory. Interestingly, these motor actions can also be expressed during naturally occurring changes in direction. Specifically, however, while the head yaw rotation often precedes the change in body orientation, the relative timing, or even the presence at all, of a locomotor deceleration was more variable (Figures S3A and S3B). Indeed, we found examples of turnings associated with a transient arrest of the 4 limbs followed by a reprise driven by the forelimbs, as well as some with continuing alternating movements of the 4 limbs (Figure S3C). This suggests that the motor sequence evoked by the photo-activation of V2a neurons can be mobilized, in whole or in part, during spontaneous directional changes.

Ablating V2a Gi Neurons or Impairing Their Activity Unilaterally Biases Locomotor Trajectory

We next addressed whether V2a Gi neurons are required for spontaneous changes of locomotor trajectory. We first virally delivered the genetically engineered caspase-3 unilaterally to V2a Gi neurons, to commit them to apoptosis [43]. In an open field test, injected animals showed a time-dependent bias to turn on the contralateral side (Figure 3K). Since this approach may mobilize compensatory circuits and does not allow us to quantify cell death, we next transiently silenced V2a Gi neurons using the inhibitory DREADD hM4Di delivered virally. Four weeks later, intracranial delivery of 1 m CNO was performed by another surgery (Figure 3L). Injections were unilaterally restricted and comparable to those of optogenetic activations, i.e., targeted to the Gi and GiA of the rostral medulla (Figure S1B). When examined immediately after the CNO delivery, animals showed only few episodes of locomotion owing to the partial recovery from anesthesia. Yet when they engaged in walking, either spontaneously or following motivation by the experimenter, they showed a very strong bias toward the contralateral side (Figures 3M–3O; Video S3). Moreover, the head was abnormally bent

photo-activations (F) across all trials (Gi) compared with mock trials from control mice (Ctl, n = 48 trials from 4 mice, 12 trials each). ***p < 0.001 (unpaired t test). See also Figure S2 for the calculation of movement changes and responses of control mice.

(G) Color plot of the first derivative of each motor parameter showing their temporal evolution from 100 ms before to 200 ms after light onset (the dashed white line indicates light onset). Note the rapid head movement and locomotor deceleration and the delayed change in body orientation.

(H) Setup for bottom-view video recordings and one example of a photo-evoked trajectory change. Colored numbers indicate the order of limb movements. See also Video S2 for the corresponding video and another example and Figure S3 for naturally occurring turns.

(I and J) Color plots of the velocity of the paws of the hindlimbs (I) and forelimbs (J) from 1 s before to 1 s after the 500 ms photo-activation. The y axis represents 3 example trials from distinct animals; the top one is shown in (H). The color gradient to red indicates speed values in cm/s. During photo-activations, the hindlimbs remain still after having terminated the ongoing step but the forelimbs continue moving.

(K) Caspase3-mediated ablation of V2a Gi neurons leads to a time-dependent increase of spontaneous turns toward the contralateral side, represented as the average angular speed per minute of walking (i.e., instantaneous speed > 10 cm/s), and to a biased orientation of the head. Gray open circles are the means of individual animals, and red circles are the means ± SEM across animals. 2 w, 2 weeks post-injection; 6 w, 6 weeks post-injection. Number of videos: Ctl, 13; 2w, 10; 6w, 11 (from 5 mice). *p < 0.05; ns, not significant (unpaired t test).

(L) Transient silencing of V2a Gi neurons by an hM4Di virus followed by intracranial delivery of 1 mM CNO by surgery (detected by fluorescent beads, yellow). Scale bar, 1 mm. See also Figures S1B and S1C.

(M) Trajectory of one representative mouse during 3 min in an open field before and 10 min after intracranial CNO delivery. Scale bar, 10 cm.

(N) Snapshots, taken every 500 ms, of one representative animal injected on the left side, showing a bias in locomotor trajectory and head position, even during stationary periods, toward the contralateral side. See also Video S3.

(O) Average angular speed per minute of walking (left) and average head rotation angle (right) showing the significant bias toward the contralateral side of hM4Di-injected CNO-treated mice (hM4Di, number of videos: before, 13; <15 min, 10; >15 min, 11; from 5 mice), but not following CNO delivery alone using a similar surgical procedure (Ctl mice, number of videos: before, 17; <15 min, 10; >15 min, 12; from 5 mice). Gray open circles are the means of individual animals, and red circles are the means ± SEM across animals. *p < 0.05; ***p < 0.001; ns, not significant (unpaired t test).

Current Biology
Article

CellPress
OPEN ACCESS

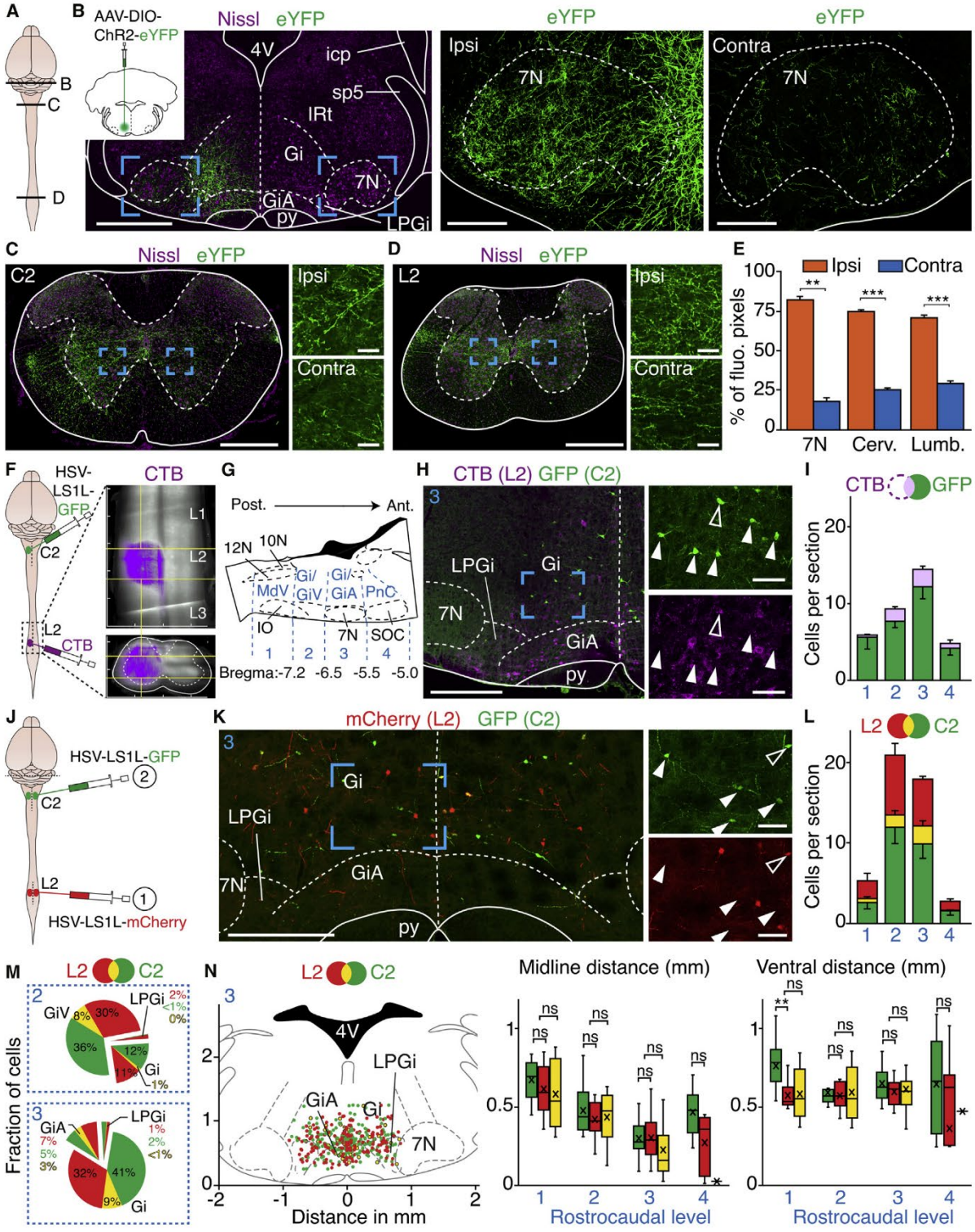

(legend on next page)

toward the contralateral side, an effect also noticeable during stationary periods (Figures 3N and 3O; Video S3). To exclude that these motor abnormalities are caused by the surgical procedure used to deliver the CNO, control (wild-type) mice that did not receive the hM4Di virus underwent a similar procedure, including anesthesia, CNO injection, and behavioral testing. These showed globally no bias toward the ipsilateral or contralateral sides (Figure 3O). The activity of V2a Gi neurons is therefore necessary for controlling locomotor trajectory and may also help to maintain an upright head position.

Distinct Subsets of V2a RS Neurons Show Preferential Projections to Specific Spinal Segments

Since V2a Gi neurons control multiple oriented actions, they should have lateralized access to the corresponding motor circuits. Indeed, V2a axonal projections densely innervate the facial motor nucleus (7N), associated with the whisker and snout musculature [17], as well as the upper cervical and lumbar segments, containing, respectively, the neck [20] and hindlimb [23, 24] motor circuits (Figures 4A–4D). Projections were found on both sides with a predominant ipsilateral contribution (Figure 4E). We next addressed whether these distinct target regions are contacted by a unique population of V2a neurons with branched collaterals or, instead, by distinct subsets with target-specific projections. For the rest of the study, we focused on the head rotation, body orientation, and control of the hindlimbs since these actions are piloted by spinal circuits and may therefore be under a common control by branched RS neurons. We first combined a Cre-dependent retrogradely transported herpes-simplex virus (HSV) [44, 45], injected into the 2nd cervical segment (C2), with cholera toxin B (CTB) injected into the 2nd lumbar segment (L2; Figure 4F). Retrogradely labeled V2a neurons from C2 were found throughout the RF, but only a minority were co-labeled with CTB (14% ± 2% overall; 12% ± 3% at the level of the Gi/GiA where optogenetic activations are performed; Figures 4G–4I). This indicates that the majority of V2a neurons do not have access to both spinal levels. To corroborate this further, we retrogradely labeled V2a neurons from both the C2 and L2 segments conjointly, using two Cre-dependent HSVs each coding a distinct fluorophore (Figure 4J). The majority of labeled V2a neurons were again expressing one, but rarely both, fluorophores (Figures 4K and 4L). Specifically, at rostrocaudal levels where photo-activations are performed, double-labeled V2a neurons represented only 11% ± 2% of all labeled cells. In contrast, when the two HSVs were injected at the same spinal segment (L2) either conjointly or sequentially, we found >90% of co-labeling (Figure S4), confirming previous reports that multiple HSVs can be expressed in individual cells [46]. Therefore, the preferential expression of either fluorophore in the dual C2/L2 HSV injection reflects the existence of distinct V2a subsets each having preferential projections to a specific spinal segment. Interestingly, these subsets were similarly distributed across the different nuclei of the ventral RF (Figures 4L and 4M). Moreover, reporting their mediolateral and dorsoventral positioning did not reveal any spatial segregation except at caudal-most levels (MdV) where the C2-projecting ones tended to be positioned more dorsally (Figure 4N). Finally, using a projection-based delivery of the rabies proteins oG and TVA, we found that both the C2 and L2-projecting V2a subsets receive inputs from the SC and, qualitatively, share similar input structures, albeit in varied proportions and with lower degrees of lateralization than the overall population (Figure S5). These observations altogether demonstrate the existence of distinct

Figure 4. Distinct but Spatially Intermingled V2a RS Neurons Show Preferential Projections to Specific Spinal Segments

(A) Schematic illustrating the position of the sections displayed in the following panels.

(B) Left: transverse section at the level of the Gi, where optogenetic activations are performed, showing the unilateral transfection of V2a neurons with an AAV-DIO-ChR2-eYFP. Scale bar, 1 mm. Right: magnifications of the blue boxed areas showing V2a projections in the ipsilateral and contralateral facial motor nuclei (7N). Scale bar, 200 μm.

(C and D) Transverse spinal cord sections from the same animal (representative of 3 mice), showing V2a projections at the 2nd cervical (C2) and 2nd lumbar (L2) levels. Dashed lines delineate the white matter. Scale bars, 500 μm and 50 μm (insets).

(E) Bar graphs showing the average percentage ± SEM of eYFP^{+} pixels located ipsilaterally and contralaterally in the 7N and in the cervical and lumbar white matter. ***$p < 0.001$; **$p < 0.01$ (unpaired t test; 7N, 10 sections; spinal cord, 12 sections; from n = 3 mice).

(F) Left: experimental strategy for labeling V2a RS neurons projecting to C2 with a Cre-dependent HSV and all L2-projecting neurons with CTB. LS1L, Lox-Stop-Lox. Right: example blend projection along the rostrocaudal (top) and transverse axis (bottom) of a CUBIC-cleared spinal cord imaged with light-sheet microscopy, showing the typical spread of dye load following an injection of CTB at L2 unilaterally. Thick marks, 500 μm.

(G) Sagittal schematic of the brainstem indicating the rostrocaudal levels (1 to 4, in blue), used for reporting labeled neurons.

(H) Transverse section (representative of 4 mice) at the rostrocaudal level 3 showing C2-projecting V2a neurons (GFP) and all lumbar-projecting neurons (CTB). Scale bar, 500 μm. Insets to the right are magnifications of the blue boxed area, showing the scarcity of double-labeled neurons (open arrowheads). Scale bar, 100 μm.

(I) Bar graphs showing, at the 4 rostrocaudal levels, the average number ± SEM of HSV and HSV;CTB-labeled neurons per histological section (n = 4 mice, 756 HSV^{+} cells counted in total; average per animal, 189 ± 24).

(J) Viral strategy for labeling V2a RS neurons projecting to C2 and L2 using Cre-dependent HSVs injected bilaterally.

(K) Left: transverse section (representative of 3 mice) at the rostrocaudal level 3 showing C2- (GFP) and L2-projecting (mCherry) V2a RS neurons. Scale bar, 500 μm. Insets to the right are magnifications of the blue boxed area, showing the scarcity of double-labeled neurons (open arrowheads). Scale bar, 100 μm.

(L) Bar graphs showing, at the 4 rostrocaudal levels, the average number ± SEM per histological section of V2a RS neurons projecting to either or both of the C2 and L2 segments (n = 3 mice; 844 cells counted in total; average cells per animal, 281 ± 33).

(M) Pie graphs showing the distribution, at rostrocaudal levels 2 and 3, of labeled neurons within the indicated subnuclei (in percent of all neurons at each level, pooled from the 3 mice). All cells at level 1 were in the MdV and all cells at level 4 were in the PnC.

(N) Left: transverse position of single- and double-labeled neurons at rostrocaudal level 3 where optogenetic activations are performed. Middle and right: mediolateral (in mm from the midline, absolute values from the left and the right sides are pooled) and dorsoventral (in mm from the ventral border) positions of single- and double-labeled neurons, presented as the mean (crosses) and box-and-whisker plots, which give the median, 25th and 75th percentiles, and range (844 cells pooled from 3 mice). **$p < 0.01$; ns, not significant (unpaired t test). See also Figures S4 and S5.

Current Biology
Article

CellPress
OPEN ACCESS

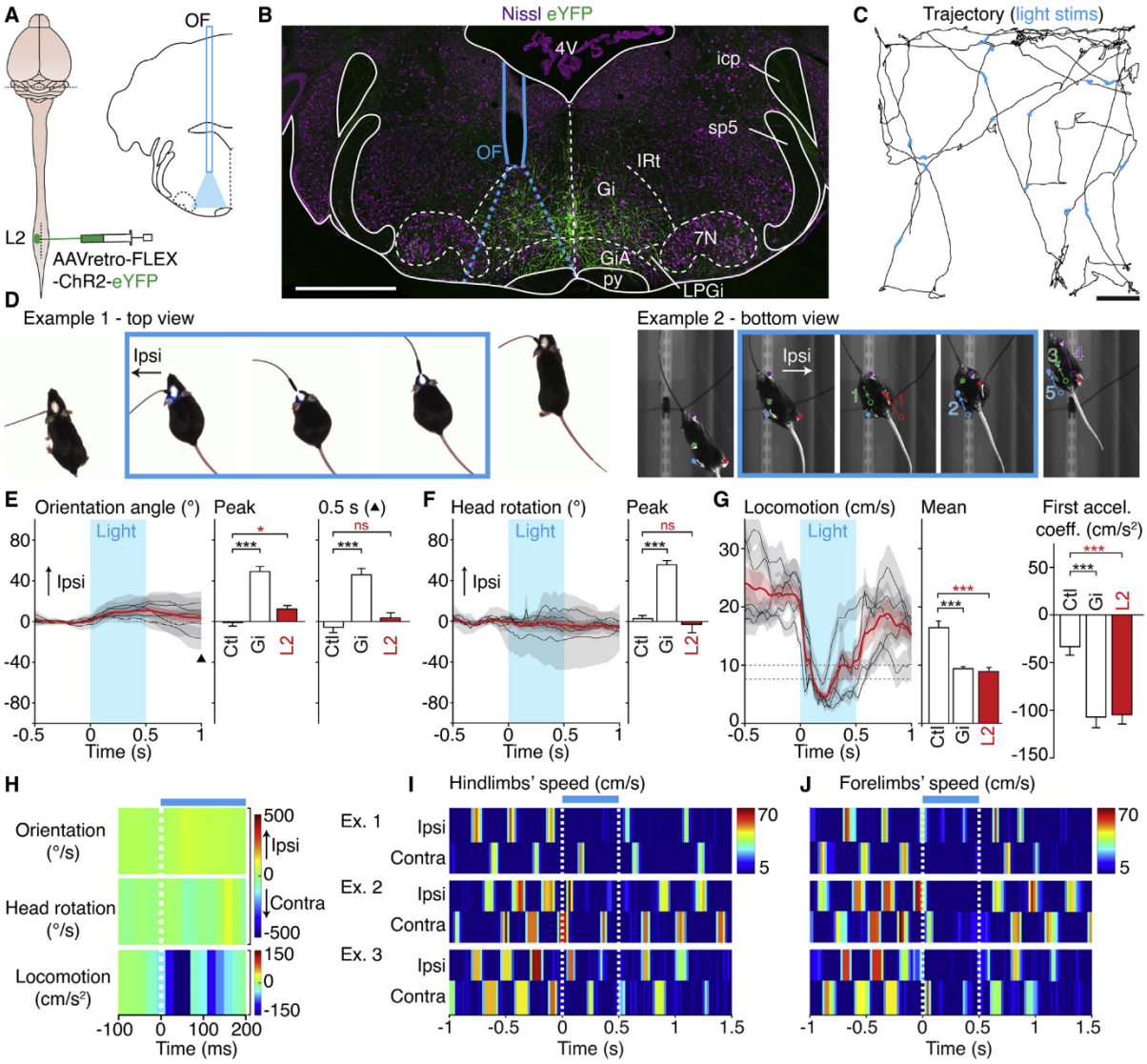

Figure 5. Unilateral Photo-Activations of L2-Projecting V2a Gi Neurons Arrest but Do Not Steer Ongoing Locomotion

(A) Experimental strategy for photo-activating L2-projecting V2a Gi neurons. OF, optic fiber.

(B) Example transverse section showing virally transfected V2a neurons (eYFP) on a Nissl background, the position of the optic fiber (OF), and the theoretical light cone at the fiber tip (dashed blue lines) that restricts activations to the implanted side. Scale bar, 1 mm. See also Figure S1D.

(C) Trajectory of one representative animal for 3 min in the open field. Scale bar, 10 cm.

(D) Example snapshots from two distinct animals, showing the locomotor arrest with no change in trajectory evoked by 500 ms light trains (15 ms pulses at 40 Hz, in blue) delivered unilaterally on the left side. Snapshots are taken 150 ms before light onset; 50 ms, 250 ms, and 450 ms after light onset; and 200 ms after light offset. See also Video S4.

(E–G) Left: mean ± SEM light-evoked changes in body orientation (E), head yaw rotation (F), and locomotor speed (G) of each animal (gray, n = 5 mice, 8 trials each) and across animals (red). The black arrowhead in (E) indicates the time point at 0.5 s after light offset. The dashed zone in (G) indicates the threshold from stationary (<7.5 cm/s) to locomoting (>10 cm/s) conditions. Bar graphs to the right show, for each parameter, the mean ± SEM of all trials when activating L2-projecting V2a neurons (in red, n = 40 trials from 5 mice, 8 trials each) compared with the same measurement in mock trials in control mice (Ctl, n = 48 trials from 4 mice, 12 trials each) and following activation of all V2a Gi neurons (Gi, n = 48 trials from 6 mice, 8 trials each). ***p < 0.001; *p < 0.05; ns, not significant (unpaired t test).

(legend continued on next page)

V2a subsets contacted by the SC but that differ by their segmental projections to the spinal cord.

Differential Control of Head and Hindlimb Movements by Subsets of V2a Gi Neurons

The existence of projection-defined subsets of V2a Gi neurons prompted us to test their respective function. For this, a cre-dependent ChR2 was delivered retrogradely by unilateral injections of an AAVretro-FLEX-ChR2-eYFP [47–49] in the C2 or L2 spinal segments and an optic fiber was placed in the Gi on the same side. Since left-right unbalanced activation of lumbar circuits could steer trajectory [7, 8, 35], we first manipulated the L2-projecting V2a neurons (Figures 5A and 5B; see Figure S1D for implantation sites). Most surprisingly, however, their unilateral activation during locomotion did not change the animals' trajectory (Figures 5C and 5D; Video S4). Specifically, the animal's body orientation only showed a slight and transient bias that was not maintained after light offset (Figure 5E). Animals also did not show any head yaw rotation movements (Figures 5D and 5F). Locomotor speed was nevertheless strongly reduced similarly to the activation of all V2a Gi neurons: animals reached the stationary threshold on average 70 ± 17 ms after light onset (Figures 5D and 5G) and locomotor deceleration peaked at 40 ms after light onset (Figure 5H). Bottom-view examinations revealed that both hindlimbs and forelimbs were halted and positioned symmetrically (Figures 5D, 5I, and 5J; Video S4). On stationary animals, photo-stimulations did not evoke detectable changes in these motor parameters (Figures S6A–S6G and S6O). Hence, L2-projecting V2a neurons, when activated unilaterally, arrest locomotion but do not evoke head and orofacial orienting responses, nor steer trajectory.

The directional change evoked when activating V2a Gi neurons collectively might thus be driven by the C2-projecting subset. Indeed, when ChR2 was retrogradely delivered from the C2 segment and photo-activations performed in the Gi unilaterally during locomotion (Figures 6A and 6B; see Figure S1E for implantation sites), we observed a pronounced change in trajectory toward the stimulated side (Figures 6C and 6D; Video S5). Reminiscent of what we observed when activating V2a neurons collectively, the change in body orientation was highly significant from mock trials in control mice, persisted after light offset (Figure 6E), and was preceded by a rapid rotation of the head (Figure 6F). Remarkably, however, animals did not arrest their locomotion. Specifically, while a locomotor deceleration was observed, it was comparable to that of control mice subjected to mock trials (Figure 6G; see also Figure S2K for the responses of control mice). This ChR2-independent deceleration reflects the limited size of open field, which makes running episodes inevitably short, even in the absence of photo-activation. This locomotor deceleration also occurred later following light onset than when activating all V2a Gi neurons or the L2-projecting ones (Figure 6H; compare with Figures 5H and 3G), suggesting that it is not a primary response from photo-activations. Indeed left-right alternating movements of both hindlimbs and forelimbs persisted during the directional change (Figures 6D, 6I, and 6J; Video S5). Photo-activations on still trials evoked a strong yaw rotation of the head and a re-orientation of the body, and animals could perform a few walking steps toward the stimulated side; there was, however, no deflection of the snout (Figures S6H–S6O). Finally, we excluded a contribution of antidromic activation of C2-located V2a neurons with projections to the brainstem (Figure S7) and found no projections in the reticular formation from Chx10-expressing neurons located in L2 (data not shown). Overall, these results indicate that (1) the C2- and L2-projecting subsets of V2a Gi neurons are specifically dedicated to control head rotation and locomotor speed, respectively, and (2) the former action suffices to steer the animal's trajectory. They also suggest the existence of other V2a Gi neurons with no spinal projections that may control orofacial musculature.

C2-Projecting, but Not L2-Projecting, V2a Neurons Elicit Short-Latency Responses on Neck Muscle Fibers

Since our results underscore the importance of head rotation for locomotor trajectory and since neck premotor circuits reside in the Gi [20–22], we hypothesized that some V2a Gi neurons might be connected to neck motoneurons. We therefore recorded, by electromyography in non-anesthetized awake mice, photo-evoked responses of the splenius muscle, the most vigorously activated during horizontal orienting head movements [20, 50] (Figure 7).

Only animals showing spontaneous activity on both the ipsilateral and contralateral muscles (Figures 7B, 7F, and 7J) were included. When V2a Gi neurons were activated collectively by short (5 ms) light pulses, reliable EMG responses were detected on the ipsilateral side in nearly all trials (Figures 7C and 7D). These occurred at an average latency of 5.57 ± 0.13 ms (min, 3.8 ms; max, 6.8 ms) compatible with the crossing of 2 synapses [51–53]. However contralateral responses were less reliable and significantly more delayed (14.64 ± 0.96 ms, min, 9.6 ms; max, 25 ms). Photo-activating C2-projecting V2a neurons also led short responses ipsilaterally (latency, 6.13 ± 0.10 ms), but not contralaterally (10.74 ± 0.66 ms; Figures 7E–7H). In stark contrast, only occasional responses were observed both ipsilaterally and contralaterally when activating the L2-projecting subset (Figures 7I–7L), and when a response was elicited, its latency was longer on both sides (ipsilateral, 18.39 ± 0.63 ms, min 13.4 ms, max 24.4 ms; contralateral, 19.65 ± 0.65 ms, min 15.6 ms; max 25 ms). Finally, examination of anterograde projections of V2a Gi neurons in the upper cervical spinal cord revealed putative contacts onto motoneurons (Figures 7M and 7N). Overall, these experiments reinforce the existence of distinct functional V2a

(H) Color plot showing the temporal evolution of the motor parameters from 100 ms before to 200 ms after light onset (the dashed white line indicates light onset). Note the absence of trajectory change and head rotation, but a rapid locomotor deceleration (peak at 40 ms) reminiscent of activating V2a Gi neurons collectively (Figure 3G).

(I and J) Color plots of the velocity of the paws of the hindlimbs (I) and forelimbs (J) from 1 s before to 1 s after the photo-activation. A color gradient to red indicates high speed values in cm/s. The y axis represents 3 example trials from distinct animals. The second one corresponds to the snapshots in (D). See also Figure S2 for the responses of control mice and Figure S6 for still trials.

Current Biology
Article

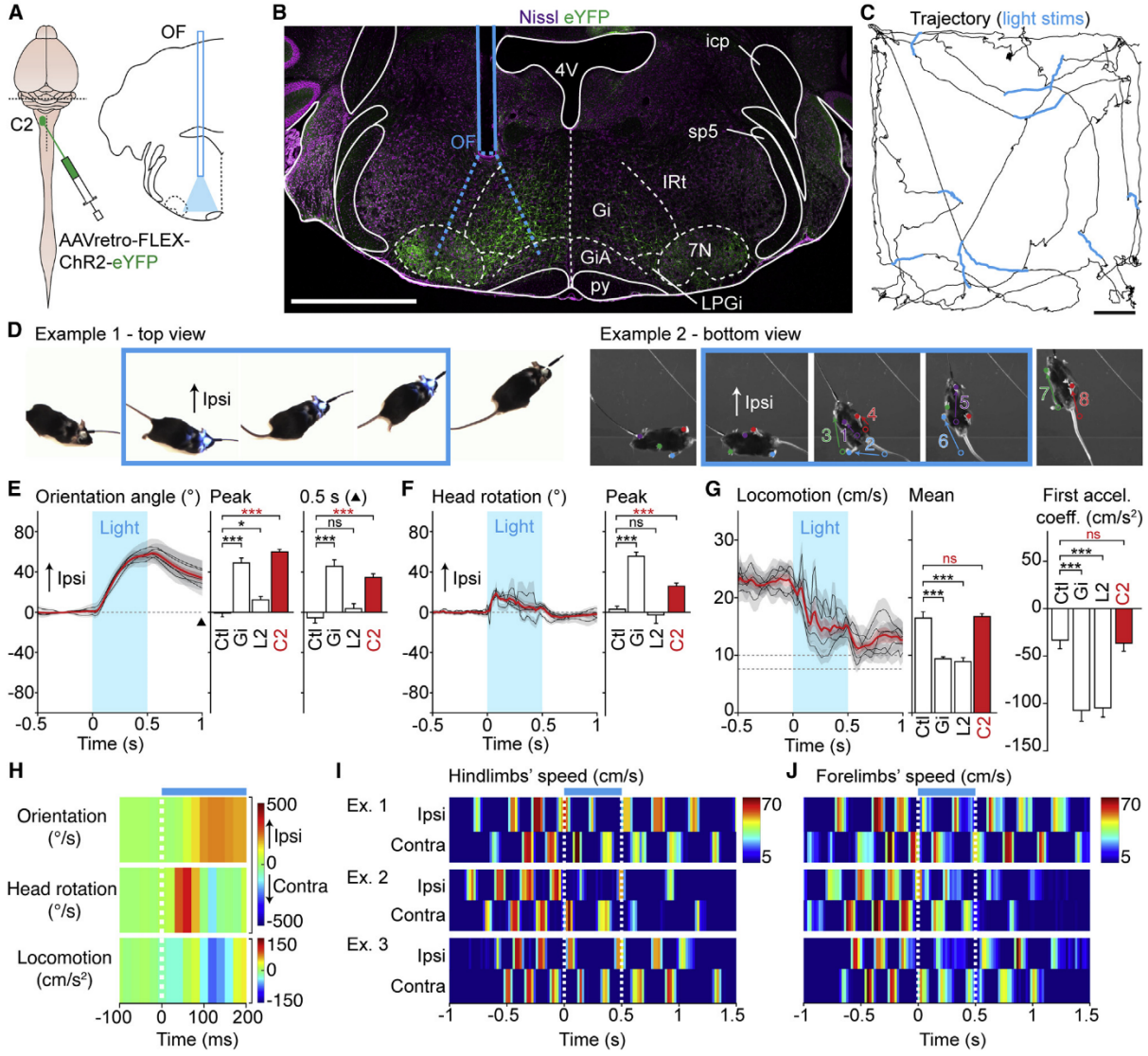

Figure 6. Unilateral Photo-Activations of C2-Projecting V2a Gi Neurons Steer, but Do Not Arrest, Ongoing Locomotion

(A) Experimental strategy for photo-activating C2-projecting V2a Gi neurons. OF, optic fiber.

(B) Example transverse section showing virally transfected V2a neurons (eYFP) on a Nissl background, the position of the optic fiber (OF), and the theoretical light cone at the fiber tip (dashed blue lines) that restricts activations to the implanted side. Scale bar, 1 mm. See also Figure S1E.

(C) Trajectory of one representative animal during 3 min in the open field. Scale bar, 10 cm.

(D) Example snapshots from two distinct animals, showing the change in trajectory without locomotor arrest, evoked by 500 ms light trains (15 ms pulses at 40 Hz, in blue). Snapshots are taken 150 ms before light onset; 50 ms, 250 ms, and 450 ms after light onset; and 200 ms after light offset. See also Video S5.

(E–G) Left: mean ± SEM light-evoked changes in body orientation (E), head yaw rotation (F), and locomotor speed (G) of each animal (gray, n = 5 mice, 23 trials each) and across animals (red). The black arrowhead in (E) indicates the time point at 0.5 s after light offset. The dashed zone in (G) indicates the threshold from stationary (<7.5 cm/s) to locomoting (>10 cm/s) conditions. Bar graphs to the right show, for each parameter, the mean ± SEM obtained across all trials when activating C2-projecting V2a neurons (in red, n = 115 trials from 5 mice, 23 trials each) compared with the same measurement in mock trials in control mice (Ctl, n = 48 trials from 4 mice, 12 trials each) and following activation of all V2a Gi neurons (Gi, n = 48 trials from 6 mice, 8 trials each) or the L2-projecting ones (L2, n = 40 trials from 5 mice, 8 trials each). ***p < 0.001; *p < 0.05; ns, not significant (unpaired t test).

(H) Color plot showing the temporal evolution of motor parameters from 100 ms before to 200 ms after light onset (the dashed white line indicates light onset). Note the rapid head rotation (peak at 60 ms) and the delayed body orientation (peak at 120 ms), but the absence of rapid deceleration of locomotion.

(I and J) Color plots of the velocity of the paws of the hindlimbs (I) and forelimbs (J) from 1 s before to 1 s after the photo-activations. A color gradient to red indicates high speed values in cm/s. The y axis represents 3 example trials from distinct animals. The first example corresponds to the snapshots in (D). See also Figure S2 for the responses of control mice and Figure S6 for still trials.

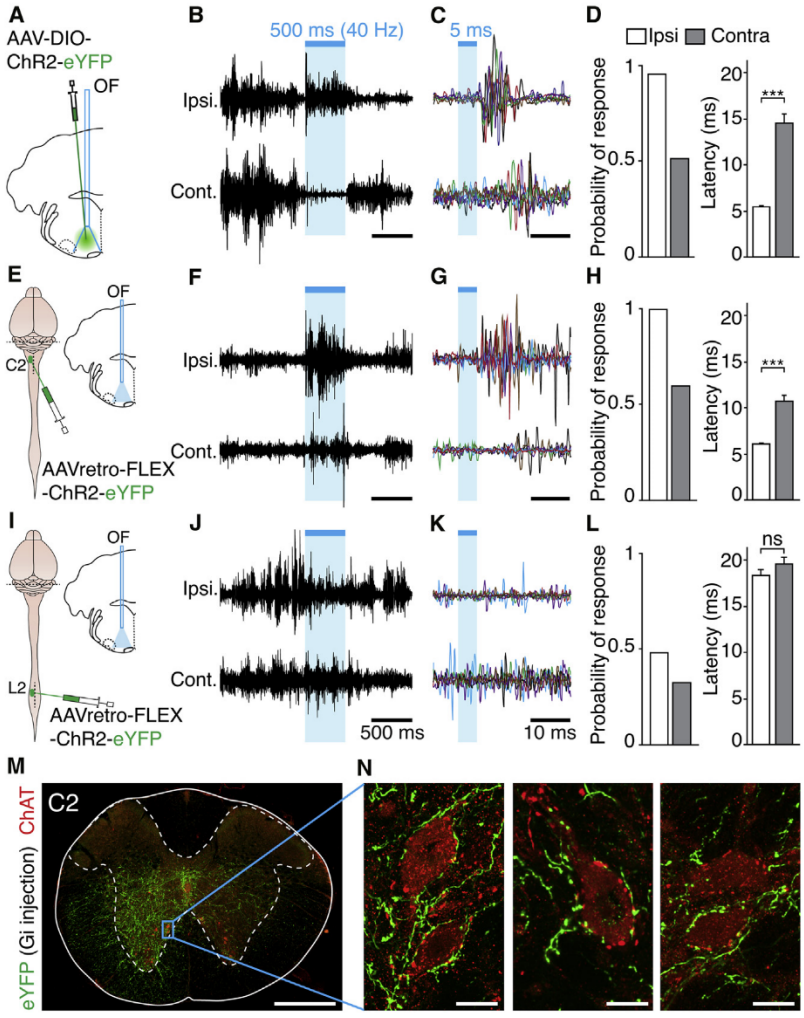

Figure 7. C2-Projecting V2a Neurons Elicit Short-Latency Responses on Neck Muscle Fibers

(A) Experimental strategy for photo-activating V2a Gi neurons. OF, optic fiber.

(B) Example EMG recording showing spontaneous activity on both the ipsilateral and contralateral neck muscles, and the increased activity ipsilaterally following photo-activation of V2a Gi neurons (15 ms pulses at 40 Hz, for a duration of 500 ms).

(C) Six superimposed EMG traces following a single 5 ms light pulse, each shown in a specific color.

(D) Bar graphs showing the presence of reliable (95% success) and low-latency responses (mean, 5.6 ± 0.1 ms; min, 3.8; max, 6.8) ipsilaterally, but not contralaterally (51% success; mean, 14.7 ± 1.0 ms; min, 9.6; max, 25). ***$p < 0.001$ (unpaired t test on n = 68 trials from 3 mice). Data are presented as means across all trials; errors bars in the latency bar graph indicate SEM.

(E–H) Similar recordings and analyses for C2-projecting V2a neurons. Note the reliable and low-latency responses on the ipsilateral (100% success; mean, 6.1 ± 0.1 ms; min, 4.0; max, 8.0), but not on the contralateral muscle (60% success; mean, 10.7 ± 0.7 ms; min, 5.1; max, 19.6). ***$p < 0.001$ (unpaired t test on n = 62 trials from 3 mice).

(I–L) Similar recordings and analyses for L2-projecting V2a neurons. Note the low probability and long latency of responses on both the ipsilateral (48% success; mean, 18.4 ± 0.6 ms; min, 13.4; max, 24.4) and contralateral muscles (33% success; mean, 19.7 ± 0.7 ms; min, 15.6 ms; max, 25 ms). ns, not significant (unpaired t test on n = 78 trials from 4 mice).

(M) Confocal microscopy picture of a transverse section at C2 of an animal injected unilaterally in the Gi with an AAV-DIO-ChR2-EYFP (experimental individual illustrated in Figure 2B), showing anterograde V2a projections (eYFP) and motoneurons (ChAT). Scale bar, 500 μm.

(N) Left: higher magnification of the blue boxed area in (M), showing putative V2a contacts onto 2 motoneurons. The middle and right panels are other examples from the same (middle) and from another (right) animal. Scale bars, 20 μm.

subtypes with specialized projections, and indicate that the C2-projecting, but not the L2-projecting one, has rapid—possibly direct—access to neck motoneurons.

DISCUSSION

Methodological Considerations

A large part of our study relies on projection-based manipulations of neuronal subtypes. While retrogradely transported HSV and AAVretro vectors have already proven to be extremely powerful tools [45, 47–49], notably owing to their restricted entry at terminals [45, 54, 55], there are potential concerns that deserve clarification. First, if wild HSVs can prevent a single cell from being infected by multiple viruses [56], the replication-deficient ones used here are deprived of viral genome [44] and allow multiple infections [46] (Figure S4). Furthermore, little co-labeling was also observed when combining an HSV injection at C2 with CTB at L2 (Figures 4F–4I), unambiguously ascertaining that distinct V2a neurons contact the cervical and lumbar segments. Another concern with dual injections is the risk of severing axons at the rostral site, which can cause an underestimation of neurons projecting more caudally. However, here, all spinal injections were done starting from the lumbar site and performed in the white matter to spare the lateral funiculus where most RS axons travel [19], and animals showed no motor deficits. Furthermore, the existence of distinct V2a subsets is not only supported anatomically but is also demonstrated functionally. Indeed, following a unique injection of a ChR2-coding AAVretro in the L2 segment, i.e., without possible axonal damage at the cervical level, no head movements or short-latency EMG responses on neck muscle fibers were detected (Figures 5 and 7). V2a neurons transfected from L2 therefore do not have a similar access to cervical segments as the overall population or the C2-projecting ones. Finally, the contribution of antidromic activation of spinally located

V2a neurons with projections to the brainstem can be ruled out since (1) motor actions evoked after retrograde delivery of ChR2 are seen when manipulating V2a Gi neurons locally, i.e., without the possibility for distant V2a neurons to express ChR2; (2) activating ascending projections of V2a neurons residing in C2 led to no orienting responses (Figure S7); and (3) Chx10-expressing neurons in L2 do not project to the RF. Overall, the selectivity and convergence of our anatomical (HSV) and functional (AAVretro) investigations firmly establish the existence of distinct functional V2a subsets with preferential projections to the upper cervical or lumbar segments.

The Presynaptic Connectome of V2a Gi Neurons Hints at Their Integrative Function

Aside from the dominant local connectivity, a high fraction of presumed inputs to V2a Gi neurons was found in the SC, in positions matching the output layers known to project to the RF [12, 15]. The majority of SC output neurons are excitatory and the ipsilateral orienting responses we observed are reminiscent of those elicited contralaterally when activating the SC [14, 42]. This suggests that V2a Gi neurons are embedded in an excitatory crossed pathway, as also indicated by a coincident and independent investigation [35]. Interestingly, we found that the SC contacts both the C2- and L2-projecting V2a subsets. Therefore, the latter, while not directly mediating lateralized motor actions, may still relay orientation-related signals. Indeed, the animal's locomotor speed is often encoded together with its directional heading [57, 58], suggesting a tight correlation of these two variables. Allowing a transient arrest of locomotion appears notably pertinent for exploring a fixed object while on the move. Alternatively, the SC projections to L2-projecting V2a neurons may be related to defensive behaviors, also manifested by a behavioral arrest [59]. The role and excitatory or inhibitory nature of the uncrossed pathway from the SC to V2a neurons, less predominant, will need to be uncovered. Finally, the detection of transneuronally labeled neurons in other brain regions known to regulate motor actions or posture [60–62] indicates that V2a Gi neurons may be shared by several modalities that require spatially tuned movements. Here again, examining the neurotransmitter identity of these upstream neurons will be required to fully appreciate their role in mobilizing or inactivating V2a Gi neurons. However, we found no transneuronal labeling in the cuneiform and pedunculopontine nuclei, together forming the mesencephalic locomotor region (MLR) that engages forward locomotion [40, 41]. This could reflect that forward locomotion may be, at least in mice, principally controlled by non-V2a glutamatergic or serotonergic neuronal classes [26, 63]. However, MLR to V2a connections have been suggested functionally *in vitro* [36]. These connections may thus target V2a neurons not investigated here (notably located more caudally) or may be more refractory to rabies transfer.

Differential Control of Head and Hindlimb Movements by Subsets of V2a Neurons

We report here that V2a Gi neurons trigger both "strict" orienting responses ipsilaterally, i.e., lateralized head and orofacial movements, and steer trajectory when activated during locomotion. Conversely, ablating or silencing V2a Gi neurons led to a biased contralateral turning during exploration, in line with a coincident and independent investigation [35]. Such opposite findings from gain and loss of functions exclude that photo-evoked responses owe to an unintentional suppression of activity by over-activation, as previously ruled out for the locomotor aspect [34]. Most importantly, they strongly argue that V2a Gi neurons might be mobilized during—and are causal to—naturally occurring changes of direction. Interestingly, the bias in the head orientation suggests that these neurons might not only be transiently activated at turns, but may also help maintain an upright posture.

The V2a-driven directional change is associated with a bilateral arrest of the hindlimbs, which is reminiscent (i.e., gradual, leading to a stereotypic stationary posture) of what was previously reported when activating the same cells bilaterally [34]. Remarkably, however—and this is certainly the most disruptive finding reported here—the directional change and the locomotor halt are in fact controlled by distinct V2a populations with segment-specific projections. This specialization of V2a neurons is demonstrated both anatomically (Figures 4 and S4) and functionally (Figures 5, 6, 7, and S6). Specifically, activating C2-projecting V2a neurons led to an ipsilateral head yaw rotation followed by a change in trajectory but no locomotor arrest, suggesting that this population does not reach or functionally impact hindlimb-related segments. While these C2-projecting V2a neurons were inevitably activated in previous work [34], their function may have then been hindered by the bilateral nature of the stimulations that may have caused left-right co-contractions of neck muscles (but see [26] for head movements when photo-activating glutamatergic Gi neurons). Conversely, we report a rapid locomotor arrest, but no head rotation, short neck EMG responses, or directional change, when activating L2-projecting V2a neurons (Figures 5 and S6). Therefore, L2-projecting V2a neurons do not reach or functionally impact neck-related cervical segments. Even though our retrograde approach transfects somata on both sides since V2a Gi neurons have crossed projections (Figures 4C–4E), the locomotor halt cannot be due to an unintentional synchronous activation of the left and right sides since (1) the lateral placement of the optic fiber secures unilateral photo-activations [64], and (2) a bilateral arrest is systematically evoked when the ChR2 is delivered locally and unilaterally to the Gi (Figure 3), where there is no possible activation of neurons located across the midline (Figure S1A). This diversification of descending neurons by targeted segment is reminiscent to what was recently uncovered for cerebello-spinal neurons [49]. However, here, we highlight a salt and pepper, body-oriented functional organization at the connectomics levels rather than a spatial topography. While we also detected a numerically smaller subset of V2a neurons with projections to both spinal segments, it is unlikely that it controls head and limb movements synergistically since activating the L2- and C2-projecting subsets evoked mutually exclusive responses. Finally, nose movements were only observed when activating V2a Gi neurons collectively. The snout musculature may thus be controlled by yet another population with only local projections [17]. Therefore, and considering that some brainstem V2a neurons may also modulate breathing [32], this neuronal class appears heterogeneous and may host projection-specialized subsets that each control a specific muscle group.

The Head Orientation as a Prime Driver for Locomotor Trajectory?

On the role of V2a neurons on locomotor trajectory, we converge with a coincident work by Cregg et al. [35]. However, in this independent study, V2a Gi neurons were only manipulated collectively, i.e., regardless of their efferent connectivity. Consequently, our conclusions on the implicated circuits diverge. Cregg et al. propose that locomotor trajectory changes owe to a depression of hindlimb circuits and movements on the side of activated V2a descending neurons. This implies that a unique V2a population steers locomotion when mobilized unilaterally and halts it when mobilized bilaterally. Instead we establish here that the directional change and the locomotor halt are controlled by distinct V2a subsets that differ by their segmental projections and can therefore be experimentally manipulated independently. Our work altogether argues that the impact of V2a Gi neurons on locomotor trajectory is rather primarily supported by their capacity to impose the head orientation. In fact, the head rotation precedes the trajectory changes evoked experimentally (Figure 3G) or occurring spontaneously (Figure S3) and has been postulated as a prime driver for locomotor trajectory in humans [4–6]. In swimming species, trajectory changes are also initiated by a bending of the head and trunk [13]. Our work hence highlights the importance of the head in directing movement path across species. To be clear, we do not dispute that activating V2a Gi neurons collectively—or the C2-projecting subset selectively—leads to asymmetric limb movements [35] (Figures 3H and 6D). Yet we show here that this asymmetry does not appear to be a primary consequence of activated descending V2a neurons reaching the hindlimb controllers in the lumbar spinal cord. It may rather be an adaptive adjustment to the displacement of the body axis, primed by the head (and possibly the forelimbs), which *is* driven by C2-projecting V2a Gi neurons. Changes in body orientation can in fact be imposed by activating V2a neurons on stationary animals (Figures 2C–2E, S6I, and S6J). How such displacement translates in an asymmetric limb pattern while on the move remains to be determined. Limb sensory inputs can adjust stance patterns during mechanically forced directional changes [65, 66] and should notably be examined.

Limitations

Our opposite findings from gain and loss of function indicate that V2a neurons' activity is both causal to, and required for, head orientating movements and trajectory changes. Our results, however, do not speak to whether V2a neurons are mobilized during natural behaviors and at all situations that need oriented movements. Interestingly, natural turnings can be, but do not have to be, associated with a locomotor arrest (Figure S3), suggesting that each subtype could even be recruited independently. Head-mounted microscopes [67] should be considered in future experiments with some developments to overcome the sparsity and deep location of the V2a population. Another intriguing finding reported here is that the two V2a subsets evoke opposing actions: motor excitation for the C2-projecting one, functional inhibition for the L2-projecting one. Yet V2a neurons at all positions of the medullary RF are glutamatergic and do not co-express inhibitory or serotonergic markers [34, 36]. The functional outcome of each subset may therefore owe to the cell types contacted in the spinal cord. Admittedly, we have not examined V2a targets in detail, but the short-latency responses on neck muscles and the putative contacts on cervical motoneurons (Figure 7) raise the possibility that V2a RS neurons may include neck premotoneurons [20, 22]. V2a neurons can indeed be premotoneurons, at least in the spinal cord [68, 69]. Dedicated tracings from muscles [70] will be needed to ascertain this possibility in the brainstem. Instead, the L2-projecting subset may correspond to the previously identified V2a "stop neurons" and may depress locomotor circuits indirectly via inhibitory spinal neurons [34], whose activation can halt locomotion [71]. Characterizing the V2a postsynaptic targets will therefore be extremely informative and should now be achievable with anterograde transneuronal vectors [72]. Finally, while we focused on the rostral medulla (i.e., levels encompassing the Gi and GiA), V2a neurons located more caudally also project to the spinal cord (Figures 4I and 4L) and their function will need to be determined.

General Conclusion

Our work has identified subtypes of reticular neurons that are downstream of the superior colliculus and that control multiple motor actions pertinent for orientation. These subtypes share a common genetic identity and anatomical positioning, but differ by their efferent connectivity. Our study therefore underscores the organization of the reticular formation in functional modules defined by transcription factors, and at the same time argues for a further segregation within modules whereby a functional connectivity organized by muscles or muscle groups may underlie the execution of individual motor actions of a coherent behavior. This represents an entry point to further decipher the neuronal basis for the diversity of motor repertoires and how the brain elaborates complex movements.

STAR★METHODS

Detailed methods are provided in the online version of this paper and include the following:

- KEY RESOURCES TABLE
- RESOURCE AVAILABILITY
  - Lead Contact
  - Materials Availability
  - Data and Code Availability
- EXPERIMENTAL MODEL AND SUBJECT DETAILS
  - Mice
  - Viruses used
- METHOD DETAILS
  - Surgical procedures for injections and implants in the brainstem
  - Surgical procedures for injections in the spinal cord
  - Histology
  - Delineation of brainstem structures and cellular counts
  - Behavioral experiments
  - Electromyographic Recordings
- QUANTIFICATION AND STATISTICAL ANALYSIS
  - Pose estimation using DeepLabCut and quantifications of body and head movements
  - Calculations of limb velocity

- Statistical analysis for optogenetic experiments
- Statistical analysis for ablation and silencing experiments
- Statistical analysis for electromyographic recordings

SUPPLEMENTAL INFORMATION

Supplemental Information can be found online at https://doi.org/10.1016/j.cub.2020.09.014.

ACKNOWLEDGMENTS

This work was funded by an Agence Nationale pour la Recherche grant (ANR-17-CE16-0027) to J.B. and by NeuroPSI, CNRS, and Université Paris-Saclay. G.U. holds a Université Paris-Saclay doctoral fellowship. C.H. holds doctoral fellowships from Région Ile-de-France and Fondation pour la Recherche Médicale. We thank Séverine Diem for assistance with genotyping, Tihana Jovanic for critical reading of the manuscript, and Beatrice Cerocchi for the mouse drawings in the graphical abstract. Other schematics are from Scidraw.io.

AUTHOR CONTRIBUTIONS

J.B. designed the study and supervised the work. G.U. performed experiments with contributions from J.B. and A.H. and analyzed anatomical data. E.G. designed tracking scripts and analyzed the behavioral data with J.B. C.H. helped establish and performed initial transneuronal tracings. G.U. and J.B. prepared figures. J.B. wrote the paper and all authors contributed to its editing.

DECLARATION OF INTERESTS

The authors declare no competing interests.

Received: April 1, 2020
Revised: August 3, 2020
Accepted: September 4, 2020
Published: October 1, 2020

REFERENCES

1. Mitchinson, B., and Prescott, T.J. (2013). Whisker movements reveal spatial attention: a unified computational model of active sensing control in the rat. PLoS Comput. Biol. *9*, e1003236.
2. Kurnikova, A., Moore, J.D., Liao, S.M., Deschênes, M., and Kleinfeld, D. (2017). Coordination of orofacial motor actions into exploratory behavior by rat. Curr. Biol. *27*, 688–696.
3. Guitton, D. (1992). Control of eye-head coordination during orienting gaze shifts. Trends Neurosci. *15*, 174–179.
4. Grasso, R., Glasauer, S., Takei, Y., and Berthoz, A. (1996). The predictive brain: anticipatory control of head direction for the steering of locomotion. Neuroreport *7*, 1170–1174.
5. Dollack, F., Perusquía-Hernández, M., Kadone, H., and Suzuki, K. (2019). Head anticipation during locomotion with auditory instruction in the presence and absence of visual input. Front. Hum. Neurosci. *13*, 293.
6. Grasso, R., Prévost, P., Ivanenko, Y.P., and Berthoz, A. (1998). Eye-head coordination for the steering of locomotion in humans: an anticipatory synergy. Neurosci. Lett. *253*, 115–118.
7. Oueghlani, Z., Simonnet, C., Cardoit, L., Courtand, G., Cazalets, J.R., Morin, D., Juvin, L., and Barrière, G. (2018). Brainstem steering of locomotor activity in the newborn rat. J. Neurosci. *38*, 7725–7740.
8. Fagerstedt, P., and Ullén, F. (2001). Lateral turns in the lamprey. I. Patterns of motoneuron activity. J. Neurophysiol. *86*, 2246–2256.
9. Basso, M.A., and May, P.J. (2017). Circuits for action and cognition: a view from the superior colliculus. Annu. Rev. Vis. Sci. *3*, 197–226.
10. Song, J.H., Rafal, R.D., and McPeek, R.M. (2011). Deficits in reach target selection during inactivation of the midbrain superior colliculus. Proc. Natl. Acad. Sci. USA *108*, E1433–E1440.
11. Stubblefield, E.A., Costabile, J.D., and Felsen, G. (2013). Optogenetic investigation of the role of the superior colliculus in orienting movements. Behav. Brain Res. *255*, 55–63.
12. Felsen, G., and Mainen, Z.F. (2008). Neural substrates of sensory-guided locomotor decisions in the rat superior colliculus. Neuron *60*, 137–148.
13. Saitoh, K., Ménard, A., and Grillner, S. (2007). Tectal control of locomotion, steering, and eye movements in lamprey. J. Neurophysiol. *97*, 3093–3108.
14. Sahibzada, N., Dean, P., and Redgrave, P. (1986). Movements resembling orientation or avoidance elicited by electrical stimulation of the superior colliculus in rats. J. Neurosci. *6*, 723–733.
15. Sparks, D.L., and Hartwich-Young, R. (1989). The deep layers of the superior colliculus. Rev. Oculomot. Res. *3*, 213–255.
16. Redgrave, P., Mitchell, I.J., and Dean, P. (1987). Descending projections from the superior colliculus in rat: a study using orthograde transport of wheatgerm-agglutinin conjugated horseradish peroxidase. Exp. Brain Res. *68*, 147–167.
17. Kleinfeld, D., Moore, J.D., Wang, F., and Deschenes, M. (2014). The brainstem oscillator for whisking and the case for breathing as the master clock for orofacial motor actions. Cold Spring Harb. Symp. Quant. Biol. *79*, 29–39.
18. Sparks, D.L. (2002). The brainstem control of saccadic eye movements. Nat. Rev. Neurosci. *3*, 952–964.
19. Liang, H., Watson, C., and Paxinos, G. (2016). Terminations of reticulospinal fibers originating from the gigantocellular reticular formation in the mouse spinal cord. Brain Struct. Funct. *221*, 1623–1633.
20. Isa, T., and Sasaki, S. (2002). Brainstem control of head movements during orienting; organization of the premotor circuits. Prog. Neurobiol. *66*, 205–241.
21. Sasaki, S., Yoshimura, K., and Naito, K. (2004). The neural control of orienting: role of multiple-branching reticulospinal neurons. Prog. Brain Res. *143*, 383–389.
22. Peterson, B.W., Pitts, N.G., Fukushima, K., and Mackel, R. (1978). Reticulospinal excitation and inhibition of neck motoneurons. Exp. Brain Res. *32*, 471–489.
23. Kiehn, O. (2016). Decoding the organization of spinal circuits that control locomotion. Nat. Rev. Neurosci. *17*, 224–238.
24. Grillner, S., and El Manira, A. (2020). Current principles of motor control, with special reference to vertebrate locomotion. Physiol. Rev. *100*, 271–320.
25. Jordan, L.M., Liu, J., Hedlund, P.B., Akay, T., and Pearson, K.G. (2008). Descending command systems for the initiation of locomotion in mammals. Brain Res. Brain Res. Rev. *57*, 183–191.
26. Capelli, P., Pivetta, C., Soledad Esposito, M., and Arber, S. (2017). Locomotor speed control circuits in the caudal brainstem. Nature *551*, 373–377.
27. Kim, L.H., Sharma, S., Sharples, S.A., Mayr, K.A., Kwok, C.H.T., and Whelan, P.J. (2017). Integration of descending command systems for the generation of context-specific locomotor behaviors. Front. Neurosci. *11*, 581.
28. Ferreira-Pinto, M.J., Ruder, L., Capelli, P., and Arber, S. (2018). Connecting circuits for supraspinal control of locomotion. Neuron *100*, 361–374.
29. Isa, T., and Sasaki, S. (1988). Effects of lesion of paramedian pontomedullary reticular formation by kainic acid injection on the visually triggered horizontal orienting movements in the cat. Neurosci. Lett. *87*, 233–239.
30. Li, S., Misra, K., Matise, M.P., and Xiang, M. (2005). Foxn4 acts synergistically with Mash1 to specify subtype identity of V2 interneurons in the spinal cord. Proc. Natl. Acad. Sci. USA *102*, 10688–10693.
31. Briscoe, J., and Ericson, J. (2001). Specification of neuronal fates in the ventral neural tube. Curr. Opin. Neurobiol. *11*, 43–49.

32. Crone, S.A., Viemari, J.C., Droho, S., Mrejeru, A., Ramirez, J.M., and Sharma, K. (2012). Irregular breathing in mice following genetic ablation of V2a neurons. J. Neurosci. *32*, 7895–7906.

33. Kimura, Y., Satou, C., Fujioka, S., Shoji, W., Umeda, K., Ishizuka, T., Yawo, H., and Higashijima, S. (2013). Hindbrain V2a neurons in the excitation of spinal locomotor circuits during zebrafish swimming. Curr. Biol. *23*, 843–849.

34. Bouvier, J., Caggiano, V., Leiras, R., Caldeira, V., Bellardita, C., Balueva, K., Fuchs, A., and Kiehn, O. (2015). Descending command neurons in the brainstem that halt locomotion. Cell *163*, 1191–1203.

35. Cregg, J.M., Leiras, R., Montalant, A., Wanken, P., Wickersham, I.R., and Kiehn, O. (2020). Brainstem neurons that command mammalian locomotor asymmetries. Nat. Neurosci. *23*, 730–740.

36. Bretzner, F., and Brownstone, R.M. (2013). Lhx3-Chx10 reticulospinal neurons in locomotor circuits. J. Neurosci. *33*, 14681–14692.

37. Kim, E.J., Jacobs, M.W., Ito-Cole, T., and Callaway, E.M. (2016). Improved monosynaptic neural circuit tracing using engineered rabies virus glycoproteins. Cell Rep. *15*, 692–699.

38. Azim, E., Jiang, J., Alstermark, B., and Jessell, T.M. (2014). Skilled reaching relies on a V2a propriospinal internal copy circuit. Nature *508*, 357–363.

39. Romer, S.H., Seedle, K., Turner, S.M., Li, J., Baccei, M.L., and Crone, S.A. (2017). Accessory respiratory muscles enhance ventilation in ALS model mice and are activated by excitatory V2a neurons. Exp. Neurol. *287*, 192–204.

40. Caggiano, V., Leiras, R., Goñi-Erro, H., Masini, D., Bellardita, C., Bouvier, J., Caldeira, V., Fisone, G., and Kiehn, O. (2018). Midbrain circuits that set locomotor speed and gait selection. Nature *553*, 455–460.

41. Josset, N., Roussel, M., Lemieux, M., Lafrance-Zoubga, D., Rastqar, A., and Bretzner, F. (2018). Distinct contributions of mesencephalic locomotor region nuclei to locomotor control in the freely behaving mouse. Curr. Biol. *28*, 884–901.e3.

42. Masullo, L., Mariotti, L., Alexandre, N., Freire-Pritchett, P., Boulanger, J., and Tripodi, M. (2019). Genetically defined functional modules for spatial orienting in the mouse superior colliculus. Curr. Biol. *29*, 2892–2904.e8.

43. Yang, C.F., Chiang, M.C., Gray, D.C., Prabhakaran, M., Alvarado, M., Juntti, S.A., Unger, E.K., Wells, J.A., and Shah, N.M. (2013). Sexually dimorphic neurons in the ventromedial hypothalamus govern mating in both sexes and aggression in males. Cell *153*, 896–909.

44. Neve, R.L., Neve, K.A., Nestler, E.J., and Carlezon, W.A., Jr. (2005). Use of herpes virus amplicon vectors to study brain disorders. Biotechniques *39*, 381–391.

45. Reinhard, K., Li, C., Do, Q., Burke, E.G., Heynderickx, S., and Farrow, K. (2019). A projection specific logic to sampling visual inputs in mouse superior colliculus. eLife *8*, e50697.

46. Coopersmith, R., and Neve, R.L. (1999). Expression of multiple proteins within single primary cortical neurons using a replication deficient HSV vector. Biotechniques *27*, 1156–1160.

47. Tervo, D.G., Hwang, B.Y., Viswanathan, S., Gaj, T., Lavzin, M., Ritola, K.D., Lindo, S., Michael, S., Kuleshova, E., Ojala, D., et al. (2016). A designer AAV variant permits efficient retrograde access to projection neurons. Neuron *92*, 372–382.

48. Ren, J., Friedmann, D., Xiong, J., Liu, C.D., Ferguson, B.R., Weerakkody, T., DeLoach, K.E., Ran, C., Pun, A., Sun, Y., et al. (2018). Anatomically defined and functionally distinct dorsal raphe serotonin sub-systems. Cell *175*, 472–487.e20.

49. Sathyamurthy, A., Barik, A., Dobrott, C.I., Matson, K.J.E., Stoica, S., Pursley, R., Chesler, A.T., and Levine, A.J. (2020). Cerebellospinal neurons regulate motor performance and motor learning. Cell Rep. *31*, 107595.

50. Roucoux, A., Crommelinck, M., and Decostre, M.F. (1989). Neck muscle activity in eye–head coordinated movements. Prog. Brain Res. *80*, 351–362, discussion 347–349.

51. Ueno, M., Nakamura, Y., Li, J., Gu, Z., Niehaus, J., Maezawa, M., Crone, S.A., Goulding, M., Baccei, M.L., and Yoshida, Y. (2018). Corticospinal circuits from the sensory and motor cortices differentially regulate skilled movements through distinct spinal interneurons. Cell Rep. *23*, 1286–1300.e7.

52. Maeda, H., Fukuda, S., Kameda, H., Murabe, N., Isoo, N., Mizukami, H., Ozawa, K., and Sakurai, M. (2016). Corticospinal axons make direct synaptic connections with spinal motoneurons innervating forearm muscles early during postnatal development in the rat. J. Physiol. *594*, 189–205.

53. Palmieri, R.M., Ingersoll, C.D., and Hoffman, M.A. (2004). The hoffmann reflex: methodologic considerations and applications for use in sports medicine and athletic training research. J. Athl. Train. *39*, 268–277.

54. McGavern, D.B., and Kang, S.S. (2011). Illuminating viral infections in the nervous system. Nat. Rev. Immunol. *11*, 318–329.

55. Antinone, S.E., and Smith, G.A. (2010). Retrograde axon transport of herpes simplex virus and pseudorabies virus: a live-cell comparative analysis. J. Virol. *84*, 1504–1512.

56. Criddle, A., Thornburg, T., Kochetkova, I., DePartee, M., and Taylor, M.P. (2016). gD-independent superinfection exclusion of alphaherpesviruses. J. Virol. *90*, 4049–4058.

57. Sargolini, F., Fyhn, M., Hafting, T., McNaughton, B.L., Witter, M.P., Moser, M.B., and Moser, E.I. (2006). Conjunctive representation of position, direction, and velocity in entorhinal cortex. Science *312*, 758–762.

58. Muzzu, T., Mitolo, S., Gava, G.P., and Schultz, S.R. (2018). Encoding of locomotion kinematics in the mouse cerebellum. PLoS ONE *13*, e0203900.

59. Shang, C., Chen, Z., Liu, A., Li, Y., Zhang, J., Qu, B., Yan, F., Zhang, Y., Liu, W., Liu, Z., et al. (2018). Divergent midbrain circuits orchestrate escape and freezing responses to looming stimuli in mice. Nat. Commun. *9*, 1232.

60. Murer, M.G., and Pazo, J.H. (1993). Circling behaviour induced by activation of GABAA receptors in the subthalamic nucleus. Neuroreport *4*, 1219–1222.

61. Supko, D.E., Uretsky, N.J., and Wallace, L.J. (1991). Activation of AMPA/kainic acid glutamate receptors in the zona incerta stimulates locomotor activity. Brain Res. *564*, 159–163.

62. Darmohray, D.M., Jacobs, J.R., Marques, H.G., and Carey, M.R. (2019). Spatial and temporal locomotor learning in mouse cerebellum. Neuron *102*, 217–231.e4.

63. Cabaj, A.M., Majczynski, H., Couto, E., Gardiner, P.F., Stecina, K., Slawinska, U., and Jordan, L.M. (2017). Serotonin controls initiation of locomotion and afferent modulation of coordination via 5-HT7 receptors in adult rats. J. Physiol. *595*, 301–320.

64. Stujenske, J.M., Spellman, T., and Gordon, J.A. (2015). Modeling the spatiotemporal dynamics of light and heat propagation for in vivo optogenetics. Cell Rep. *12*, 525–534.

65. Musienko, P.E., Zelenin, P.V., Lyalka, V.F., Gerasimenko, Y.P., Orlovsky, G.N., and Deliagina, T.G. (2012). Spinal and supraspinal control of the direction of stepping during locomotion. J. Neurosci. *32*, 17442–17453.

66. Karayannidou, A., Zelenin, P.V., Orlovsky, G.N., Sirota, M.G., Beloozerova, I.N., and Deliagina, T.G. (2009). Maintenance of lateral stability during standing and walking in the cat. J. Neurophysiol. *101*, 8–19.

67. Ghosh, K.K., Burns, L.D., Cocker, E.D., Nimmerjahn, A., Ziv, Y., Gamal, A.E., and Schnitzer, M.J. (2011). Miniaturized integration of a fluorescence microscope. Nat. Methods *8*, 871–878.

68. Dougherty, K.J., Zagoraiou, L., Satoh, D., Rozani, I., Doobar, S., Arber, S., Jessell, T.M., and Kiehn, O. (2013). Locomotor rhythm generation linked to the output of spinal shox2 excitatory interneurons. Neuron *80*, 920–933.

69. Kimura, Y., Okamura, Y., and Higashijima, S. (2006). alx, a zebrafish homolog of Chx10, marks ipsilateral descending excitatory interneurons that participate in the regulation of spinal locomotor circuits. J. Neurosci. *26*, 5684–5697.

70. Wu, J., Capelli, P., Bouvier, J., Goulding, M., Arber, S., and Fortin, G. (2017). A V0 core neuronal circuit for inspiration. Nat. Commun. *8*, 544.

71. Caggiano, V., Sur, M., and Bizzi, E. (2014). Rostro-caudal inhibition of hindlimb movements in the spinal cord of mice. PLoS ONE *9*, e100865.

72. Zingg, B., Chou, X.L., Zhang, Z.G., Mesik, L., Liang, F., Tao, H.W., and Zhang, L.I. (2017). AAV-mediated anterograde transsynaptic tagging: mapping corticocollicular input-defined neural pathways for defense behaviors. Neuron *93*, 33–47.

73. Mattis, J., Tye, K.M., Ferenczi, E.A., Ramakrishnan, C., O'Shea, D.J., Prakash, R., Gunaydin, L.A., Hyun, M., Fenno, L.E., Gradinaru, V., et al. (2011). Principles for applying optogenetic tools derived from direct comparative analysis of microbial opsins. Nat. Methods *9*, 159–172.

74. Harrison, M., O'Brien, A., Adams, L., Cowin, G., Ruitenberg, M.J., Sengul, G., and Watson, C. (2013). Vertebral landmarks for the identification of spinal cord segments in the mouse. Neuroimage *68*, 22–29.

75. Ueda, H.R., Ertürk, A., Chung, K., Gradinaru, V., Chédotal, A., Tomancak, P., and Keller, P.J. (2020). Tissue clearing and its applications in neuroscience. Nat. Rev. Neurosci. *21*, 61–79.

76. Franklin, K.B., and Paxinos, G. (2007). The Mouse Brain in Stereotaxic Coordinates, Third Edition (Elsevier).

77. Pearson, K.G., Acharya, H., and Fouad, K. (2005). A new electrode configuration for recording electromyographic activity in behaving mice. J. Neurosci. Methods *148*, 36–42.

78. Mathis, A., Mamidanna, P., Cury, K.M., Abe, T., Murthy, V.N., Mathis, M.W., and Bethge, M. (2018). DeepLabCut: markerless pose estimation of user-defined body parts with deep learning. Nat. Neurosci. *21*, 1281–1289.

STAR★METHODS

KEY RESOURCES TABLE

REAGENT or RESOURCE	SOURCE	IDENTIFIER
Antibodies		
Goat anti-Choline Acetyltransferase (ChAT)	Merck Millipore	Cat #: AB144P; RRID: AB_2079751
Chicken anti-Green Fluorescent Protein (GFP) Antibody	Aves Labs	Cat #: 1020; RRID: AB_10000240
Rabbit anti-Red Fluorescent Protein (RFP)	Rockland	Cat #: 600-401-379; RRID: AB_2209751
Sheep anti-Tyrosine Hydroxylase (TH)	Merck Millipore	Cat #: AB1542; RRID: AB_90755
Bacterial and Virus Strains		
AAV8-hSyn-FLEX-TVA-p2a-eGFP-2a-oG	SALK GT3	RRID: Addgene_85225
HSV1-hEF1a-LS1L-TVA950-T2A-rabiesOG-IRES-mCherry	Rachael Neve	Rachael Neve, Massachusetts General Hospital
HSV1-hEF1a-LS1L-hChR2(H134R)-p2A-EYFP	Rachael Neve	Rachael Neve, Massachusetts General Hospital
EnvA-ΔG-Rabies-mCherry	SALK GT3	RRID: Addgene_32636
EnvA-ΔG-Rabies-GFP	SALK GT3	RRID: Addgene_32635
AAV9-Ef1a-DIO-hChR2(E123T/T159C)-EYFP	Addgene	RRID: Addgene_35509
AAV5-FLEX-taCasp3-TEVp	UNC	RRID: Addgene_45580
AAV8.2-hEF1a-DIO-hM4Di-mCherry-WPRE	Rachael Neve	Rachael Neve, Massachusetts General Hospital
AAVretro-EF1a-doublefloxed-hChR2(H134R)-EYFP-WPRE-HGHpA	Addgene	RRID: Addgene_20298
Chemicals, Peptides, and Recombinant Proteins		
Clozapine N-oxide (CNO)	Enzo Life Sciences	Cat #: BML-NS105-0005
Cholera Toxin B (CTB) – AF647 conjugate	ThermoFisher Scientific	Cat #: C-34778
NeuroTrace 640/660 Deep-Red	ThermoFisher Scientific	Cat #: N21483
NeuroTrace 435/445 blue	ThermoFisher Scientific	Cat #: N21479
Fluoro-Max blue beads	ThermoFisher Scientific	Cat #: B500
Prolong Diamond Antifade Montant	ThermoFisher Scientific	Cat #: P36970
ibidi Mounting Medium	ibidi	Cat #: 50001
Deposited Data		
Original datasets on Mendeley Data	This paper	http://doi.org/10.17632/54x8rjppfz.1
Experimental Models: Organisms/Strains		
Mouse: Chx10-Cre	S. Crone, K. Sharma, L. Zagoraiou, and T.M. Jessell	[34, 38, 39]
Software and Algorithms		
MATLAB R2018a	Mathworks	https://www.mathworks.com/products/matlab.html; RRID: SCR_001622
DeelLabCut	Mathis Lab	http://www.mousemotorlab.org/deeplabcut
ImageJ	https://imagej.net/	RRID: SCR_003070
ZEN Lite	Zeiss	https://www.zeiss.fr/microscopie/produits/microscope-software/zen-lite/zen-2-lite-download.html; RRID: SCR_013672
Leica LASX	Leica	https://www.leica-microsystems.com/products/microscope-software/p/leica-las-x-ls/; RRID: SCR_013673
LabScribe NI	iWorxs	https://www.iworx.com/products/biomedical-engineering/labscribeni/
2nd LOOK	IO Industries	http://ioindustries.com/2ndlook.html
Kdenlive video editor	Kdenlive	https://kdenlive.org/fr/

RESOURCE AVAILABILITY

Lead Contact

Further information and requests for resources and reagents should be directed to and will be fulfilled by the Lead Contact, Julien Bouvier (julien.bouvier@cnrs.fr).

Materials Availability

This study did not generate new unique reagents.

Data and Code Availability

Original data have been deposited to Mendeley Data (http://dx.doi.org/10.17632/54x8rjppfz.1). This study did not generate any computer code.

EXPERIMENTAL MODEL AND SUBJECT DETAILS

Mice

The *Chx10-Cre* was kindly provided by S. Crone, K. Sharma, L. Zagoraiou, and T.M. Jessell [34, 38, 39]. C57BL6 wilt-type mice were obtained by Janvier Labs (Le Genest-Saint-Isle, France). Animals were group-housed with free access to food and water in controlled temperature conditions and exposed to a conventional 12-h light/dark cycle. Experiments were performed on animals of either sex, aged 2 to 3 months at the time of first injection. All procedures were approved by the French Ethical Committee (authorization 2020-022410231878) and conducted in accordance with EU Directive 2010/63/EU. All efforts were made to reduce animal suffering and minimize the number of animals.

Viruses used

For Cre-dependent expression of ChR2 in the Gi we injected unilaterally 100 to 200 nL of an AAV9-Ef1a-DIO-hChR2(E123T/T159C)-eYFP (addgene #35509, titer 3.2×10^{12} vp/mL [73]). For cellular ablation of V2a Gi neurons we used 400 nL of a AAV5-FLEX-taCasp3-TEVp (titer 4.6×10^{12} vp/mL) obtained from UNC (addgene plasmid #45580 [43]). For reversible silencing of V2a Gi neurons we used 400 nL of a AAV8.2-hEF1a-DIO-hM4Di-mCherry-WPRE (titer 2.25×10^{13}) obtained from Dr. Rachael Neve (Gene Delivery Technology Core, Massachusetts General Hospital, USA). For transsynaptic labeling of inputs onto V2a Gi neurons, we used 500 nL of an AAV8-hSyn-FLEX-TVA-p2a-eGFP-2a-oG (titer: 2.8×10^{12} vp/mL) obtained by the GT3 core (Salk Institute). For retrograde labeling of spinally-projecting V2a neurons we used 500nL per injection spot of HSV1-hEF1a-LS1L-TVA950-T2A-rabiesOG-IRES-mCherry and HSV1-hEF1a-LS1L-hChR2(H134R)-p2A-eYFP obtained from Dr. Rachael Neve (Gene Delivery Technology Core, Massachusetts General Hospital, USA). Rabies viruses used were EnvA-ΔG-rabies-mCherry (titer: 3.12×10^{8} vp/mL) and EnvA-ΔG-rabies-GFP (titer: 2.26×10^{8} vp/mL) both obtained by the GT3 core (Salk Institute, USA). For optogenetic manipulations of spinally-projecting V2a neurons we used 500 nL per injection spot of AAVretro-EF1a-doublefloxed-hChR2(H134R)-eYFP-WPRE-HGHpA (Karl Deisseroth, Addgene plasmid # 20298; http://n2t.net/addgene:20298; RRID: Addgene_20298; titer 1.0×10^{13} vp/mL).

METHOD DETAILS

Surgical procedures for injections and implants in the brainstem

Animals were anesthetized with isoflurane throughout the surgery (4% at 1 L/min for induction, and 2%–3% at 0.3 L/min for maintenance). Buprenorphine (0,025 mg/kg) was administered subcutaneously for analgesia before the surgery. The temperature of the mice was maintained at 36°C with a feedback-controlled heating pad. Anesthetized animals were placed on a stereotaxic frame (Kopf) and the skull was exposed. Viral vectors were delivered using a pulled glass pipette connected to a syringe pump (Legato 130, KD Scientific, customized by Phymep, France). The infusion flow was set to 100 nL/min. Coordinates (in mm) used to target V2a Gi neurons were: −6.0 from bregma, 0.8 lateral, and 4.5 from the dorsal brain surface. After the injection, the pipette was held in place for 5 min before being slowly retracted. For optogenetic activations, a 200 μm core 0.39 NA optic fiber (Thorlabs) connected to a 1.25 mm diameter ferrule (Thorlabs) was implanted ~500 μm above the injection site (Figure 2A). This operation was performed during the same surgery as the viral injection when both were targeted to the brainstem. For activating spinally-projecting V2a neurons, the spinal injection was performed first (see below) and the optic fiber was implanted 5 to 7 days later. Dental cement (Tetric Evoflow) was used to secure the implanted ferrules. Animals were followed daily after the surgery.

Surgical procedures for injections in the spinal cord

Animals were anesthetized as described above and spinal injections were performed as previously done [34]. A two cm incision of the skin was performed dorsally on anesthetized animals and the exposed spinal column was fixed with two holders on the left and right sides to a stereotaxic frame to minimize movements. Vertebral spinous processes were used as landmarks to target specific segments [74]. A small incision of the ligamentum Flavum allowed access to the spinal cord. A pulled glass pipette connected to

a motorized syringe pump injector (Legato 130, KD Scientific, customized by Phymep, France) was positioned into the ventromedial area of the L2 (between the 11th and 12th vertebral body) or C2 (between the 1st and 2nd vertebral body) spinal segment using the following coordinates: 400 mm laterally from the dorsal artery and 500 to 850 mm (L2 injections) or 800 to 1200 μm (C2 injections) depth from the dorsal surface. This lateral positioning ensures that the injection pipette does not pass through the lateral funiculus where descending axons of RS neurons travel. A total volume of 500 nL of virus was injected at 100 nL/min in 2 distinct spots separated rostrocaudally by 600 to 800 μm. For CTB injections, we used 500 nL of CTB-AF647 conjugate (Thermofisher Scientific, Cat # C-34778) diluted at 0.5% in sterile saline. Dual HSVs injections (Figures 4J and S4) were done bilaterally to increase the number of labeled cells for quantifications but AAVretro injections (Figures 5, 6, and S6) were done unilaterally. Dual injections of HSVs in both the L2 and C2 spinal segments were performed successively, starting from L2, during the same surgical procedure. For controls, two consecutive HSV injections were performed at L2, either during the same day or at one day apart (Figure S4). After each injection, the pipette was held in place for 5 min before being slowly retracted. The skin was sutured, and animals were followed daily after the surgery. All animals recovered without motor impairments.

Histology

Adult mice were anesthetized with Euthasol Vet (140 mg/kg) and perfused with 4% paraformaldehyde (PFA) in 1X Phosphate Buffered Saline (PBS). Brains and spinal cord were dissected out and fixed overnight in 4% PFA at 4°C. After fixation, tissues were rinsed in 1X PBS. Brain and spinal cord were cryoprotected overnight at 4°C, respectively in 16% and 20% sucrose in PBS. Tissues were rapidly cryoembedded in OCT mounting medium and sectioned at 30 μm using a cryostat. Sections were blocked in a solution of 1X Tris Buffered Saline (TBS), 5% normal donkey serum and 0.5% Triton X-100. The primary antibodies, carried out 24 to 48 h at 4°C, were: goat anti-ChAt (1:500, ref: AB144P, Merck Millipore), chicken anti-GFP (1:500, ref: 1020, Aves Labs), rabbit anti-RFP (1:500, ref: 600-401-379, Rockland) and sheep anti-TH (1:500, ref: AB1542, Merck Millipore). Primary antibodies were detected after 2 h of incubation at room temperature with appropriate secondary antibodies coupled to Alexa Fluor 488, 647, Cy-3 or Cy-5 (1:500, Jackson ImmunoResearch). Sections were counterstained with a fluorescent Nissl stain (NeuroTrace 435/445 blue, ref: N21479, 1:200 or NeuroTrace 640/660 deep-red, ref: N21483, 1:1000, Thermo Fisher Scientific) and mounted in Prolong Diamond Antifade Montant (P36970, Thermo Fisher Scientific) or ibidi Mounting Medium (50001, Ibidi). For counting neurons in the entire brain in transneuronal labeling experiments, all sections were scanned on a Zeiss Axioscan Z1 Digital Slide Scanner (histology platform of the ICM, Paris, France). For all other purposes, sections were acquired with a Leica TCS SP8 confocal microscope (imaging platform of the NeuroPSI Institute, Gif-sur-Yvette, France) with 10x, 25x and 40x objectives. For illustrating a representative spinal cord injection (Figure 4F), whole lumbar spinal cords were cleared using CUBIC-R+ [75] and endogenous CTB fluorescence imaged on a light-sheet microscope (UltraMicroscope II, 4x objective, Miltenyi Biotec).

Delineation of brainstem structures and cellular counts

Brainstem areas were delineated by systematically performing a Nissl stain on experimental sections. The relative distance to Bregma was established by comparing the Nissl stain with that of the Mouse Brain atlas [76]. To examine the distribution of labeled neurons within the rostrocaudal axis of the RF, we considered four major subdivisions, similarly to a previous investigation [34] on the basis of the following criteria (see schematics in Figures 1C and 4G): the most caudal levels (encompassing the MdV) from the rostral edge of the pyramidal decussation caudally, to the opening of the 4th ventricle (obex) rostrally (from approximately −8.0 to −7.2 from Bregma); the caudal extent of the Gigantocellular reticular (Gi) nucleus (encompassing also its ventral part GiV) between the obex caudally and the caudal edge of the facial motor nucleus (7N) rostrally (approximately −6.5 from Bregma); the rostral extent of the Gi nucleus (encompassing its alpha part GiA and the IRt) from the caudal edge of the 7N caudally, to the caudal edge of the superior olivary complex (SOC) rostrally (approximately −5.5 from Bregma); the ponto-medularry junction (encompassing the PnC and the IRt) from caudal edge of the SOC to the motor trigeminal nucleus rostrally (approximately - 5.0 from Bregma). All neurons were counted on 30 μm-thick cryosections. For counting starter cells (Figures 1A–1E and S5) and HSV-labeled neurons (Figures 4 and S4), sections were scanned with a confocal microscope (Leica SP8) using a 25x objective. Counts were done manually with the help of the cell-counter tool in LASX (Leica), in non-adjacent sections. The number of cells per section were averaged per animal, and a grand-mean ± standard error of the mean (SEM) was calculated across animals to produce cells per section bar graphs. At each of the four rostrocaudal subdivision, labeled neurons were allocated into specific subnuclei (e.g., Gi, GiV, GiA, LPGi, IRt, PnC) by overlaying the histological section to the corresponding atlas slide. Pie graphs illustrate the fraction of labeled neurons located in each subnuclei (pooled from all animals) over the total number of labeled contained in the corresponding rostrocaudal subdivision. For counting rabies-labeled neurons, images were obtained from an automated epifluorescence microscope (Zeiss Axioscan Z1 Digital Slide Scanner). For illustrating the percentage of rabies-labeled neurons in each brain area (Figures 1J, S5E, and S5J) neurons in each area were counted using ZEN-Lite (Zeiss) and pooled across all sections for one animal, and expressed as the fraction of the total number of rabies-positive neurons detected automatically by threshold throughout the brain in that same animal. A grand-mean ± SEM was calculated across animals to produce bar graphs. For calculating the fractions of fluorescent anterograde projections in different structures (Figure 4E), maximum z stack projections were made and thresholded. Regions of interests were manually drawn in ImageJ and the densities of fluorescent pixels were measured for 4-5 sections per animal using the Measure plugin. These values were averaged across all sections from all animals and expressed in bar graphs ± SEM.

Behavioral experiments

Optogenetic activations

Behavioral experiments started 15 to 21 days after the viral injection. Implanted animals were connected to a laser source (473 nm DPSS system, LaserGlow Technologies, Toronto, Canada) through a mating sleeve (Thorlabs). In all conditions except EMG recordings, light was delivered in trains of pulses of 15 ms at 40 Hz frequency for a duration of 500 ms. For EMG recordings we also used single pulses of 5 ms duration. We used the minimal laser power sufficient to evoke a response, which was measured to be between 5-12 mW at the fiber tip using a power meter (PM100USB with S120C silicon power head, Thorlabs) to restrict photo-activations unilaterally [64], prevent heat, and exclude an unintentional silencing by over-activation [34].

Behavioral setting and video recordings

For analyzing changes in head movements, trajectory orientation and locomotor speed, animals were placed in a custom open field box (opaque PVC, 60 × 70 cm) without prior habituation and filmed from above at 50 images/sec using a CMOS camera (Jai GO-5000-USB). For analyzing limb movements during optogenetic activations, animals were placed in a custom transparent open-field (40 × 40 cm) and filmed from below at 100 images/sec (Jai GO-2400-USB). For optogenetic activations, open-field recording sessions lasted for a maximum of 30 min per animal. For silencing and ablation experiments, several 3-min videos were recorded per animal. For analyzing snout motion, animals were head-fixed for a maximum of 10 min, and filmed from above at 400 images/sec (Jai GO-2400–USB). Images were streamed to disk on a computer using 2nd Look (IO Industries). Timings of photo-activations were recorded using the TTL output of the laser connected to a National Instruments acquisition card (USB-6211) and the LabScribe NI software (iWorxs). Both recordings were synchronized using hardware trigger. Photo-activations were delivered manually using the NI MAX tool with a minimal interval of 30 s between two consecutive activations. Throughout the manuscript, one trial correspond to one photo-activation. Extracts of videos presented in the supplemental material were edited using Kdenlive (https://kdenlive.org/).

CNO administration

Four weeks following the injection of the hM4Di virus, animals were anesthetized and a surgery was performed as detailed earlier for intracranial viral injection. CNO (Enzo Life science, cat #: BML-NS105-0005) was diluted at 1 mM in freshly made and filtered artificial cerebrospinal fluid (aCSF) of composition (in mM): 126 NaCl; 3 KCl; 1.25 NaH_2PO_4; 2 $MgSO_4$; 26 $NaHCO_3$; 2 CaCl2; 11 D-Glucose. Fluorescent beads (Fluoro-Max blue beads, 0.5 μm, ThermoFischer Scientific, Cat#: B500) were added at a dilution of 1:4000 for subsequent histological validation. A total of 500 nL of CNO/fluorescent beads solution was delivered at the same coordinates used for the hM4Di virus (left side: 4 animals, right side: 1 animal). The pipette was immediately withdrawn after the injection, the skin incision closed rapidly with surgical glue (Vetbond, 3M Cat#: 1469SB) and animals immediately removed from the anesthesia mask. They were kept on an isothermal heating pad (Agnthos, Sweden) for a maximum of 10 min before being placed in the open-field to be filmed from above during 3 min. Since animals had only partially recovered from anesthesia, occasional motivation to move was given by a brief air puff or by the experimenter's hand. Animals were placed back on the heat pad for 2 min, before being filmed again in the open field for 3 min. The 2 videos started within the 15 min that follow the pipette withdrawal are used to produce the "CNO < 15 min" data (Figure 3O). Two or 3 more videos are recorded between 16 and 30 min following pipette withdrawal and used to produce the "CNO > 15 min" data. For controls, similar CNO injections were done on animals that did not receive the hM4Di virus.

Electromyographic Recordings

Electrodes were made of Teflon-insulated silver wire with an outside diameter of 0.14 mm (A-M systems, #793200), inspired by previous work [77]. For each animal, 2 pairs of electrodes were prepared as follows. For each electrode pair, two pieces of wire were lightly twisted together and a knot was placed about 2 cm of one end. A few millimeters from the knot, the Teflon insulation was removed over ~1 mm from each wire so that the two bared regions were separated by about 2 mm. The ends of two wires were glued to a miniature dissecting pin. The opposite ends of the wires were soldered to a miniature connector (Antelec). To implant electrodes in the splenius muscle, animals were anaesthetized using isoflurane and placed in a stereotaxic frame as detailed above. A small incision of the skin was performed dorsally to expose the muscles. The dissecting pin attached to the end of each pair of electrodes was used to draw the twisted pair of wires through the splenius muscle until the knot proximal to the bared regions was firmly against the muscle. The distal end of the electrode exiting the muscle was knotted. The needle was removed by cutting the electrode wires about 0.5 mm distal to this knot. The miniaturized connector was cemented on the skull, caudally to the existing optic fiber. The skin was sutured, and animals were followed daily after the surgery. Between 2 to 3 days following the surgery, implanted animals were connected to an AC amplifier (BMA-400, CWE) and signals were filtered (high-pass: 100 Hz, low-pass: 10 KHz) and collected at 10.000 samples/sec using a National Acquisition card (USB 6211) and the LabScribe NI software (iWorxs). Animals were placed in the open-field and optogenetic activations were delivered manually using the NI MAX tool. A TTL signal from the laser was connected to the same acquisition board for registering the timing of optogenetic activations.

QUANTIFICATION AND STATISTICAL ANALYSIS

Pose estimation using DeepLabCut and quantifications of body and head movements

To compute changes in body orientation, head rotation and locomotor speed, we labeled manually 4 points of interest (POIs) from 3204 frames taken across 80 top-view videos using DeepLabCut version 2.1.5.2 [78]: the head (H), the left and right ears (E_L, E_r) and

the base of the tail (T, see Figure S2A). We then used 95% of the labeled frames to train the network using a ResNet-101-based neural network with default parameters for 1 training iteration. We validated with 3 shuffles, and found that the test error was: 3,84 pixels, train: 3,21 pixels (image size was 2384 by 2048). We then used a p-cutoff of 0,5 to condition the X,Y coordinates for future analyses. This network was then used to analyze all other videos taken with same experimental settings.

Custom scripts were written in MATLAB (Mathworks) and used for computation. The orientation of the animal is defined as the angle α between the vector from T to the median point of E_L and E_R (E_M) and the origin axis $\vec{x}$ (Figure S2B).

$$\frac{\overrightarrow{TE_M}}{\left\|\overrightarrow{TE_M}\right\|} = \begin{pmatrix} X_1 \\ Y_1 \end{pmatrix}$$

$$\begin{pmatrix} X_1 \\ Y_1 \end{pmatrix} = \begin{pmatrix} \cos(\alpha) & -\sin(\alpha) \\ \sin(\alpha) & \cos(\alpha) \end{pmatrix} * \begin{pmatrix} 1 \\ 0 \end{pmatrix}$$

$$\alpha mod 360 = sign(Y_1) * \cos^{-1}(X_1)$$

The head rotation is defined by the angle β between the vector from T to E_M and the vector from E_L to E_R. A bias of 90° is introduced to set the zero when the 2 vectors are orthogonal, resulting in a positive angle when the head turns to the left and a negative angle when the head turns to the right (Figure S2C).

$$\frac{\overrightarrow{E_L E_R}}{\left\|\overrightarrow{E_L E_R}\right\|} = \begin{pmatrix} X_0 \\ Y_0 \end{pmatrix}$$

$$\begin{pmatrix} X_1 \\ Y_1 \end{pmatrix} = \begin{pmatrix} \cos(\beta) & -\sin(\beta) \\ \sin(\beta) & \cos(\beta) \end{pmatrix} * \begin{pmatrix} X_0 \\ Y_0 \end{pmatrix}$$

$$\beta mod 360 = sign\left(\frac{Y_1 - (X_0 X_1 + Y_0 Y_1) Y_0}{X_0}\right) * \cos^{-1}(X_0 X_1 + Y_0 Y_1) - 90$$

The barycenter (G) of the 4 POIs was computed to generate the locomotor trajectory of each mouse and its position derived to obtained the instantaneous speed (s) of the animal across the recording (Figure S2D).

$$\vec{s} = \frac{\partial \vec{u}}{\partial t}$$

With $\vec{u}$ being the displacement of G

$$\vec{u} = \vec{x} + \vec{y} \text{ and } \begin{cases} \vec{s_x} = \frac{\partial \vec{x}}{\partial t}, \ \vec{x} \text{ being the displacement of G along the x axis} \\ \vec{s_y} = \frac{\partial \vec{y}}{\partial t}, \ \vec{y} \text{ being the displacement of G along the y axis} \end{cases}$$

$$\vec{s} = \vec{s_x} + \vec{s_y} \text{ and} \vec{s_x} \perp \vec{s_y}$$

$$s = \sqrt{s_x^2 + s_y^2}$$

For optogenetic activations, trials were sorted as during locomotion when the animal's instantaneous speed was above 10 cm/s and during stationary when it was under 7.5 cm/s during 250 consecutive ms prior to light onset. Indeed, when animals were between these 2 speed values, their behavior was difficult to score (some steps interleaved with immobility) and corresponding trials were therefore not included. For each mouse, trials falling into either category (locomoting or stationary) were merged into matrices and each variable computed (var: α, β, speed):

$$A_{var} = \begin{pmatrix} a_{1,1} & \cdots & a_{1,j} \\ \vdots & \ddots & \vdots \\ a_{i,1} & \cdots & a_{i,j} \end{pmatrix}$$

with i the number of trials and j the number of frames per trial.

In the case of angles (ex: α, β), we normalized, at each trial, the changes induced by light stimulation to the average angle during 0,5 s before light onset.

Finally for each type of injection (Gi, C2, L2) and behavioral condition (stationary or locomoting), the mean response of each animal was computed across all trials (the same number of trials per animal, at least 3 trials) and expressed ± standard error (SEM). A grand-mean ± SEM across animals is also illustrated in figures (colored curves).

Calculations of limb velocity

To produce color-plots histograms, we attempted to label the 4 paws using DeepLabCut. However, this led to significant number of errors and inversions between paws. All errors were then manually corrected on 9 videos from 3 mice. Points were then filtered (maximum speed and group cutoff followed by linear interpolation) and the instantaneous speed of each limb speed was then computed, and a color matrix produced using MATLAB.

Statistical analysis for optogenetic experiments

To perform statistical tests for body orientation, we calculated, for each trial, the peak change in orientation of the mouse during photo-activations as well as the orientation 0.5 s after light offset (black arrowhead in graphs). For the head rotation, we calculated the maximum angle variation to baseline during photo-activations. Both the body orientation and head rotation angles of all trials (numbers are given in figure legends) from all mice within each category (i.e., Gi, L2 or C2 injection and stationary or locomoting) were statistically compared to the same measurements obtained from all trials from 4 injected and implanted wild-type mice (stationary: 44 trials from 4 mice, 11 trials each; locomotion: 48 trials from 4 mice, 12 trials each), using unpaired t tests. For evaluating the effect of photo-activations on locomotor speed we took into account the spontaneous gradual deceleration that occurs independently of activating V2a neurons, as seen in mock photo-activation trials in control mice (Figure S2K). This likely owes to the episodic nature of locomotion in this specie and our intentional delivery of photo-activations when animals just engaged in a vigorous locomotor bout which is bound to be short due to the limited size of the open field. We therefore computed, for each trial, the mean locomotor speed during light stimulations as well as the first deceleration coefficient of the first monotonic part of the curve during the light-stimulation as the best fitted linear regression. Both the mean speed and the slope coefficients of all trials of all mice within a given category were statistically compared to those obtained from control mice. For snout motion recordings, the mean position of the nose snout during the 500 ms photo-activations was computed for each trial, and statistically compared to the mean position during the preceding 500 ms.

Statistical analysis for ablation and silencing experiments

We computed, for each video of each mice, i) the instantaneous angular speed of the animal as the first derivative of the body orientation during locomotion (i.e., instantaneous speed > 10 cm/s) and ii) the average head orientation during the entire video recording. These values were statistically compared between appropriate groups (e.g., before and after CNO) using unpaired t tests.

Statistical analysis for electromyographic recordings

EMG recordings were exported to Clampfit (Molecular Devices) and responses to photo-activations were detected manually as events with a pointed peak (either negative of positive), with an amplitude larger than 5 times the mean baseline before the light pulse and occurring within 25 ms following light onset. The latency was defined as the interval between light onset and the time point when the EGM signal reaches the above detection threshold. Data were collected for ~15 trials per animal and a grand-mean ± SEM across all trials was computed to produce bar graphs illustrated in Figure 7. Differences in latency between the ipsilateral and contralateral sides were evaluated by unpaired t tests across all trials.

Current Biology, Volume *30*

Supplemental Information

Control of Orienting Movements and Locomotion by Projection-Defined Subsets of Brainstem V2a Neurons

Giovanni Usseglio, Edwin Gatier, Aurélie Heuzé, Coralie Hérent, and Julien Bouvier

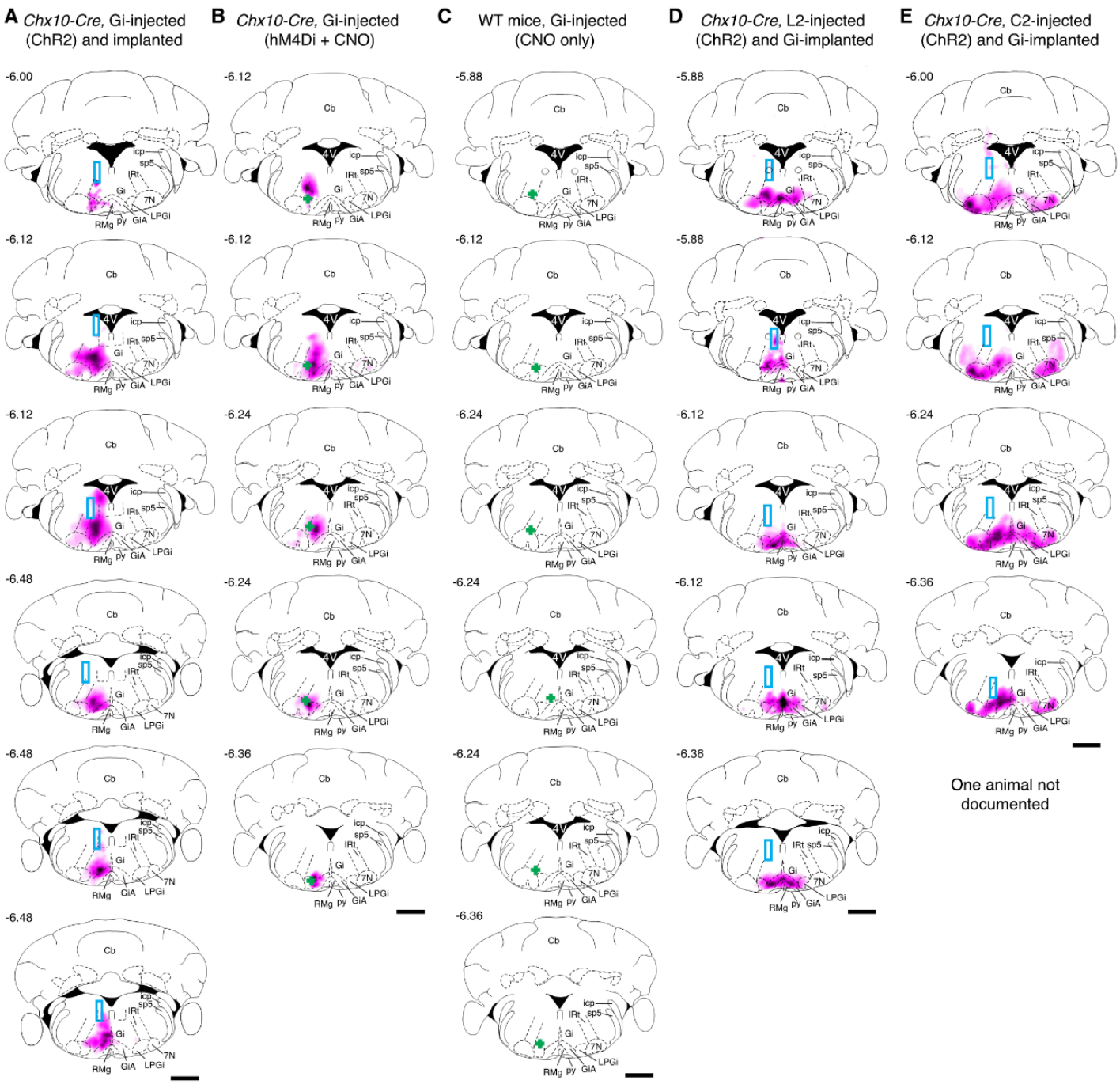

Figure S1. Anatomical sites of viral expression and optic fiber implantations. Related to Figures 2, 3, 5, 6, 7, S6.

Virally-driven fluorescence (both from somata and processes) was color-coded in a pink gradient and mapped onto the stereotaxic mouse brain atlas by Franklin and Paxinos [S1]. Each section is from one animal and sections are ordered from rostral (top) to caudal (bottom). Numbers on the left of each section indicate the approximate rostrocaudal position from Bregma.

(A) Reconstructions following injections of an AAV-DIO-ChR2-eYFP in the Gi of *Chx10-Cre* mice. The blue rectangles depict the locations of the optic fibers.

(B) Reconstructions following CNO-mediated silencing of V2a neurons in the Gi using an AAV-DIO-hM4Di-mCherry followed by intracranial injection of 1 mM CNO in *Chx10-Cre* mice (green crosses, assessed by fluorescent beads injected conjointly).

(C) Reconstructions of injection sites for CNO (green crosses) on wild-types mice, without prior injection of the hM4Di virus.

(D, E) Reconstructions following injections of an AAVretro-FLEX-ChR2-eYFP in the L2 (D) or C2 (E) spinal segments of *Chx10-Cre* mice. The blue rectangles depict the locations of the optic fibers. Altough one animal injected in C2 could not be documented, it was injected using the same procedures, viral volume and coordinates for lens implantation, and it responds similarly to the others to photo-activations; it was therefore not excluded.

Scale bars: 1mm. Cb: cerebellum; RMg: raphe magnus nucleus; Amb: ambiguus nucleus. See Figure 1 for other abbreviations used.

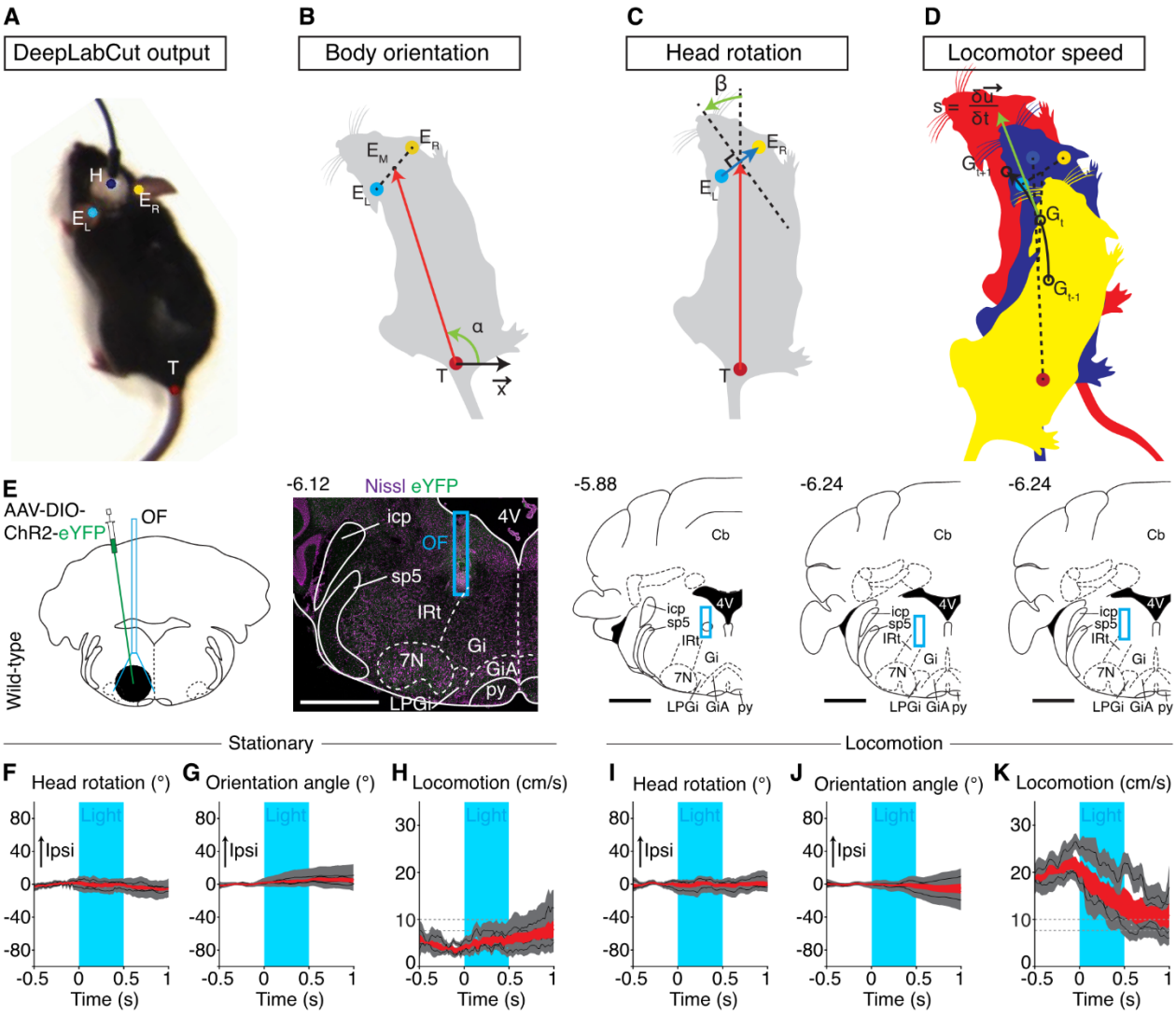

Figure S2. Detection of the animal's body parts and controls for optogenetic activations. Related to Figures 2, 3, 5, 6, S6 and S7.

(A) Snapshot from a mouse filmed from above in the open-field. Using DeepLabCut [S2, S3], we extracted 4 point of interests (POIs) for each frame: the head (H) at the base of the optic fiber implant, the right and left ears (E_R & E_L) and the base of the tail (T).

(B) The angle α between the x-axis of the open field and the vector from the tail to the middle of E_LE_R (TE_M, in red) is computed for each frame, giving the orientation of the body at every instant. This angle is normalized to the average angle during the 500 ms preceding the photo-activations for comparison purposes between trials. See also STAR Methods for details.

(C) The head rotation is defined as the angle β between the body axis vector TE_M (red) and the vector E_LE_R (blue). An offset of 90° is introduced to obtain a left (ipsilateral) head turn as a positive angle and a right (contralateral) head turn as a negative angle. The head rotation angle is normalized to the average angle during the 500 ms preceding the photo-activations for comparison purposes between trials.

(D) The instantaneous speed (s, green arrow) of the animal is computed as the gradient over time of the displacement (u) of the POIs' barycenter (G) at each frame (t). Mouse schematics in (B-D) are from Scidraw.io.

(E) Left: schematic transverse brainstem section depicting the site of viral injection and of the chronic optic fiber (OF) implant on a wild-type mouse. The injection pipette is depicted with an angle for clarity, but the injection was performed without angle. Middle: representative transverse brainstem section at the rostrocaudal level of the injection on a Nissl background, showing the location of the optic fiber and the absence of eYFP-expressing neurons. Right: reconstructions on the mouse brain atlas by Franklin and Paxinos [S1] of optic fiber positions (blue rectangles) of the 3 other wild-type mice; each section is from one animal. Numbers on the left of each section indicate the approximate rostrocaudal position from Bregma. Scale bars: 1 mm.

(F-H) Changes in motor parameters during photo-activations (15 ms pulses at 40 Hz, for a duration of 500 ms, blue area) when animals are stationary. Data are presented as the means ± SEM for each animal (grey, n = 4 mice, 11 trials each) and as the means ± SEM across animals (in red).

(I-K) Similar representations for photo-activations delivered during ongoing locomotion (n = 4 mice, 12 trials each).

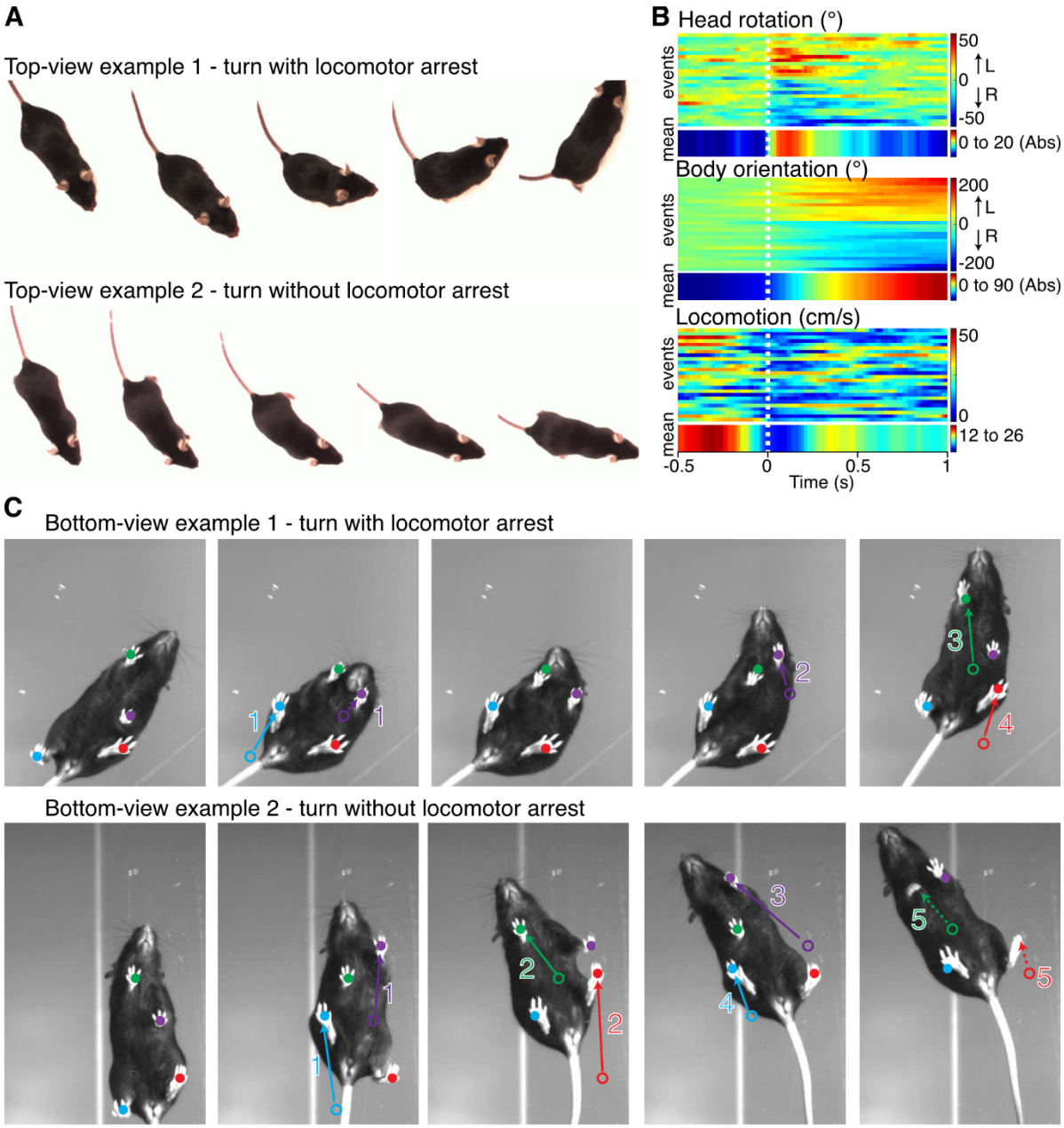

Figure S3. Naturally-occurring directional changes are preceded by a head yaw rotation and can be associated with a decrease in locomotor velocity. Related to Figures 3, 5 and 6.

(A) Two example snapshots of the same wild-type mouse in the open-field. The first one illustrates a change in trajectory associated with a complete locomotor arrest. A rotation of the head precedes the resumption of locomotion in the new direction. In the second example, the mouse does not arrest walking, but note again the rotation of the head towards the new direction.

(B) Color plot of the head rotation, the body orientation and the locomotor velocity for 1.5 s during spontaneously-occurring turns in wild-type mice. For each parameter, 26 turning events from 6 mice are shown on the y axis (events), and the mean across all events is shown below. Events are presented in the same order in the 3 plots. Events are synchronized (time = 0 s, white dashed line) on the peak head rotation velocity (obtained as the first derivative of the head rotation, not shown). The body orientation at each frame is normalized to its mean value during the 500 ms that precede the peak head rotation. For the head rotation and body orientation, the color gradient indicates degrees to the left (positive values, gradient to red) and to the right (negative values, gradient to blue). For the mean color plots, all events were expressed positively regardless of their direction to the left or right side (Abs); blue therefore indicates no change and red a maximal change. For the locomotor velocity, the color gradient to red indicates high values in cm/s.

(C) Two example snapshots of naturally-occurring turnings in a wild-type mouse filmed from below. Colored numbers indicate the order of limb movements. Filled and open circles indicate respectively the current and previous position of the paw. The first example illustrates a change in locomotor trajectory associated with a complete locomotor arrest. Note the symmetric positioning of the 4 limbs and the rotation of the head that precedes the resumption of locomotion in a novel direction which is primed by the forelimbs. In the second example, the mouse does not arrest walking. Note again the rotation of the head towards the new direction.

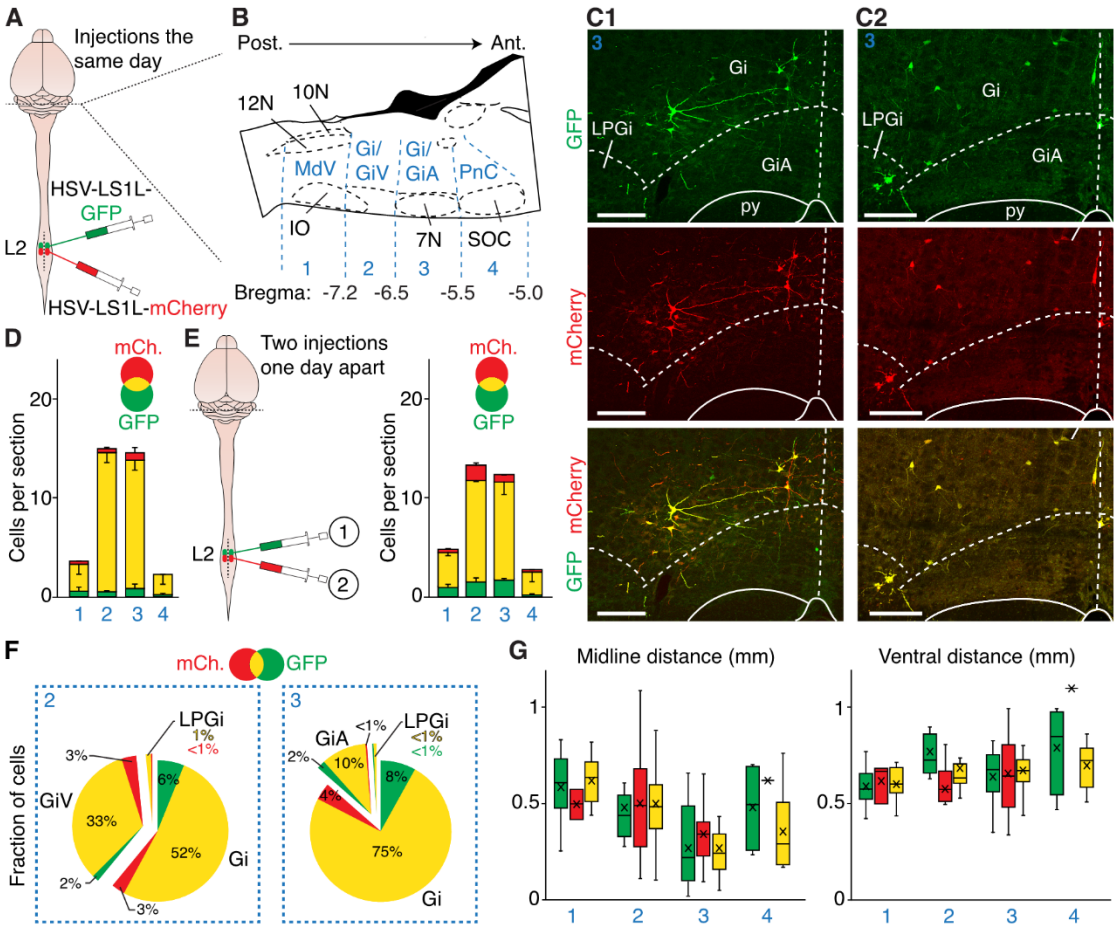

Figure S4. Dual HSV expression in individual V2a neurons. Related to Figure 4.

(A) Injection strategy for labelling L2-projecting V2a RS neurons with two HSVs, each coding a distinct fluorophore and injected sequentially during the same surgery (~15 minutes apart).

(B) Sagittal schematic of the brainstem indicating the rostrocaudal levels (1 to 4, with their approximate distance from Bregma) used to allocate labelled neurons in the subsequent panels.

(C) Transverse brainstem sections at the rostrocaudal level 3, where functional manipulations are performed in this study, showing that the majority of virally-transfected V2a Gi neurons express both HSV-driven fluorophores. C1 and C2 are examples from two distinct animals. Scale bars: 200 µm.

(D) Bar-graph showing, at each rostrocaudal level, the mean number ± SEM of single and double-labelled neurons per histological section (n = 2 mice; total cells counted: 354; average cells per animal: 177 ± 59).

(E) Left: injection strategy for labelling L2-projecting V2a RS neurons with the same two HSVs as in (A), this time injected one day apart. Right: bar-graph showing, at each rostrocaudal level, the mean number ± SEM of single and double-labelled neurons per histological section (n = 2 mice; total cells counted: 442; average cells per animal: 221 ± 43).

(F) Pie-graphs showing the distribution of labelled neurons within the indicated Gi subnuclei at rostrocaudal levels 2 and 3 (in percent of the total number of cells counted at each rostrocaudal level, pooled from the 4 animals shown above). All cells at the rostrocaudal level 1 were in the MdV and all cells at level 4 in the PnC.

(G) Mediolateral (on the left, in mm from the midline) and dorsoventral (on the right, in mm from the ventral border) positions of single and double-labelled cells from the 4 animals illustrated above. Data are presented as the means (crosses) and box-and-whisker plots which give the median, 25th and 75th percentiles, and range.

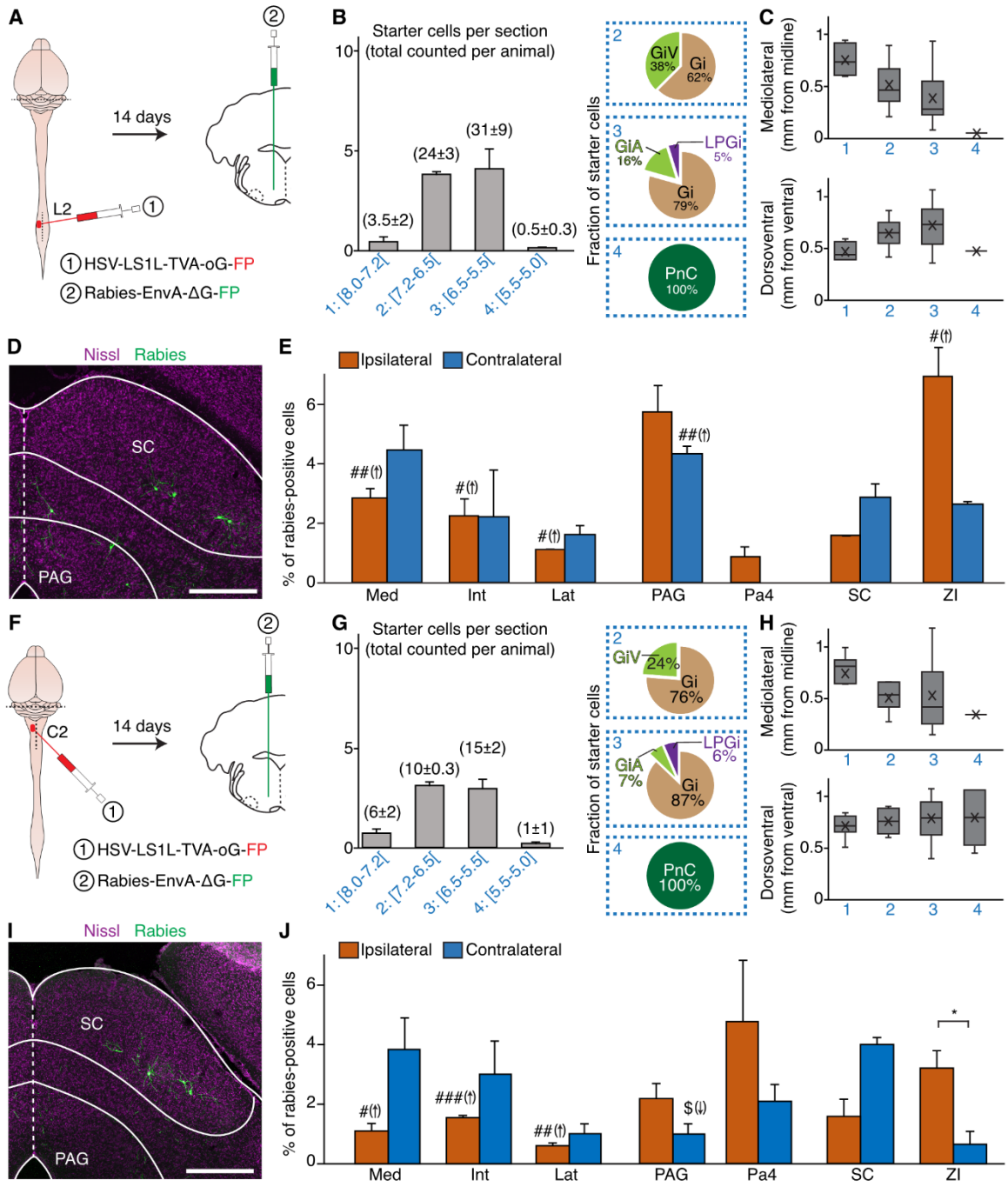

Figure S5. Putative inputs to L2-projecting and C2-projecting subsets of V2a Gi neurons. Related to Figure 4.

(A) Schematic representations of the retrograde transneuronal labelling strategy initiated from L2-projecting V2a neurons. The rabies proteins TVA and oG are retrogradelly-delivered to V2a neurons using a cre-dependent HSV helper, injected in the L2 segment on *Chx10-Cre* adult mice. An EnvA-ΔG-rabies-FP is subsequently injected in the Gi, thereby restricting its entry to V2a Gi neurons that project to the L2 segment.

(B) Left: average number ± SEM of starter cells per histological section at the 4 representative rostrocaudal levels indicated in blue (with the corresponding range of negative coordinates from Bregma, see Figures 1C, 4G & S4B for a schematic representation). Pie-graphs to the right show the distribution of starter cells within the indicated Gi subnuclei at rostrocaudal levels 2, 3 and 4 (in percent of the total number of starter cells counted at each rostrocaudal level). All cells at the rostrocaudal level 1 were in the MdV. See STAR Methods for the delineation of brainstem nuclei. Total starter cells counted: 119 from 2 animals; average per animal: 60 ± 15.

(C) Mediolateral (top, in mm from the midline) and dorsoventral (bottom, in mm from the ventral border) positions of all starter neurons (pooled from the 2 animals) presented as the means (crosses) and box-and-whisker plots which give the median, 25th and 75th percentiles, and range.

(D) Representative transverse section showing rabies$^+$, i.e. putative presynaptic, neurons in the superior colliculus (SC). Scale bar: 500 µm.

(E) Average percentage ± SEM of rabies$^+$ cells in each indicated region over the total amount of rabies$^+$ cells detected in each brain (n = 2 mice, total cells counted: 3476; average per animal: 1738 ± 491). Putative presynaptic neurons in the reticular formation are not shown and accounted for 25 ± 6 % (ipsilaterally) and 28 ± 5 % (contralaterally) of all rabies$^+$ neurons counted. Differences between the ipsilateral and the contralateral sides are not significant (paired t-tests, not represented). $^{###}p < 0.001$, $^{##}p < 0.01$, $^{#}p < 0.05$, unpaired t-test between helper virus injected in the Gi (see Figure 1) and helper virus injected at L2. Non-significant p values are not indicated.

(F-J) Similar representations and quantifications for C2-projecting V2a Gi neurons. Total starter cells counted: 67 from 2 mice; average per mice: 34 ± 6; total rabies$^+$ cells counted: 756; average per animal: 378 ± 170. Putative presynaptic neurons in the reticular formation are not shown and accounted for 35 ± 3 % (ipsilaterally) and 25 ± 3 % (contralaterally) of all rabies$^+$ neurons counted. * $p < 0.05$, paired t-test between ipsilateral and contralateral sides. $^{###}p < 0.001$, $^{##}p < 0.01$, $^{#}p < 0.05$, unpaired t-test between helper virus injected in the Gi (see Figure 1) and helper virus injected at C2. $^{\$}p < 0.05$, unpaired t-test between helper virus injected in L2 and C2. Non-significant p values are not indicated.

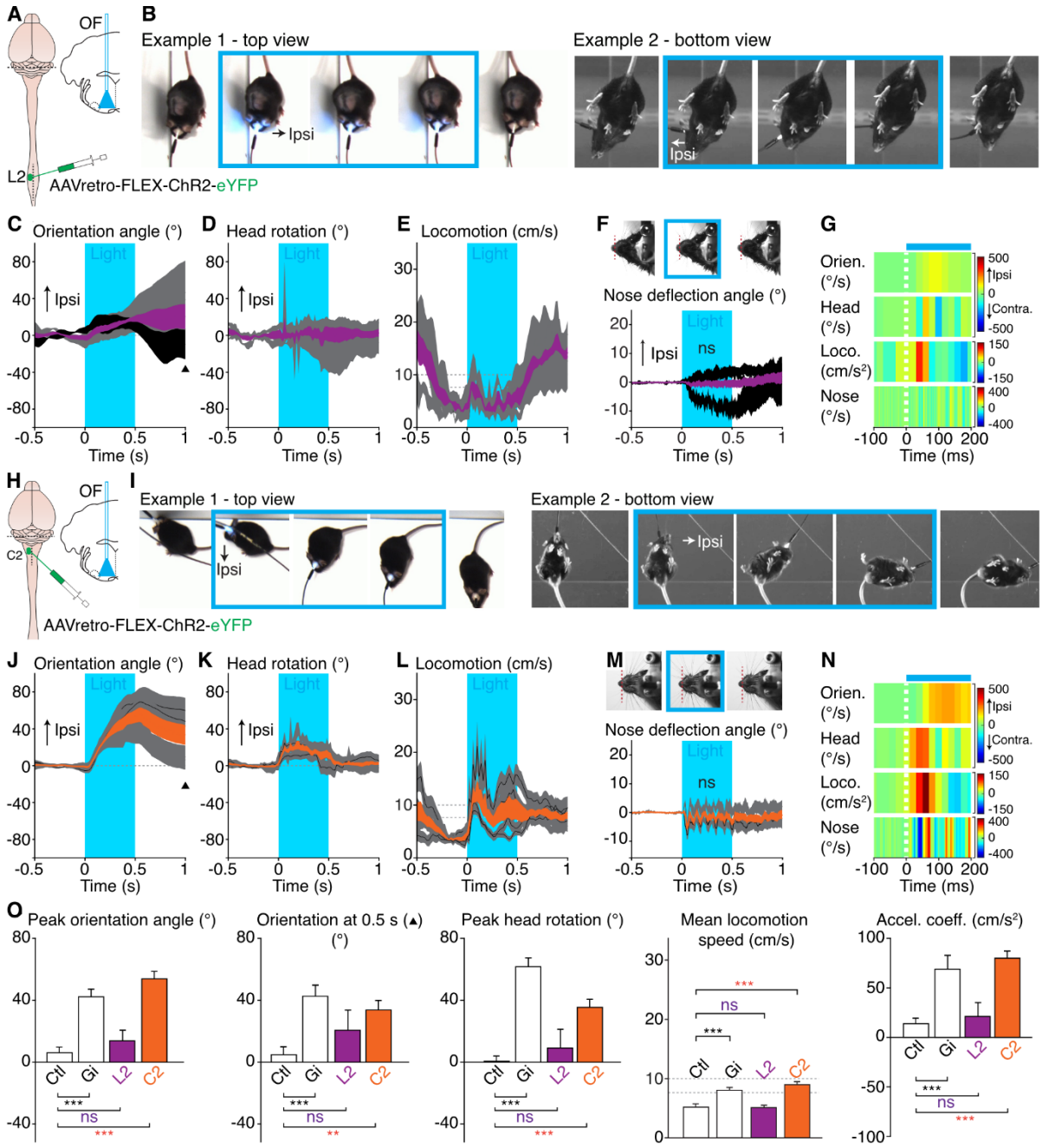

Figure S6. Motor responses when photo-activating L2 or C2-projecting V2a neurons on stationary mice. Related to Figures 5 and 6.

(A) Schematic strategy for photo-activating L2-projecting V2a Gi neurons. See also Figure S1D for all implantation sites.

(B) Example snapshots from two distinct animals (taken 250 ms before light onset, at light onset, 250 ms after onset, just before light offset, and 250 ms after light offset), showing the absence of orienting motor responses during a 500 ms light train (15 ms pulses at 40 Hz) delivered unilaterally.

(C-E) Left: light-evoked changes in the indicated motor parameters. Black lines and grey shaded areas depict the means ± SEM of each animal (n = 4 mice, 3 trials each) and thick purple lines with purple shaded area represent the means ± SEM across animals. The black arrowhead in (C) indicates the time point at 0.5 s after light offset. The dashed zone in (E) indicates the threshold from stationary (< 7.5 cm/s) to locomoting (> 10 cm/s) conditions.

(F) Top: example view of one head-fixed mouse used for measuring the angular displacement of the snout during photo-activations on the left side. Bottom: mean normalized angular deflection ± SEM of the snout, for each animal (grey) and across animals (purple). ns, not significant (paired t-test between the mean angles for 0.5 s before and 0.5 s during photo-activations, n = 24 trials from 4 mice, 6 trials each).

(G) Color plot showing the first derivative of the above motor parameters from 100 ms before to 200 ms after light onset (the dashed white line indicates light onset).

(H-N) Similar illustrations for C2-projecting V2a neurons (orientation/head/locomotion: n = 5 mice, 19 trials each). See also Figure S1E for implantation sites. Note a change in body orientation, in head rotation and the engagement in a few steps of quadrupedal locomotion, but no significant displacement of the snout, in response to photo-activations. In (M): ns, not significant (paired t-test between the mean angles for 0.5 s before and 0.5 s during the photo-activations, n = 21 trials from 3 mice).

(O) Mean ± SEM of the peak change in orientation during photo-activations, the orientation angle 0.5 s after light offset (▲in C and J), the peak head rotation during photo-activations, the mean locomotor velocity and the first acceleration coefficient during photo-activations across all trials for L2-projecting (purple) and C2-projecting (orange) V2a Gi neurons compared with the same measurements in mock trials from control mice (Ctl, n = 44 trials from 4 mice, 11 trials each) and following activation of V2a Gi neurons collectively (Gi, n = 35 trials from 5 mice, 7 trials each). ** $p < 0.01$; *** $p < 0.001$; ns, not significant (unpaired t-test).

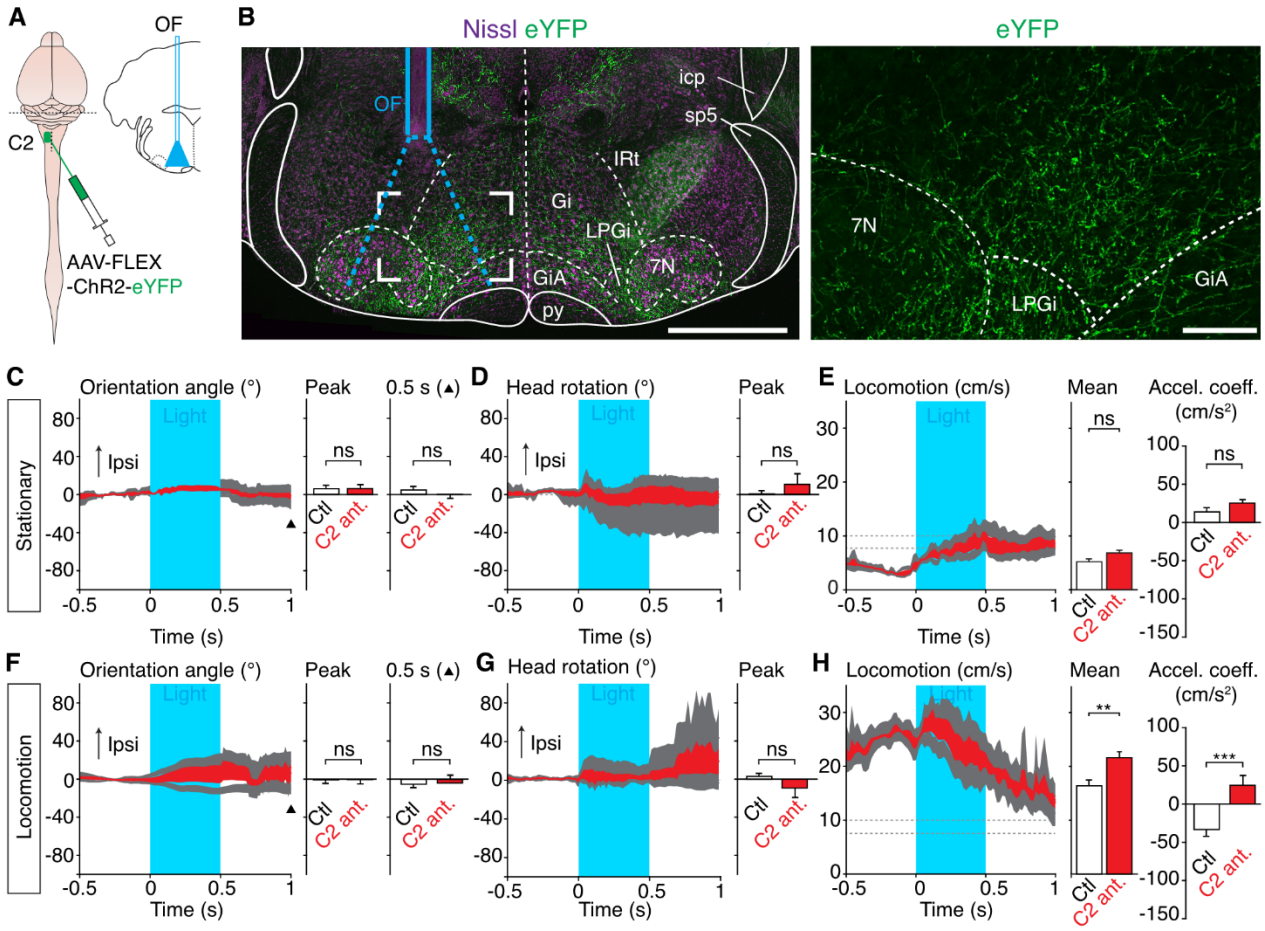

Figure S7. Activating anterograde projections in the Gi of C2-located V2a neurons does not elicit orienting motor responses. Related to Figures 6 and S6.

(A) Experimental strategy for photo-activating, in the Gi, anterograde fibers of V2a neurons residing in the 2nd cervical segment using an AAV-FLEX-ChR2-eYFP. Chx10-expressing neurons located in L2 do not send ascending projections to the reticular formation (not shown).

(B) Example transverse section at the level of the optic fiber implant in the Gi (representative of 3 animals) showing virally-transfected V2a processes (eYFP), the position of the optic fiber (OF) and the theoretical light cone at the fiber tip (dashed blue lines) that restricts activations to the implanted side [S4]. Scale bar: 1 mm. To the right is an enlarged view of the boxed area, showing eYFP processes, but no neuronal somata, in the Gi and adjacent nuclei. Scale bar: 200 µm

(C-E) Left: changes in motor parameters during photo-activations (15 ms pulses at 40 Hz, for a duration of 500 ms, blue area) delivered unilaterally when animals are stationary. Data are presented as the means ± SEM for each animal (grey, n = 3 animals, 56 trials each) and across animals (red). The black arrowhead in (C) indicates the time point at 0.5 s after light offset. The dashed zone in (E) indicates the threshold from stationary (< 7.5 cm/s) to locomoting (> 10 cm/s) conditions. Bar-graphs to the right show the mean ± SEM of the peak change in orientation during photo-activations and the orientation angle 0.5 s after light offset (C), the peak head rotation during photo-activations (D), and the mean locomotor speed and the first acceleration coefficient during photo-activations (E) across all trials (C2 ant., n = 168 trials from 3 mice, 56 trials each) compared with mock trials from control mice (Ctl, n = 44 trials from 4 mice, 11 trials each). ns, not significant (unpaired t-test).

(F-H) Similar illustrations and quantifications during ongoing locomotion (C2 ant.: n = 54 trials from 3 mice, 18 trials each; Ctl: n = 48 trials from 4 mice, 12 trials each). ** $p < 0.01$; *** $p < 0.001$ (unpaired t-test), ns, not significant. See also Figure S2 for the calculation of movements and the responses of control mice.

SUPPLEMENTAL REFERENCES

S1. Franklin, K.B., and Paxinos, G. (2007). The Mouse Brain in Stereotaxic Coordinates 3rd edn. Elsevier.

S2. Mathis, A., Mamidanna, P., Cury, K.M., Abe, T., Murthy, V.N., Mathis, M.W., and Bethge, M. (2018). DeepLabCut: markerless pose estimation of user-defined body parts with deep learning. Nat Neurosci *21*, 1281-1289.

S3. Nath, T., Mathis, A., Chen, A.C., Patel, A., Bethge, M., and Mathis, M.W. (2019). Using DeepLabCut for 3D markerless pose estimation across species and behaviors. Nat Protoc *14*, 2152-2176.

S4. Stujenske, J.M., Spellman, T., and Gordon, J.A. (2015). Modeling the Spatiotemporal Dynamics of Light and Heat Propagation for In Vivo Optogenetics. Cell Rep *12*, 525-534.

ANNEX 2: Paper 4

Cell Reports

Afadin Signaling at the Spinal Neuroepithelium Regulates Central Canal Formation and Gait Selection

Graphical Abstract

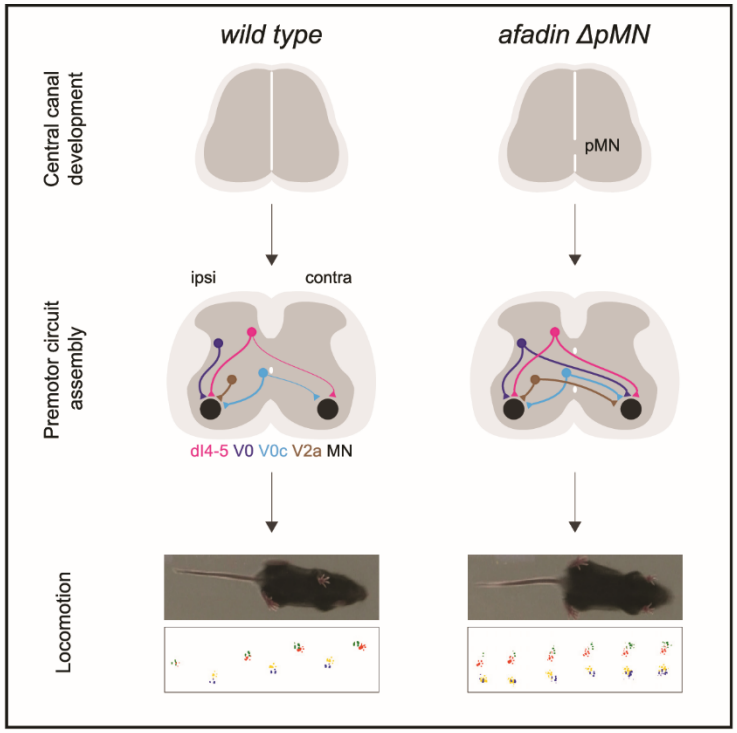

Highlights

- Afadin elimination from motor neuron progenitors causes hopping phenotype
- Afadin function at the neuroepithelium controls organization of spinal midline
- Miswiring of dI4-5, V0, and V2a premotor interneurons in afadin mutant mice

Authors

Sophie Skarlatou, Coralie Hérent, Elisa Toscano, César S. Mendes, Julien Bouvier, Niccolò Zampieri

Correspondence

niccolo.zampieri@mdc-berlin.de

In Brief

Skarlatou et al. report that afadin function in the developing spinal neuroepithelium controls organization of the midline. Afadin elimination from the motor neuron progenitor zone results in duplication of the central canal, aberrant wiring of dI4-5, V0, and V2a premotor neurons, and loss of left-right limb alternation.

Skarlatou et al., 2020, Cell Reports *31*, 107741
June 9, 2020
https://doi.org/10.1016/j.celrep.2020.107741

Cell Reports

CellPress
OPEN ACCESS

Article

Afadin Signaling at the Spinal Neuroepithelium Regulates Central Canal Formation and Gait Selection

Sophie Skarlatou,[1,2] Coralie Hérent,[3] Elisa Toscano,[2] César S. Mendes,[4] Julien Bouvier,[3] and Niccolò Zampieri[1,2,5,*]
[1]Cluster of Excellence NeuroCure, Charité-Universitätsmedizin Berlin, Charitéplatz 1, 10117 Berlin, Germany
[2]Max Delbrück Center for Molecular Medicine, Robert-Rössle-Str. 10, 13125 Berlin, Germany
[3]Paris-Saclay Institute of Neuroscience, UMR 9197 CNRS & Université Paris-Saclay, Avenue de La Terrasse, 91190 Gif sur Yvette, France
[4]CEDOC, Faculdade de Ciências Médicas, Universidade Nova de Lisboa, 1169-056 Lisboa, Portugal
[5]Lead Contact
*Correspondence: niccolo.zampieri@mdc-berlin.de
https://doi.org/10.1016/j.celrep.2020.107741

SUMMARY

Afadin, a scaffold protein controlling the activity of the nectin family of cell adhesion molecules, regulates important morphogenetic processes during development. In the central nervous system, afadin has critical roles in neuronal migration, axonal elongation, and synapse formation. Here we examine the role of afadin in development of spinal motor circuits. Afadin elimination in motor neuron progenitors results in striking locomotor behavior: left-right limb alternation is substituted by synchronous activation, characteristic of bound gait. We find that afadin function at the neuroepithelium is required for structural organization of the spinal midline and central canal morphogenesis. Perturbation of afadin results in formation of two central canals, aberrant contralateral wiring of different classes of spinal premotor interneurons, and loss of left-right limb alternation, highlighting important developmental principles controlling the assembly of spinal motor circuits.

INTRODUCTION

The ability to generate coordinated and adaptable movements is essential for survival. In vertebrates, spinal motor circuits orchestrate execution of complex motor programs by integrating descending commands and sensory information to activate biomechanically coherent ensembles of motor neurons in precise sequences (Kiehn, 2006; Goulding, 2009; Arber, 2012). Several classes of interneurons in the spinal cord are involved in wiring of circuits at the basis of motor function, such as coordination of antagonist muscle contraction and left-right alternation of limb movements (Grillner and Jessell, 2009; Gosgnach et al., 2017). Spinal networks controlling the rhythm and pattern of muscle contraction provide a substrate for different locomotor actions ranging from swimming to walking and running. In this context, the relative timing of limb activation is a key element for the control of gait selection in tetrapods (Grillner, 2006; Kiehn, 2016). However, despite the importance of spinal circuits regulating the coordination of limb movement, the principles controlling their assembly and function are not completely understood.

Mouse genetic analysis has revealed specific functions for different spinal interneuron classes in gait control. V0 neurons originating from Dbx1 progenitors have important roles in the coordination of left-right limb movements (Lanuza et al., 2004). Inhibitory $V0_D$ neurons have been linked to generation of alternating patterns at low frequencies of locomotion, whereas excitatory $V0_V$ neurons control alternation at higher locomotor frequencies (Talpalar et al., 2013). V2a neurons have been shown to influence gait selection depending on the speed of locomotion (Crone et al., 2008, 2009). In addition, roles in coordinating limb activity have been proposed for V3 neurons (Zhang et al., 2008). However, teasing out the precise composition and wiring of spinal motor circuits has been challenging because of the limited ability to selectively access and interrogate the function of discrete neuronal subtypes and circuits *in vivo*.

Several studies have highlighted the importance of axon guidance molecules such as netrins, slits, and ephrins in directing neuronal connectivity across the neuraxis as a developmental strategy to regulate wiring of spinal circuits (Chédotal, 2019). In particular, ephrin B3 expression at the midline of the hindbrain and spinal cord has been shown to provide a repulsive signal that controls unilateral wiring of EphA4-expressing axons (Kullander et al., 2001). As a consequence, genetic manipulation of ephrin B3-EphA4 signaling results in a dramatic switch from alternation to synchronous activation of limbs (Kullander et al., 2003; Beg et al., 2007; Iwasato et al., 2007). These studies elucidate some of the molecular underpinnings controlling the development of circuits for left-right alternation but also offer an entry point for identification of neurons contributing to these networks. Indeed, selective ablation of EphA4 in spinal excitatory interneurons has been shown to be sufficient to perturb left-right alternation (Borgius et al., 2014). Moreover, elimination of EphA4 expression in spinal interneurons derived from the Lbx1 progenitor domain results in their aberrant bilateral wiring and in a

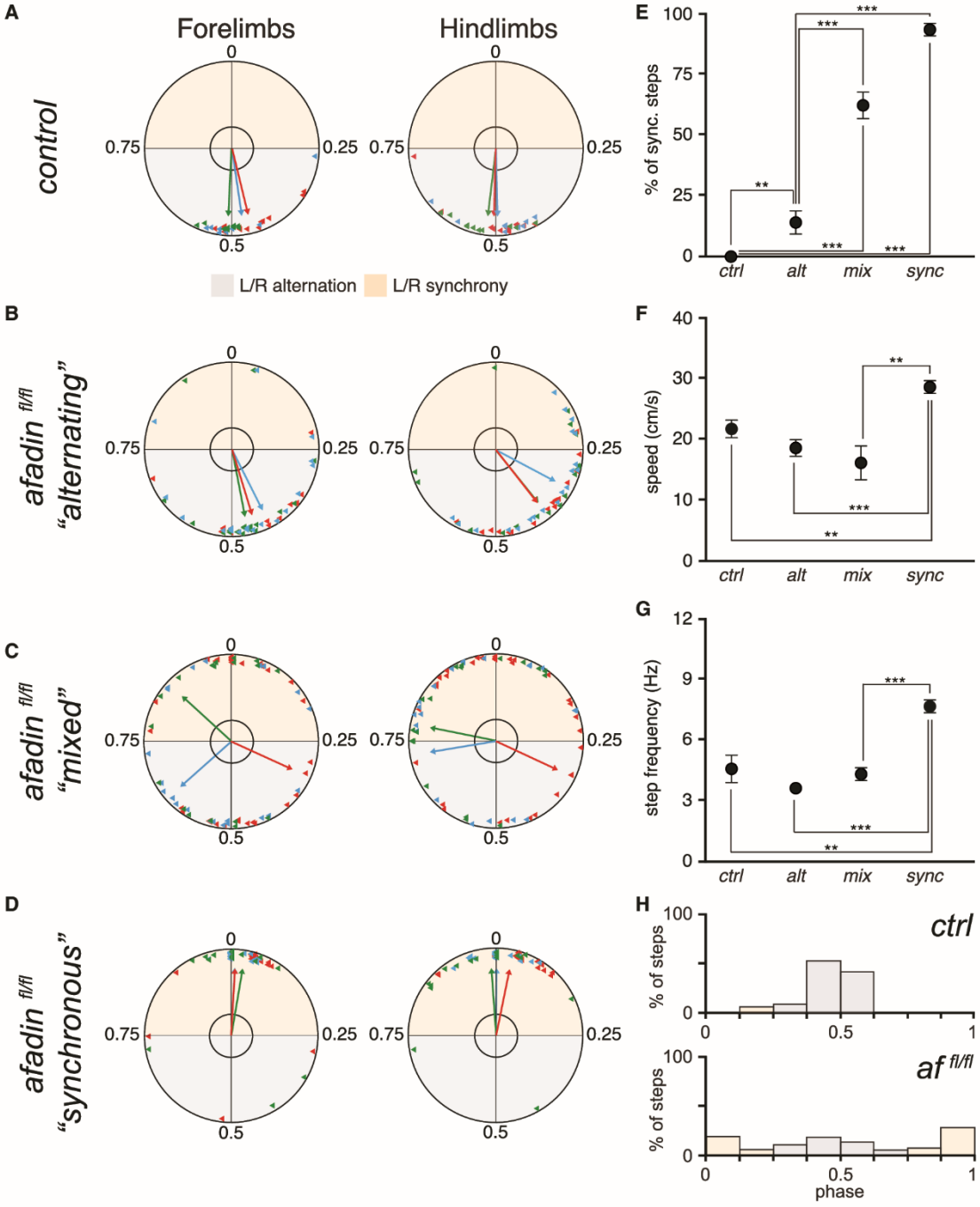

Figure 1. Loss of Left-RightLimb Alternation in Afadin Mutant Mice

(A) Circular plots showing the phase relationship of fore- and hindlimb movements and the average orientation vector of three individual control mice. The gray area indicates alternation and the orange area synchrony.

(B) Circular plots showing the phase relationship of fore- and hindlimb movements and the average orientation vector of three individual *afadin* $^{fl/fl}$ mice with the "alternating" phenotype.

(C) Circular plots showing the phase relationship of fore- and hindlimb movements and the average orientation vector of three individual *afadin* $^{fl/fl}$ mice with the "mixed" alternating and synchronous phenotype.

(legend continued on next page)

context-dependent switch to left-right synchrony (Satoh et al., 2016).

In this study, we set out to investigate the consequences of afadin elimination for the development of spinal motor circuits. Afadin, a scaffold molecule coordinating adhesive function of the nectin and classical cadherin families, has been shown to be involved in the control of neuronal migration and positioning, axonal guidance, and synapse formation (Okabe et al., 2004; Beaudoin et al., 2012; Gil-Sanz et al., 2014; Dewitz et al., 2018). We eliminated afadin from motor neuron progenitors and found that alternation of limb movement is substituted by synchronous activation. To understand the mechanism underlying this phenotype, we studied spinal cord development and assembly of motor circuits in afadin mutant mice. Our data indicate that afadin expression at the neuroepithelium is necessary for lumen formation during development and that its elimination from the motor neuron progenitor zone results in generation of two central canals. As a consequence, the structural integrity of the spinal cord midline is compromised, and the wiring of motor circuits is altered. We identified aberrant contralateral connectivity patterns of dI4-5, V0, V0c, and V2a spinal premotor interneurons, underlining their importance for the control of gait selection.

RESULTS

Loss of Left-Right Limb Alternation in Afadin Mutant Mice

In previous work, we eliminated afadin from mouse motor neurons by crossing a copy of a floxed allele and a copy of a null allele with the *olig2::cre* driver line to achieve selective deletion from motor neurons. However, *afadin* $^{fl/-}$; *olig2::cre*$^{+/-}$ (*afadin* $^{fl/-}$) mice die at perinatal stages because of severe hydrocephalus, precluding analysis of motor behavior (Dewitz et al., 2018). To extend the lifespan, we generated a fully conditional afadin model (*afadin* $^{fl/fl}$; *olig2::cre*$^{+/-}$ mice, hereafter referred to as *afadin* $^{fl/fl}$; Figures S1A and S1B). *Afadin* $^{fl/fl}$ mice are born at expected Mendelian frequency and display a defect in the pattern of activation of left-right limbs during on-ground locomotion.

We performed quantitative gait analysis to precisely characterize the locomotor phenotype of afadin mutant mice (Mendes et al., 2015). Control animals exclusively used alternation of left-right limbs during locomotion, a characteristic feature of a normal walking gait (Figures 1A and 1E; Video S1). In contrast, we observed that one-third of mutant mice mostly used alternating steps but showed a significant increase in the incidence of synchronous ones (Figures 1B and 1E; Video S2), another third presented bouts of alternating and synchronous steps (Figures 1C and 1E; Video S3), and the remaining animals showed constant synchronous activation of left and right limbs (Figures 1D and 1E; Video S4). In this last cohort, step frequency and locomotor speed were significantly increased to values characteristic of boundgait (Figures 1F and 1G; Bellardita and Kiehn, 2015; Lemieux et al., 2016). These data indicate that afadin elimination perturbs the circuits controlling coordination of left-right limb movement, resulting in loss of alternation in favor of synchronous activation (Figure 1H).

Afadin Mutant Mice Show Abnormal Left-Right Alternation in Isolated Spinal Cord Preparations

Next we asked whether the phenotype observed in afadin mutant mice depends exclusively on spinal motor circuits and analyzed fictive locomotor activity in isolated lumbar spinal cord preparations from newborn mice (Figure 2A; Kjaerulff and Kiehn, 1996). In control experiments, induction of locomotor-like activity following application of N-methyl-D-aspartate and serotonin produced clear alternating patterns in left (l) and right (r) lumbar (L) roots (Figures 2B and 2C). In agreement with the behavioral data, preparations from *afadin*$^{fl/fl}$ mice presented a defect in generation of the left-right alternating pattern, ranging from complete synchrony to less penetrant phenotypes characterized by bouts of alternation intermixed with bouts of synchrony (Figures 2D and 2E). In contrast, the pattern of rL2-rL5 roots, which is used as a correlate for flexor-extensor muscle activities, was not affected in mutant spinal cords (Figures 2B and 2D).These experiments suggest that loss of left-right alternation in afadin mutant mice is due to changes in spinal motor circuits and does not require sensory or supraspinal input.

Afadin Elimination Does Not Affect Motor Neuron Development

We next considered how afadin elimination influences gait selection. The precision of motor neuron spatial organization in the spinal cord is thought to be an important determinant for assembly of motor circuits (Sürmeli et al., 2011; Bikoff et al., 2016). We previously observed defects in motor neuron positioning in *afadin* $^{fl/-}$ embryos; thus, we investigated motor neuron generation, identity, and positional organization in fully conditional afadin mice (Dewitz et al., 2018).

We did not find any disruption in the generation and specification of motor neurons in *afadin* $^{fl/fl}$ embryos (Figures S1C). Three-dimensional positional analysis was used to assess motor neuron spatial organization, and we observed perturbation in the divisional segregation of the lateral motor column (LMC) in *afadin* $^{fl/fl}$ embryos (Figures S1D–S1I; Dewitz et al., 2018). Medio-lateral distribution and average settling position analyses showed selective impairment of lateral (LMCl) motor neurons migration, as found previously in *afadin* $^{fl/-}$ mice, but with a significantly lower phenotypic penetrance (Figures S1J and S1K).

(D) Circular plots showing the phase relationship of fore- and hindlimb movements and the average orientation vector of three individual *afadin* $^{fl/fl}$ mice with the "synchronous" phenotype.
(E) Average percentage of synchronous steps in control, *afadin* $^{fl/fl}$ (alt), *afadin* $^{fl/fl}$ (mix), and *afadin* $^{fl/fl}$ (sync) mice (mean ± SEM; t test, **p < 0.01, ***p < 0.001; n = 3 for each genotype).
(F) Average speed in control, *afadin* $^{fl/fl}$ (alt), *afadin* $^{fl/fl}$ (mix), and *afadin* $^{fl/fl}$ (sync) mice (mean ± SEM; t test, **p < 0.01, ***p < 0.001; n = 3 for each genotype).
(G) Average step frequency in control, *afadin* $^{fl/fl}$ (alt), *afadin* $^{fl/fl}$ (mix), and *afadin* $^{fl/fl}$ (sync) mice (mean ± SEM; t test, **p < 0.01, ***p < 0.001; n = 3 for each genotype).
(H) Phase distribution histogram for all the steps analyzed in control mice (top panel, n = 3) and *afadin* $^{fl/fl}$ mice (bottom panel, n = 9).

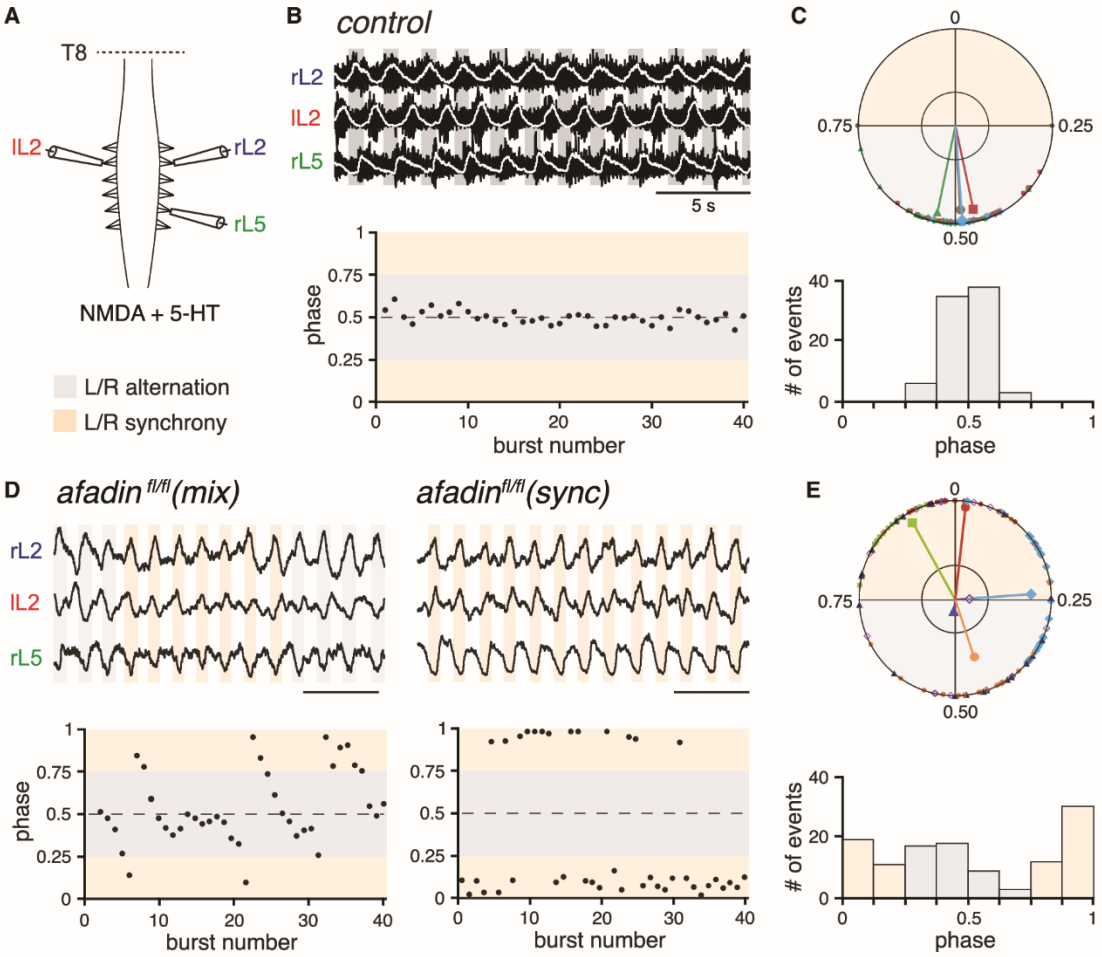

Figure 2. Afadin Mutant Mice Show Abnormal Left-Right Alternation in Isolated Spinal Cord Preparations

(A) *Exvivo* lumbar spinal cord preparation from neonatal mice (0–3 days) spanning lower thoracic to sacral segments. Simultaneous recordings were performed from the left and right second lumbar ventral roots (rL2 and lL2, flexor-related) and the right fifth lumbar ventral root (rL5, extensor-related) using extracellular glass pipettes.

(B) Top panel: recordings of the rL2, lL2, and rL5 roots from a control animal during locomotor-like activity. Raw (black) and integrated (white) activities are superimposed. Grey bars show alternation between rL2/lL2 and rL2/rL5 roots. Bottom panel: locomotor phase between rL2 and lL2 over 40 consecutive bursts from the same animal as above. The gray area indicates alternation and the orange area synchrony.

(C) Top panel: circular plot showing the rL2/lL2 phase-relationship for 80 locomotor cycles and average orientation vectors of four individual control animals. Bottom panel: phase distribution histogram between rL2 and lL2 for all events shown in the circular plot.

(D) Top panel: integrated activities of the rL2, lL2, and rL5 L roots from two *afadin* $^{fl/fl}$ cords during locomotor-like activity. Bottom panel: locomotor phase between rL2 and lL2 over 40 consecutive bursts from the same animals as above. Example 1 (left) shows episodes of alternation and synchrony, whereas example 2 (right) shows only synchronized bursts.

(E) Top panel: circular plot showing the rL2/lL2 phase relationship for 120 locomotor cycles and average orientation vectors of six individual *afadin* $^{fl/fl}$ animals. Bottom panel: phase distribution histogram between rL2 and lL2 for all events shown in the circular plot.

Next we studied motor neuron organization in adult mice. Because transcription factors defining motor neuron subtype identities are no longer expressed at postnatal stages, we assessed the position of medial and lateral LMC neurons using retrograde labeling of cell bodies by muscle injection of the cholera toxin B subunit (CTB). We chose the gastrocnemius (GS) and tibialis anterior (TA) muscles to label a medial and a lateral motor pool. We found CTB-labeled TA and GS motor neurons at the expected rostral lumbar levels of the spinal cord (Figures S1L and S1M; McHanwell and Biscoe 1981; Sürmeli et al., 2011). Transverse and coronal contour analyses showed that the two pools were clustered and clearly segregated from each other (Figures S1N–S1Q). Accordingly, no significant difference was observed in average settling positions and correlation analysis indicated conservation of motor neuron spatial organization in control and *afadin* $^{fl/fl}$ mutant mice (Figures S1R–S1T).

Altogether, these data indicate that elimination of afadin from motor neurons causes a developmental delay in their positioning

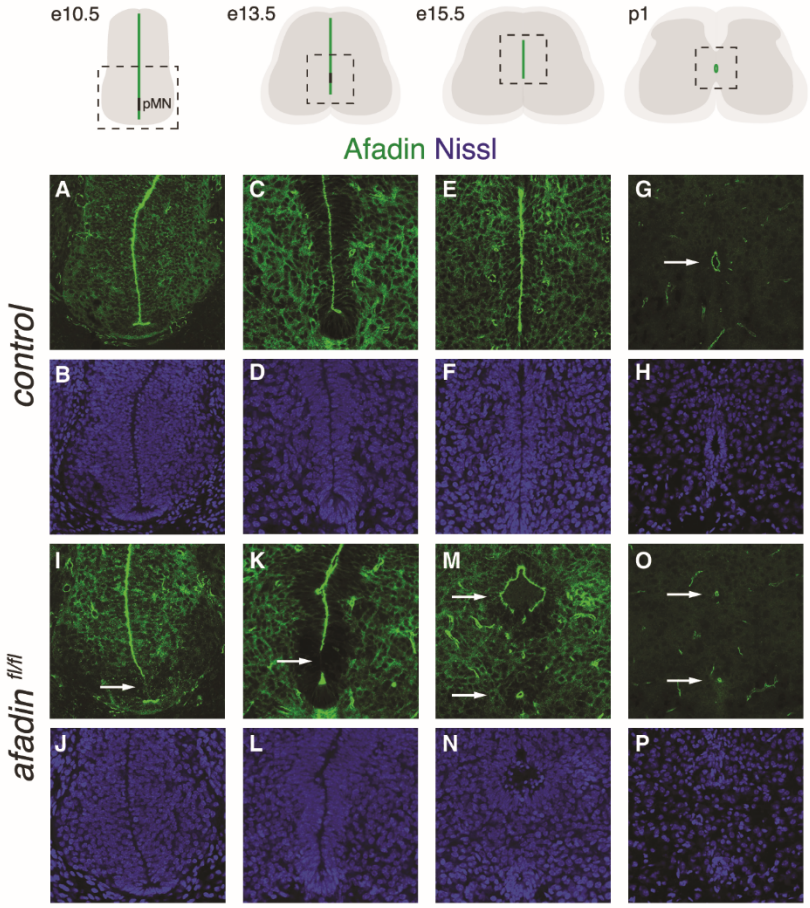

Figure 3. Afadin Mutant Mice Present a Double Central Canal Phenotype

(A–H) Afadin expression in E10.5 (A and B), E13.5 (C and D), E15.5 (E and F), and P1 (G and H) control spinal cords. The arrow in (G) points to the central canal.

(I–P) Afadin expression in E10.5 (I and J), E13.5 (K and L), E15.5 (M and N), and P1 (O and P) *afadin* $^{fl/fl}$ spinal cords. Arrows in (I) and (K) point to the pMN. Arrows in (M) and (O) point to the central canals.

that is resolved during late embryonic development and no longer apparent at postnatal stages.

Afadin Mutant Mice Present a Double Central Canal Phenotype

The absence of a motor neuron positioning defect in adult *afadin* $^{fl/fl}$ mice suggests that the locomotor phenotype does not depend on changes in motor pool organization, raising the question of how afadin elimination affects gait selection. Afadin is ubiquitously expressed in the spinal cord during embryonic development, with higher levels found at the neuroepithelium (Figures 3A–3F and S2A–S2D). Conditional elimination of afadin using the *olig2::cre* allele results in its loss in motor neuron progenitors, suggesting that lack of afadin function at the neuroepithelium might be responsible for the locomotor phenotype (Figures 3I–3L, S2G, and S2H). To test this hypothesis, we analyzed afadin expression during spinal cord development. We observed that, until embryonic day 13.5 (E13.5), the neuroepithelium extends along the whole dorsoventral axis of the spinal cord (Figures 3A–3D, S2A, and S2B). At E14.5 it starts constricting, and the tubular structure of the central canal is clearly visible by postnatal day 1 (P1) (Figures 3E–3H, S2C–S2F, and S2M–S2O). Afadin is localized at the neuroepithelium lining the midline during embryonic development and remains expressed around the central canal until adult stages. In mutant embryos, afadin expression is eliminated from the motor neuron progenitor zone (pMN) as early as E10.5 while remaining unaffected in the rest of the neuroepithelium (Figures 3I–3L, S2G, and S2H). At E14.5, we observed a clear disruption in the morphology of the midline, resulting in formation of two independent tubular structures above and below the pMN (Figures 3M, 3N, S2I, S2J, and S2P). As a result, a double central canal is evident by P1 and maintained into adult stages (Figures 3O, 3P, S2K, S2L, S2Q, and S2R; data not shown). These data suggest that afadin function at the neuroepithelium is required for central canal formation.

Afadin Regulates Development of the Spinal Cord Midline

To examine whether afadin has a general role in the organization of midline structures during development, we generated a conditional mutant using the *Wnt1::cre* line, which recombines in dorsal spinal cord progenitors (*af* $^{fl/fl}$ *Wnt1*; Rowitch et al., 1999). *Af* $^{fl/fl}$ *Wnt1* mice die at late embryonic stages as a result of exencephaly. At E14.5, we observed a reduction in the dorso-ventral extent of afadin and phalloidin expression at the neuroepithelium of mutant mice (Figures 4E and S3A–S3D). The defect was significantly more pronounced at E16.5 (Figures 4A–4E). In addition, we found that the extent of the dorsal gray matter at the midline was significantly increased whereas the ventral one was reduced, resulting in a ventral shift in positioning of the developing central canal in *af* $^{fl/fl}$ *Wnt1* mice (Figures 4A, 4B, 4F–4K, S3E, and S3F). Thus, elimination of afadin from dorsal progenitors also affects anatomical organization of the midline.

Next, to directly test whether afadin function in motor neuron progenitors is required for the double central canal and locomotor phenotypes, we eliminated afadin using the *ChAT::cre* allele, which selectively recombines in postmitotic motor neurons, sparing the progenitor zone (*af* $^{fl/fl}$ *ChAT*; Rossi et al., 2011). *Af* $^{fl/fl}$ *ChAT* mice are born at expected Mendelian frequency, do not show any defect in central canal development, and present a normal alternating locomotor pattern (Figures 4L–4P). These data indicate that afadin plays an important role in

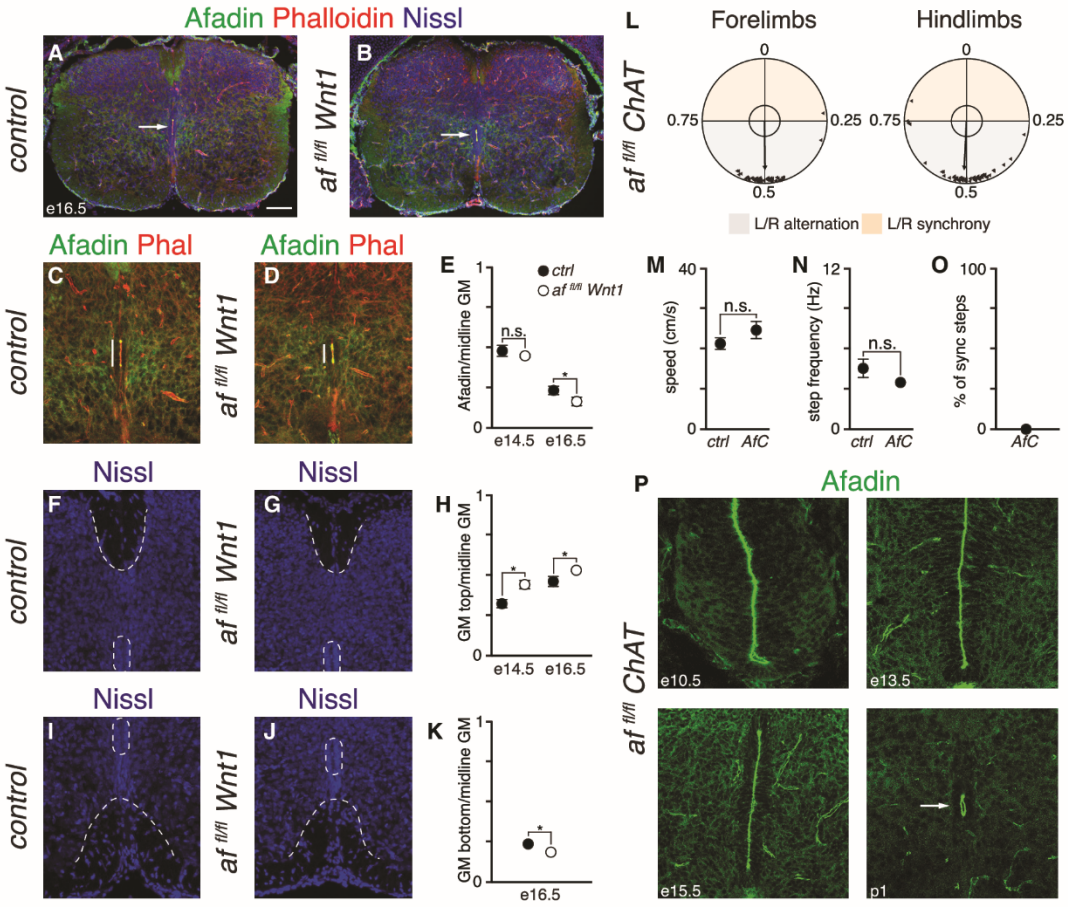

Figure 4. Afadin Function at the Neuroepithelium Regulates Development of the Spinal Cord Midline

(A and B) Transverse sections of an E16.5 control (A) and *afadin* $^{fl/fl}$ *Wnt1* (B) spinal cords. Arrows point to the central canal. Scale bar, 100 μm.

(C and D) Afadin and phalloidin expression in the central canal area of E16.5 control (C) and *afadin* $^{fl/fl}$ *Wnt1* (D) spinal cords. Bars represent the extent of afadin/phalloidin expression.

(E) Quantification of afadin expression at the midline in E14.5 and E16.5 control and *afadin* $^{fl/fl}$ *Wnt1* spinal cords (mean ± SEM; t test, *$p < 0.05$; n = 3).

(F and G) High magnification of the dorsal midline area in E16.5 control (F) and *afadin* $^{fl/fl}$ *Wnt1* (G) spinal cords. Dashed lines delineate the neuroepithelium and the border between the dorsal gray and white matter.

(H) Quantification of the extent of dorsal gray matter in E14.5 and E16.5 control and *afadin* $^{fl/fl}$ *Wnt1* spinal cords (mean ± SEM; t test, *$p < 0.05$; n = 3).

(I and J) High magnification of the ventral midline area in E16.5 control (I) and *afadin* $^{fl/fl}$ *Wnt1* (J) spinal cords. Dashed lines delineate the neuroepithelium and the border between the ventral gray and white matter.

(K) Quantification of the extent of ventral gray matter in e16.5 control and *afadin* $^{fl/fl}$ *Wnt1* spinal cords (mean ± SEM; t test, *$p < 0.05$; n = 3).

(L) Circular plots showing the phase relationship of fore- and hindlimb movements and the average orientation vector in *af* $^{fl/fl}$ *ChAT* mice (n = 3).

(M) Average speed in control and *af* $^{fl/fl}$ *ChAT* mice (mean ± SEM; t test, $p > 0.05$; n = 3).

(N) Average step frequency in control and *af* $^{fl/fl}$ *ChAT* mice (mean ± SEM; t test, $p > 0.05$; n = 3).

(O) Average percentage of synchronous steps in *af* $^{fl/fl}$ *ChAT* mice (mean ± SEM; n = 3).

(P) Afadin expression in E10.5, E13.5, E15.5, and p1 *af* $^{fl/fl}$ *ChAT* spinal cords. The arrow points to the central canal.

maintaining neuroepithelial organization along the spinal midline and that its elimination from the pMN results in double central canal formation and perturbation of circuits controlling left-right alternation.

Midline Expression of Netrin 1 and Ephrin B3 Is Perturbed in Afadin Mutants

The locomotor and anatomical phenotypes observed in *afadin* $^{fl/fl}$ mice raise the question of whether the signals controlling axonal guidance across the midline are perturbed. Netrin 1 and ephrin B3 are prominent examples of such molecules (Serafini et al., 1996; Kullander et al., 2001). Disruption of netrin 1 or ephrin B3 signaling results in loss of left-right limb alternation (Kullander et al., 2003; Rabe et al., 2009). Thus, we examined the expression of these molecules in *afadin* $^{fl/fl}$ mutant mice.

In control mice, netrin 1 is localized in the ventral part of the midline ranging from the central canal to the white matter

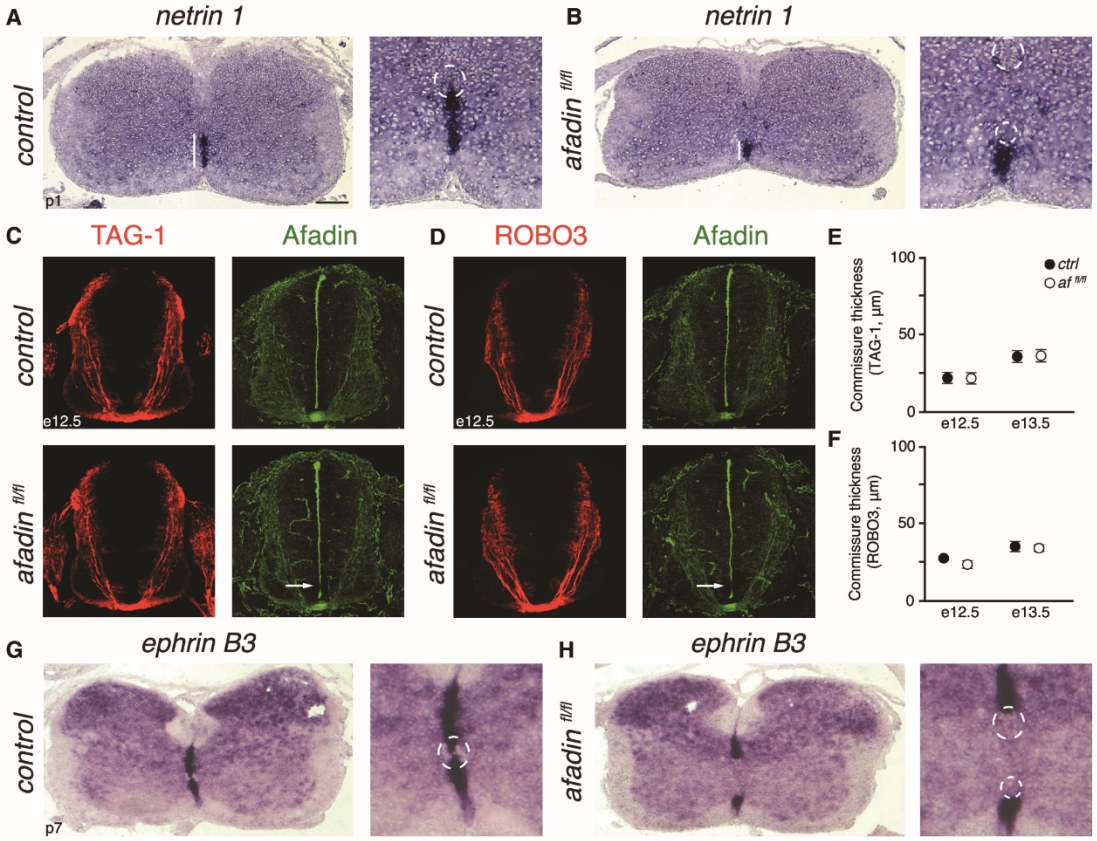

Figure 5. Midline Expression of Netrin 1 and Ephrin B3 Is Perturbed in Afadin Mutants

(A and B) Left panel: netrin 1 mRNA expression in P1 control (A) and *afadin* $^{fl/fl}$ (B) spinal cords. Right panel: magnification of the ventral midline area below the central canal. The central canal is delineated by a dashed line. The bar represents the extent of netrin 1 expression. Scale bar, 100 µm.

(C) Transverse sections of an E12.5 control and *afadin* $^{fl/fl}$ spinal cords showing TAG-1 (left) and afadin (right) expression. The arrow points to the pMN.

(D) Transverse sections of an E12.5 control and *afadin* $^{fl/fl}$ spinal cords showing ROBO3 (left) and afadin (right) expression. The arrow points to the pMN.

(E) Quantification of TAG-1^{+} ventral commissure thickness in E12.5 and E13.5 control and *afadin* $^{fl/fl}$ spinal cords (mean ± SEM; t test, $p > 0.05$; $n = 2$).

(F) Quantification of ROBO3^{+} ventral commissure thickness in E12.5 and E13.5 control and *afadin* $^{fl/fl}$ spinal cords (mean ± SEM; t test, $p > 0.05$; $n = 2$).

(G and H) Left panel: ephrin B3 mRNA expression in a P7 control (G) and *afadin* $^{fl/fl}$ (H) spinal cord. Right panel: magnification of the central canal area. The central canal is delineated by a dashed line.

(Figure 5A). The presence of a double central canal in afadin mutant mice resulted in a reduction in the extent of netrin 1 expression, raising the possibility that development of commissural axons could also be perturbed (Figure 5B). To address this question, we analyzed TAG-1 and ROBO3 expression and localization in the spinal cord of afadin mutant mice, and we did not observe any difference in the trajectory of commissural axons approaching the floor plate or in the thickness of the ventral commissure (Figures 5C–5F and S4A–S4D).

Next, we examined ephrin B3 expression. In control mice, ephrin B3 was localized along the whole dorsoventral extent of the spinal cord gray matter above and below the central canal (Figures 5G). In contrast, in *afadin* $^{fl/fl}$ mice, ephrin B3 expression was absent between the two central canals (Figures 5H). Moreover, this phenotype is tightly linked to the central canal defect because localization of ephrin B3 at the midline of *af* $^{fl/fl}$ *ChAT* mice was not affected (Figure S4E).

Aberrant Wiring of Premotor Circuits in Afadin Mutant Mice

Ephrin B3 serves as a molecular barrier that prevents EphA4-expressing neurons from sending axons to the contralateral side of the spinal cord (Kullander et al., 2001). The disruption in expression of ephrin B3 raises the possibility that the defect in left-right limb coordination could result from aberrant midline crossing of ipsilaterally projecting neurons expressing EphA4 (Paixão et al., 2013; Borgius et al., 2014). Indeed, we observed an increase in contralaterally projecting axons in *afadin* $^{fl/fl}$ mice as early as E15.5 (Figures S4F and S4G). Dorsal premotor interneurons originating from the Lbx1 progenitor domain have been shown to aberrantly connect to contralateral motor neurons upon disruption of ephrin B3-EphA4 signaling (Satoh et al., 2016). Thus, we analyzed premotor connectivity using rabies virus (RV) monosynaptic tracing (Wickersham et al., 2007). Expression of RV glycoprotein (G) in motor neurons was obtained using the

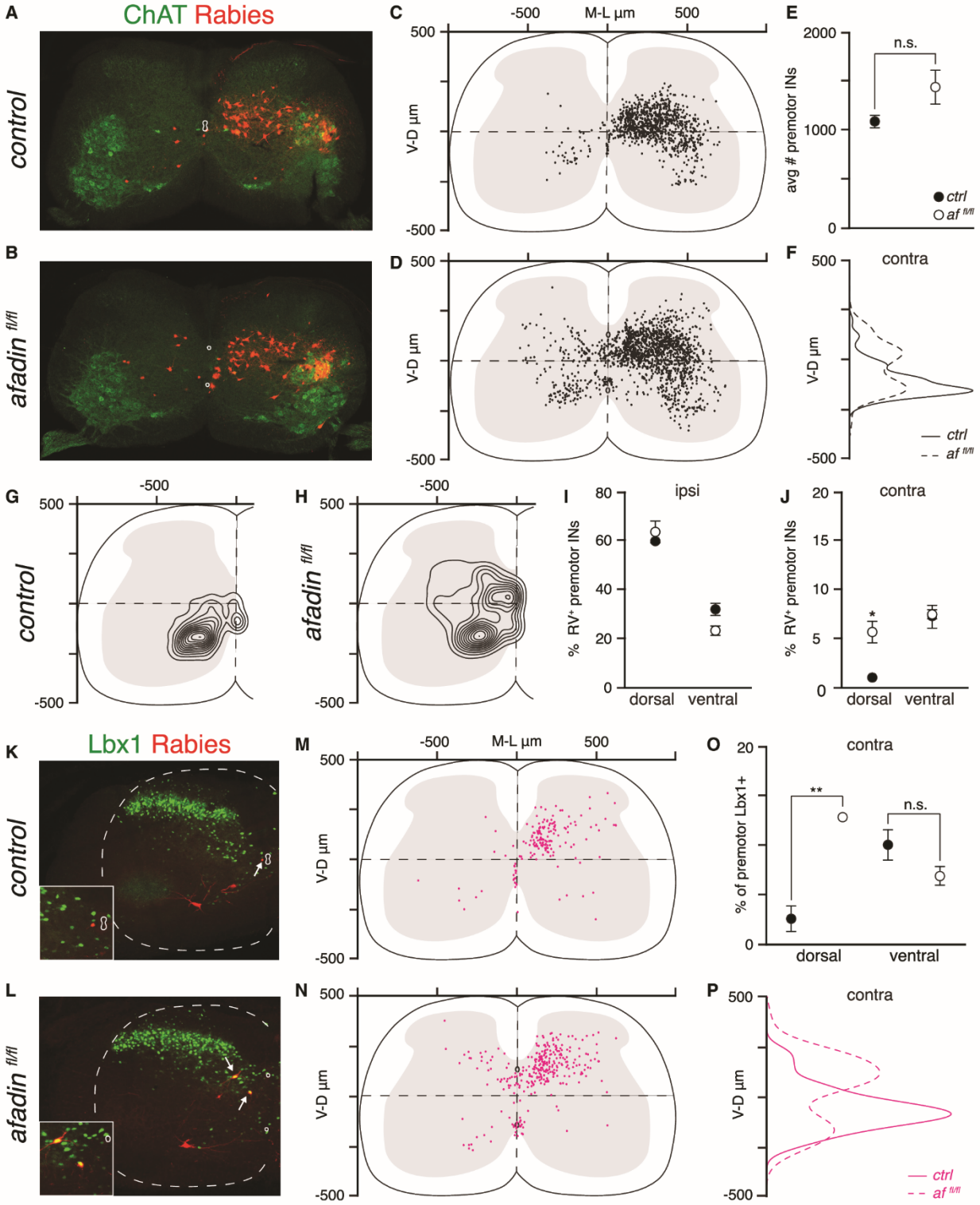

Figure 6. Aberrant Wiring of Premotor Circuits in Afadin Mutant Mice

(A and B) Transverse sections of a control (A) and an *afadin* $^{fl/fl}$ (B) spinal cords showing rabies-labeled interneurons.

(legend continued on next page)

Rosa-lsl-G-ires-TVA line (*RΦGT*; Takatoh et al., 2013) and monosynaptic tracing by muscle injection of G-deficient RV (RVΔG-mCherry). Efficient labeling of neurons was observed in control and *afadin* $^{fl/fl}$ mice (Figures 6A, 6B, and 6E; Table S1). To quantitatively analyze the spatial organization of premotor interneurons, we digitally reconstructed their three-dimensional positions and compared their distributions. In control mice, most premotor interneurons were located ipsilaterally in Rexed laminae VI, VII, and X, whereas on the contralateral side, they were mainly confined to lamina VIII, as described previously (Figures 6C, 6G, and S5A; Stepien et al., 2010). The overall distribution of premotor interneurons in *afadin* $^{fl/fl}$ mice was similar; however, an increase in the incidence of contralateral neurons was clearly evident (Figures 6D, 6H, and S5B). We found a significantly higher number of premotor interneurons in the dorsal contralateral quadrant, but we did not observe differences in the numbers of labeled cells in other quadrants (Figures 6F, 6I, 6J, S5C, and S5D).

We next analyzed the connectivity of Lbx1-expressing premotor interneurons and found an ectopic cluster in the dorsal contralateral side of *afadin* $^{fl/fl}$ mice (Figures 6K–6N, S5E, and S5F). Quantitative analysis confirmed this observation and revealed that significantly more Lbx1$^+$ premotor neurons are present in the dorsal contralateral quadrant in mutant mice, whereas no significant difference was found in the number of cells labeled in the ventral one (Figure 6O). Accordingly, distribution analysis of contralateral Lbx1$^+$ premotor neurons revealed a dorsal peak in *afadin* $^{fl/fl}$ mice (Figure 6P). Altogether, these data reveal the presence of an ectopic cluster of contralateral interneurons in mutant mice, some of which originate from the Lbx1 progenitor zone, as predicted by perturbation of ephrin B3 signaling at the midline.

Multiple Cardinal Interneuron Subtypes Are Miswired in Afadin Mutant Mice

Comparison of total and Lbx1$^+$ premotor interneuron maps in *afadin* $^{fl/fl}$ mice indicated the presence of other populations of ectopically wired interneurons (Figures S6A and S6B). Thus, we expanded our analysis to other subtypes implicated previously in the control of locomotion for which markers are available at early postnatal stages (Lu et al., 2015; Ziskind-Conhaim and Hochman, 2017).

First, we focused on interneurons arising from the V0 progenitor domain. In the absence of a defining marker still expressed at postnatal stages, we characterized these cells by combining immunohistochemistry for Lhx1, which labels a mixed population, including V0, V1, and subsets of dorsal interneurons (dI4 and dIL$_A$), with FoxD3, which captures V1 interneurons (Pillai et al., 2007; Francius et al., 2013; Lu et al., 2015). In *afadin* $^{fl/fl}$ mice, we found an ectopic cluster of Lhx1$^+$/FoxD3$^-$ neurons in the dorsal contralateral spinal cord (Figures 7A–7F and S6I). These cells are found in more lateral positions compared with the premotor Lbx1$^+$ population, indicating that they might represent a different subtype (Figures 7G and 7H). We also examined the number and distribution of FoxD3$^+$ premotor interneurons in *afadin* $^{fl/fl}$ mice, but we did not find any significant difference compared with control animals (Figures S6C–S6H). Next we analyzed V0c neurons, a subset of V0 neurons recognizable by their cholinergic character and position in lamina X (Zagoraiou et al., 2009). V0c neurons have been shown to affect the modulation of motor output and to bilaterally connect to motor neurons (Zagoraiou et al., 2009; Stepien et al., 2010). As expected, we observed contralaterally projecting V0c premotor neurons in control and *afadin* $^{fl/fl}$ mice (Figures 7I–7L). However, we found a significant increase in the percentage of contralateral V0c premotor neurons in mutant mice, whereas the number and distribution of the ipsilateral ones was not changed (Figures 7M and 7N). We next checked whether the position of V0c neurons was affected by the presence of a double central canal in *afadin* $^{fl/fl}$ mice, but we did not observe any significant difference in their positioning (Figures 7O, 7P, and S7A–S7D). Finally, we analyzed premotor connectivity of V2a interneurons, a population consisting of ipsilaterally projecting excitatory interneurons defined by Chx10 expression (Al-Mosawie et al., 2007; Lundfald et al., 2007). In control mice, we observed Chx10$^+$ premotor interneurons exclusively in the ipsilateral side of the spinal cord (Figures 7Q and 7S). In contrast, contralateral Chx10$^+$ premotor neurons were found in *afadin* $^{fl/fl}$ mice (Figures 7R and 7T–7V). Moreover, we did not observe any difference in the number or location of ipsilateral V2a premotor neurons or the general V2a population (Figures 7W, 7X, and S7E–S7H). Altogether, these data indicate ectopic contralateral connectivity in multiple cardinal interneuron subtypes in afadin mutant mice.

DISCUSSION

The precise rhythm and pattern of muscle activation underlie execution of coordinated movements and rely on correct assembly and function of spinal circuits. We found that conditional elimination of afadin in motor neuron progenitors results in loss

(C and D) Digital reconstructions of interneuron positions after rabies injection in the extensor carpi radialis muscle of a control (C) and an *afadin* $^{fl/fl}$ (D) mouse.
(E) Average number of interneurons labeled in control and *afadin* $^{fl/fl}$ mice (mean ± SEM; t test, $p > 0.05$; n = 3).
(F) Dorso-ventral density analysis of contralateral interneurons in control and *afadin* $^{fl/fl}$ mice (n = 3).
(G and H) Transverse contour density plots of contralateral interneurons in control (G) and *afadin* $^{fl/fl}$ mice (H) (n = 3).
(I and J) Percentage of interneurons in the dorsal and ventral quadrant of the ipsilateral (I) and contralateral (J) sides of the spinal cords in control and *afadin* $^{fl/fl}$ mice (mean ± SEM; t test, * = $p < 0.05$; n = 3).
(K and L) Contralateral transverse sections of a control (K) and an *afadin* $^{fl/fl}$ (L) spinal cords showing rabies-labeled interneurons and Lbx1 expression. Insets show magnification of a representative neuron marked by the arrow.
(M and N) Digital reconstruction of rabies$^+$/Lbx1$^+$ interneuron positions in control (M) and *afadin* $^{fl/fl}$ (N) mice (n = 3).
(O) Percentage of rabies$^+$/Lbx1$^+$ interneurons in the contralateral dorsal and ventral quadrants of the spinal cord (mean ± SEM; t test, ** = $p < 0.01$; n = 3).
(P) Dorso-ventral density analysis of contralateral rabies$^+$/Lbx1$^+$ interneurons in control and *afadin* $^{fl/fl}$ mice (n = 3).

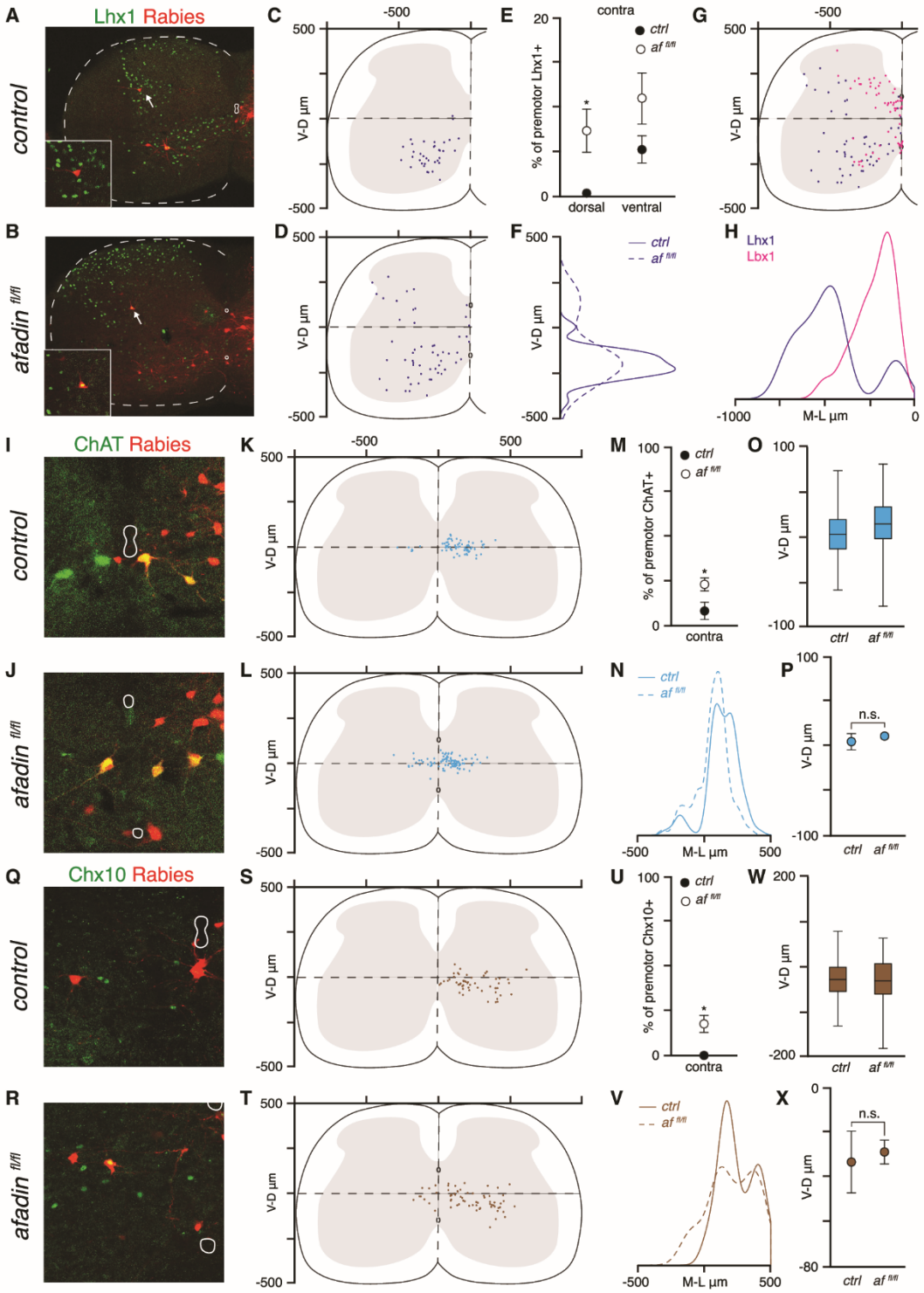

Figure 7. Multiple Interneuron Subtypes Are Miswired in Afadin Mutant Mice

(A and B) Contralateral transverse sections of a control (A) and an *afadin* $^{fl/fl}$ (B) spinal cords showing rabies-labeled interneurons and Lhx1 expression. Insets show magnification of a representative neuron marked by the arrow.

(legend continued on next page)

of left-right limb alternation in favor of synchronous movement. Our data show that afadin function at the neuroepithelium is important for lumen formation and that, in its absence, development of midline structures is perturbed. In particular, afadin elimination from the pMN results in a double central canal phenotype. As a consequence, the anatomical organization of the spinal midline is disrupted. Analysis of premotor circuit assembly shows the emergence of ectopic clusters of contralateral premotor interneurons in afadin mutant mice. In particular, our data indicate that miswiring of multiple subtypes, including dI4-5, V0, V0c, and V2a identities, is necessary to cause loss of left-right limb alternation.

Afadin Is a Key Regulator of Lumen Formation

Generation of tubular structures is a morphogenetic process essential for functional organization of many organs and relies on establishment of epithelial polarity and actin cytoskeleton remodeling (Datta et al., 2011). Afadin is known to have important roles in epithelial cells in the formation of adherens and tight junctions as well as in the organization of apicobasal polarity (Mandai et al., 2013). In the developing kidney and pancreas, afadin has been shown to be a central element in the generation and elongation of epithelial tubules. Lumen formation in the kidney requires alignment of apical membrane domains on adjacent epithelial cells that coalesce to generate a lumen, and, upon afadin elimination, nephrons develop a discontinuous lumen (Yang et al., 2013). Similarly, formation of uninterrupted pancreatic lumens occurs via apical membrane biogenesis in a highly coordinated process between epithelial cells that depends on afadin function (Azizoglu et al., 2017). Our findings in the spinal cord are in line with these observations. Elimination of afadin from the pMN creates a gap between adjoining neuroepithelial areas at the midline, precluding their coalescence and causing formation of two independent luminal structures. Moreover, elimination of afadin from dorsal progenitors expressing Wnt1 also perturbs organization of the midline and results in displacement of the central canal to a more ventral position, highlighting the important role of afadin along the whole dorso-ventral extent of the spinal neuroepithelium.

Lumen morphogenesis in the pancreas has been shown to rely on the cooperation of afadin and RhoA activities in the control of cytoskeletal remodeling (Azizoglu et al., 2017). In the spinal cord, previous work showed that elimination of RhoA from the neuroepithelium leads to defects in midline development, indicating that the same signaling pathway controls tubulogenesis in different organs and raising the question of whether specific cell surface receptors are required for this function (Katayama et al., 2012; Mulherkar et al., 2013). Afadin is known to support function of the classical cadherin and nectin families of adhesion molecules (Takai et al., 2008; Mandai et al., 2013). We showed that elimination of afadin in motor neuron progenitors does not affect classical cadherin localization and function (Dewitz et al., 2018). The nectin family consists of four members: nectin-1, nectin-2, and nectin-3 are expressed at the spinal neuroepithelium during development, whereas nectin-4 is not detectable (Okabe et al., 2004; Dewitz et al., 2018). We observed perturbation in nectin-1, nectin-2, and nectin-3 expression at the pMN upon elimination of afadin in motor neuron progenitors (data not shown). However, single nectin mutant mice do not present anatomical or locomotor phenotypes similar to the ones found after elimination of afadin (Takai et al., 2008; Mandai et al., 2015). These observations indicate that nectins may have a redundant function, upstream of afadin, in the control of neuroepithelial integrity in the spinal cord. Finally, afadin has also been implicated in control of the ephrin/Eph and Slit/Robo pathways, raising the possibility that multiple effectors could contribute to the phenotype (Hock et al., 1998; Slováková et al., 2012).

The Double Central Canal and Wiring of Spinal Motor Circuits

How does generation of a double central canal affect wiring of spinal motor circuits? Our data show that perturbation of central canal formation results in altered organization of the spinal cord midline. We found that ephrin B3, which is normally expressed along the entire dorso-ventral extent of the gray matter, is lost between the two canals, suggesting that the tissue in the central area of the spinal cord is not properly organized (Imondi et al., 2000; Kullander et al., 2001). Similarly, the extent of netrin 1 expression along the ventral half of the midline is also reduced (Serafini et al., 1996). Despite these

(C and D) Digital reconstructions of contralateral rabies$^+$/Lhx1$^+$ interneuron positions in control (C) and *afadin* $^{fl/fl}$ (D) mice (n = 3).
(E) Percentage of rabies$^+$/Lhx1$^+$ interneurons in the contralateral dorsal and ventral quadrants of the spinal cord (mean ± SEM; t test, *p < 0.05; n = 3).
(F) Dorso-ventral density analysis of contralateral rabies$^+$/Lhx1$^+$ interneurons in control and *afadin* $^{fl/fl}$ mice (n = 3).
(G) Digital reconstruction of contralateral rabies$^+$/Lhx1$^+$ (dark blue) and rabies$^+$/Lbx1$^+$ (magenta) interneuron positions in *afadin* $^{fl/fl}$ mice (n = 3).
(H) Medio-lateral density analysis in the contralateral dorsal quadrant of rabies$^+$/Lhx1$^+$ (dark blue) and rabies$^+$/Lbx1$^+$ (magenta) interneurons in *afadin* $^{fl/fl}$ mice (n = 3).
(I and J) Transverse spinal cord sections showing rabies-labeled interneurons and ChAT expression in the central canal area in control (I) and *afadin* $^{fl/fl}$ (J) mice.
(K and L) Digital reconstruction of rabies$^+$/ChAT$^+$ interneuron positions in control (K) and *afadin* $^{fl/fl}$ (L) mice (n = 3).
(M) Percentage of rabies$^+$/ChAT$^+$ interneurons in the contralateral side of the spinal cord (mean ± SEM; t test, *p < 0.05; n = 3).
(N) Medio-lateral density analysis of rabies$^+$/ChAT$^+$ interneurons in control and *afadin* $^{fl/fl}$ mice (n = 3).
(O) Boxplots showing distribution of rabies$^+$/ChAT$^+$ interneurons in control and *afadin* $^{fl/fl}$ mice along the dorso-ventral axis (n = 3).
(P) Average dorso-ventral position of rabies$^+$/ChAT$^+$ interneurons in control and *afadin* $^{fl/fl}$ mice (mean ± SEM; t test, p > 0.05; n = 3).
(Q and R) Transverse spinal cord sections showing rabies-labeled interneurons and Chx10 expression in the central canal area in control (Q) and *afadin* $^{fl/fl}$ (R) mice.
(S and T) Digital reconstruction of rabies$^+$/Chx10$^+$ interneuron positions in control (S) and *afadin* $^{fl/fl}$ (T) mice (n = 4).
(U) Percentage of rabies$^+$/Chx10$^+$ interneurons on the contralateral side of the spinal cord (mean ± SEM; t test, *p < 0.05; n = 4).
(V) Medio-lateral density analysis of rabies$^+$/Chx10$^+$ interneurons in control and *afadin* $^{fl/fl}$ mice (n = 4).
(W) Boxplots showing distribution of rabies$^+$/Chx10$^+$ interneurons in control and *afadin* $^{fl/fl}$ mice along the dorso-ventral axis (n = 4).
(X) Average dorso-ventral position of rabies$^+$/Chx10$^+$ interneurons in control and *afadin* $^{fl/fl}$ mice (mean ± SEM; t test, p > 0.05; n = 4).

remarkable anatomical defects, we did not observe any change in the stereotypic positioning of spinal interneurons normally residing in the intermediate zone of the spinal cord, indicating that the generation and migration of interneurons are not affected by formation of a double central canal. Thus, our data suggest that impairment in lumen morphogenesis compromises the organization of midline signals ensuring laterality in circuit wiring.

Connectivity Defects in Multiple Premotor Neuron Subtypes in Afadin Mutant Mice

Perturbation of the localization of midline cues controlling guidance of developing axons is predicted to affect laterality in wiring of motor circuits (Kullander et al., 2001; Rabe et al., 2009). Despite the reduction in the extent of netrin 1 expression in the ventral spinal cord in afadin mutant mice, we did not observe any obvious defect in commissural axon organization. Elimination of ephrin B3 expression between the two central canals in afadin mutant mice is predicted to open a way across the midline for EphA4-expressing axons during assembly of spinal circuits. It has been shown that perturbation of EphA4 signaling in interneurons derived from the Lbx1 progenitor domain results in aberrant contralateral projections (Paixão et al., 2013). Lbx1-derived interneurons can be divided into three main subpopulations: dI4 and dI5 neurons residing in the dorsal spinal cord and ventral dI6 neurons (Gross et al., 2002; Müller et al., 2002). In afadin mutant mice, we found Lbx1^{+} contralateral premotor neurons in the dorsal spinal cord, indicating a role of dI4-5 neurons in circuits controlling gait selection. The same population of interneurons has been identified as a source of ectopic contralateral projections to motor neurons in EphA4 knockout mice, and conditional elimination of EphA4 in Lbx1-derived interneurons is sufficient to result in connectivity defects (Satoh et al., 2016). These mice present an alternating gait during on-ground locomotion but conditionally switch to a synchronous gait when performing locomotor tasks demanding less weight load, such as swimming or air stepping. These observations suggest that changes in the connectivity of multiple interneurons subtypes are required to constitutively synchronize paired limb movement.

Our experiments with afadin mutant mice provide important clues for identification of additional defects in premotor connectivity required for a complete switch to synchrony. We found an ectopic premotor cluster of Lhx1^{+}/FoxD3^{-} neurons in the dorsal contralateral spinal cord. These cells reside in a more lateral position compared to the Lbx1^{+} cluster, indicating that they constitute a different subset of Lbx1-derived neurons or may originate from V0 progenitors (Lu et al., 2015). Interestingly, we did not observe any difference in premotor connectivity of neurons labeled by FoxD3, which comprise mostly V1 inhibitory interneurons that have no described role in left-right alternation (Arber, 2012). A fraction of V0 neurons has been shown to express EphA4 during embryonic development; however, no defects in connectivity across the midline for V0 neurons in mice with perturbed ephrin signaling have been reported yet (Lundfald et al., 2007). We observed an increase in contralateral connectivity of V0c neurons, a small cholinergic subset of V0 neurons that has been shown to bilaterally connect to motor neurons and participate in modulation of motor output (Zagoraiou et al., 2009; Stepien et al., 2010). Thus, our data suggest that incorrect wiring of V0c could also contribute to the deregulation of circuits controlling gait choice. Finally, we found ectopic contralateral premotor neurons characterized by expression of Chx10. V2a neurons are predicted to be a main culprit for the loss of left-right alternation in the absence of ephrin signaling because of their exclusive ipsilateral connectivity, glutamatergic character, and expression of EphA4 (Al-Mosawie et al., 2007; Lundfald et al., 2007; Borgius et al., 2014). Moreover, genetic ablation of V2a neurons results in loss of left-right alternation in a speed-dependent manner (Crone et al., 2009). However, contralaterally projecting V2a neurons have not been observed previously in EphA4-null mice (Lundfald et al., 2007). In contrast, our data also show that laterality in V2a neuron connectivity is compromised in the absence of ephrin signaling and suggest that this defect contributes to the constitutive emergence of a bound gait.

STAR★METHODS

Detailed methods are provided in the online version of this paper and include the following:

- KEY RESOURCES TABLE
- RESOURCE AVAILABILITY
  - Lead Contact
  - Materials Availability
  - Data and Code Availability
- EXPERIMENTAL MODEL AND SUBJECT DETAILS
  - Animal Experimentation Ethical Approval
  - Animal models
- METHOD DETAILS
  - Gait analysis
  - Rabies virus production
  - Intramuscular injections
  - Perfusion
  - Dissection and tissue processing
  - Contralateral interneurons tracing
  - Immunohistochemistry
  - *In situ* hybridization
  - Three-dimensional positional analysis
- QUANTIFICATION AND STATISTICAL ANALYSIS

SUPPLEMENTAL INFORMATION

Supplemental Information can be found online at https://doi.org/10.1016/j.celrep.2020.107741.

ACKNOWLEDGMENTS

We thank Liana Kosizki, Isabelle Werner, and Aurélie Heuzé for technical support and the MDC Advanced Light Microscope Facility for assistance with image acquisition and analysis. We are grateful to Carmen Birchmeier for the gift of the Lbx1 and FoxD3 antibodies. The Lhx1 antibody was a gift from Susan Morton. Dario Bonanomi provided the probe against netrin-1. We thank Marco Beato, Stephan Dietrich, Katrin Gerstmann, and Sofia Pimpinella for valuable discussions and comments on the manuscript. S.S. and N.Z. were supported

by the DFG (ZA 885/1-1 and EXC 257 NeuroCure) and J.B. by ANR grant ANR-17-CE16-0027.

AUTHOR CONTRIBUTIONS

Conceptualization, S.S. and N.Z.; Investigation, S.S., C.H., and E.T.; Formal Analysis, S.S, C.S.M., and J.B.; Writing – Original Draft, S.S. and N.Z.; Writing – Review and Editing, S.S., J.B. and N.Z.; Supervision, J.B. and N.Z.

DECLARATION OF INTERESTS

The authors declare no competing interests.

Received: June 28, 2019
Revised: April 3, 2020
Accepted: May 15, 2020
Published: June 9, 2020

REFERENCES

Al-Mosawie, A., Wilson, J.M., and Brownstone, R.M. (2007). Heterogeneity of V2-derived interneurons in the adult mouse spinal cord. Eur. J. Neurosci. *26*, 3003–3015.

Arber, S. (2012). Motor circuits in action: specification, connectivity, and function. Neuron *74*, 975–989.

Azizoglu, D.B., Braitsch, C., Marciano, D.K., and Cleaver, O. (2017). Afadin and RhoA control pancreatic endocrine mass via lumen morphogenesis. Genes Dev. *31*, 2376–2390.

Beaudoin, G.M.J., 3rd, Schofield, C.M., Nuwal, T., Zang, K., Ullian, E.M., Huang, B., and Reichardt, L.F. (2012). Afadin, a Ras/Rap effector that controls cadherin function, promotes spine and excitatory synapse density in the hippocampus. J. Neurosci. *32*, 99–110.

Beg, A.A., Sommer, J.E., Martin, J.H., and Scheiffele, P. (2007). α2-Chimaerin is an essential EphA4 effector in the assembly of neuronal locomotor circuits. Neuron *55*, 768–778.

Bellardita, C., and Kiehn, O. (2015). Phenotypic characterization of speed-associated gait changes in mice reveals modular organization of locomotor networks. Curr. Biol. *25*, 1426–1436.

Bikoff, J.B., Gabitto, M.I., Rivard, A.F., Drobac, E., Machado, T.A., Miri, A., Brenner-Morton, S., Famojure, E., Diaz, C., Alvarez, F.J., et al. (2016). Spinal Inhibitory Interneuron Diversity Delineates Variant Motor Microcircuits. Cell *165*, 207–219.

Borgius, L., Nishimaru, H., Caldeira, V., Kunugise, Y., Löw, P., Reig, R., Itohara, S., Iwasato, T., and Kiehn, O. (2014). Spinal glutamatergic neurons defined by EphA4 signaling are essential components of normal locomotor circuits. J. Neurosci. *34*, 3841–3853.

Chédotal, A. (2019). Roles of axon guidance molecules in neuronal wiring in the developing spinal cord. Nat. Rev. Neurosci. *20*, 380–396.

Crone, S.A., Quinlan, K.A., Zagoraiou, L., Droho, S., Restrepo, C.E., Lundfald, L., Endo, T., Setlak, J., Jessell, T.M., Kiehn, O., and Sharma, K. (2008). Genetic ablation of V2a ipsilateral interneurons disrupts left-right locomotor coordination in mammalian spinal cord. Neuron *60*, 70–83.

Crone, S.A., Zhong, G., Harris-Warrick, R., and Sharma, K. (2009). In mice lacking V2a interneurons, gait depends on speed of locomotion. J. Neurosci. *29*, 7098–7109.

Dasen, J.S., Tice, B.C., Brenner-Morton, S., and Jessell, T.M. (2005). A Hox regulatory network establishes motor neuron pool identity and target-muscle connectivity. Cell *123*, 477–491.

Datta, A., Bryant, D.M., and Mostov, K.E. (2011). Molecular regulation of lumen morphogenesis. Curr. Biol. *21*, R126–R136.

Demireva, E.Y., Shapiro, L., Jessell, T.M., and Zampieri, N. (2011). Motor Neuron Position and Topographic Order Imposed by β- and γ-Catenin Activities. Cell *147*, 641–652.

Dessaud, E., Yang, L.L., Hill, K., Cox, B., Ulloa, F., Ribeiro, A., Mynett, A., Novitch, B.G., and Briscoe, J. (2007). Interpretation of the sonic hedgehog morphogen gradient by a temporal adaptation mechanism. Nature *450*, 717–720.

Dewitz, C., Pimpinella, S., Hackel, P., Akalin, A., Jessell, T.M., and Zampieri, N. (2018). Nuclear Organization in the Spinal Cord Depends on Motor Neuron Lamination Orchestrated by Catenin and Afadin Function. Cell Rep. *22*, 1681–1694.

Francius, C., Harris, A., Rucchin, V., Hendricks, T.J., Stam, F.J., Barber, M., Kurek, D., Grosveld, F.G., Pierani, A., Goulding, M., and Clotman, F. (2013). Identification of multiple subsets of ventral interneurons and differential distribution along the rostrocaudal axis of the developing spinal cord. PLoS ONE *8*, e70325.

Gil-Sanz, C., Landeira, B., Ramos, C., Costa, M.R., and Müller, U. (2014). Proliferative defects and formation of a double cortex in mice lacking Mltt4 and Cdh2 in the dorsal telencephalon. J. Neurosci. *34*, 10475–10487.

Gosgnach, S., Bikoff, J.B., Dougherty, K.J., El Manira, A., Lanuza, G.M., and Zhang, Y. (2017). Delineating the Diversity of Spinal Interneurons in Locomotor Circuits. J. Neurosci. *37*, 10835–10841.

Goulding, M. (2009). Circuits controlling vertebrate locomotion: moving in a new direction. Nat. Rev. Neurosci. *10*, 507–518.

Grillner, S. (2006). Biological pattern generation: the cellular and computational logic of networks in motion. Neuron *52*, 751–766.

Grillner, S., and Jessell, T.M. (2009). Measured motion: searching for simplicity in spinal locomotor networks. Curr. Opin. Neurobiol. *19*, 572–586.

Gross, M.K., Dottori, M., and Goulding, M. (2002). Lbx1 specifies somatosensory association interneurons in the dorsal spinal cord. Neuron *34*, 535–549.

Hock, B., Böhme, B., Karn, T., Yamamoto, T., Kaibuchi, K., Holtrich, U., Holland, S., Pawson, T., Rübsamen-Waigmann, H., and Strebhardt, K. (1998). PDZ-domain-mediated interaction of the Eph-related receptor tyrosine kinase EphB3 and the ras-binding protein AF6 depends on the kinase activity of the receptor. Proc. Natl. Acad. Sci. USA *95*, 9779–9784.

Imondi, R., Wideman, C., and Kaprielian, Z. (2000). Complementary expression of transmembrane ephrins and their receptors in the mouse spinal cord: a possible role in constraining the orientation of longitudinally projecting axons. Development *127*, 1397–1410.

Iwasato, T., Katoh, H., Nishimaru, H., Ishikawa, Y., Inoue, H., Saito, Y.M., Ando, R., Iwama, M., Takahashi, R., Negishi, M., and Itohara, S. (2007). Rac-GAP α-chimerin regulates motor-circuit formation as a key mediator of EphrinB3/EphA4 forward signaling. Cell *130*, 742–753.

Katayama, K., Leslie, J.R., Lang, R.A., Zheng, Y., and Yoshida, Y. (2012). Left-right locomotor circuitry depends on RhoA-driven organization of the neuroepithelium in the developing spinal cord. J. Neurosci. *32*, 10396–10407.

Kiehn, O. (2006). Locomotor circuits in the mammalian spinal cord. Annu. Rev. Neurosci. *29*, 279–306.

Kiehn, O. (2016). Decoding the organization of spinal circuits that control locomotion. Nat. Rev. Neurosci. *17*, 224–238.

Kjaerulff, O., and Kiehn, O. (1996). Distribution of networks generating and coordinating locomotor activity in the neonatal rat spinal cord in vitro: a lesion study. J. Neurosci. *16*, 5777–5794.

Kullander, K., Croll, S.D., Zimmer, M., Pan, L., McClain, J., Hughes, V., Zabski, S., DeChiara, T.M., Klein, R., Yancopoulos, G.D., and Gale, N.W. (2001). Ephrin-B3 is the midline barrier that prevents corticospinal tract axons from recrossing, allowing for unilateral motor control. Genes Dev. *15*, 877–888.

Kullander, K., Butt, S.J.B., Lebret, J.M., Lundfald, L., Restrepo, C.E., Rydström, A., Klein, R., and Kiehn, O. (2003). Role of EphA4 and EphrinB3 in local neuronal circuits that control walking. Science *299*, 1889–1892.

Lanuza, G.M., Gosgnach, S., Pierani, A., Jessell, T.M., and Goulding, M. (2004). Genetic identification of spinal interneurons that coordinate left-right locomotor activity necessary for walking movements. Neuron *42*, 375–386.

Lemieux, M., Josset, N., Roussel, M., Couraud, S., and Bretzner, F. (2016). Speed-dependent modulation of the locomotor behavior in adult mice reveals attractor and transitional gaits. Front. Neurosci. *10*, 42.

Lu, D.C., Niu, T., and Alaynick, W.A. (2015). Molecular and cellular development of spinal cord locomotor circuitry. Front. Mol. Neurosci. *8*, 25.

Lundfald, L., Restrepo, C.E., Butt, S.J.B., Peng, C.Y., Droho, S., Endo, T., Zeilhofer, H.U., Sharma, K., and Kiehn, O. (2007). Phenotype of V2-derived interneurons and their relationship to the axon guidance molecule EphA4 in the developing mouse spinal cord. Eur. J. Neurosci. *26*, 2989–3002.

Mandai, K., Rikitake, Y., Shimono, Y., and Takai, Y. (2013). Afadin/AF-6 and canoe: roles in cell adhesion and beyond. Prog. Mol. Biol. Transl. Sci. *116*, 433–454.

McHanwell, S., and Biscoe, T.J. (1981). The sizes of motoneurons supplying hindlimb muscles in the mouse. Proc. R. Soc. Lond. B Biol. Sci. *213*, 201–216.

Mendes, C.S., Bartos, I., Márka, Z., Akay, T., Márka, S., and Mann, R.S. (2015). Quantification of gait parameters in freely walking rodents. BMC Biol. *13*, 50.

Mulherkar, S., Liu, F., Chen, Q., Narayanan, A., Couvillon, A.D., Shine, H.D., and Tolias, K.F. (2013). The small GTPase RhoA is required for proper locomotor circuit assembly. PLoS ONE *8*, e67015.

Müller, T., Brohmann, H., Pierani, A., Heppenstall, P.A., Lewin, G.R., Jessell, T.M., and Birchmeier, C. (2002). The homeodomain factor lbx1 distinguishes two major programs of neuronal differentiation in the dorsal spinal cord. Neuron *34*, 551–562.

Müller, T., Anlag, K., Wildner, H., Britsch, S., Treier, M., and Birchmeier, C. (2005). The bHLH factor Olig3 coordinates the specification of dorsal neurons in the spinal cord. Genes Dev. *19*, 733–743.

Okabe, N., Shimizu, K., Ozaki-Kuroda, K., Nakanishi, H., Morimoto, K., Takeuchi, M., Katsumaru, H., Murakami, F., and Takai, Y. (2004). Contacts between the commissural axons and the floor plate cells are mediated by nectins. Dev. Biol. *273*, 244–256.

Osakada, F., and Callaway, E.M. (2013). Design and generation of recombinant rabies virus vectors. Nat. Protoc. *8*, 1583–1601.

Paixão, S., Balijepalli, A., Serradj, N., Niu, J., Luo, W., Martin, J.H., and Klein, R. (2013). EphrinB3/EphA4-mediated guidance of ascending and descending spinal tracts. Neuron *80*, 1407–1420.

Pillai, A., Mansouri, A., Behringer, R., Westphal, H., and Goulding, M. (2007). Lhx1 and Lhx5 maintain the inhibitory-neurotransmitter status of interneurons in the dorsal spinal cord. Development *134*, 357–366.

Rabe, N., Gezelius, H., Vallstedt, A., Memic, F., and Kullander, K. (2009). Netrin-1-dependent spinal interneuron subtypes are required for the formation of left-right alternating locomotor circuitry. J. Neurosci. *29*, 15642–15649.

Rossi, J., Balthasar, N., Olson, D., Scott, M., Berglund, E., Lee, C.E., Choi, M.J., Lauzon, D., Lowell, B.B., and Elmquist, J.K. (2011). Melanocortin-4 receptors expressed by cholinergic neurons regulate energy balance and glucose homeostasis. Cell Metab. *13*, 195–204.

Rowitch, D.H., S-Jacques, B., Lee, S.M.K., Flax, J.D., Snyder, E.Y., and McMahon, A.P. (1999). Sonic hedgehog regulates proliferation and inhibits differentiation of CNS precursor cells. J. Neurosci. *19*, 8954–8965.

Satoh, D., Pudenz, C., and Arber, S. (2016). Context-Dependent Gait Choice Elicited by EphA4 Mutation in Lbx1 Spinal Interneurons. Neuron *89*, 1046–1058.

Serafini, T., Colamarino, S.A., Leonardo, E.D., Wang, H., Beddington, R., Skarnes, W.C., and Tessier-Lavigne, M. (1996). Netrin-1 is required for commissural axon guidance in the developing vertebrate nervous system. Cell *87*, 1001–1014.

Slováková, J., Speicher, S., Sánchez-Soriano, N., Prokop, A., and Carmena, A. (2012). The actin-binding protein Canoe/AF-6 forms a complex with Robo and is required for Slit-Robo signaling during axon pathfinding at the CNS midline. J. Neurosci. *32*, 10035–10044.

Stepien, A.E., Tripodi, M., and Arber, S. (2010). Monosynaptic rabies virus reveals premotor network organization and synaptic specificity of cholinergic partition cells. Neuron *68*, 456–472.

Sürmeli, G., Akay, T., Ippolito, G.C., Tucker, P.W., and Jessell, T.M. (2011). Patterns of spinal sensory-motor connectivity prescribed by a dorsoventral positional template. Cell *147*, 653–665.

Takai, Y., Ikeda, W., Ogita, H., and Rikitake, Y. (2008). The Immunoglobulin-Like Cell Adhesion Molecule Nectin and Its Associated Protein Afadin. Annual Review of Cell and Developmental Biology *24*, 309–342.

Takatoh, J., Nelson, A., Zhou, X., Bolton, M.M., Ehlers, M.D., Arenkiel, B.R., Mooney, R., and Wang, F. (2013). New modules are added to vibrissal premotor circuitry with the emergence of exploratory whisking. Neuron *77*, 346–360.

Talpalar, A.E., Bouvier, J., Borgius, L., Fortin, G., Pierani, A., and Kiehn, O. (2013). Dual-mode operation of neuronal networks involved in left-right alternation. Nature *500*, 85–88.

Wickersham, I.R., Lyon, D.C., Barnard, R.J.O., Mori, T., Finke, S., Conzelmann, K.-K., Young, J.A., and Callaway, E.M. (2007). Monosynaptic restriction of transsynaptic tracing from single, genetically targeted neurons. Neuron *53*, 639–647.

Yang, Z., Zimmerman, S., Brakeman, P.R., Beaudoin, G.M., 3rd, Reichardt, L.F., and Marciano, D.K. (2013). De novo lumen formation and elongation in the developing nephron: a central role for afadin in apical polarity. Development *140*, 1774–1784.

Zagoraiou, L., Akay, T., Martin, J.F., Brownstone, R.M., Jessell, T.M., and Miles, G.B. (2009). A cluster of cholinergic premotor interneurons modulates mouse locomotor activity. Neuron *64*, 645–662.

Zhang, Y., Narayan, S., Geiman, E., Lanuza, G.M., Velasquez, T., Shanks, B., Akay, T., Dyck, J., Pearson, K., Gosgnach, S., et al. (2008). V3 spinal neurons establish a robust and balanced locomotor rhythm during walking. Neuron *60*, 84–96.

Ziskind-Conhaim, L., and Hochman, S. (2017). Diversity of molecularly defined spinal interneurons engaged in mammalian locomotor pattern generation. J. Neurophysiol. *118*, 2956–2974.

STAR★METHODS

KEY RESOURCES TABLE

REAGENT or RESOURCE	SOURCE	IDENTIFIER
Antibodies		
anti-afadin antibody (guinea pig)	Dewitz et al., 2018	N/A
anti-ChAT antibody (rabbit)	Sürmeli et al., 2011	RRID:AB_2750952
anti-Chx10 antibody (sheep)	Abcam	RRID:AB_302278
anti-FoxD3 antibody (guinea pig)	Müller et al., 2005	N/A
anti-Hb9 antibody (rabbit)	Generated in Jessell laboratory	N/A
anti-Isl1/2 antibody (guinea pig)	Dasen et al., 2005	RRID:AB_2801512
anti-Lbx1 antibody (rabbit)	Müller et al., 2002	N/A
anti-Lhx1 antibody (rabbit)	Generated in the Jessell laboratory	RRID:AB_2827967
anti-ROBO3 antibody (goat)	R&D Systems	RRID:AB_2181865
anti-TAG1 antibody (goat)	R&D Systems	RRID:AB_2044647
Phalloidin-FITC	Sigma Aldrich	Cat #: P5282
NeuroTrace 640/660 Deep Red Fluorescent Nissl Stain antibody	Thermo Fisher	RRID:AB_2572212
Bacterial and Virus Strains		
Rabies virus-ΔG-mCherry	Generated in the Zampieri laboratory	N/A
Experimental Models: Cell Lines		
BHK B7GG	Osakada and Callaway, 2013	N/A
HEK293T	American Type Culture Collection	Cat #: CRL-3216
Experimental Models: Organisms/Strains		
Afdn $^{tm1.1Lfr}$	Beaudoin et al., 2012	MGI:5308214
Olig2$^{tm1(cre)Tmj}$	Dessaud et al., 2007	MGI:3774124
H2az2 $^{Tg(Wnt1-cre)11Rth}$	Rowitch et al., 1999	MGI:2386570
Chat $^{tm1(cre)Lowl}$	Rossi et al., 2011	MGI:3699161
Gt(Rosa)26Sor $^{tm1(CAG-RABVgp4,-TVA)Arenk}$	Takatoh et al., 2013	MGI:5550559
Oligonucleotides		
Netrin 1 *In situ* hybridization probe fw primer: CGT GAA CAT CAT CTC CGT GT	Eurofins Scientific	N/A
Netrin 1 *In situ* hybridization probe rev primer: GCA GTG GAG ACC AAA GCT G	Eurofins Scientific	N/A
Ephrin B3 *In situ* hybridization probe fw primer: GTT AGG TTT TGC GGG GCT	Eurofins Scientific	N/A
Ephrin B3 *In situ* hybridization probe fw primer: TTC CTA GCT CCC CAG GCT	Eurofins Scientific	N/A
Software and Algorithms		
MouseWalker	Mendes et al., 2015	N/A
R	R Development Core Team (2008)	RRID:SCR_000432

RESOURCE AVAILABILITY

Lead Contact

Further information and requests for resources and reagents should be directed to and will be fulfilled by the Lead Contact, Niccolò Zampieri (niccolo.zampieri@mdc-berlin.de).

Materials Availability

All unique reagents generated in this study are available from the Lead Contact without restriction.

Data and Code Availability

Original datasets supporting the current study are available from the Lead Contact upon request. This study did not generate any new code.

EXPERIMENTAL MODEL AND SUBJECT DETAILS

Animal Experimentation Ethical Approval

All experiments were performed in compliance with the German Animal Welfare Act and approved by the Regional Office for Health and Social Affairs Berlin (LAGeSo) under license numbers G0121/15 and G0122/15.

Animal models

Mice were bred under standard husbandry and housing conditions. The mouse lines were used in this study maintained on a C57B6/J background: *Olig2::Cre* (Dessaud et al., 2007), *ChAT::Cre* (Rossi et al., 2011), *Wnt1::Cre* (Rowitch et al., 1999), *afadin* ^{fl} (Beaudoin et al., 2012) and *RΦGT* (Takatoh et al., 2013). *afadin* ^{fl} and *RΦGT* were kept homozygous whereas all Cre-lines were kept heterozygous. Animals of both sexes were used interchangeably and we did not anticipate nor observe any influence to the outcome. Following ages were used in this study: *Afadin* $^{fl/fl}$*; Olig2Cre* $^{+/-}$ (E10.5-P63. These mice sporadically develop hydrocephalus. Mice with hydrocephalus were sacrificed as soon as the disease was diagnosed); *afadin* $^{fl/fl}$*; Wnt1Cre* $^{+/-}$ (E13.5-E16.5. These mice display exencephaly); *afadin* $^{fl/fl}$*; ChATCre* $^{+/-}$ (E10.5-P21); *afadin* $^{fl/fl}$*; Olig2Cre* $^{+/-}$; *RΦGT* $^{fl/+}$ (P4-P10. These mice sporadically develop hydrocephalus. Mice with hydrocephalus were euthanised as soon as the disease was diagnosed).

METHOD DETAILS

Gait analysis

Quantitative gait analysis was performed as previously described (Mendes et al., 2015). Briefly, a customized acrylic glass walkway was constructed and surrounded by LED lights to generate the frustrated total internal reflection effect that is at the basis of the optical touch sensor that tracks the footprints. A lightbox was positioned above the walkway to visualize the body outline of the animals and a mirror was placed at a 45° angle below the walkway to reflect the signal to a high-speed camera. Before data acquisition, animals were habituated to the walkway setup and trained to walk straight from end to end. Three control animals and a total of nine *afadin* $^{fl/fl}$ mutant mice were analyzed. For each subject, three representative videos with uninterrupted runs at similar velocities were evaluated using the customized open-source MouseWalker software and the quantifiable parameters averaged.

Rabies virus production

Production of rabies virus was performed as previously described (Osakada and Callaway, 2013). Briefly, rabies virus production was started by infecting one T175 flask of BHK B7GG cells with stocks of rabies virusΔG-mCherry (RVΔG-mCherry) supernatant with a titer of at least 10^6 virus particles/ml. Cells were kept at 35°C and 3% CO_2 and medium was collected after four and seven days, centrifuged at 1000 rpm for 5 minutes and filtered. Amplification was started by infecting ten T175 flasks of BHK B7GG cells with the filtered starter culture. Medium was collected after four, seven and ten days, centrifuged at 1000 rpm for 5 minutes and filtered. To concentrate the virus, the medium was centrifuged at 24000 rpm for 2 hours. Pellets were resuspended in 400 μL Hanks' balanced salt solution (HBSS), tubes were covered with parafilm and incubated ON on a shaker at 4°C. Resuspended pellets were pooled and concentrated at 4°C using an Amicon Ultra 4 mL Filter (Merck Millipore) until a volume of approximately 100 μL was reached. Virus suspension was aliquoted and stored at −80°C until further use. Titer was determined by infecting HEK293T with serial dilutions of virus suspension.

Intramuscular injections

For motor pools analysis at adult stages, p60 animals were injected subcutaneously with 5 mg of carprofen per kg of weight as preemptive analgesia 30 minutes prior to surgery. Animals were then initially anesthetized with 4% isoflurane and checked for the toe pinch reflex before any procedure was done. Once sedated, they were placed on top of a circulating warm water blanket maintained at 37°C while keeping them under the effect of 2% isoflurane. Eye lubricant was applied to prevent their eyes from drying out. Head and body were gently fixed with tape to minimize movement during the surgery. To avoid any infection during the procedure, the hindlimbs were treated with iodine solution. A small incision was made in the skin to reveal the gastrocnemius (GS) and tibialis anterior (TA) muscles and a glass capillary was used to introduce 1 μL of cholera toxin subunit B (CTB) conjugated to either Alexa Fluor 488 or 555 (Thermo Fisher). Following injection, the skin was sutured with a nylon surgical suture. Animals were sacrificed three days post-surgery.

For monosynaptic tracing analysis P4 animals were anesthetized as described above and injected with 1.5 μL of RVΔG-mCherry in the extensor carpis radialis (ECR) muscle. Animals were sacrificed six days post-surgery.

Perfusion

Animals were anesthetized by intraperitoneal injection of 0.1 mL ketamine /xylazine mix per 10 g of weight (final concentrations: 120 mg/kg and 10 mg/kg, respectively) and checked for toe-pinch reflex before any procedure was done. Animals were first transcardially perfused with ice-cold PBS until the liver was cleared of blood, followed by freshly made ice-cold 4% PFA until no tremors could be observed anymore. Amount of PBS and PFA needed for a complete fixation depended on the age and weight of the animal (approximately 6 mL of each solution were used for neonates and 12-15 mL for adult animals).

Dissection and tissue processing

Spinal cords were dissected by decapitating the animals, opening up the belly and rib cage and removing the visceral organs. For all animals older than E13.5, ventral laminectomy was performed to allow better penetration of the fixative solution. Spinal cords were fixed for 90 minutes in 4% PFA on ice. This was followed by three washes with ice-cold PBS for 5 minutes each and over night incubation in 30% sucrose in 0.1M PB at 4°C for cryoprotection. Samples were embedded in Optimal Cutting Temperature (O.C.T., TissueTek) compound, frozen on dry ice and stored at −80°C.

Contralateral interneurons tracing

E15.5 embryos were dissected as described above. 0.5 μL of 1% tetramethylrhodamine-dextran solution was injected unilaterally with a glass capillary in the spinal cord between C5 and C8. Injected embryos were incubated in oxygenated 1x ACSF (127 mM NaCl; 3 mM KCl; 1.25 mM NaH_2PO_4 * 2 H_2O; 26 mM $NaHCO_3$; 10 mM glucose; 2 mM $CaCl_2$; 1 mM $MgCl_2$) over night at room temperature, followed by 5 hours of fixation in 4% PFA at 4°C. Embryos were subsequently processed as described above.

Immunohistochemistry

16 μm or 40 μm spinal cord cryosections were acquired with a Leica cryostat and collected on superfrost microscope slide. Slides were kept at room temperature for approximately 30 minutes to ensure good adhesion of the tissue on the glass. Sections were then first rehydrated with PBS for 10 minutes before adding freshly prepared dilutions of primary antibodies in 0.1% Triton X-100 in PBS (PBX, 16 μm) or 0.3% PBX (40 μm) for over night incubation at 4°C. Primary antibody dilutions were used as follows: guinea pig anti-afadin 1/20000, rabbit anti-ChAT 1/16000, sheep anti-Chx10 1/500, guinea pig anti-FoxD3 1/20000, rabbit anti-Hb9 1/8000, guinea pig anti-Isl1 1/30000, rabbit anti-Lbx1 1/10000, rabbit anti-Lhx1 1/10000, goat anti-ROBO3 1/200, goat anti-TAG1 1/200. After three washes with 0.1% PBX for 5 min each, secondary antibodies diluted in 0.1% or 0.3% PBX were added for 1 hour at room temperature. Alexa Fluor 488- and Cy3-conjugated secondary antibodies were used at 1/1000, Cy5-conjugated secondary antibodies at 1/500. Sections were then washed twice with 0.1% PBX for 5 minutes, followed by a final wash with PBS for 10 minutes. Slides were mounted with Vectashield (Vector). Nissl and phalloidin stainings were performed by adding NeuroTrace (Thermo Fisher) at 1/250 or Phalloidin-FITC (Sigma Aldrich) at 1/2000 along with the secondary antibodies.

In situ hybridization

In situ hybridization histochemistry was performed on 12 μm cryosections using digoxigenin (DIG)-labeled cRNA probes. DNA templates for mouse ephrin B3 and netrin 1 were cloned from cDNAs into pBluescript II SK^+ vector. Antisense DIG-cRNA probes were generated from DNA templates by RT-PCR using a DIG RNA Labeling Kit (Roche).

In situ hybridization was performed as previously described (Demireva et al., 2011). Briefly, slides were treated as follows: air-dried for 30 minutes, fixed with freshly made 4% PFA for 10 minutes, washed with PBS three times, treated with Proteinase K at 1mg/ml for 5 minutes, fixed with 4% PFA for 5 minutes, washed with PBS three times, acetylated for 10 minutes in 1.25% triethanolamine; 0.25% acetic acid anhydride; 0.175% HCl, washed with PBS three times and equilibrated with hybridization buffer (50% formamide; 1x Denhardt's solution; 0.25 mg/ml Baker's yeast RNA; 0.1 mg/ml Salmon sperm DNA in 5x SSC buffer) for 2 hours at room temperature in a humidified chamber. Slides were dried and hybridization buffer containing 100 ng of DIG-labeled probe were added, coverslipped and incubated at 70°C over night. Post-hybridization, slides were treated as follows: rinsed in 0.2x SSC buffer for 1 hour at 72°C, washed with 0.2x SSC buffer at room temperature for 5 minutes, washed with B1 buffer (100 mM Tris HCl pH 7.5; 150 mM NaCl) for 5 minutes, equilibrated with 10% heat-inactivated normal goat serum (HINGS) in B1 buffer for 1 hour, washed with B1 buffer three times and incubated with anti-DIG antibody (Roche) at 1/5000 in 1% HINGS in B1 buffer for 3 hours in a humidified dark chamber at room temperature. For signal detection, slides were washed with B1 buffer three times, equilibrated with B3 buffer (40 mM Tris HCl pH 9.5; 40 mM NaCl; 20 mM $MgCl_2$) for 15 minutes, dried, developing solution (0.24 mg/ml tetramisole hydrochloride; 0.35 mg/ml NBT; 0.18 mg/ml BCIP in B3 buffer) was added, coverslipped and kept in a dark chamber at room temperature until signal was detected. To stop the reaction, slides were incubated in ddH_2O for 20 minutes at room temperature four times and mounted with prewarmed Glycergel (Agilent).

Three-dimensional positional analysis

Three-dimensional positional analysis was performed as previously described (Dewitz et al., 2018). Briefly, for embryonic analysis, lumbar levels 1 - 3 of E13.5 spinal cords were analyzed by cutting 16 μm consecutive cryosections and performing immunostaining with Isl1 antibody for LMCm neurons and Hb9 antibody for LMCl neurons. Cartesian coordinates of motor neurons belonging to each division were obtained using the imaging software IMARIS. To account for differences in spinal cord size, orientation and shape, the

datasets were rotated and normalized against a standardized spinal cord whose size was determined empirically (Medio-lateral size: 365 μm, dorso-verntral size: 340 μm). To align the datasets along the rostro-caudal axis (z coordinate), the section where the first Isl1^{+} LMCm neurons were observed was defined as z = 0. The rostro-caudal position of each neuron was obtained by keeping track of the order of the sections. The x, y and z coordinates were then used to digitally reconstruct the distribution of the neurons. The same method was applied to postnatal datasets (motor pools positional analysis and retrograde tracing analysis). The first cryosection was defined as z = 0 and the size of the standardized spinal cord was adjusted (Medio-lateral size: 1000 μm, dorso-verntral size: 700 μm for motor pools positional analysis and medio-lateral size: 1000 μm, dorso-verntral size:: 500 μm for RV tracing experiments).

Positional datasets were analyzed using custom scripts in "R" (R Foundation for Statistical Computing, Vienna, Austria, 2005). In particular, contour and density plots were generated using the "ggplot2" package, which estimates the two-dimensional Gaussian density for the distribution of the given values. Correlation analysis was done with the "corrplot" package, which calculates the similarity between pairs of experiments using the Pearson correlation coefficient. Datasets were clustered hierarchically.

QUANTIFICATION AND STATISTICAL ANALYSIS

Statistical details about experiments can be found in figure legends. Unless otherwise stated, quantifications were performed by averaging parameters of three biological replicates per genotype. Significance was determined by applying unpaired, two-tailed t test. Significance was defined as: $p < 0.05$ = *; $p < 0.01$ = **; $p < 0.001$ = ***. Statistical analyses were performed with GraphPad Prism v7.2.

In order to account for differences in size and shape of the spinal cords, the extent of afadin/phalloidin expression and the length of dorsal and ventral gray matter in *afadin* $^{fl/fl}$ *Wnt1* mice were normalized against the total dorso-ventral extent of gray matter. Measurements of five sections per animal were averaged.

Cell Reports, Volume *31*

Supplemental Information

Afadin Signaling at the Spinal Neuroepithelium Regulates Central Canal Formation and Gait Selection

Sophie Skarlatou, Coralie Hérent, Elisa Toscano, César S. Mendes, Julien Bouvier, and Niccolò Zampieri

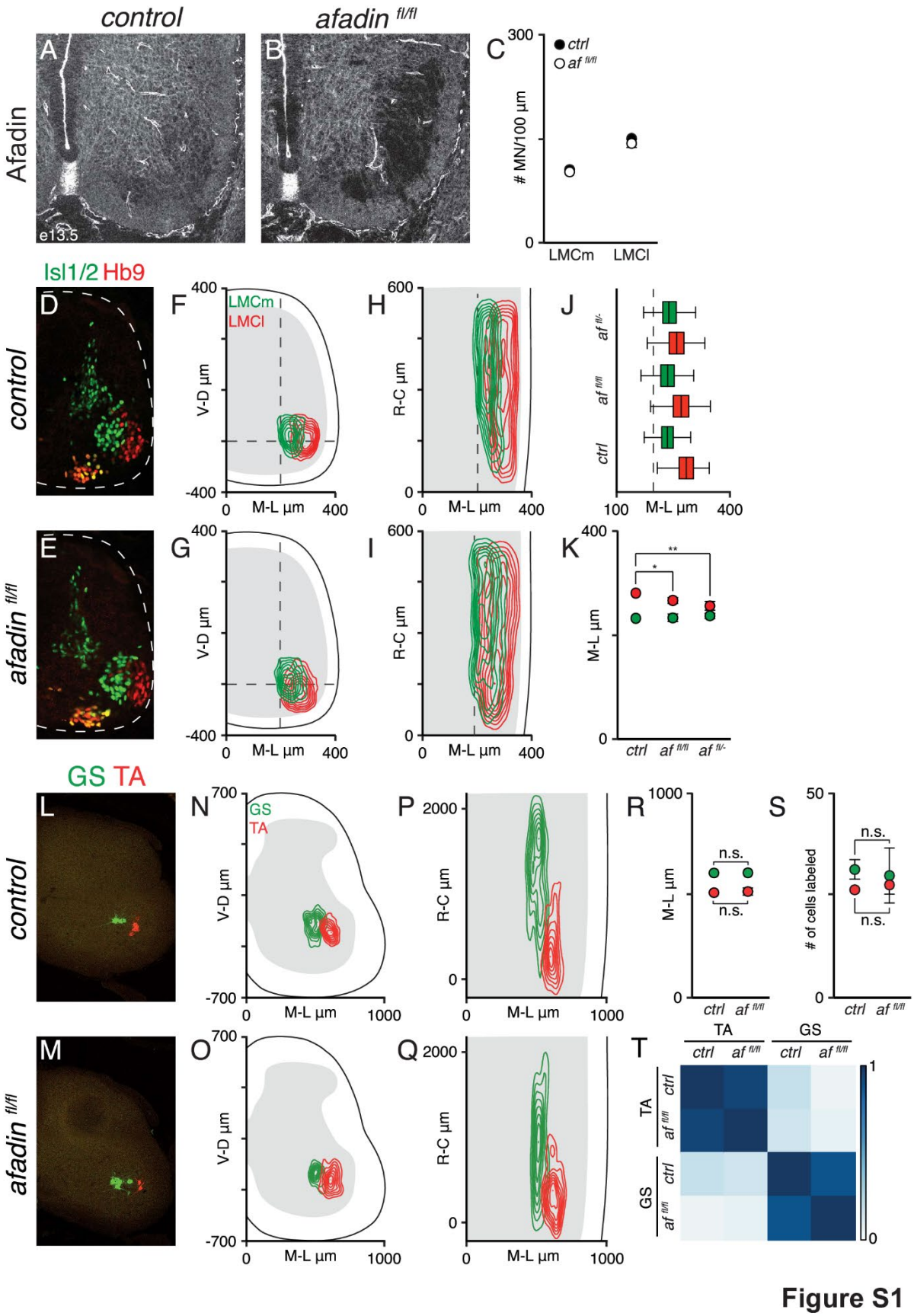
control
afadin fl/fl
Afadin
A
B
e13.5
C
ctrl
af fl/fl
MN/100 µm
LMCm
LMCl
Isl1/2 Hb9
control
afadin fl/fl
D
E
F
G
H
I
J
K
LMCm
LMCl
V-D µm
R-C µm
M-L µm
af fl/-
af fl/fl
ctrl
ctrl
af fl/fl
af fl/-
GS TA
L
M
N
O
P
Q
R
S
T
GS
TA
n.s.
# of cells labeled
TA
GS

Figure S1

Figure S1. Afadin elimination does not affect motor neuron development (related to Figure 1).

A and B) Afadin expression in e13.5 control (A) and *afadin*$^{fl/fl}$ (B) spinal cords.

C) Average number of medial and lateral LMC neurons (LMCm and LMCl) per 100 µm in control and *afadin*$^{fl/fl}$ embryos (mean ± SEM; t-test, $p > 0.05$; $n = 3$ for each genotype).

D and E) Transverse sections showing Isl1^{+} LMCm and Hb9^{+} LMCl neurons in e13.5 control (D) and *afadin*$^{fl/fl}$ (E) hemicords.

F and G) Transverse contour density plots of Isl1^{+} LMCm (green) and Hb9^{+} LMCl (red) neurons in control (F) and *afadin*$^{fl/fl}$ (G) embryos.

H and I) Longitudinal contour density plots of Isl1^{+} LMCm (green) and Hb9^{+} LMCl (red) neurons in control (H) and *afadin*$^{fl/fl}$ (I) embryos.

J) Boxplots showing medio-lateral distribution of LMCm and LMCl neurons in control, *afadin*$^{fl/fl}$ and *afadin*$^{fl/-}$ (*afadin*$^{fl/-}$ dataset from Dewitz et al., 2018) embryos.

K) Average medio-lateral position of LMCm (green) and LMCl (red) neurons in control, *afadin*$^{fl/fl}$ and *afadin*$^{fl/-}$ (*afadin*$^{fl/-}$ dataset from Dewitz et al., 2018) embryos.

L and M) CTB-labeled GS (Alexa-488) and TA (Alexa-555) motor neurons in control (L) and *afadin*$^{fl/fl}$ (M) adult mice.

N and O) Transverse contour density plots of GS (green) and TA (red) motor neurons in control (N) and *afadin*$^{fl/fl}$ (O) adult mice.

P and Q) Longitudinal contour density plots of GS (green) and TA (red) motor neurons in control (P) and *afadin*$^{fl/fl}$ (Q) adult mice.

R) Average medio-lateral position of GS (green) and TA (red) motor neurons in control and *afadin*$^{fl/fl}$ adult mice (mean ± SEM; t-test, $p > 0.05$; $n = 3$).

S) Average number of GS (green) and TA (red) cells labeled in control and *afadin* $^{fl/fl}$ adult mice (mean ± SEM; t-test, $p > 0.05$; $n = 3$).

T) Correlation analysis of GS and TA neurons Cartesian coordinates in control and *afadin* $^{fl/fl}$ adult mice. Scale bar indicates correlation values.

edio-lateral axis (n = 3).

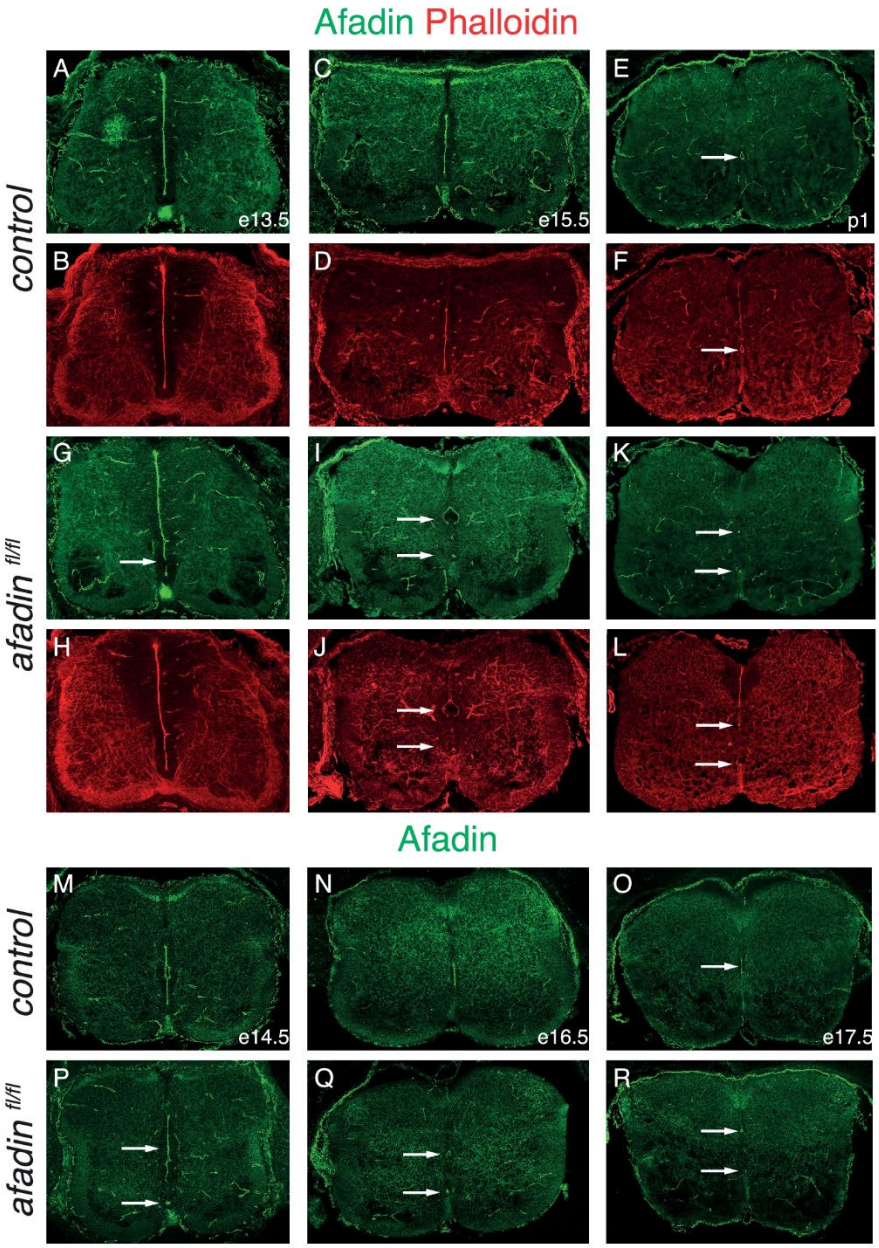
Afadin Phalloidin
control
afadin fl/fl
A
B
C
D
E
F
G
H
I
J
K
L
e13.5
e15.5
p1
Afadin
control
afadin fl/fl
M
N
O
P
Q
R
e14.5
e16.5
e17.5

Figure S2

Figure S2. Central canal development upon elimination of afadin in motor neuron progenitors (related to Figure 3).

A - F) Transverse sections of e13.5 (A, B), e15.5 (C, D) and p1 (E, F) control spinal cords showing afadin (A, C, and E) and phalloidin (B, D and F) expression.

G - L) Transverse sections of e13.5 (G, H), e15.5 (I, J) and p1 (K, L) afadin$^{fl/fl}$ spinal cords showing afadin (G, I and K) and phalloidin (H, J and L) expression.

M - O) Transverse sections of e14.5 (M), e16.5 (N) and e17.5 (O) control spinal cords showing afadin expression. Arrow points to the developing central canal.

P - R) Transverse sections of e14.5 (P), e16.5 (Q) and e17.5 (R) *afadin*$^{fl/fl}$ spinal cords showing afadin expression. Arrows point to the developing central canals.

lateral axis (n = 3).

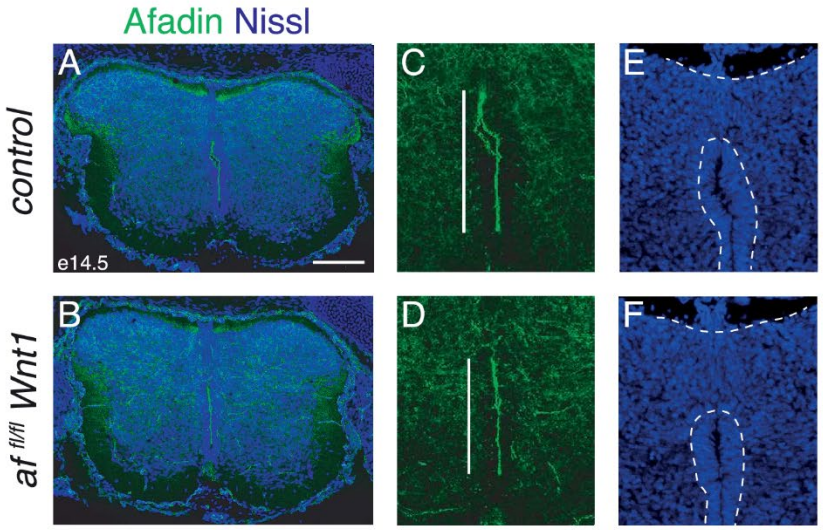

Figure S3

Figure S3. Afadin has a general role in regulating the organization of the midline (related to Figure 4).

A and B) Transverse sections of e14.5 control (A) and *af*$^{fl/fl}$ *Wnt1* (B) spinal cords. Scale bar represents 100 μm.

C and D) Afadin expression in the developing central canal area of the images in A (C) and B (D). Bars represent extent of afadin expression.

E and F) Nissl staining in the dorsal midline area of the images in A (E) and B (F). Dashed lines delineate the neuroepithelium and the border between the ventral grey and white matter.

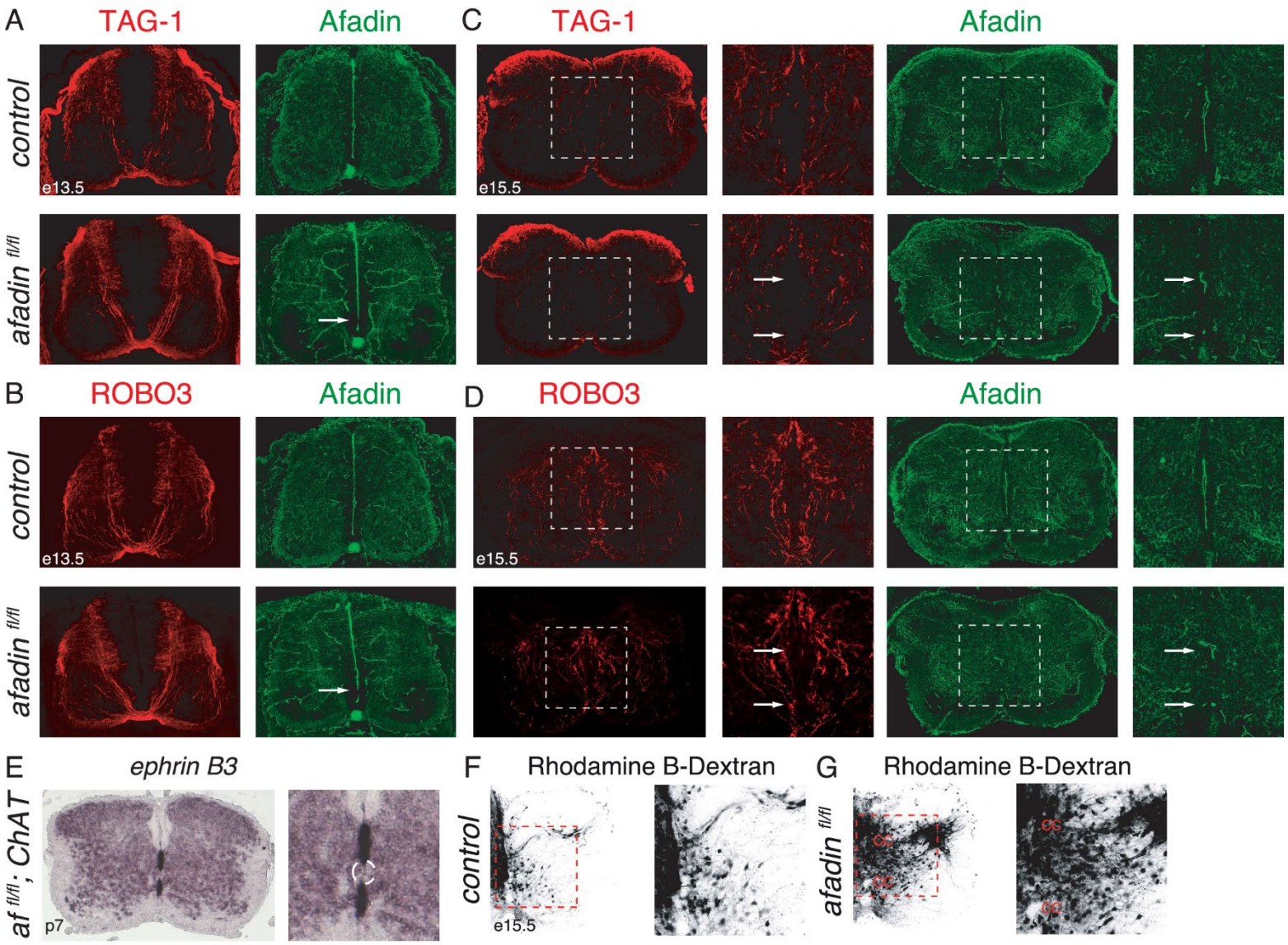
A
TAG-1
Afadin
C
TAG-1
Afadin
control
afadin fl/fl
e13.5
e15.5
B
ROBO3
Afadin
D
ROBO3
Afadin
control
afadin fl/fl
e13.5
e15.5
E
ephrin B3
af fl/fl; ChAT
p7
F
Rhodamine B-Dextran
control
e15.5
G
Rhodamine B-Dextran
afadin fl/fl
cc
cc
cc
cc

Figure S4

Figure S4. Analysis of commissural axon organization in afadin $^{fl/fl}$ mice (related to Figure 5).

A) Transverse sections of e13.5 control and *afadin* $^{fl/fl}$ spinal cords showing TAG-1 (left) and afadin (right) expression. Arrow points to the pMN.

B) Transverse sections of e13.5 control and *afadin* $^{fl/fl}$ spinal cords showing ROBO3 (left) and afadin (right) expression. Arrow points to the pMN.

C) Transverse sections of e15.5 control and *afadin* $^{fl/fl}$ spinal cords and higher magnification of the central canal area showing TAG-1 (left) and afadin (right) expression. Arrows point to the central canals.

D) Transverse sections of e15.5 control and *afadin* $^{fl/fl}$ spinal cords and higher magnification of the central canal area showing ROBO3 (left) and afadin (right) expression. Arrows point to the central canals.

E) Left panel: Ephrin B3 mRNA expression in a p7 *af* $^{fl/fl}$ *ChAT* spinal cord. Right panel: Magnification of the central canal area. Central canal is delineated by a dashed line.

F) Transverse section of an e15.5 control hemicord (left) and higher magnification of central canal area (right) showing tracing of spinal interneurons by rhodamine dextran.

G) Transverse section of an e15.5 *afadin* $^{fl/fl}$ hemicord (left) and higher magnification of central canal area (right) showing tracing of spinal interneurons by rhodamine dextran.

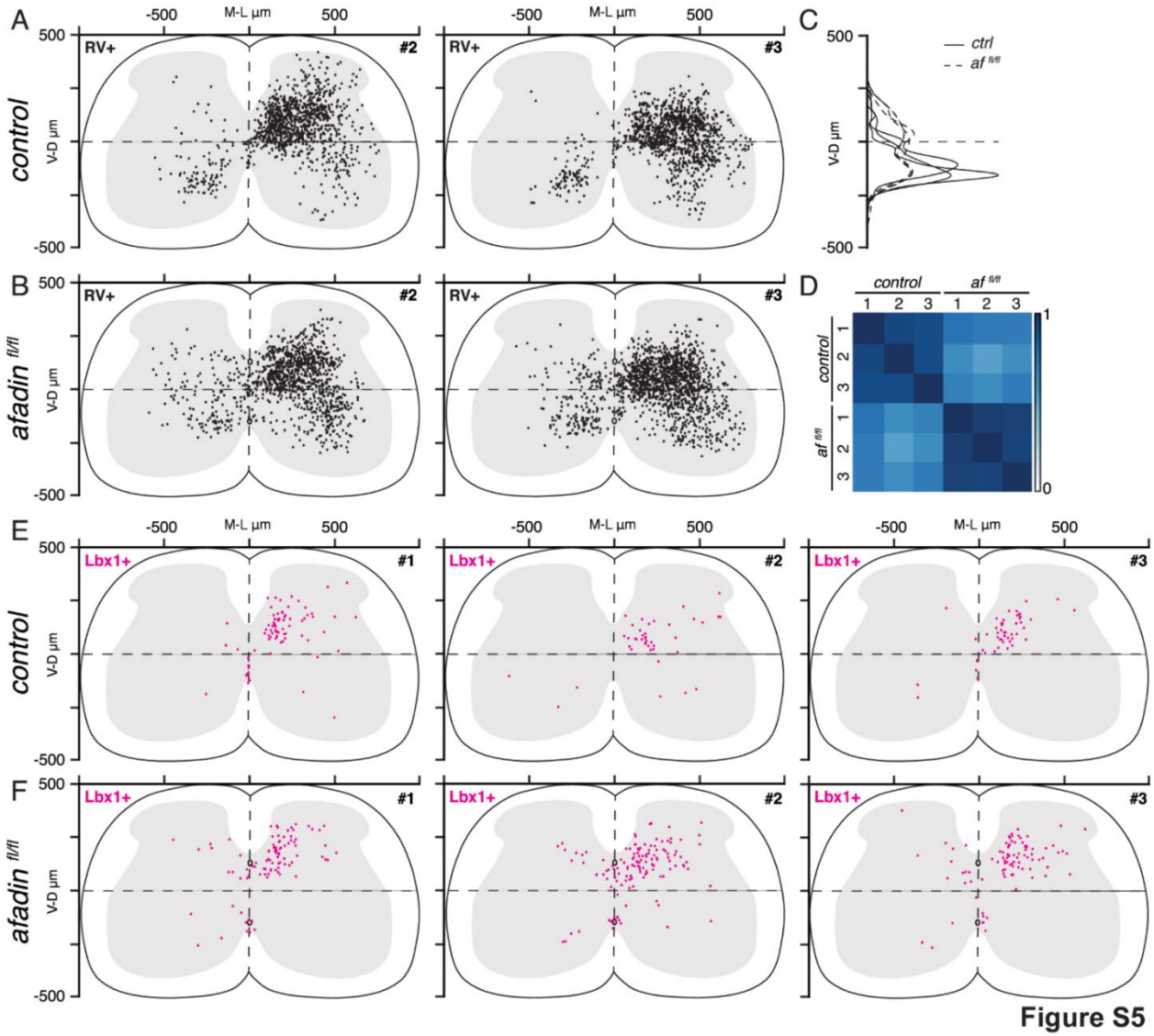

Figure S5. Premotor connectivity maps in control and afadin $^{fl/fl}$ mice (related to Figure 6).

A and B) Digital reconstruction of premotor interneurons positions in two control (A) and *afadin* $^{fl/fl}$ (B) mice.

C) Dorso-ventral density analysis of contralateral rabies-labeled premotor interneurons in control and *afadin* $^{fl/fl}$ mice (n = 3; each trace represents one animal).

D) Correlation analysis of rabies-labeled premotor interneuron cartesian coordinates in control and *afadin* $^{fl/fl}$ mice. The scale indicates correlation values.

E and F) Digital reconstruction of rabies^{+}/Lbx1^{+} premotor interneuron positions in three control (E) and *afadin* $^{fl/fl}$ (F) mice.

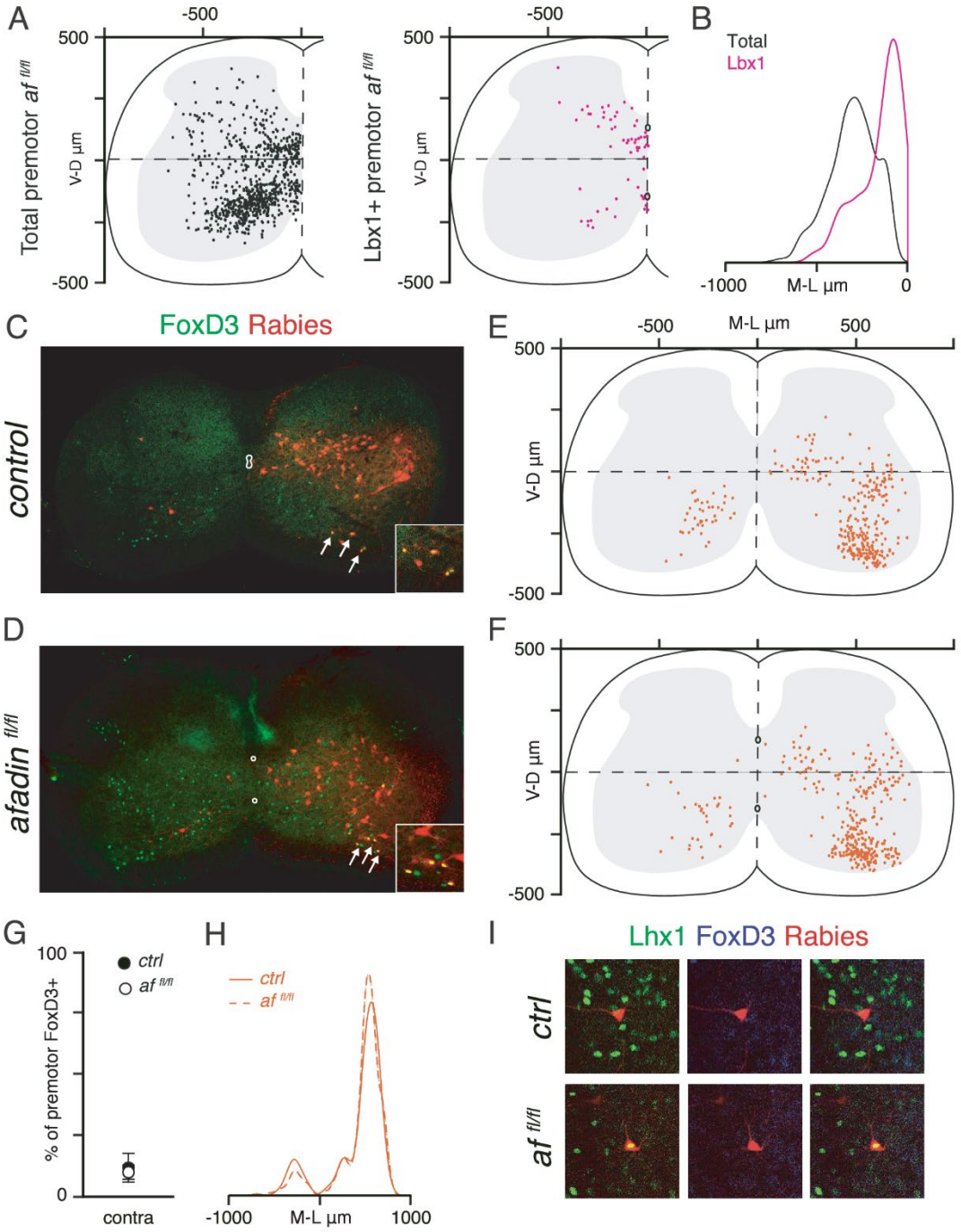
A
-500
500
V-D µm
-500
Total premotor af fl/fl
Lbx1+ premotor af fl/fl
B
Total
Lbx1
-1000
M-L µm
0
C
FoxD3 Rabies
control
D
afadin fl/fl
E
-500
M-L µm
500
F
G
100
% of premotor FoxD3+
ctrl
af fl/fl
0
contra
H
-1000
1000
I
Lhx1 FoxD3 Rabies
ctrl
af fl/fl

Figure S6

Figure S6. FoxD3^{+} premotor interneuron connectivity is unaffected in afadin$^{fl/fl}$ mice (related to Figure 7).

A) Left panel: Digital reconstruction of total contralateral premotor interneurons mice (n = 3). Right panel: Digital reconstruction of rabies^{+}/Lbx1^{+} subset in *afadin*$^{fl/fl}$ mice (n = 3).

B) Medio-lateral density analysis in the contralateral side of total (black) and rabies^{+}/Lbx1^{+} (magenta) premotor interneurons in *afadin*$^{fl/fl}$ mice (n = 3 for each).

C and D) Ipsilateral transverse sections of a control (C) and an *afadin*$^{fl/fl}$ (D) spinal cord showing rabies-labeled premotor interneurons and FoxD3 expression. Arrows are pointing at double positive cells magnified in the insets.

E and F) Digital reconstruction of rabies^{+}/FoxD3^{+} premotor interneuron positions in control (E) and *afadin*$^{fl/fl}$ (F) mice (n = 3).

G) Percentage of contralateral rabies^{+}/FoxD3^{+} premotor interneurons (mean ± SEM; t-test, $p > 0.05$; n = 3).

H) Medio-lateral density analysis of rabies^{+}/FoxD3^{+} premotor interneurons in control and *afadin*$^{fl/fl}$ mice (n = 3).

I) Representative images of a premotor interneuron in the dorsal contralateral quadrant of a control and an *afadin*$^{fl/fl}$ spinal cord stained for Lhx1 and FoxD3.

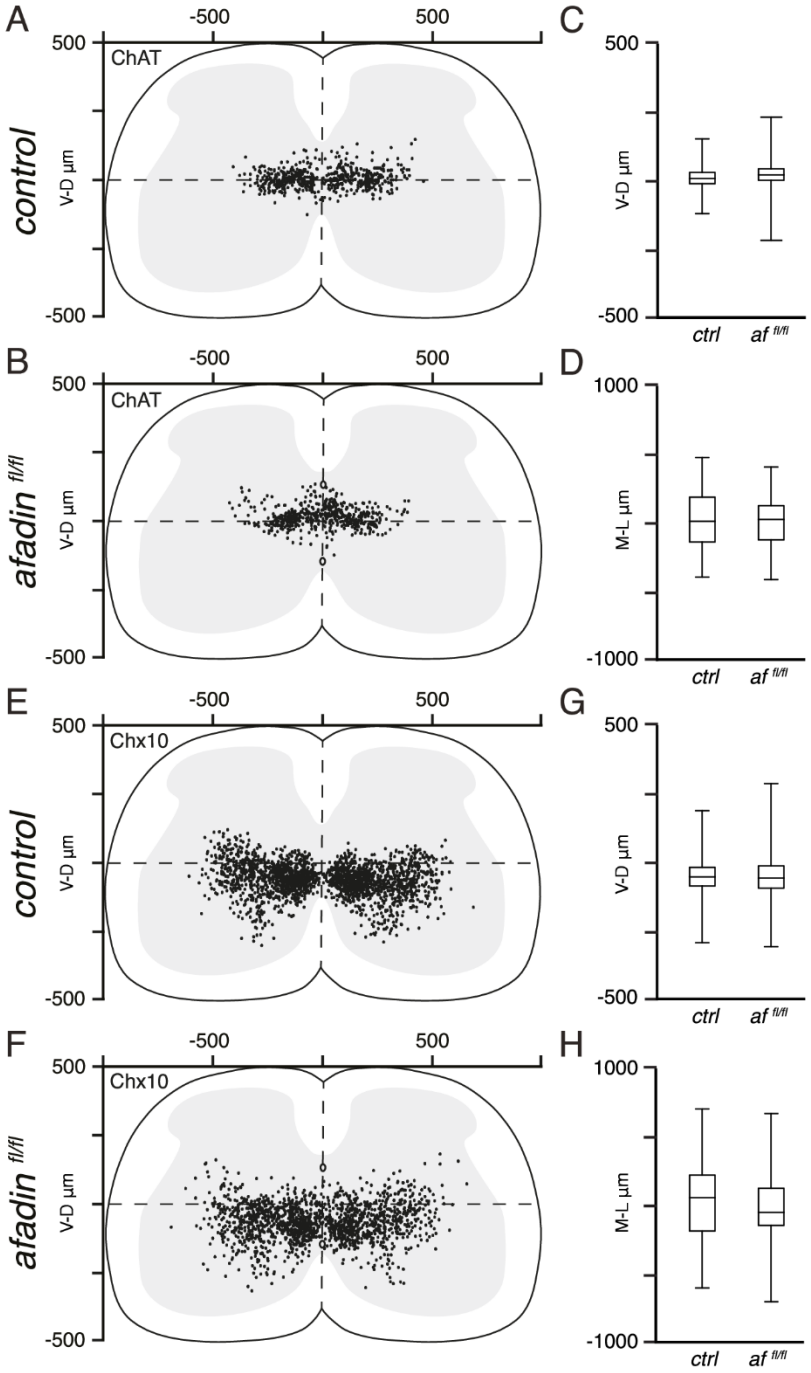
A
B
C
D
E
F
G
H
ChAT
Chx10
control
afadin fl/fl
V-D µm
M-L µm
-500
500
1000
-1000
ctrl
af fl/fl

Figure S7

Figure S7. Positional organization of interneuron subtypes is not perturbed in afadin $^{fl/fl}$ mice (related to Figure 7).

A and B) Digital reconstruction of ChAT^{+} interneuron positions in control (A) and *afadin* $^{fl/fl}$ (B) mice (n = 3).

C) Boxplots showing distribution of ChAT^{+} interneurons in control and *afadin* $^{fl/fl}$ mice along the dorso-ventral axis (n = 3).

D) Boxplots showing distribution of ChAT^{+} interneurons in control and *afadin* $^{fl/fl}$ mice along the medio-lateral axis (n = 3).

E and F) Digital reconstruction of Chx10^{+} interneuron positions in control (E) and *afadin* $^{fl/fl}$ (F) mice (n = 3).

G) Boxplots showing distribution of Chx10^{+} interneurons in control and *afadin* $^{fl/fl}$ mice along the dorso-ventral axis (n = 3).

H) Boxplots showing distribution of Chx10^{+} interneurons in control and *afadin* $^{fl/fl}$ mice along the medio-lateral axis (n = 3).

Supplemental Table 1. Related to Figure 6 and 7.

Number of neurons labeled in each rabies experiment performed (The ChAT^{+} datasets have also been used for total premotor neuron analysis in Figures 6A-J and S5A-D).

Animal	Experiment	Total	Ipsi	Contra
Control #1	ChAT	1128	1017	111
Control #2		1179	1075	104
Control #3		968	913	55
afadin$^{fl/fl}$ #1		1101	924	177
afadin$^{fl/fl}$ #2		1585	1344	241
afadin$^{fl/fl}$ #3		1478	1269	209
Control #1	Lbx1	846	753	93
Control #2		743	704	39
Control #3		677	624	53
afadin$^{fl/fl}$ #1		1070	984	86
afadin$^{fl/fl}$ #2		1730	1566	164
afadin$^{fl/fl}$ #3		1569	1398	171
Control #1	Lhx1/FoxD3	1933	1691	242
Control #2		1175	1053	122
Control #3		667	635	32
afadin$^{fl/fl}$ #1		854	789	65
afadin$^{fl/fl}$ #2		1677	1436	241
afadin$^{fl/fl}$ #3		1875	1582	293
Control #1	Chx10	1740	1599	141
Control #2		2504	2308	196

Control #3		1160	1102	58
Control #4		1635	1464	171
afadin $^{fl/fl}$ #1		1782	1552	230
afadin $^{fl/fl}$ #2		2066	1811	255
afadin $^{fl/fl}$ #3		2190	1940	250
afadin $^{fl/fl}$ #4		1791	511	280

ANNEX 3: French Summary

Nous respirons en permanence de la naissance à la mort de façon rythmique, automatique, sans effort et le plus souvent inconsciemment. La commande respiratoire est donc robuste. Elle est aussi labile car avec les ajustements cardio-vasculaires, elle est au centre de l'homéostasie énergétique. Ainsi l'activité respiratoire doit s'adapter aux changements de l'environnement (par ex. altitude) ou aux actions menées dans celui-ci (par ex. effort physique) pour assurer les apports, et l'élimination des déchets, métaboliques induits dans tous les tissus de l'organisme. J'ai étudié dans mon travail de thèse de neurobiologie, l'adaptation respiratoire à l'exercice en considérant le comportement locomoteur (la course). La caractéristique ou signature obligatoire de l'adaptation respiratoire à l'exercice est l'augmentation immédiate et drastique de la ventilation - ou hyperpnée - qui se produit dès le début de l'effort. Deux autres signatures présumées mais controversées considèrent d'une part que l'hyperpnée pourrait être proportionnelle à la vitesse de déplacement des membres et d'autre part que les respirations pourraient être temporellement synchronisées aux phases d'activité des membres de manière générale chez les vertébrés. Une partie des incertitudes provient de la grande variété des espèces étudiées dont les variations allométriques (liées à leur poids), les variations adaptatives des stratégies locomotrices (nage, marche, vol) ainsi que les déterminismes prédateur/proie qui occultent sans doute la manifestation de régularités qui pourraient faire loi. Le but de la neurophysiologie est de comprendre comment des séquences d'activité neurales codent les comportements et dans notre cas aussi les conditions métaboliques de leur réalisation. Il s'agit donc de caractériser les neurones impliqués, leurs cibles (la connectivité du réseau) et par des interférences fonctionnelles couplées à des mesures quantitatives des comportements respiratoire et locomoteur d'en préciser les mécanismes. Pour aborder ces questions, nous avons choisi le modèle expérimental de la souris qui donne accès à un large éventail d'outils génétiques et moléculaires de pointe pour manipuler les cellules et les circuits de manière spécifique et étudier leur impact fonctionnel. De plus, les bases neurales des circuits respiratoire et locomoteur longtemps étudiés pour leur propre compte sont parmi les mieux documentés.

Dans ma première étude (**Papier 1**), nous avons mené une analyse au niveau comportemental dans le but de clarifier les aspects temporels de l'adaptation des commandes neurales respiratoire et locomotrice. Pour cela, nous avons développé une nouvelle méthode d'enregistrements électromyographiques (EMG) du diaphragme (muscle inspiratoire), pour la première fois chez la souris qui court, combinés au suivi vidéo de la dynamique des membres. Nous montrons que pour une gamme de vitesses de course au trot sur tapis roulant, lente à modérée, la fréquence respiratoire augmente immédiatement et de manière drastique. De manière surprenante, cette augmentation atteint une valeur fixe, indépendamment de la vitesse du trot ou de l'inclinaison du tapis (augmentation de la charge de l'effort). Néanmoins, lorsque les souris s'engagent dans des comportements de fuite plus rapides, comme le galop, la fréquence respiratoire augmente davantage. Ces résultats suggèrent que l'augmentation des fréquences respiratoires, dépend plus du contexte de l'effort locomoteur dans lequel la souris est engagée (exploration vs fuite) que de la vitesse de course donc de la cinétique des membres. Nous montrons aussi que les respirations ne sont jamais temporellement synchronisées avec les

foulées quelle que soit la vitesse, la charge de l'effort ou l'allure locomotrice (trot ou galop). Ceci démontre que la synchronisation temporelle entre respiration et mouvements des membres n'est pas une signature obligatoire de l'adaptation respiratoire, du moins chez la souris.

Dans l'ensemble, mes travaux indiquent que l'adaptation respiratoire requiert un signal déclencheur dès la mise en place de l'exercice, des signaux spécifiques dépendants de l'allure locomotrice pour en moduler la fréquence mais s'affranchit de signaux phasiques du cycle locomoteur provenant des retours sensoriels ou des oscillations internes viscérales qui imposeraient une synchronisation des deux commandes centrales.

Dans ma seconde étude (**Papier 2**), nous avons donc cherché à identifier, au sein des centres locomoteurs, les neurones déclencheurs de l'hyperpnée à l'exercice, ainsi que leurs cibles dans les centres respiratoires chez la souris. Dans un premier temps, nous avons abordé la possibilité que le centre principal d'initiation locomotrice – la région locomotrice mésencéphalique (MLR) – puisse moduler l'activité respiratoire en lien avec la course. En utilisant des outils viraux de traçage transsynaptique (qui atteste de la présence d'une connexion entre deux neurones), nous montrons que les neurones glutamatergiques (excitateurs) de la MLR contactent directement les neurones, notamment glutamatergiques, du générateur inspiratoire principal – le complexe préBötzinger (préBötC). Nous utilisons également des outils optogénétiques *in vivo* et montrons que des stimulations courtes de la MLR imposent la survenue précipitée d'inspiration pendant la phase expiratoire et peuvent de ce fait augmenter la fréquence du rythme. De plus, la photostimulation prolongée de la MLR entraîne une augmentation de la fréquence respiratoire, en l'absence, et avant même le début de tout mouvement locomoteur. De manière intéressante, la fréquence respiratoire augmente encore davantage lorsque la course est activée par la photostimulation de la MLR. Par conséquent, dans un deuxième temps, nous avons étudié la possibilité que les circuits exécutifs locomoteurs de la moelle épinière ventrale, – le générateur central de rythme et de pattern locomoteur (CPG locomoteur) – puissent réguler à la hausse la respiration pendant la course. Pour cela, nous avons utilisé des préparations réduites *ex vivo* de tronc cérébral attaché à la moelle épinière de souris nouveau-nées, combinées à des enregistrements électrophysiologiques de racines nerveuses ventrales locomotrices et inspiratoires. Nous montrons que l'activation pharmacologique *ex vivo* du CPG locomoteur déclenche une augmentation des fréquences inspiratoires. De plus, nos expériences de traçage ont révélé que les neurones du CPG locomoteur contactent ceux d'une autre population respiratoire essentielle, le groupe respiratoire parafacial (pF). L'élimination sélective d'une partie des neurones du pF définis de manière génétique stricte (neurones *Phox2b*/*Atoh1,* RTN$^{Phox2b/Atoh1}$) dans les préparations réduites *ex vivo* abolit l'augmentation des fréquences inspiratoires déclenchée par activation pharmacologique du CPG locomoteur. Une démonstration similaire a pu être faite *in vivo* par des moyens complémentaires de chémogénétique (mise sous silence des neurones RTN$^{Phox2b/Atoh1}$ pendant la course).

Finalement, nos travaux démontrent la nature multifonctionnelle des circuits locomoteurs, qui envoient des signaux activateurs distincts aux centres respiratoires : **1**) un circuit descendant de la MLR au preBötC permettrait une augmentation respiratoire en prévision de la course et **2**) un circuit ascendant du CPG locomoteur vers le RTN$^{Phox2b/Atoh1}$ qui régulerait à la hausse les fréquences respiratoires une fois la course enclenchée.

REFERENCES

Abbott, S.B., Stornetta, R.L., Fortuna, M.G., Depuy, S.D., West, G.H., Harris, T.E., Guyenet, P.G. (2009). *Photostimulation of retrotrapezoid nucleus phox2b-expressing neurons in vivo produces long-lasting activation of breathing in rats*. J Neurosci 29, 5806-5819.

Abdala, A.P., Rybak, I.A., Smith, J.C., Paton, J.F. (2009). *Abdominal expiratory activity in the rat brainstem-spinal cord in situ: patterns, origins and implications for respiratory rhythm generation*. The Journal of physiology 587, 3539-3559.

Abraham, K.A., Feingold, H., Fuller, D.D., Jenkins, M., Mateika, J.H., Fregosi, R.F. (2002). *Respiratory-related activation of human abdominal muscles during exercise*. The Journal of physiology 541, 653-663.

Ainsworth, D.M., Smith, C.A., Eicker, S.W., Henderson, K.S., Dempsey, J.A. (1989). *The effects of locomotion on respiratory muscle activity in the awake dog*. Respir Physiol 78, 145-162.

Akay, T., Tourtellotte, W.G., Arber, S., Jessell, T.M. (2014). *Degradation of mouse locomotor pattern in the absence of proprioceptive sensory feedback*. Proc Natl Acad Sci U S A 111, 16877-16882.

Alexander, R.M. (1989). *On the synchronization of breathing with running in wallabies (Macropus spp.) and horses (Equus caballus)*. Journal of Zoology 218, 69-85.

Alheid, G.F., McCrimmon, D.R. (2008). *The chemical neuroanatomy of breathing*. Respir Physiol Neurobiol 164, 3-11.

Aliverti, A. (2016). *The respiratory muscles during exercise*. Breathe 12, 165-168.

Alsahafi, Z., Dickson, C.T., Pagliardini, S. (2015). *Optogenetic excitation of preBötzinger complex neurons potently drives inspiratory activity in vivo*. The Journal of physiology 593, 3673-3692.

Amiel, J., Laudier, B., Attié-Bitach, T., Trang, H., de Pontual, L., Gener, B., Trochet, D., Etchevers, H., Ray, P., Simonneau, M., Vekemans, M., Munnich, A., Gaultier, C., Lyonnet, S. (2003). *Polyalanine expansion and frameshift mutations of the paired-like homeobox gene PHOX2B in congenital central hypoventilation syndrome*. Nature genetics 33, 459-461.

Avila, J.J., Kim, S.K., Massett, M.P. (2017). *Differences in Exercise Capacity and Responses to Training in 24 Inbred Mouse Strains*. Frontiers in physiology 8, 974.

Azim, E., Jiang, J., Alstermark, B., Jessell, T.M. (2014). *Skilled reaching relies on a V2a propriospinal internal copy circuit*. Nature 508, 357-363.

Baertsch, N.A., Baertsch, H.C., Ramirez, J.M. (2018). *The interdependence of excitation and inhibition for the control of dynamic breathing rhythms*. Nat Commun 9, 843.

Bannister, R.G., Cunningham, D.J., Douglas, C.G. (1954). *The carbon dioxide stimulus to breathing in severe exercise*. The Journal of physiology 125, 90-117.

Banzett, R.B., Mead, J., Reid, M.B., Topulos, G.P. (1992). *Locomotion in men has no appreciable mechanical effect on breathing*. J Appl Physiol (1985) 72, 1922-1926.

Barik, A., Thompson, J.H., Seltzer, M., Ghitani, N., Chesler, A.T. (2018). *A Brainstem-Spinal Circuit Controlling Nocifensive Behavior*. Neuron 100, 1491-1503.e1493.

Barna, B.F., Takakura, A.C., Moreira, T.S. (2014). *Acute exercise-induced activation of Phox2b-expressing neurons of the retrotrapezoid nucleus in rats may involve the hypothalamus*. Neuroscience 258, 355-363.

Basting, T.M., Burke, P.G., Kanbar, R., Viar, K.E., Stornetta, D.S., Stornetta, R.L., Guyenet, P.G. (2015). *Hypoxia silences retrotrapezoid nucleus respiratory chemoreceptors via alkalosis*. J Neurosci 35, 527-543.

Bechbache, R.R., Duffin, J. (1977). *The entrainment of breathing frequency by exercise rhythm*. The Journal of physiology 272, 553-561.

Bell, H.J., Duffin, J. (2006). *Rapid increases in ventilation accompany the transition from passive to active movement*. Respir Physiol Neurobiol 152, 128-142.

Bellardita, C., Kiehn, O. (2015). *Phenotypic characterization of speed-associated gait changes in mice reveals modular organization of locomotor networks*. Curr Biol 25, 1426-1436.

Bernasconi, P., Kohl, J. (1993). *Analysis of co-ordination between breathing and exercise rhythms in man*. The Journal of physiology 471, 693-706.

Berry, M.J., Bacharach, D.W., Moritani, T. (1985). *Stride frequency and ventilation at constant carbon dioxide output*. British journal of sports medicine 19, 210-213.

Bertrand, F., Hugelin, A., Vibert, J.F. (1973). *Quantitative study of anatomical distribution of respiration related neurons in the pons*. Experimental Brain Research 16, 383-399.

Bevan, A.T., Honour, A.J., Stott, F.H. (1969). *Direct arterial pressure recording in unrestricted man*. British heart journal 31, 387-388.

Bianchi, A.L., Denavit-Saubié, M., Champagnat, J. (1995). *Central control of breathing in mammals: neuronal circuitry, membrane properties, and neurotransmitters*. Physiol Rev 75, 1-45.

Bisgard, G.E., Forster, H.V., Mesina, J., Sarazin, R.G. (1982). *Role of the carotid body in hyperpnea of moderate exercise in goats*. J Appl Physiol Respir Environ Exerc Physiol 52, 1216-1222.

Boggs, D.F. (2002). *Interactions between locomotion and ventilation in tetrapods*. Comp Biochem Physiol A Mol Integr Physiol 133, 269-288.

Boscan, P., Pickering, A.E., Paton, J.F. (2002). *The nucleus of the solitary tract: an integrating station for nociceptive and cardiorespiratory afferents*. Experimental physiology 87, 259-266.

Bouvier, J., Thoby-Brisson, M., Renier, N., Dubreuil, V., Ericson, J., Champagnat, J., Pierani, A., Chedotal, A., Fortin, G. (2010). *Hindbrain interneurons and axon guidance signaling critical for breathing*. Nature neuroscience 13, 1066-1074.

Bouvier, J., Caggiano, V., Leiras, R., Caldeira, V., Bellardita, C., Balueva, K., Fuchs, A., Kiehn, O. (2015). *Descending Command Neurons in the Brainstem that Halt Locomotion*. Cell 163, 1191-1203.

Bramble, D.M., Carrier, D.R. (1983). *Running and breathing in mammals*. Science 219, 251-256.

Bramble, D.M., Jenkins, F.A., Jr. (1993). *Mammalian locomotor-respiratory integration: implications for diaphragmatic and pulmonary design*. Science 262, 235-240.

Branchereau, P., Morin, D., Bonnot, A., Ballion, B., Chapron, J., Viala, D. (2000). *Development of lumbar rhythmic networks: from embryonic to neonate locomotor-like patterns in the mouse*. Brain Res Bull 53, 711-718.

Brocard, F., Dubuc, R. (2003). *Differential Contribution of Reticulospinal Cells to the Control of Locomotion Induced By the Mesencephalic Locomotor Region*. Journal of Neurophysiology 90, 1714-1727.

Brownstone, R.M., Chopek, J.W. (2018). *Reticulospinal Systems for Tuning Motor Commands*. Frontiers in neural circuits 12.

Buchanan, J.T., Einum, J.F. (2008). *The spinobulbar system in lamprey*. Brain research reviews 57, 37-45.

Buono, M.J., Burnsed-Torres, M., Hess, B., Lopez, K., Ortiz, C., Girodo, A., Lolli, K., Bloom, B., Bailey, D., Kolkhorst, F.W. (2015). *Alterations in the rate of limb movement using a lower body positive pressure treadmill do not influence respiratory rate or phase III ventilation*. BioMed research international 2015, 618291.

Burke, P.G., Abbott, S.B., McMullan, S., Goodchild, A.K., Pilowsky, P.M. (2010). *Somatostatin selectively ablates post-inspiratory activity after injection into the Bötzinger complex*. Neuroscience 167, 528-539.

Butler, P.J., Woakes, A.J. (1980). *Heart Rate, Respiratory Frequency and Wing Beat Frequency of Free Flying Barnacle Geese <em>Branta Leucopsis</em&gt*. The Journal of experimental biology 85, 213.

Caggiano, V., Leiras, R., Goni-Erro, H., Masini, D., Bellardita, C., Bouvier, J., Caldeira, V., Fisone, G., Kiehn, O. (2018). *Midbrain circuits that set locomotor speed and gait selection*. Nature 553, 455-460.

Caldeira, V., Dougherty, K.J., Borgius, L., Kiehn, O. (2017). *Spinal Hb9::Cre-derived excitatory interneurons contribute to rhythm generation in the mouse*. Scientific Reports 7, 41369.

Callaway, E.M., Luo, L. (2015). *Monosynaptic Circuit Tracing with Glycoprotein-Deleted Rabies Viruses*. J Neurosci 35, 8979-8985.

Cameron, D., Polgár, E., Gutierrez-Mecinas, M., Gomez-Lima, M., Watanabe, M., Todd, A.J. (2015). *The organisation of spinoparabrachial neurons in the mouse*. Pain 156, 2061-2071.

Capelli, P., Pivetta, C., Soledad Esposito, M., Arber, S. (2017). *Locomotor speed control circuits in the caudal brainstem*. Nature 551, 373-377.

Casey, K., Duffin, J., Kelsey, C.J., McAvoy, G.V. (1987). *The effect of treadmill speed on ventilation at the start of exercise in man*. The Journal of physiology 391, 13-24.

Cazalets, J.R., Borde, M., Clarac, F. (1995). *Localization and organization of the central pattern generator for hindlimb locomotion in newborn rat*. J Neurosci 15, 4943-4951.

Chédotal, A. (2019). *Roles of axon guidance molecules in neuronal wiring in the developing spinal cord*. Nat Rev Neurosci 20, 380-396.

Chiang, M.C., Bowen, A., Schier, L.A., Tupone, D., Uddin, O., Heinricher, M.M. (2019). *Parabrachial Complex: A Hub for Pain and Aversion*. The Journal of Neuroscience 39, 8225.

Clarac, F., Pearlstein, E., Pflieger, J.F., Vinay, L. (2004). *The in vitro neonatal rat spinal cord preparation: a new insight into mammalian locomotor mechanisms*. Journal of comparative physiology. A, Neuroethology, sensory, neural, and behavioral physiology 190, 343-357.

Connelly, C.A., Dobbins, E.G., Feldman, J.L. (1992). *Pre-Bötzinger complex in cats: respiratory neuronal discharge patterns*. Brain research 590, 337-340.

Conway, B.A., Hultborn, H., Kiehn, O. (1987). *Proprioceptive input resets central locomotor rhythm in the spinal cat*. Exp Brain Res 68, 643-656.

Cordero-Erausquin, M., Allard, S., Dolique, T., Bachand, K., Ribeiro-da-Silva, A., De Koninck, Y. (2009). *Dorsal horn neurons presynaptic to lamina I spinoparabrachial neurons revealed by transynaptic labeling*. J Comp Neurol 517, 601-615.

Cordero-Erausquin, M., Inquimbert, P., Schlichter, R., Hugel, S. (2016). *Neuronal networks and nociceptive processing in the dorsal horn of the spinal cord*. Neuroscience 338, 230-247.

Corio, M., Palisses, R., Viala, D. (1993). *Origin of the central entrainment of respiration by locomotion facilitated by MK 801 in the decerebrate rabbit*. Exp Brain Res 95, 84-90.

Crone, S.A., Quinlan, K.A., Zagoraiou, L., Droho, S., Restrepo, C.E., Lundfald, L., Endo, T., Setlak, J., Jessell, T.M., Kiehn, O., Sharma, K. (2008). *Genetic ablation of V2a ipsilateral interneurons disrupts left-right locomotor coordination in mammalian spinal cord*. Neuron 60, 70-83.

Crone, S.A., Zhong, G., Harris-Warrick, R., Sharma, K. (2009). *In mice lacking V2a interneurons, gait depends on speed of locomotion*. J Neurosci 29, 7098-7109.

Crone, S.A., Viemari, J.-C., Droho, S., Mrejeru, A., Ramirez, J.-M., Sharma, K. (2012). *Irregular Breathing in Mice following Genetic Ablation of V2a Neurons*. The Journal of Neuroscience 32, 7895-7906.

Cui, Y., Kam, K., Sherman, D., Janczewski, W.A., Zheng, Y., Feldman, J.L. (2016). *Defining preBötzinger Complex Rhythm- and Pattern-Generating Neural Microcircuits In Vivo*. Neuron 91, 602-614.

Dagg, A.I. (1973). *Gaits in mammals*. Mammal Review 3, 135-154.

Daley, M.A., Bramble, D.M., Carrier, D.R. (2013). *Impact loading and locomotor-respiratory coordination significantly influence breathing dynamics in running humans*. PloS one 8, e70752.

Darmohray, D.M., Jacobs, J.R., Marques, H.G., Carey, M.R. (2019). *Spatial and Temporal Locomotor Learning in Mouse Cerebellum*. Neuron 102, 217-231 e214.

Dautan, D., Kovács, A., Bayasgalan, T., Diaz-Acevedo, M.A., Pal, B., Mena-Segovia, J. (2020). *Modulation of motor behavior by the mesencephalic locomotor region*. bioRxiv, 2020.2006.2025.172296.

Davern, P.J. (2014). *A role for the lateral parabrachial nucleus in cardiovascular function and fluid homeostasis*. Frontiers in physiology 5.

de Britto, A.A., Moraes, D.J. (2017). *Non-chemosensitive parafacial neurons simultaneously regulate active expiration and airway patency under hypercapnia in rats*. The Journal of physiology 595, 2043-2064.

Decety, J., Jeannerod, M., Germain, M., Pastene, J. (1991). *Vegetative response during imagined movement is proportional to mental effort*. Behav Brain Res 42, 1-5.

Decety, J. (1993). *Analysis of actual and mental movement times in graphic tasks*. Acta Psychol (Amst) 82, 367-372.

Decety, J., Jeannerod, M., Durozard, D., Baverel, G. (1993). *Central activation of autonomic effectors during mental simulation of motor actions in man*. The Journal of physiology 461, 549-563.

Dejours, P., Raynaud, J., Flandrois, R. (1959). *Etude du controle de la ventilation par certain stimulus neurogeniques au cours de l'exercise musculaire chez l'homme.* C R Acad Sci 248, 1709–1712.

Del Negro, C.A., Morgado-Valle, C., Feldman, J.L. (2002). *Respiratory rhythm: an emergent network property?* Neuron 34, 821-830.

Del Negro, C.A., Morgado-Valle, C., Hayes, J.A., Mackay, D.D., Pace, R.W., Crowder, E.A., Feldman, J.L. (2005). *Sodium and Calcium Current-Mediated Pacemaker Neurons and Respiratory Rhythm Generation*. The Journal of Neuroscience 25, 446.

Del Negro, C.A., Funk, G.D., Feldman, J.L. (2018). *Breathing matters*. Nat Rev Neurosci 19, 351-367.

Dempsey, J.A. (2012). *New perspectives concerning feedback influences on cardiorespiratory control during rhythmic exercise and on exercise performance*. The Journal of physiology 590, 4129-4144.

DiMarco, A.F., Romaniuk, J.R., Von Euler, C., Yamamoto, Y. (1983). *Immediate changes in ventilation and respiratory pattern associated with onset and cessation of locomotion in the cat*. The Journal of physiology 343, 1-16.

Dougherty, K.J., Zagoraiou, L., Satoh, D., Rozani, I., Doobar, S., Arber, S., Jessell, T.M., Kiehn, O. (2013). *Locomotor rhythm generation linked to the output of spinal shox2 excitatory interneurons*. Neuron 80, 920-933.

Dubreuil, V., Ramanantsoa, N., Trochet, D., Vaubourg, V., Amiel, J., Gallego, J., Brunet, J.F., Goridis, C. (2008). *A human mutation in Phox2b causes lack of CO2 chemosensitivity, fatal central apnea, and specific loss of parafacial neurons*. Proc Natl Acad Sci U S A.

Dubreuil, V., Thoby-Brisson, M., Rallu, M., Persson, K., Pattyn, A., Birchmeier, C., Brunet, J.F., Fortin, G., Goridis, C. (2009). *Defective Respiratory Rhythmogenesis and Loss of Central Chemosensitivity in Phox2b Mutants Targeting Retrotrapezoid Nucleus Neurons*. J Neurosci 29, 14836-14846.

Dubuc, R., Grillner, S. (1989). *The role of spinal cord inputs in modulating the activity of reticulospinal neurons during fictive locomotion in the lamprey*. Brain research 483, 196-200.

Duffin, J., Bechbache, R.R. (1983). *The changes in ventilation and heart rate at the start of treadmill exercise*. Canadian journal of physiology and pharmacology 61, 120-126.

Duffin, J. (2014). *The fast exercise drive to breathe*. The Journal of physiology 592, 445-451.

Dutschmann, M., Herbert, H. (2006). *The Kölliker-Fuse nucleus gates the postinspiratory phase of the respiratory cycle to control inspiratory off-switch and upper airway resistance in rat*. European Journal of Neuroscience 24, 1071-1084.

Duysens, J., Clarac, F., Cruse, H. (2000). *Load-regulating mechanisms in gait and posture: comparative aspects*. Physiol Rev 80, 83-133.

El Manira, A., Pombal, M.A., Grillner, S. (1997). *Diencephalic projection to reticulospinal neurons involved in the initiation of locomotion in adult lampreys Lampetra fluviatilis*. J Comp Neurol 389, 603-616.

Eldridge, F.L., Millhorn, D.E., Waldrop, T.G. (1981). *Exercise hyperpnea and locomotion: parallel activation from the hypothalamus*. Science 211, 844-846.

Eldridge, F.L., Millhorn, D.E., Kiley, J.P., Waldrop, T.G. (1985). *Stimulation by central command of locomotion, respiration and circulation during exercise*. Respir Physiol 59, 313-337.

Eldridge, F.L. (1994). *Central integration of mechanisms in exercise hyperpnea*. Medicine and science in sports and exercise 26, 319-327.

Eldridge, F.L., Morin, D., Romaniuk, J.R., Yamashiro, S., Potts, J.T., Ichiyama, R.M., Bell, H., Phillipson, E.A., Killian, K.J., Jones, N.L., Nattie, E. (2006). *Supraspinal locomotor centers do/do not contribute significantly to the hyperpnea of dynamic exercise in humans*. J Appl Physiol (1985) 100, 1743-1747.

Entin, P.L., Robertshaw, D., Rawson, R.E. (1999). *Effect of locomotor respiratory coupling on respiratory evaporative heat loss in the sheep*. J Appl Physiol (1985) 87, 1887-1893.

Fedirchuk, B., Stecina, K., Kristensen, K.K., Zhang, M., Meehan, C.F., Bennett, D.J., Hultborn, H. (2013). *Rhythmic activity of feline dorsal and ventral spinocerebellar tract neurons during fictive motor actions*. J Neurophysiol 109, 375-388.

Feldman, J.L., Mitchell, G.S., Nattie, E.E. (2003). *Breathing: rhythmicity, plasticity, chemosensitivity*. Annual review of neuroscience 26, 239-266.

Feldman, J.L., Del Negro, C.A. (2006). *Looking for inspiration: new perspectives on respiratory rhythm*. Nat Rev Neurosci 7, 232-242.

Feldman, J.L., McCrimmon, D.R., Morrison, S.F., 2013. Chapter 35 - Neural Control of Respiratory and Cardiovascular Functions, in: Squire, L.R., Berg, D., Bloom, F.E., du Lac, S., Ghosh, A., Spitzer, N.C. (Eds.), Fundamental Neuroscience (Fourth Edition). San Diego: Academic Press, pp. 749-766.

Fernandes, A., Galbo, H., Kjaer, M., Mitchell, J.H., Secher, N.H., Thomas, S.N. (1990). *Cardiovascular and ventilatory responses to dynamic exercise during epidural anaesthesia in man*. The Journal of physiology 420, 281-293.

Ferreira-Pinto, M.J., Ruder, L., Capelli, P., Arber, S. (2018). *Connecting Circuits for Supraspinal Control of Locomotion*. Neuron 100, 361-374.

Flandrois, R., Lacour, J.R., Islas-Maroquin, J., Charlot, J. (1967). *Limbs mechanoreceptors inducing the reflex hyperpnea of exercise*. Respir Physiol 2, 335-343.

Flandrois, R., Lacour, J.R., Osman, H. (1971). *Control of breathing in the exercising dog*. Respir Physiol 13, 361-371.

Forster, H.V., Pan, L.G., Funahashi, A. (1986). *Temporal pattern of arterial CO2 partial pressure during exercise in humans*. J Appl Physiol 60, 653-660.

Forster, H.V., Haouzi, P., Dempsey, J.A. (2012). *Control of breathing during exercise*. Comprehensive Physiology 2, 743-777.

Fortuna, M.G., West, G.H., Stornetta, R.L., Guyenet, P.G. (2008). *Bötzinger Expiratory-Augmenting Neurons and the Parafacial Respiratory Group*. The Journal of Neuroscience 28, 2506.

Fortuna, M.G., Stornetta, R.L., West, G.H., Guyenet, P.G. (2009). *Activation of the retrotrapezoid nucleus by posterior hypothalamic stimulation*. The Journal of physiology 587, 5121-5138.

Fregosi, R.F., Dempsey, J.A. (1984). *Arterial blood acid-base regulation during exercise in rats*. J Appl Physiol Respir Environ Exerc Physiol 57, 396-402.

Frigon, A. (2017). *The neural control of interlimb coordination during mammalian locomotion*. J Neurophysiol 117, 2224-2241.

Funk, G.D., Smith, J.C., Feldman, J.L. (1993). *Generation and transmission of respiratory oscillations in medullary slices: role of excitatory amino acids*. J Neurophysiol 70, 1497-1515.

Gariepy, J.F., Missaghi, K., Dubuc, R. (2010). *The interactions between locomotion and respiration*. Progress in brain research 187, 173-188.

Gariepy, J.F., Missaghi, K., Chevallier, S., Chartre, S., Robert, M., Auclair, F., Lund, J.P., Dubuc, R. (2012). *Specific neural substrate linking respiration to locomotion*. Proc Natl Acad Sci U S A 109, E84-92.

Giraudin, A., Cabirol-Pol, M.J., Simmers, J., Morin, D. (2008). *Intercostal and abdominal respiratory motoneurons in the neonatal rat spinal cord: spatiotemporal organization and responses to limb afferent stimulation*. J Neurophysiol 99, 2626-2640.

Giraudin, A., Le Bon-Jego, M., Cabirol, M.J., Simmers, J., Morin, D. (2012). *Spinal and pontine relay pathways mediating respiratory rhythm entrainment by limb proprioceptive inputs in the neonatal rat*. J Neurosci 32, 11841-11853.

Goetz, L., Bhattacharjee, M., Ferraye, M.U., Fraix, V., Maineri, C., Nosko, D., Fenoy, A.J., Piallat, B., Torres, N., Krainik, A., Seigneuret, E., David, O., Parent, M., Parent, A., Pollak, P., Benabid, A.L., Debu, B., Chabardès, S. (2019). *Deep Brain Stimulation of the Pedunculopontine Nucleus Area in Parkinson Disease: MRI-Based Anatomoclinical Correlations and Optimal Target*. Neurosurgery 84, 506-518.

Goulding, M. (2009). *Circuits controlling vertebrate locomotion: Moving in a new direction*. Nature reviews. Neuroscience 10, 507-518.

Gravel, J., Brocard, F., Gariepy, J.F., Lund, J.P., Dubuc, R. (2007). *Modulation of respiratory activity by locomotion in lampreys*. Neuroscience 144, 1120-1132.

Gray, P.A., Rekling, J.C., Bocchiaro, C.M., Feldman, J.L. (1999). *Modulation of respiratory frequency by peptidergic input to rhythmogenic neurons in the preBötzinger complex*. Science 286, 1566-1568.

Gray, P.A., Janczewski, W.A., Mellen, N., McCrimmon, D.R., Feldman, J.L. (2001). *Normal breathing requires preBötzinger complex neurokinin-1 receptor-expressing neurons*. Nature neuroscience 4, 927-930.

Gray, P.A., Hayes, J.A., Ling, G.Y., Llona, I., Tupal, S., Picardo, M.C., Ross, S.E., Hirata, T., Corbin, J.G., Eugenín, J., Del Negro, C.A. (2010). *Developmental origin of preBötzinger complex respiratory neurons*. J Neurosci 30, 14883-14895.

Grillner, S., Georgopoulos, A., Jordan, L. (1997). Selection and initiation of motor behavior. **Journal**.

Grillner, S. (2003). *The motor infrastructure: from ion channels to neuronal networks*. Nature Reviews Neuroscience 4, 573-586.

Grillner, S., 2011. Control of Locomotion in Bipeds, Tetrapods, and Fish, Comprehensive Physiology, pp. 1179-1236.

Grillner, S., El Manira, A. (2020). *Current Principles of Motor Control, with Special Reference to Vertebrate Locomotion*. Physiol Rev 100, 271-320.

Guerrier, C., Hayes, J.A., Fortin, G., Holcman, D. (2015). *Robust network oscillations during mammalian respiratory rhythm generation driven by synaptic dynamics*. Proceedings of the National Academy of Sciences 112, 9728.

Gutting, S.M., Forster, H.V., Brice, A.G., Lowry, T.F., Pan, L.G., Murphy, C.L. (1988). *The pattern of respiratory muscle activity during exercise in normal and hilar nerve denervated ponies*. FASEB Journal 2, A1297.

Guyenet, P.G., Wang, H. (2001). *Pre-Bötzinger neurons with preinspiratory discharges "in vivo" express NK1 receptors in the rat*. J Neurophysiol 86, 438-446.

Guyenet, P.G., Mulkey, D.K., Stornetta, R.L., Bayliss, D.A. (2005). *Regulation of ventral surface chemoreceptors by the central respiratory pattern generator*. J Neurosci 25, 8938-8947.

Guyenet, P.G., Stornetta, R.L., Bayliss, D.A. (2008). *Retrotrapezoid nucleus and central chemoreception*. The Journal of physiology 586, 2043-2048.

Guyenet, P.G., Mulkey, D.K. (2010). *Retrotrapezoid nucleus and parafacial respiratory group*. Respiratory physiology & neurobiology 173, 244-255.

Guyenet, P.G., Bayliss, D.A. (2015). *Neural Control of Breathing and CO2 Homeostasis*. Neuron 87, 946-961.

Guyenet, P.G., Bayliss, D.A., Stornetta, R.L., Ludwig, M.G., Kumar, N.N., Shi, Y., Burke, P.G., Kanbar, R., Basting, T.M., Holloway, B.B., Wenker, I.C. (2016). *Proton detection and breathing regulation by the retrotrapezoid nucleus*. The Journal of physiology.

Hagglund, M., Borgius, L., Dougherty, K.J., Kiehn, O. (2010). *Activation of groups of excitatory neurons in the mammalian spinal cord or hindbrain evokes locomotion*. Nature neuroscience 13, 246-253.

Hagglund, M., Dougherty, K.J., Borgius, L., Itohara, S., Iwasato, T., Kiehn, O. (2013). *Optogenetic dissection reveals multiple rhythmogenic modules underlying locomotion*. Proc Natl Acad Sci U S A.

Haldane, J.S., Priestley, J.G. (1905). *The regulation of the lung-ventilation*. The Journal of physiology 32, 225-266.

Haouzi, P., Chenuel, B., Chalon, B. (2004). *The control of ventilation is dissociated from locomotion during walking in sheep*. The Journal of physiology 559, 315-325.

Haouzi, P. (2006). *Point:Counterpoint authors respond to commentaries on "Supraspinal locomotor centers do/do not contribute significantly to the hyperpnea of dynamic exercise in humans"*. J Appl Physiol (1985) 101, 371.

Hastings, A.B., White, F.C., Sanders, T.M., Bloor, C.M. (1982). *Comparative physiological responses to exercise stress*. J Appl Physiol Respir Environ Exerc Physiol 52, 1077-1083.

Helleringer, R., Le Verger, D., Li, X., Izabelle, C., Chaussenot, R., Belmaati-Cherkaoui, M., Dammak, R., Decottignies, P., Daniel, H., Galante, M., Vaillend, C. (2018). *Cerebellar synapse properties and cerebellum-dependent motor and non-motor performance in Dp71-null mice*. Disease Models & Mechanisms 11, dmm033258.

Herbert, H., Moga, M.M., Saper, C.B. (1990). *Connections of the parabrachial nucleus with the nucleus of the solitary tract and the medullary reticular formation in the rat*. J Comp Neurol 293, 540-580.

Hérent, C., Diem, S., Fortin, G., Bouvier, J. (2020). *Absent phasing of respiratory and locomotor rhythms in running mice*. eLife 9, e61919.

Hernandez-Miranda, L.R., Ruffault, P.L., Bouvier, J.C., Murray, A.J., Morin-Surun, M.P., Zampieri, N., Cholewa-Waclaw, J.B., Ey, E., Brunet, J.F., Champagnat, J., Fortin, G., Birchmeier, C. (2017). *Genetic identification of a hindbrain nucleus essential for innate vocalization*. Proc Natl Acad Sci U S A 114, 8095-8100.

Heymans, J., Heymans, C. (1927). *Sur les modifications directes et sur la régulation réflexe de l'activité du centre respiratoire de la tête isolée du chien*. Arch Int Pharmacodyn Ther 33, 273-372.

Hoffmann, C.P., Torregrosa, G., Bardy, B.G. (2012). *Sound stabilizes locomotor-respiratory coupling and reduces energy cost*. PloS one 7, e45206.

Honda, Y. (1985). *Role of carotid chemoreceptors in control of breathing at rest and in exercise: studies on human subjects with bilateral carotid body resection*. Jpn J Physiol 35, 535-544.

Howard, P., Bromberger-Barnea, B., Fitzgerald, R.S., Bane, H.N. (1969). *Ventilatory responses to peripheral nerve stimulation at different times in the respiratory cycle*. Respir Physiol 7, 389-398.

Huckstepp, R.T., Cardoza, K.P., Henderson, L.E., Feldman, J.L. (2015). *Role of parafacial nuclei in control of breathing in adult rats*. J Neurosci 35, 1052-1067.

Hughes, J., Jacobs, N. (1979). *Normal human locomotion*. Prosthetics and orthotics international 3, 4-12.

Iscoe, S., Polosa, C. (1976). *Synchronization of respiratory frequency by somatic afferent stimulation*. J Appl Physiol 40, 138-148.

Iscoe, S. (1981). *Respiratory and stepping frequencies in conscious exercising cats*. J Appl Physiol Respir Environ Exerc Physiol 51, 835-839.

Iscoe, S. (1998). *Control of abdominal muscles*. Progress in neurobiology 56, 433-506.

Ismail, H., Radwan, I., Suominen, H., Goecke, R. (2019). Gait Estimation and Analysis from Noisy Observations. **Journal** 2019, 2707-2712.

Jahn, K., Deutschländer, A., Stephan, T., Kalla, R., Wiesmann, M., Strupp, M., Brandt, T. (2008). *Imaging human supraspinal locomotor centers in brainstem and cerebellum*. NeuroImage 39, 786-792.

Janczewski, W.A., Onimaru, H., Homma, I., Feldman, J.L. (2002). *Opioid-resistant respiratory pathway from the preinspiratory neurones to abdominal muscles: in vivo and in vitro study in the newborn rat*. The Journal of physiology 545, 1017-1026.

Janczewski, W.A., Feldman, J.L. (2006). *Distinct rhythm generators for inspiration and expiration in the juvenile rat*. The Journal of physiology 570, 407-420.

Janczewski, W.A., Tashima, A., Hsu, P., Cui, Y., Feldman, J.L. (2013). *Role of inhibition in respiratory pattern generation*. J Neurosci 33, 5454-5465.

Jenkin, S.E.M., Milsom, W.K., 2014. Chapter 8 - Expiration: Breathing's other face, in: Holstege, G., Beers, C.M., Subramanian, H.H. (Eds.), Progress in brain research: Elsevier, pp. 131-147.

Jeyaranjan, R., Goode, R., Beamish, S., Duffin, J. (1987). *The contribution of peripheral chemoreceptors to ventilation during heavy exercise*. Respir Physiol 68, 203-213.

Jiang, M., Alheid, G.F., Calandriello, T., McCrimmon, D.R. (2004). *Parabrachial-lateral pontine neurons link nociception and breathing*. Respir Physiol Neurobiol 143, 215-233.

Jordan, L.M., Liu, J., Hedlund, P.B., Akay, T., Pearson, K.G. (2008). *Descending command systems for the initiation of locomotion in mammals*. Brain research reviews 57, 183-191.

Josset, N., Roussel, M., Lemieux, M., Lafrance-Zoubga, D., Rastqar, A., Bretzner, F. (2018). *Distinct Contributions of Mesencephalic Locomotor Region Nuclei to Locomotor Control in the Freely Behaving Mouse*. Curr Biol 28, 884-901.e883.

Juvin, L., Grätsch, S., Trillaud-Doppia, E., Gariépy, J.-F., Büschges, A., Dubuc, R. (2016). *A Specific Population of Reticulospinal Neurons Controls the Termination of Locomotion*. Cell Reports 15, 2377-2386.

Kalia, M., Mesulam, M.M. (1980). *Brain stem projections of sensory and motor components of the vagus complex in the cat: I. The cervical vagus and nodose ganglion*. J Comp Neurol 193, 435-465.

Kam, K., Worrell, J.W., Janczewski, W.A., Cui, Y., Feldman, J.L. (2013). *Distinct inspiratory rhythm and pattern generating mechanisms in the preBötzinger complex*. J Neurosci 33, 9235-9245.

Kanbar, R., Stornetta, R.L., Cash, D.R., Lewis, S.J., Guyenet, P.G. (2010). *Photostimulation of Phox2b medullary neurons activates cardiorespiratory function in conscious rats*. American journal of respiratory and critical care medicine 182, 1184-1194.

Karachi, C., Grabli, D., Bernard, F.A., Tandé, D., Wattiez, N., Belaid, H., Bardinet, E., Prigent, A., Nothacker, H.P., Hunot, S., Hartmann, A., Lehéricy, S., Hirsch, E.C., François, C. (2010). *Cholinergic mesencephalic neurons are involved in gait and postural disorders in Parkinson disease*. The Journal of clinical investigation 120, 2745-2754.

Kawahara, K., Nakazono, Y., Yamauchi, Y., Miyamoto, Y. (1989). *Coupling between respiratory and locomotor rhythms during fictive locomotion in decerebrate cats*. Neurosci Lett 103, 326-330.

Kay, J.D., Petersen, E.S., Vejby-Christensen, H. (1975). *Breathing in man during steady-state exercise on the bicycle at two pedalling frequencies, and during treadmill walking*. The Journal of physiology 251, 645-656.

Kiehn, O. (2006). *Locomotor circuits in the mammalian spinal cord*. Annual review of neuroscience 29, 279-306.

Kiehn, O., Quinlan, K.A., Restrepo, C.E., Lundfald, L., Borgius, L., Talpalar, A.E., Endo, T. (2008). *Excitatory components of the mammalian locomotor CPG*. Brain research reviews 57, 56-63.

Kiehn, O., Dougherty, K., 2013. Locomotion: Circuits and Physiology, in: Pfaff, D.W., Volkow, N.D. (Eds.), Neuroscience in the 21st Century: From Basic to Clinical. New York, NY: Springer New York, pp. 1337-1365.

Kiehn, O. (2016). *Decoding the organization of spinal circuits that control locomotion*. Nat Rev Neurosci 17, 224-238.

Kim, L.H., Sharma, S., Sharples, S.A., Mayr, K.A., Kwok, C.H.T., Whelan, P.J. (2017). *Integration of Descending Command Systems for the Generation of Context-Specific Locomotor Behaviors*. Front Neurosci 11, 581.

Kjaerulff, O., Kiehn, O. (1996). *Distribution of networks generating and coordinating locomotor activity in the neonatal rat spinal cord in vitro: a lesion study*. J Neurosci 16, 5777-5794.

Klarner, T., Zehr, E.P. (2018). *Sherlock Holmes and the curious case of the human locomotor central pattern generator*. J Neurophysiol 120, 53-77.

Koch, S.C., Acton, D., Goulding, M. (2018). *Spinal Circuits for Touch, Pain, and Itch*. Annual review of physiology 80, 189-217.

Kohl, J., Koller, E.A., Jäger, M. (1981). *Relation between pedalling- and breathing rhythm*. Eur J Appl Physiol Occup Physiol 47, 223-237.

Koizumi, H., Koshiya, N., Chia, J.X., Cao, F., Nugent, J., Zhang, R., Smith, J.C. (2013). *Structural-functional properties of identified excitatory and inhibitory interneurons within pre-Botzinger complex respiratory microcircuits*. J Neurosci 33, 2994-3009.

Korsak, A., Sheikhbahaei, S., Machhada, A., Gourine, A.V., Huckstepp, R.T.R. (2018). *The Role Of Parafacial Neurons In The Control Of Breathing During Exercise*. Sci Rep 8, 400.

Koshiya, N., Smith, J.C. (1999). *Neuronal pacemaker for breathing visualized in vitro*. Nature 400, 360-363.

Kottick, A., Del Negro, C.A. (2015). *Synaptic Depression Influences Inspiratory-Expiratory Phase Transition in Dbx1 Interneurons of the preBötzinger Complex in Neonatal Mice*. J Neurosci 35, 11606-11611.

Kottick, A., Martin, C.A., Del Negro, C.A. (2017). *Fate mapping neurons and glia derived from Dbx1-expressing progenitors in mouse preBötzinger complex*. Physiol Rep 5, e13300.

Krogh, L. (1913). *The regulation of respiration and circulation during the initial stages of muscular work*. The Journal of physiology.

Kuwana, S., Tsunekawa, N., Yanagawa, Y., Okada, Y., Kuribayashi, J., Obata, K. (2006). *Electrophysiological and morphological characteristics of GABAergic respiratory neurons in the mouse pre-Bötzinger complex*. The European journal of neuroscience 23, 667-674.

Lafortuna, C.L., Reinach, E., Saibene, F. (1996). *The effects of locomotor-respiratory coupling on the pattern of breathing in horses*. The Journal of physiology 492 (Pt 2), 587-596.

Lam, T., Pearson, K.G. (2002). *The role of proprioceptive feedback in the regulation and adaptation of locomotor activity*. Advances in experimental medicine and biology 508, 343-355.

Lambert, F.M., Combes, D., Simmers, J., Straka, H. (2012). *Gaze stabilization by efference copy signaling without sensory feedback during vertebrate locomotion*. Curr Biol 22, 1649-1658.

Lanuza, G.M., Gosgnach, S., Pierani, A., Jessell, T.M., Goulding, M. (2004). *Genetic identification of spinal interneurons that coordinate left-right locomotor activity necessary for walking movements*. Neuron 42, 375-386.

Lau, B., François, C., Karachi, C. (2019). *Structure and function of the mesencephalic locomotor region in normal and parkinsonian primates*. Current opinion in physiology 8, 121-128.

Le Gal, J.-P., Colnot, E., Cardoit, L., Bacqué-Cazenave, J., Thoby-Brisson, M., Juvin, L., Morin, D. (2020). *Modulation of respiratory network activity by forelimb and hindlimb locomotor generators*. European Journal of Neuroscience 52, 3181-3195.

Le Gal, J.P., Juvin, L., Cardoit, L., Thoby-Brisson, M., Morin, D. (2014). *Remote control of respiratory neural network by spinal locomotor generators*. PloS one 9, e89670.

Le Ray, D., Juvin, L., Ryczko, D., Dubuc, R. (2011). *Chapter 4--supraspinal control of locomotion: the mesencephalic locomotor region*. Progress in brain research 188, 51-70.

Lemieux, M., Josset, N., Roussel, M., Couraud, S., Bretzner, F. (2016). *Speed-Dependent Modulation of the Locomotor Behavior in Adult Mice Reveals Attractor and Transitional Gaits*. Front Neurosci 10, 42.

Lemon, R.N. (2008). *Descending pathways in motor control*. Annual review of neuroscience 31, 195-218.

Lichtenberg, N.T., Pennington, Z.T., Holley, S.M., Greenfield, V.Y., Cepeda, C., Levine, M.S., Wassum, K.M. (2017). *Basolateral Amygdala to Orbitofrontal Cortex Projections Enable Cue-Triggered Reward Expectations*. J Neurosci 37, 8374-8384.

Liu, J., Jordan, L.M. (2005). *Stimulation of the parapyramidal region of the neonatal rat brain stem produces locomotor-like activity involving spinal 5-HT7 and 5-HT2A receptors*. J Neurophysiol 94, 1392-1404.

Liu, Y.Y., Ju, G., Wong-Riley, M.T. (2001). *Distribution and colocalization of neurotransmitters and receptors in the pre-Bötzinger complex of rats*. J Appl Physiol (1985) 91, 1387-1395.

Mahler, S.V., Vazey, E.M., Beckley, J.T., Keistler, C.R., McGlinchey, E.M., Kaufling, J., Wilson, S.P., Deisseroth, K., Woodward, J.J., Aston-Jones, G. (2014). *Designer receptors show role for ventral pallidum input to ventral tegmental area in cocaine seeking*. Nature neuroscience 17, 577-585.

Marina, N., Abdala, A.P., Trapp, S., Li, A., Nattie, E.E., Hewinson, J., Smith, J.C., Paton, J.F., Gourine, A.V. (2010). *Essential role of Phox2b-expressing ventrolateral brainstem neurons in the chemosensory control of inspiration and expiration*. J Neurosci 30, 12466-12473.

Martinez-Gonzalez, C., Bolam, J.P., Mena-Segovia, J. (2011). *Topographical organization of the pedunculopontine nucleus*. Front Neuroanat 5, 22.

Mateika, J.H., Duffin, J. (1992). *Changes in ventilation at the start and end of moderate and heavy exercise of short and long duration*. Eur J Appl Physiol Occup Physiol 65, 234-240.

Mateika, J.H., Duffin, J. (1995). *A review of the control of breathing during exercise*. Eur J Appl Physiol Occup Physiol 71, 1-27.

Matsushita, M. (1999). *Projections from the lowest lumbar and sacral-caudal segments to the cerebellar nuclei in the rat, studied by anterograde axonal tracing*. Journal of Comparative Neurology 404, 21-32.

Mayer, W.P., Murray, A.J., Brenner-Morton, S., Jessell, T.M., Tourtellotte, W.G., Akay, T. (2018). *Role of muscle spindle feedback in regulating muscle activity strength during walking at different speed in mice*. J Neurophysiol.

McKay, L.C., Janczewski, W.A., Feldman, J.L. (2005). *Sleep-disordered breathing after targeted ablation of preBötzinger complex neurons*. Nature neuroscience 8, 1142-1144.

Mellen, N.M., Janczewski, W.A., Bocchiaro, C.M., Feldman, J.L. (2003). *Opioid-induced quantal slowing reveals dual networks for respiratory rhythm generation*. Neuron 37, 821-826.

Ménard, A., Grillner, S. (2008). *Diencephalic locomotor region in the lamprey--afferents and efferent control*. J Neurophysiol 100, 1343-1353.

Menuet, C., Kourdougli, N., Hilaire, G., Voituron, N. (2011). *Differences in serotoninergic metabolism possibly contribute to differences in breathing phenotype of FVB/N and C57BL/6J mice*. J Appl Physiol (1985) 110, 1572-1581.

Menuet, C., Connelly, A.A., Bassi, J.K., Melo, M.R., Le, S., Kamar, J., Kumar, N.N., McDougall, S.J., McMullan, S., Allen, A.M. (2020). *PreBötzinger complex neurons drive respiratory modulation of blood pressure and heart rate*. eLife 9, e57288.

Minassian, K., Hofstoetter, U.S., Dzeladini, F., Guertin, P.A., Ijspeert, A. (2017). *The Human Central Pattern Generator for Locomotion: Does It Exist and Contribute to Walking?* Neuroscientist 23, 649-663.

Mitchell, R.A., Loeschcke, H.H., Massion, W.H., Severinghaus, J.W. (1963). *Respiratory responses mediated through superficial chemosensitive areas on the medulla*. J Appl Physiol (1985) 18, 523-533.

Morgado-Valle, C., Baca, S.M., Feldman, J.L. (2010). *Glycinergic pacemaker neurons in preBötzinger complex of neonatal mouse*. J Neurosci 30, 3634-3639.

Morgado-Valle, C., Fernandez-Ruiz, J., Lopez-Meraz, L., Beltran-Parrazal, L. (2015). *Substitution of extracellular Ca2+ by Sr2+ prolongs inspiratory burst in pre-Bötzinger complex inspiratory neurons*. Journal of Neurophysiology 113, 1175-1183.

Morin, D., Viala, D. (2002). *Coordinations of locomotor and respiratory rhythms in vitro are critically dependent on hindlimb sensory inputs*. J Neurosci 22, 4756-4765.

Moro, E., Hamani, C., Poon, Y.-Y., Al-Khairallah, T., Dostrovsky, J.O., Hutchison, W.D., Lozano, A.M. (2009). *Unilateral pedunculopontine stimulation improves falls in Parkinson's disease*. Brain : a journal of neurology 133, 215-224.

Mörschel, M., Dutschmann, M. (2009). *Pontine respiratory activity involved in inspiratory/expiratory phase transition*. Philosophical transactions of the Royal Society of London. Series B, Biological sciences 364, 2517-2526.

Morton, S.M., Bastian, A.J. (2004). *Cerebellar control of balance and locomotion*. Neuroscientist 10, 247-259.

Mulkey, D.K., Stornetta, R.L., Weston, M.C., Simmons, J.R., Parker, A., Bayliss, D.A., Guyenet, P.G. (2004). *Respiratory control by ventral surface chemoreceptor neurons in rats*. Nature neuroscience 7, 1360-1369.

Multon, S., Franzen, R., Poirrier, A.L., Scholtes, F., Schoenen, J. (2003). *The effect of treadmill training on motor recovery after a partial spinal cord compression-injury in the adult rat*. Journal of neurotrauma 20, 699-706.

Mutolo, D., Bongianni, F., Einum, J., Dubuc, R., Pantaleo, T. (2007). *Opioid-induced depression in the lamprey respiratory network*. Neuroscience 150, 720-729.

Muzzu, T., Mitolo, S., Gava, G.P., Schultz, S.R. (2018). *Encoding of locomotion kinematics in the mouse cerebellum*. PloS one 13, e0203900.

Nattie, E. (1999). *CO2, brainstem chemoreceptors and breathing*. Progress in neurobiology 59, 299-331.

Oku, Y., Masumiya, H., Okada, Y. (2007). *Postnatal developmental changes in activation profiles of the respiratory neuronal network in the rat ventral medulla*. The Journal of physiology 585, 175-186.

Onimaru, H., Arata, A., Homma, I. (1987). *Localization of respiratory rhythm-generating neurons in the medulla of brainstem-spinal cord preparations from newborn rats*. Neurosci Lett 78, 151-155.

Onimaru, H., Homma, I. (2003). *A novel functional neuron group for respiratory rhythm generation in the ventral medulla*. J Neurosci 23, 1478-1486.

Onimaru, H., Ikeda, K., Kawakami, K. (2008). *CO2-sensitive preinspiratory neurons of the parafacial respiratory group express Phox2b in the neonatal rat*. J Neurosci 28, 12845-12850.

Onimaru, H., Ikeda, K., Kawakami, K. (2009). *Phox2b, RTN/pFRG neurons and respiratory rhythmogenesis*. Respir Physiol Neurobiol 168, 13-18.

Orlovsky, G.N. (1969). *Spontaneous and induced locomotion of thalamic cat*. BIOPHYSICS-USSR 14, 1154.

Oueghlani, Z., Simonnet, C., Cardoit, L., Courtand, G., Cazalets, J.R., Morin, D., Juvin, L., Barrière, G. (2018). *Brainstem Steering of Locomotor Activity in the Newborn Rat*. J Neurosci 38, 7725-7740.

Pagliardini, S., Janczewski, W.A., Tan, W., Dickson, C.T., Deisseroth, K., Feldman, J.L. (2011). *Active expiration induced by excitation of ventral medulla in adult anesthetized rats*. J Neurosci 31, 2895-2905.

Palisses, R., Persegol, L., Viala, D., Viala, G. (1988). *Reflex modulation of phrenic activity through hindlimb passive motion in decorticate and spinal rabbit preparation*. Neuroscience 24, 719-728.

Palmiter, R.D. (2018). *The Parabrachial Nucleus: CGRP Neurons Function as a General Alarm*. Trends in Neurosciences 41, 280-293.

Pan, L.G., Forster, H.V., Bisgard, G.E., Kaminski, R.P., Dorsey, S.M., Busch, M.A. (1983). *Hyperventilation in ponies at the onset of and during steady-state exercise*. J Appl Physiol Respir Environ Exerc Physiol 54, 1394-1402.

Pantaleo, T., Mutolo, D., Cinelli, E., Bongianni, F. (2011). *Respiratory responses to somatostatin microinjections into the Bötzinger complex and the pre-Bötzinger complex of the rabbit*. Neurosci Lett 498, 26-30.

Park, J.-W., Bang, M.-S., Kwon, B.-S., Park, Y.-K., Kim, D.-W., Shon, S.-M., Jeong, S.-W., Lee, D.-K., Kim, D.-E. (2010). *Early treadmill training promotes motor function after hemorrhagic stroke in rats*. Neuroscience Letters 471, 104-108.

Parker, S.M., Sinnamon, H.M. (1983). *Forward locomotion elicited by electrical stimulation in the diencephalon and mesencephalon of the awake rat*. Physiology & behavior 31, 581-587.

Paterson, D.J. (2014). *Defining the neurocircuitry of exercise hyperpnoea*. The Journal of physiology 592, 433-444.

Pearce, D.H., Milhorn, H.T. (1977). *dynamic and steady-state respiratory responses to bicycle exercise*. American Physiological Society.

Pearson, K. (1976). *The control of walking*. Scientific American 235, 72-74, 79-82, 83-76.

Pearson, K.G. (2004). *Generating the walking gait: role of sensory feedback*. Progress in brain research 143, 123-129.

Peña, F., Parkis, M.A., Tryba, A.K., Ramirez, J.M. (2004). *Differential contribution of pacemaker properties to the generation of respiratory rhythms during normoxia and hypoxia*. Neuron 43, 105-117.

Pereira, E.A., Nandi, D., Jenkinson, N., Stein, J.F., Green, A.L., Aziz, T.Z. (2011). *Pedunculopontine stimulation from primate to patient*. Journal of neural transmission (Vienna, Austria : 1996) 118, 1453-1460.

Pierani, A., Brenner-Morton, S., Chiang, C., Jessell, T.M. (1999). *A sonic hedgehog-independent, retinoid-activated pathway of neurogenesis in the ventral spinal cord*. Cell 97, 903-915.

Pierani, A., Moran-Rivard, L., Sunshine, M.J., Littman, D.R., Goulding, M., Jessell, T.M. (2001). *Control of interneuron fate in the developing spinal cord by the progenitor homeodomain protein Dbx1*. Neuron 29, 367-384.

Pisanski, A., Pagliardini, S. (2019). *The parafacial respiratory group and the control of active expiration*. Respir Physiol Neurobiol 265, 153-160.

Pivetta, C., Esposito, M.S., Sigrist, M., Arber, S. (2014). *Motor-circuit communication matrix from spinal cord to brainstem neurons revealed by developmental origin*. Cell 156, 537-548.

Potts, J.T., Rybak, I.A., Paton, J.F. (2005). *Respiratory rhythm entrainment by somatic afferent stimulation*. J Neurosci 25, 1965-1978.

Purves, D., Augustine, G.J., Fitzpatrick, D., Katz, L.C., LaMantia, A., McNamara, J.O., Williams, S.M., 2001. Spinal Cord Circuitry and Locomotion
Neuroscience. 2nd edition Sunderland, Massachusetts U.S.A: Sinauer Associates.

Qiu, K., Lane, M.A., Lee, K.Z., Reier, P.J., Fuller, D.D. (2010). *The phrenic motor nucleus in the adult mouse*. Experimental neurology 226, 254-258.

Ramanantsoa, N., Hirsch, M.R., Thoby-Brisson, M., Dubreuil, V., Bouvier, J., Ruffault, P.L., Matrot, B., Fortin, G., Brunet, J.F., Gallego, J., Goridis, C. (2011). *Breathing without CO(2) chemosensitivity in conditional Phox2b mutants*. J Neurosci 31, 12880-12888.

Ramirez, J.M., Quellmalz, U.J., Richter, D.W. (1996). *Postnatal changes in the mammalian respiratory network as revealed by the transverse brainstem slice of mice*. The Journal of physiology 491 (Pt 3), 799-812.

Ramirez, J.M., Tryba, A.K., Peña, F. (2004). *Pacemaker neurons and neuronal networks: an integrative view*. Curr Opin Neurobiol 14, 665-674.

Ramirez, J.M. (2011). *The human pre-Bötzinger complex identified*. Brain : a journal of neurology 134, 8-10.

Regan, R.G., Majcherczyk, S. (1982). *Role of peripheral chemoreceptors and central chemosensitivity in the regulation of respiration and circulation*. Journal of Experimental Biology 100, 23.

Remmers, J.E. (2005). *A century of control of breathing*. American journal of respiratory and critical care medicine 172, 6-11.

Robertson, B., Kardamakis, A., Capantini, L., Pérez-Fernández, J., Suryanarayana, S.M., Wallén, P., Stephenson-Jones, M., Grillner, S. (2014). *The lamprey blueprint of the mammalian nervous system*. Progress in brain research 212, 337-349.

Robinson, N.E. (1985). *Respiratory adaptations to exercise*. Vet Clin North Am Equine Pract 1, 497-512.

Romer, S.H., Seedle, K., Turner, S.M., Li, J., Baccei, M.L., Crone, S.A. (2017). *Accessory respiratory muscles enhance ventilation in ALS model mice and are activated by excitatory V2a neurons*. Experimental neurology 287, 192-204.

Roseberry, T.K., Lee, A.M., Lalive, A.L., Wilbrecht, L., Bonci, A., Kreitzer, A.C. (2016). *Cell-Type-Specific Control of Brainstem Locomotor Circuits by Basal Ganglia*. Cell 164, 526-537.

Rossignol, S., Dubuc, R., Gossard, J.P. (2006). *Dynamic sensorimotor interactions in locomotion*. Physiol Rev 86, 89-154.

Roy, R.R., Hutchison, D.L., Pierotti, D.J., Hodgson, J.A., Edgerton, V.R. (1991). *EMG patterns of rat ankle extensors and flexors during treadmill locomotion and swimming*. J Appl Physiol (1985) 70, 2522-2529.

Ruder, L., Takeoka, A., Arber, S. (2016). *Long-Distance Descending Spinal Neurons Ensure Quadrupedal Locomotor Stability*. Neuron 92, 1063-1078.

Ruffault, P.L., D'Autreaux, F., Hayes, J.A., Nomaksteinsky, M., Autran, S., Fujiyama, T., Hoshino, M., Hagglund, M., Kiehn, O., Brunet, J.F., Fortin, G., Goridis, C. (2015). *The retrotrapezoid nucleus neurons expressing Atoh1 and Phox2b are essential for the respiratory response to CO(2)*. Elife 4.

Ryczko, D., Dubuc, R. (2013). *The multifunctional mesencephalic locomotor region*. Curr Pharm Des 19, 4448-4470.

Ryczko, D., Auclair, F., Cabelguen, J.M., Dubuc, R. (2016). *The mesencephalic locomotor region sends a bilateral glutamatergic drive to hindbrain reticulospinal neurons in a tetrapod*. J Comp Neurol 524, 1361-1383.

Sathyamurthy, A., Barik, A., Dobrott, C.I., Matson, K.J.E., Stoica, S., Pursley, R., Chesler, A.T., Levine, A.J. (2020). *Cerebellospinal Neurons Regulate Motor Performance and Motor Learning*. Cell Rep 31, 107595.

Schwarzacher, S.W., Smith, J.C., Richter, D.W. (1995). *Pre-Bötzinger complex in the cat*. J Neurophysiol 73, 1452-1461.

Schwarzacher, S.W., Rüb, U., Deller, T. (2011). *Neuroanatomical characteristics of the human pre-Bötzinger complex and its involvement in neurodegenerative brainstem diseases*. Brain : a journal of neurology 134, 24-35.

Sherman, D., Worrell, J.W., Cui, Y., Feldman, J.L. (2015). *Optogenetic perturbation of preBötzinger complex inhibitory neurons modulates respiratory pattern*. Nature neuroscience 18, 408-414.

Shi, Y., Stornetta, R.L., Stornetta, D.S., Onengut-Gumuscu, S., Farber, E.A., Turner, S.D., Guyenet, P.G., Bayliss, D.A. (2017). *Neuromedin B Expression Defines the Mouse Retrotrapezoid Nucleus*. J Neurosci 37, 11744-11757.

Shik, M.L., Severin, F.V., Orlovskii, G.N. (1966). *Control of walking and running by means of electric stimulation of the midbrain*. Biofizika 11, 659-666.

Shik, M.L., Severin, F.V., Orlovsky, G.N. (1969). *Control of walking and running by means of electrical stimulation of the mesencephalon*. Electroencephalogr Clin Neurophysiol 26, 549.

Shik, M.L., Orlovsky, G.N. (1976). *Neurophysiology of locomotor automatism*. Physiol Rev 56, 465-501.

Sieck, G., Gransee, H. (2012). *Respiratory Muscles: Structure, Function, and Regulation*. Colloquium Series on Integrated Systems Physiology: From Molecule to Function 4, 1-96.

Simons, R.S. (1999). *Running, breathing and visceral motion in the domestic rabbit (Oryctolagus cuniculus): testing visceral displacement hypotheses*. The Journal of experimental biology 202, 563-577.

Sirota, M.G., Di Prisco, G.V., Dubuc, R. (2000). *Stimulation of the mesencephalic locomotor region elicits controlled swimming in semi-intact lampreys*. The European journal of neuroscience 12, 4081-4092.

Skarlatou, S., Hérent, C., Toscano, E., Mendes, C.S., Bouvier, J., Zampieri, N. (2020). *Afadin Signaling at the Spinal Neuroepithelium Regulates Central Canal Formation and Gait Selection*. Cell Rep 31, 107741.

Skinner, R.D., Garcia-Rill, E. (1984). *The mesencephalic locomotor region (MLR) in the rat*. Brain research 323, 385-389.

Smith, J.C., Feldman, J.L. (1987). *In vitro brainstem-spinal cord preparations for study of motor systems for mammalian respiration and locomotion*. Journal of neuroscience methods 21, 321-333.

Smith, J.C., Morrison, D.E., Ellenberger, H.H., Otto, M.R., Feldman, J.L. (1989). *Brainstem projections to the major respiratory neuron populations in the medulla of the cat*. J Comp Neurol 281, 69-96.

Smith, J.C., Ellenberger, H.H., Ballanyi, K., Richter, D.W., Feldman, J.L. (1991). *Pre-Bötzinger complex: a brainstem region that may generate respiratory rhythm in mammals*. Science 254, 726-729.

Smith, J.C., Abdala, A.P.L., Koizumi, H., Rybak, I.A., Paton, J.F.R. (2007). *Spatial and Functional Architecture of the Mammalian Brain Stem Respiratory Network: A Hierarchy of Three Oscillatory Mechanisms*. Journal of Neurophysiology 98, 3370-3387.

Song, G., Yu, Y., Poon, C.S. (2006). *Cytoarchitecture of pneumotaxic integration of respiratory and nonrespiratory information in the rat*. J Neurosci 26, 300-310.

Souza, G.M., Stornetta, R.L., Stornetta, D.S., Abbott, S.B.G., Guyenet, P.G. (2020). *Selective optogenetic stimulation of RTN neurons drives ventilation and active expiration in unanesthetized rats*. The FASEB Journal 34, 1-1.

Spyer, K.M., Gourine, A.V. (2009). *Chemosensory pathways in the brainstem controlling cardiorespiratory activity*. Philosophical transactions of the Royal Society of London. Series B, Biological sciences 364, 2603-2610.

Stachniak, T.J., Ghosh, A., Sternson, S.M. (2014). *Chemogenetic synaptic silencing of neural circuits localizes a hypothalamus→midbrain pathway for feeding behavior*. Neuron 82, 797-808.

Stecina, K., Fedirchuk, B., Hultborn, H. (2013). *Information to cerebellum on spinal motor networks mediated by the dorsal spinocerebellar tract*. The Journal of physiology 591.

Stickford, A.S.L., Stickford, J.L. (2014). *Ventilation and Locomotion in Humans: Mechanisms, Implications, and Perturbations to the Coupling of These Two Rhythms*. Springer Science Reviews 2, 95-118.

Stornetta, R.L., Rosin, D.L., Wang, H., Sevigny, C.P., Weston, M.C., Guyenet, P.G. (2003). *A group of glutamatergic interneurons expressing high levels of both neurokinin-1 receptors and somatostatin identifies the region of the pre-Bötzinger complex*. J Comp Neurol 455, 499-512.

Stornetta, R.L., Moreira, T.S., Takakura, A.C., Kang, B.J., Chang, D.A., West, G.H., Brunet, J.F., Mulkey, D.K., Bayliss, D.A., Guyenet, P.G. (2006). *Expression of Phox2b by brainstem neurons involved in chemosensory integration in the adult rat*. J Neurosci 26, 10305-10314.

Stornetta, R.L., Spirovski, D., Moreira, T.S., Takakura, A.C., West, G.H., Gwilt, J.M., Pilowsky, P.M., Guyenet, P.G. (2009). *Galanin is a selective marker of the retrotrapezoid nucleus in rats*. The Journal of comparative neurology 512, 373-383.

Straka, H., Simmers, J., Chagnaud, B.P. (2018). *A New Perspective on Predictive Motor Signaling*. Curr Biol 28, R232-r243.

Sun, X., Thörn Pérez, C., Halemani D, N., Shao, X.M., Greenwood, M., Heath, S., Feldman, J.L., Kam, K. (2019). *Opioids modulate an emergent rhythmogenic process to depress breathing*. eLife 8, e50613.

Suzue, T. (1984). *Respiratory rhythm generation in the in vitro brain stem-spinal cord preparation of the neonatal rat*. The Journal of physiology 354, 173-183.

Takakura, A.C., Barna, B.F., Cruz, J.C., Colombari, E., Moreira, T.S. (2014). *Phox2b-expressing retrotrapezoid neurons and the integration of central and peripheral chemosensory control of breathing in conscious rats*. Experimental physiology 99, 571-585.

Takakusaki, K., Habaguchi, T., Ohtinata-Sugimoto, J., Saitoh, K., Sakamoto, T. (2003). *Basal ganglia efferents to the brainstem centers controlling postural muscle tone and locomotion: a new concept for understanding motor disorders in basal ganglia dysfunction*. Neuroscience 119, 293-308.

Takakusaki, K., Chiba, R., Nozu, T., Okumura, T. (2016). *Brainstem control of locomotion and muscle tone with special reference to the role of the mesopontine tegmentum and medullary reticulospinal systems*. Journal of neural transmission (Vienna, Austria : 1996) 123, 695-729.

Talpalar, A.E., Kiehn, O. (2010). *Glutamatergic mechanisms for speed control and network operation in the rodent locomotor CpG*. Frontiers in neural circuits 4.

Talpalar, A.E., Endo, T., Low, P., Borgius, L., Hagglund, M., Dougherty, K.J., Ryge, J., Hnasko, T.S., Kiehn, O. (2011). *Identification of Minimal Neuronal Networks Involved in Flexor-Extensor Alternation in the Mammalian Spinal Cord*. Neuron 71, 1071-1084.

Talpalar, A.E., Bouvier, J., Borgius, L., Fortin, G., Pierani, A., Kiehn, O. (2013). *Dual-mode operation of neuronal networks involved in left-right alternation*. Nature.

Tan, W., Janczewski, W.A., Yang, P., Shao, X.M., Callaway, E.M., Feldman, J.L. (2008). *Silencing preBötzinger complex somatostatin-expressing neurons induces persistent apnea in awake rat*. Nature neuroscience 11, 538-540.

Tankersley, C.G., DiSilvestre, D.A., Jedlicka, A.E., Wilkins, H.M., Zhang, L. (1998). *Differential inspiratory timing is genetically linked to mouse chromosome 3*. J Appl Physiol (1985) 85, 360-365.

Thevathasan, W., Coyne, T.J., Hyam, J.A., Kerr, G., Jenkinson, N., Aziz, T.Z., Silburn, P.A. (2011). *Pedunculopontine nucleus stimulation improves gait freezing in Parkinson disease*. Neurosurgery 69, 1248-1253; discussion 1254.

Thoby-Brisson, M., Ramirez, J.M. (2001). *Identification of two types of inspiratory pacemaker neurons in the isolated respiratory neural network of mice*. J Neurophysiol 86, 104-112.

Thoby-Brisson, M., Trinh, J.B., Champagnat, J., Fortin, G. (2005). *Emergence of the pre-Botzinger respiratory rhythm generator in the mouse embryo*. J Neurosci 25, 4307-4318.

Thoby-Brisson, M., Karlen, M., Wu, N., Charnay, P., Champagnat, J., Fortin, G. (2009). *Genetic identification of an embryonic parafacial oscillator coupling to the preBotzinger complex*. Nature neuroscience 12, 1028-1035.

Thornton, J.M., Guz, A., Murphy, K., Griffith, A.R., Pedersen, D.L., Kardos, A., Leff, A., Adams, L., Casadei, B., Paterson, D.J. (2001). *Identification of higher brain centres that may encode the cardiorespiratory response to exercise in humans*. The Journal of physiology 533, 823-836.

Tobin, M.J., Perez, W., Guenther, S.M., D'Alonzo, G., Dantzker, D.R. (1986). *Breathing pattern and metabolic behavior during anticipation of exercise*. J Appl Physiol (1985) 60, 1306-1312.

Tsuchiya, N., Iwase, M., Izumizaki, M., Homma, I. (2012). *Dopaminergic modulation of exercise hyperpnoea via D(2) receptors in mice*. Experimental physiology 97, 228-238.

Tupal, S., Rieger, M.A., Ling, G.Y., Park, T.J., Dougherty, J.D., Goodchild, A.K., Gray, P.A. (2014). *Testing the role of preBötzinger Complex somatostatin neurons in respiratory and vocal behaviors*. The European journal of neuroscience 40, 3067-3077.

Ursino, M., Magosso, E., Avanzolini, G. (2001). *An integrated model of the human ventilatory control system: the response to hypercapnia*. Clinical physiology (Oxford, England) 21, 447-464.

Usseglio, G., Gatier, E., Heuzé, A., Hérent, C., Bouvier, J. (2020). *Control of Orienting Movements and Locomotion by Projection-Defined Subsets of Brainstem V2a Neurons*. Current Biology.

van Alphen, J., Duffin, J. (1994). *Entrained breathing and oxygen consumption during treadmill walking*. Canadian journal of applied physiology = Revue canadienne de physiologie appliquee 19, 432-440.

Vann, N.C., Pham, F.D., Hayes, J.A., Kottick, A., Del Negro, C.A. (2016). *Transient Suppression of Dbx1 PreBötzinger Interneurons Disrupts Breathing in Adult Mice*. PloS one 11, e0162418.

Vann, N.C., Pham, F.D., Dorst, K.E., Del Negro, C.A. (2018). *Dbx1 Pre-Bötzinger Complex Interneurons Comprise the Core Inspiratory Oscillator for Breathing in Unanesthetized Adult Mice*. eNeuro 5.

Waisbren, S.J., Whiting, C.S., Nadel, E.R. (1990). *Effects of passive limb movement on pulmonary ventilation*. The Yale journal of biology and medicine 63, 549-556.

Waldrop, T.G., Bauer, R.M., Iwamoto, G.A. (1988). *Microinjection of GABA antagonists into the posterior hypothalamus elicits locomotor activity and a cardiorespiratory activation*. Brain research 444, 84-94.

Waldrop, T.G., Iwamoto, G.A. (2006). *Point:Counterpoint: Supraspinal locomotor centers do/do not contribute significantly to the hyperpnea of dynamic exercise*. J Appl Physiol (1985) 100, 1077-1079.

Wallén-Mackenzie, A., Gezelius, H., Thoby-Brisson, M., Nygård, A., Enjin, A., Fujiyama, F., Fortin, G., Kullander, K. (2006). *Vesicular glutamate transporter 2 is required for central respiratory rhythm generation but not for locomotor central pattern generation*. J Neurosci 26, 12294-12307.

Wang, X., Hayes, J.A., Revill, A.L., Song, H., Kottick, A., Vann, N.C., LaMar, M.D., Picardo, M.C., Akins, V.T., Funk, G.D., Del Negro, C.A. (2014). *Laser ablation of Dbx1 neurons in the pre-Bötzinger complex stops inspiratory rhythm and impairs output in neonatal mice*. Elife 3, e03427.

Wells, G.D., Diep, T., Duffin, J. (2007). *The ventilatory response to sine wave variation in exercise loads and limb movement frequency*. Respir Physiol Neurobiol 158, 45-50.

Wenninger, J.M., Pan, L.G., Klum, L., Leekley, T., Bastastic, J., Hodges, M.R., Feroah, T., Davis, S., Forster, H.V. (2004). *Small reduction of neurokinin-1 receptor-expressing neurons in the pre-Bötzinger complex area induces abnormal breathing periods in awake goats*. J Appl Physiol (1985) 97, 1620-1628.

Whelan, P., Bonnot, A., O'Donovan, M.J. (2000). *Properties of rhythmic activity generated by the isolated spinal cord of the neonatal mouse*. J Neurophysiol 84, 2821-2833.

Wilson, J.M., Hartley, R., Maxwell, D.J., Todd, A.J., Lieberam, I., Kaltschmidt, J.A., Yoshida, Y., Jessell, T.M., Brownstone, R.M. (2005). *Conditional rhythmicity of ventral spinal interneurons defined by expression of the Hb9 homeodomain protein*. J Neurosci 25, 5710-5719.

Winter, S.M., Fresemann, J., Schnell, C., Oku, Y., Hirrlinger, J., Hülsmann, S. (2009). *Glycinergic interneurons are functionally integrated into the inspiratory network of mouse medullary slices*. Pflugers Archiv : European journal of physiology 458, 459-469.

Wu, J., Capelli, P., Bouvier, J., Goulding, M., Arber, S., Fortin, G. (2017). *A V0 core neuronal circuit for inspiration*. Nat Commun 8, 544.

Yang, C.F., Kim, E.J., Callaway, E.M., Feldman, J.L. (2020a). *Monosynaptic Projections to Excitatory and Inhibitory preBötzinger Complex Neurons*. Frontiers in Neuroanatomy 14.

Yang, Y., Lee, J., Kim, G. (2020b). *Integration of locomotion and auditory signals in the mouse inferior colliculus*. Elife 9.

Zhang, J., Lanuza, G.M., Britz, O., Wang, Z., Siembab, V.C., Zhang, Y., Velasquez, T., Alvarez, F.J., Frank, E., Goulding, M. (2014). *V1 and v2b interneurons secure the alternating flexor-extensor motor activity mice require for limbed locomotion*. Neuron 82, 138-150.

Zhang, Y., Narayan, S., Geiman, E., Lanuza, G.M., Velasquez, T., Shanks, B., Akay, T., Dyck, J., Pearson, K., Gosgnach, S., Fan, C.M., Goulding, M. (2008). *V3 spinal neurons establish a robust and balanced locomotor rhythm during walking*. Neuron 60, 84-96.

Zhuang, J., Xu, F., Zhang, C., Frazier, D.T. (2009). *Passive limb movement augments ventilatory response to CO2 via sciatic inputs in anesthetized rats*. Respir Physiol Neurobiol 167, 174-180.

ÉCOLE DOCTORALE
Signalisations et réseaux intégratifs en biologie (BIOSIGNE)

Titre : L'adaptation respiratoire à la course : comportement et circuits neuronaux chez la souris

Mots clés : Respiration, Locomotion, Souris, Circuit Neuronal, Traçage Viral, Optogénétique

Résumé : Pendant la course, la ventilation augmente pour compenser la demande énergétique accrue. Le substrat, soupçonné neuronal, de cette hyperpnée à l'exercice est néanmoins toujours méconnu. Pour le caractériser, nous avons, chez la souris, examiné les interactions entre i) mouvements des membres et cycles respiratoires, et ii) réseaux neuronaux locomoteur et respiratoire. Tout d'abord, en combinant enregistrements électromyographiques (EMG) du diaphragme combinés au suivi vidéo des membres pendant la course, nous montrons que, pour une large gamme de vitesses sur un tapis roulant, la fréquence respiratoire augmente jusqu'à une valeur fixe, indépendante des vitesses de course. Surtout, les inspirations ne sont pas temporellement synchronisées avec les foulées indiquant que l'hyperpnée à l'exercice peut opérer sans signaux phasiques provenant des retours sensoriels des membres. Nous avons ensuite cherché à identifier, au sein des centres locomoteurs, les neurones déclencheurs de cette hyperpnée, ainsi que leurs cibles dans les centres respiratoires. En combinant enregistrements EMG, traçages viraux et interférences fonctionnelles, nous montrons d'une part que le principal centre de l'initiation locomotrice (la région locomotrice mésencéphalique, MLR) peut réguler à la hausse la respiration, pendant, et même avant, la course. Cet effet repose sur des projections directes de la MLR vers le générateur inspiratoire principal, le complexe préBötzinger. D'autre part, nous montrons que les circuits locomoteurs de la moelle épinière lombaire ont également une action excitatrice sur l'activité respiratoire. Cette voie ascendante cible néanmoins un autre groupe respiratoire, le noyau rétrotrapézoïde. Ce travail met ainsi en évidence la nature multifonctionnelle des centres locomoteurs, et souligne l'existence de multiples voies neuronales capables d'augmenter la respiration pendant, voire avant, la course.

Title : Respiratory adaption to running exercise: a behavioral and neuronal circuits study in mice

Keywords : Respiration, Locomotion, Mouse, Neuronal circuit, Viral tracing, Optogenetics

Abstract : During running, ventilation increases to match the augmented energetic demand. Yet the presumed neuronal substrates for this running hyperpnea have remained elusive. To fill this gap, we have, in mice, examined the interactions between i) limb movements and respiratory cycles, and ii) locomotor and respiratory neural networks. First, by combining electromyographic recordings (EMG) of the diaphragm with limb video-tracking in running mice, we show that, for a wide range of trotting speeds on a treadmill, breathing rate increases to a fixed value, irrespective of running speeds. Importantly, breaths are never temporally synchronized to strides, highlighting that exercise hyperpnea can operate without phasic signals from limb sensory feedbacks. We next sought to identify candidate trigger neurons in the locomotor central network, and their partners in respiratory centers. Combining EMG recordings, viral tracing, and activity interference tools, we first show that the prime supraspinal center for locomotor initiation (the mesencephalic locomotor region, MLR) can upregulate breathing during, and even before, running. Indeed, the MLR contacts directly and modulates the main inspiratory generator, the preBötzinger complex. We show that the lumbar locomotor circuits also have an excitatory action onto respiratory activity, but that this ascending drive targets another essential respiratory group, the retrotrapezoid nucleus. This work highlights the multifunctional nature of locomotor command and executive centers, and points to multiple neuronal pathways capable of upregulating breathing during, or possibly even prior to, running.

Université Paris-Saclay
Espace Technologique / Immeuble Discovery
Route de l'Orme aux Merisiers RD 128 / 91190 Saint-Aubin, France